Politecnico di Torino

Doctoral Program in Electrical Engineering

Reduced-cost Permanent Magnet motor drives: a comprehensive design procedure and a universal approach to the magnetic model identification and control

PhD CANDIDATE:

Barbara Boazzo

ACADEMIC TUTOR:

Prof. Alfredo Vagati

Torino, April 2014

Abstract

This research deals with the design, identification and control of Permanent Magnet Synchronous motor drives.

Throughout the project, motor and control designs have been straightly integrated in order to meet the challenging requirements, typically coming from the industrial world. Namely, the purposes leading this research activity are: cost-reduction and standardization of both design and control tasks into straightforward and universal procedures.

As a deeper insight, this work proposes a comprehensive procedure for the design of reduced-cost Permanent Magnet based electrical machines and a universal control technique, requiring minimum calibration and a simplified preliminary commissioning stage.

The recent price volatility of rare earth raw materials has been compelling designers and manufacturers of electric motors to find out or re-evaluate alternative machine topologies, using either a reduced amount of such rare-earth magnets or lower energy density magnetic materials, such as hard ferrites, still providing for high-performance technologies.

This thesis is about facing this issue, while enhancing general approaches to the optimal design of Permanent Magnet Synchronous machines via fully-analytical models showing a twofold purpose.

First, they aim at orienting the designers to the most convenient engineering trade-

offs by means of general guidelines, suitable for machines of all sizes and applications. Moreover, they offer simple closed-form equations to determine all the design variables and performance indicators of the electrical machine, making the Finite Element Analysis not mandatory, but just useful for final refinements.

Performing and compact electrical machines, such as properly designed Permanent Magnet based Synchronous motors, exhibit relationships between flux linkages and phase currents that are highly non-linear and heavily influenced by the operating magnet temperature.

As a consequence, a reliable identification procedure, with the Permanent Magnet operating temperature stabilized, is required for both control and validation purposes.

Opportunities to perform this identification test as a quick one-time self-commissioning process have been pursued during this project, working towards a version of the algorithm that would be appropriate for commercialization.

As part of this same research effort, different Direct Flux Vector control techniques will be compared to select the best candidate for a unified control algorithm. In particular, a novel predictive-adaptive control scheme has been developed, giving the key advantage of being applicable with minimum need of calibration for any Permanent Magnet motor drives under test.

Contents

Chapter 01

Motivation, goal and methodology

It is widely recognized that Permanent Magnet (PM) based electrical drives have been the most attractive candidates for many high-performance applications during the past 30 years.

PM machine topologies are distinguished from competing motor types by their capability of achieving high torque/power density figures, advantageous efficiency levels and satisfactory behaviours in the flux-weakening region. Besides, the key performance metrics of PM electrical machines, namely their low rotor inertia and compactness, are so attractive that the direct-drive configuration is preferred in a growing number of applications, with obvious rewards deriving from the elimination of speed-changing components. As a result, electrical drive configurations using PM motors have been achieving growing success in many challenging and demanding fields, such as appliance white goods, HVAC (heating, ventilating and air conditioning), electrified transportation and power generation from renewable resources.

The aforementioned challenges raise the question of how the promising performance of such electrical drive trains can be best exploited.

A convenient integration between motor and control design tasks is mandatory for finding out the most suitable answer, while facing typical industrial needs, such as cost reduction and availability of straightforward, universal procedures.

This represents the basic idea leading the research activity that will be presented.

1.1. INTRODUCTION

The research project, that will be proposed in the following, aims at fitting in the

demanding scenario, just described, by proposing:

- a comprehensive design procedure for reduced-cost rare-earths “free” PM machines
- a universal control technique, requiring minimum calibration and a simplified commissioning stage.

In other words, an industry-friendly approach to the design, identification and control of PM motor drives will be suggested.

1.1.1. Design of reduced-cost rare-earths “free” PM machines

Concerning the design, it is worth pointing out that PM based machines have always relied for their high performance on the adoption of rare-earth magnets, which offer large energy products and ideal recoil characteristics over wide ranges of temperatures.

However, the recent price volatility of rare earth raw materials has been compelling designers and manufacturers of electric motors to test alternative solutions, using no PMs [1]-[2], a reduced amount of rare-earth PMs [3]-[4], or lower energy density PMs, such as hard ferrites [5]-[12].

High-salient SR machines have been re-evaluated [1]-[2], but they do not allow to achieve performance comparable to the one of PM based electrical machines. Analogously, the mere substitution of high energy magnets with ferrite ones into standard Surface-mounted PM (SPM) and Interior PM (IPM) rotor configurations cannot lead to satisfactory designs [6]-[7], since both SPM and IPM motors rely exclusively on Nd- or Sm-based materials for their high performance [13]-[14].

A more effective way [8]-[10] to exploit either lower energy density magnets or a reduced amount of rare-earth magnetic materials is to PM-assist Synchronous Reluctance (SR) machines, having multi-layer rotor structures (i.e. valuable starting designs in terms of torque density). In this case, the magnet excitation is needed only as an additional contribute to the torque and an improvement for the Power Factor and the speed range of the drive.

Throughout the proposed work, the design of both Ferrite Assisted SR rotor

structures and rare-earth based SR machines assisted via a minimized magnets volume will be investigated. They will be considered as alternative solutions to high-performance (and high-cost) SPM designs.

For all the aforementioned PM machine topologies, a comprehensive design procedure will be developed. Specifically, general approaches to the optimal design of such PM machines will be identified referring to fully analytical per-unit models with a twofold purpose.

First, they aim at orienting the designers to the most convenient engineering trade-offs by means of general guidelines, suitable for machines of all sizes and applications. Then, they provide for closed-form equations to determine all the design variables and performance indicators of the machine under analysis. As a result, the FEA is not mandatory, but just useful for final refinements.

1.1.2. Universal control and identification of PM motor drives

As it was anticipated, this research investigates also a unified control strategy suitable for Permanent Magnet synchronous motor drives of all kinds and a preliminary commissioning process for the automated identification of the machine magnetic model.

Synchronous PM motors exhibit relationships between flux linkages and phase currents that can be highly non-linear and are heavily influenced by the operating temperature.

As a consequence, a reliable identification procedure is required for both control and validation purposes. Moreover, the PM temperature must be stabilized during such identification.

The method, that will be proposed, evaluates the flux linkages using estimates of the phase voltages, so that no voltage measurements are needed, and controls the target temperature by alternating active and idle states with proper timing. The temperature is monitored via estimation of the no-load back-emf and the experimental results on diverse test machines confirm the consistency of the approach.

Opportunities to perform the identification process as a quick one-time self-

commissioning process will also be pursued during this project, working towards a version of the algorithm that would be appropriate for commercialization.

As part of this same research effort, different Direct Flux Vector (DFV) control techniques will be compared to select the best candidate for a unified control algorithm.

The schemes, which will be evaluated, operate using stator flux variables and their main components can be derived from direct torque control standard blocks. The exploitation of the inverter voltage and current limits is very straightforward and maximum torque production is guaranteed under all operating conditions, including flux-weakening operation.

This work will focus on a predictive-adaptive control scheme, which will be compared to standard PI-based controllers. All methods will show satisfactory performance in terms of torque response, but the predictive-adaptive scheme has the key advantage that it can be applied with minimum need of calibration for any PM machine under test.

1.2. OUTLINE OF THE PROPOSED RESEARCH PROJECT

Chapter 02 serves as an introduction for the first part of the thesis, that presents comprehensive approaches to the design of diverse PM Synchronous machines, namely SPM rotor configurations, Ferrite Assisted SR motors and rare-earths Assisted SR machines, built up with a minimized PMs volume.

Chapter 03 will propose a closed-form per-unit formulation for the design of surface-mounted PM motors, which stand for reference high-performance (and high-cost) solutions. A rotating, multipolar SPM machine will be seen there as the assembly of a proper number of poles. Each pole will be modeled by means of an elementary rectified structure, whose geometric parameters will be expressed via normalized quantities for the sake of generality. Key figures of merit such as the shear stress (that is, torque density), the Power Factor and the per-unit loss per outer surface will be expressed as functions of the main design parameters. Optimal combinations of the design variables will be found out, given the type of windings (concentrated, distributed) and the cooling

setup (loss per square meter). Particular emphasis will be put on how the Power Factor can be maximized, given the shear stress, or vice versa Last, the design approach will be tested on meaningful design examples, including all winding types, and will be validated by finite-element analysis.

Chapter 04 will introduce the design of Ferrite Assisted Synchronous Reluctance machines, considering the robustness against demagnetization a prerequisite for feasible designs. The rotor geometry of one rectified machine pole will be introduced, together with the equivalent circuit adopted to model its magnetic behavior along the quadrature axis, that is the one oriented against the PMs. The geometric rules needed for enhancing the starting SR design in terms of torque ripple, and the ones required for increasing the robustness towards demagnetization of FASR motors will be summed up. The severity of the demagnetization issue will be compared to the one of other well-known constraints, as for example the thermal limit and the one related to fault conditions.

Chapter 05 will formalize the design of Ferrite Assisted Synchronous Reluctance machines via a two steps procedure. At first one rectified machine pole is analyzed and key figures of merit will be expressed in equations and discussed to derive general guidelines for high performance designs. Then, multipolar rotating machines will be modeled as the combination of multiple rectified poles within a stack cylinder having constrained outer dimensions. It will be demonstrated that, at given output torque, the number of poles can be optimized either to minimize the machine loss or to minimize the remanence of the ferrite magnets. The design approach will be FEA tested, highlighting weaknesses and strengths of the proposed design approach

Chapter 06 will present a technique to modify the rotor lamination of rare-earth based Permanent Magnet Assisted Synchronous Reluctance motors, in order to minimize the magnet volume with no side effect on performance, thus proposing another technology for cost-reduction, alternative to Ferrite Assisted Synchronous Reluctance machines.

Chapter 07 will summarize typical requirements for electrical motor drives for both production from renewable (wind) energy and automotive applications will be summarized. Practical design examples will be presented as well, comparing all the PM

configurations analyzed in the previous Chapters.

Chapter 08 will complete the validation process of the modeling theory proposed in Chapters 04 and 05 for the design of Ferrite Assisted Synchronous Reluctance machines, proving for experimental results on a prototyped lift motor.

Chapter 09 will point out the main ideas and literature references concerning the procedure for the control and identification of PM Synchronous motor drives.

Chapter 10 will describe an experimental method to evaluate the machine flux linkages, together with their relationship to the machine phase currents, using estimates of the phase voltages, so that no voltage measurements are needed. Stator resistance and inverter voltage drops are compensated for and the issue of the iron loss impact on the machine magnetic model is solved. Alternative experimental setups, each of them distinguished by diverse hardware requirements, will be presented. It will be also suggested how to control the PMs temperature during the identification procedure, since it is well known that the magnet temperature is a main cause of detuning of the motor model. Experimental results on various test machines will be provided for as well, in order to confirm the consistency of the approach.

Chapter 11 will investigate a direct flux vector control strategy, suitable for Permanent Magnet Synchronous Motor drives with minimum need of calibration. The reference voltage vector will be obtained by means of explicit equations coming from the magnetic model of the machine, but the algorithm will turn out to be insensitive to motor parameter variations, since the stator inductances are adaptively evaluated at each sample time from the observed flux components. That is, the control algorithm aims to be appropriate with no modification for all PM machines, more or less salient or saturated, with no need of regulator tuning. The experimental tests, performed on a Permanent Magnet Assisted Synchronous motor drive, are presented to validate the proposed control algorithm and compare its performance with the ones of more standard controllers, based on proportional-integral regulators.

Chapter 02

Introduction to Part I:
"Design of reduced-cost PM machines via a general procedure and comparison to the state of art"

During recent years, both producing and using electrical energy with higher efficiency have been showing a big impact on regulating the negative effects of human activities on the earth's ecosystem. In other words, high-performance electrical machines have been achieving growing success in many challenging application fields, including electric motion and energy conversion.

Traditionally, Induction Machine (IM) [15] has been the most stronghold technology employed in applications that require electric actuators, since its invention by Nicola Tesla more than 160 years ago. The most common IM is the Alternating Current (AC) three phase, low voltage (LV), 4-pole, continuous duty, totally enclosed, fan cooled, asynchronous squirrel cage motor. This machine relies on the slip concept for torque production, provided that the rotor rotates, with a small slip frequency, lowlier than the synchronous speed of the stator field. Induction motors are appreciated because of their low price, simple network connection or inverter drive, good availability, simple construction and high reliability [16].

Since the 1980s, inverters with decreasing semiconductor costs and system energy savings have been available in the marketplace and alternative motor technologies have come up to light.

One of these competing solution is represented by Synchronous Reluctance (SR) machines [1]-[2], which exploit exclusively the rotor anisotropy for torque production.

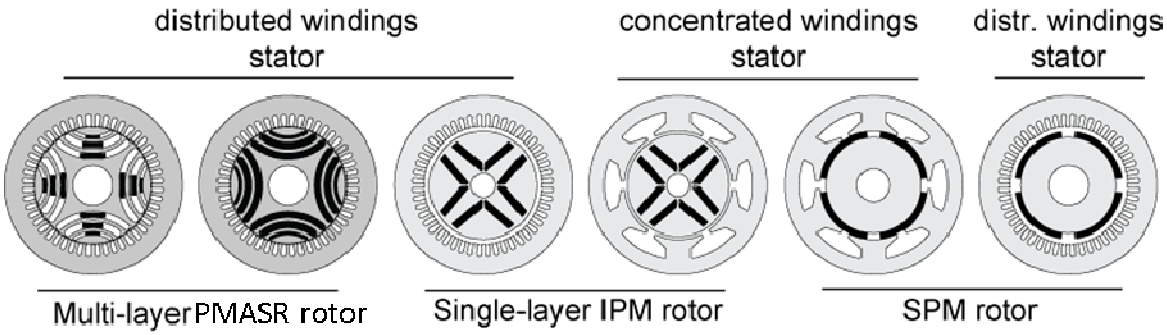

Figure 2.1 – Different rotor and stator Permanent Magnet machine configurations.

Among the others, Permanent Magnet (PM) based motors do stand for the most promising solution towards an "ideal" concept of electrical machine.

PM electrical machines are Synchronous machines (meaning that they run at synchronous speed), equipped with magnetic material in the rotor. The torque production mechanism is based on the interaction between the PM flux and the stator rotating field. Moreover, the rotor anisotropy (if present) can give an additional contribute to the torque.

Throughout years, as pointed out by Figure 2.1, many different PM motor types have been proposed, resulting in a very flexible offer.

Permanent Magnet machines can be distinguished by the rotor type:

- Surface mounted PM (SPM);
- Interior PM (IPM);
- Permanent Magnet Assisted SR (PMASR).

IPM and, above all, PMASR solutions take advantage conveniently of the magnetic saliency, typical of their rotor topologies, to produce the output torque and, thus, need a reduced PM quantity. IPM rotors usually have one or two layers of magnets embedded into the rotor stack. PMASR configurations are derived from multi-layer high-salient SR rotor structures, again by adding the magnets inside the rotor flux barriers.

The mixing of the two players (PMs and saliency) in producing the torque results in very flexible characteristics and a huge variety of configurations [19], classified in Figure 2.2, where the machine types of Figure 2.1 are organized inside a normalized plane with

the PM "quantity" varying along the horizontal axis and the magnetic saliency being increased along with the vertical axis. In Figure 2.3, main fields of application are also indicated.

Besides being classified according to the rotor structure, Permanent Magnet based machines do also difference for the stator configurations, that can be realized via:

- distributed windings (overlapping copper coils);

or

- concentrated windings (non overlapping copper coils).

Distributed coils are the traditional configuration of 3-phase AC machines and are preferably adopted in case of salient IPM and PMASR rotors, since the low harmonic content do not affect the achievable saliency ratio between the direct and quadrature axis.

Concentrated stator windings, which are more conveniently combined with SPM rotor configurations, drastically improve the fault-tolerance and are likely adopted in actuators and generators for aerospace [17]. Furthermore, concentrated-winding machines are suitable for low speed, high torque applications, such as wind generators, showing a relatively low short-circuit current in case of fault, that is also appreciated. Recently, it turned out that designs with concentrated windings get compatible also with traction specifications, if properly designed [18].

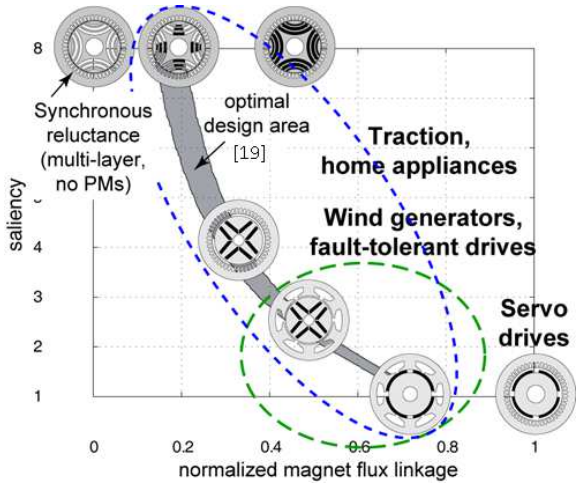

Figure 2.2 – PM based machines classification according to rotor saliency ratio and the normalized magnet flux linkage.

When dealing with the design of Permanent Magnet electrical machines, different techniques are available for modeling their magnetic behavior.

Analytical studies can be adopted, at least in the earliest design stages. Closed-form models, investigated throughout the literature, are based either on the elementary Gauss's and Ampere's laws or on more and less complicated lumped parameter magnetic circuits.

As both an alternative and a validating instrument, Finite Element Analysis (FEA) methods are considered. They are numerical techniques which determine the distribution of the electromagnetic fields inside the machine structure by solving the Maxwell's equations. They are well–suited to be applied to structures showing complex geometries and highly saturated magnetic behaviors.

The first part of this thesis will focus on the design of:

- Permanent Magnet machines of the Surface-Mounted type, equipped with rare-earth magnets.
- High-salient SR rotor structures, assisted either via low-cost ferrite magnets or a minimized quantity of performing and expensive rare-earth magnetic material.

The first machine type is considered as a high-performance (and high-cost) reference design, reduced-cost Magnet Assisted solutions are required to compete with.

All the aforementioned motor topologies will be studied by means of a fully analytical model, able to guide effectively the main design choices.

Finite Element Analysis and experiments will be introduced for validation purposes.

Chapter 03

High performance (and high cost) SPM machines as reference competitors to reduced-cost PM motors. A comprehensive approach to their design.

Permanent magnet (PM) synchronous machines are widely recognized for their performance, in terms of both torque density and efficiency. In particular, direct-drive machines of the surface mounted PM type (SPM) have been increasingly adopted as motor and/or generators in many up to date applications, such as traction and propulsion, aerospace and energy production from renewable resources [20]. Recently, the price of rare earth magnets, that are the ones SPM machines rely on for their high performance, have suffered from a significant volatility. Yet, according to recent works [20]-[21], the interest for rare-earth PM based electrical machines is high, at least as reference concurrent designs to reduced-cost PM ones. Even if distributed winding SPM machines are still adopted in many applications, over the last decade, a lot of effort has been devoted to the investigation of concentrated winding machines, for their better fault tolerance, ease of manufacturing, shorter end connections and advantageous copper filling factor [17], [21]-[28].

This chapter proposes a comprehensive design approach, suitable for three-phase SPM machines. The per-unit analysis is mainly devoted to direct-drive applications. That is, those applications, for which it is typical to have low speed values and high pole pairs number. Anyway, the investigation, that covers distributed and concentrated winding types and is based on simple analytical formulas, can be extended to any kinds of SPM machines without a significant loss of accuracy.

A rotating, multipolar SPM machine is seen here as the assembly of a proper number

of poles. Each pole is modeled by means of an elementary rectified structure, whose geometric parameters are expressed via normalized quantities for the sake of generality. Key figures of merit such as the shear stress (that is, torque density), the Power Factor and the per-unit loss per outer surface will be expressed as functions of the main design parameters.

Optimal combinations of the design variables will be found out, given the type of windings (concentrated, distributed) and the cooling setup (loss per square meter).

Particular emphasis is put on how the Power Factor can be maximized, given the shear stress, or vice versa. When the required shear stress is fixed, without further constraints on the Power Factor value, it is preferable to keep the PF as high as possible, since:

- a low Power Factor negatively affects the size of the power converter;
- disadvantageous Power Factor levels make the machine more prone to load-dependent core saturation, leading to torque reduction.

Conversely, for other applications it is first and foremost the Power Factor to be constrained. For example, it occurs when a wide Constant Power Speed Range is needed and, thus, as it will be demonstrated in Chapter 07, the nominal current is recommended to be close to the characteristic (or short circuit) one. In that cases, given the Power Factor, it might be necessary to maximize the achievable shear stress compatibly with the steady state thermal constraint.

The machine inductance will sort out to be the key design parameter to be minimized either for maximizing the Power Factor at given shear stress or, vice versa, for optimizing the shear stress at given Power Factor (so that the thermal limit, instead of the PF constraint, does still represent the most severe limitation to the torque capability). The minimum inductance condition, which has relevance especially for fractional-slot SPM machines, will be identified analytically with reference to the basic rectified SPM pole. Eventually, a design flowchart will be proposed: it will suggest how to design the final rotating machine, at given specifications and into a constrained envelope, starting from the analyzed rectified blocks and, depending on the application and the type of stator winding, remarking the convenience of fulfilling the minimum inductance

condition.

The design procedure, that will be proposed, has been applied to several machine examples, with alternative stator and rotor configurations and different characteristics, in terms of both size and application. At the end of this Chapter, with reference to some relevant examples, the model results will be compared to the respective FEA data, for proving the accuracy of the analytical model and showing the effectiveness of the developed design procedure. Conversely, the resultant performance of this reference technology in different application fields will be discussed later in this work, after introducing competitive reduced-cost solutions, SPM machines will be compared to.

3.1. PERFORMANCE INDICATORS AND MODEL OF A SPM POLE

3.1.1. Reference geometry

The elementary block reported in Figure3.1 represents one rectified pole of a SPM machine. The main geometric parameters, defined in Figure 3.1, are:

- the pole pitch a (for both distributed and concentrated winding);
- the tooth length l_t;
- the PM length l_m.

They will be normalized by the airgap length g throughout the analysis, for the sake of generality.

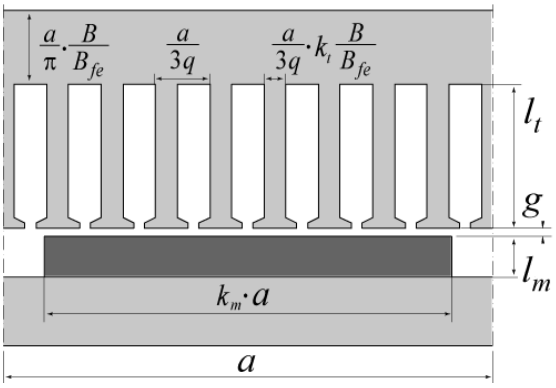

Figure 3.1 - Elementary block, corresponding to one SPM rectified pole. The example has distributed stator windings with q=3 slots per pole per phase.

l is the stack length of the reference block and another key parameter is the number

of slots per pole per phase q, which is an integer for distributed windings and a fraction for concentrated stator windings, of course. Further variables (e.g. k_m, B_{fe}, k_t), that have to do with the pole geometry, are also evidenced in Figure 3.1: their meaning will be clarified later during the analysis.

3.1.2. Magnetic loading

The magnetic loading $B_{gap,m}$(3.1) represents, here, the peak of the fundamental flux density waveform produced by the magnets at no load in the airgap.

$$B_{gap,m} = k_b \cdot \frac{B_r}{1 + k_c \cdot \frac{g}{l_m}} \tag{3.1}$$

B_r is the PM remanence, k_c is the Carter coefficient and k_b (3.2) is a shape factor that quantifies the fundamental harmonic, given the magnets' pole arc (that is $k_m.\pi/2$in electrical radians).

$$k_b = \frac{4}{\pi} \cdot sin\left(k_m \cdot \frac{\pi}{2}\right) \tag{3.2}$$

Apart from the Carter coefficient, and given the airgap length, the no load magnetic loading (3.1) is independent of the rotor pole pitch a and it does depend on rotor parameters only. In particular, Equation (3.1) points out that, over certain values, e.g. l_m/g = 6, it is not convenient to further increase the magnet thickness to improve $B_{gap,m}$. But, since the normalized PM thickness l_m/g determines the stiffness of the machine against demagnetization, besides the magnetic loading, sometimes strengthening the magnet heights is required by special overload needs and related demagnetization issues. In that cases, specific countermeasures to increase the robustness of the machine against demagnetization can be adopted and a careful analysis of the magnets stiffness in fault conditions might be required [29].

3.1.3. Electric loading and shear stress

As usual, the electric loading is defined by (3.3):

$$A_q = \frac{3}{2} \cdot \frac{N}{a} \cdot k_w \cdot I_q \tag{3.3}$$

where k_w is the winding factor, N is the number of conductors in series per pole per phase. I_q is the phase current amplitude. As reminded by the subscript "q", it is implicitly intended that the current vector is aligned with the quadrature axis, since this position is representative of the maximum force (torque) per Ampere situation.

In case of SPM machines, the torque is given by the interaction between the quadrature electric loading and the magnetic loading produced in the airgap by the PMs. Thus the average shear stress σ(3.4),that symbolizes the time-averaged tangential force acting on one machine pole, divided by its airgap surface. is simply determined by the product of $B_{gap,m}$ and A_q:

$$\sigma = B_{gap,m} \cdot A_q \tag{3.4}$$

Once the PM grade, shape and thickness are set, the magnetic loading (3.1) is univocally determined. In other words, the shear stress depends on the electric loading (3.3) only. The upper limits for the q-axis current loading are either related to the aforementioned demagnetization constraint or the Joule loss one (i.e. thermal limit or efficiency target, as it will be recalled later).

3.1.4. Specific Joule loss

The Joule loss factor $k_{j,block}$ (3.5), expressed in W/m^2,is obtained by dividing the copper loss of the elementary block in Figure 3.1 per its outer surface

$$k_{j,block} = \frac{2\rho_{Cu} k_{end}}{k_{Cu}(1 - bk_t)} \cdot \left(\frac{A}{k_w}\right)^2 \cdot \frac{1}{l_t} \tag{3.5}$$

ρ_{Cu} is the electric resistivity of copper; k_{Cu} is the slot filling factor (net copper over slot cross section); k_{end} is the length of the conductors, including their end connections, in per-unit of the active length of the machine. In (3.5) the current loading A coincides with its quadrature axis component, since the direct one is supposed to be null, as in the best control strategies.

The subscript "block" anticipates that the specific Joule loss of the rotating machine needs to be computed in a slightly different way. In fact, for modeling purposes, the heat rate density k_j of the final rotating machine will be reasonably referred to its outside

surface, but, at this stage, the adopted rectified geometry does not allow to distinguish between the airgap block surface and the outer one.

The Joule loss factor (3.5) turns out to be influenced neither by the pole pitch nor by the airgap length.

However, of course, the Joule losses, together with their specific value, do depend on the copper slot area and this explains why Equation (3.5) involves both the stator tooth length l_t and the term $(1-b\cdot k_t)$, which is indicative of the slot width (in per-unit of the respective slot pitch).

The definition of the normalized slot width via the difference $(1-b\cdot k_t)$ comes from the rules selected for sizing the stator back iron. In fact, throughout the analysis, it will be assumed to fix properly the target flux density (B_{fe}) in the stator core, at no load, and b (3.6) will represent the ratio between the no load flux density produced in the airgap by the PMs and such goal value B_{fe}.

$$b = \frac{B_{gap,m}}{B_{fe}} \tag{3.6}$$

As a consequence, both the stator tooth width w_t (3.7) and the yoke height l_y (3.8) will be univocally determined by the ratio b (3.6), together with the pole pitch a and the number of stator slots per pole per phase q.

$$w_t = b \cdot k_t \cdot \frac{a}{3q} \tag{3.7}$$

$$l_y = b \cdot \frac{a}{\pi} \tag{3.8}$$

The tooth scaling factor k_t in (3.7) is typically in the range 0.7-0.9, depending on the stator winding type.

When dealing with low-speed applications, the per-unit factor k_j (3.5) describes with good approximation the heat dissipation capability of the motor and it is also synonym of its efficiency, since the Joule losses represent the main contribute to the overall losses. This highlights the key role played by the stator tooth length l_t in improving the efficiency of the machine and fulfilling the k_j upper constraint, determined by the cooling

set up. Anyway, the tooth length impacts also the mass (and cost) of the active parts, compelling the designers to trade-off choices for all applications.

This issue will be addressed while illustrating the final design procedure and more detailed information about the impact of the iron and magnets loss on the efficiency of SPM machines will be given as well, distinguishing between different application fields.

The whole design space will be investigated and the area where the factor k_j is actually representative of the total loss of the motor will be identified, specifically for low speed direct-drive applications.

3.1.5. Power Factor

The vector diagram, referring to one machine pole, is reported in Figure 3.2. The current vector is in time quadrature with the PM flux linkage (λ_m) and the stator resistance voltage drop is neglected. The PF angle φ (3.9) can be expressed in normalized quantities as follows:

$$\tan\varphi \cong \frac{4\mu_0}{3\pi} \cdot L_{pu} \cdot \frac{A_q}{B_{gap,m}} \tag{3.9}$$

where L_{pu}, which represents the inductance of one machine pole, is considered in normalized quantities. This is reminded by the subscript "*pu*", that stands for "per-unit" and the respective base value is (3.10), being *l* the stack length.

$$L_{base} = \frac{\mu_0 \cdot l}{2} \cdot \left(\frac{2}{\pi} \cdot k_w \cdot N\right)^2 \tag{3.10}$$

Provided that rare earth magnets are used in standard SPM machines, the factor $B_{gap,m}$ in (3.9) has very little variations when changing from one prototype to another.

It follows that, according to (3.4), the per-unit inductance directly relates the Power Factor to the shear stress (read, torque density).

At given shear stress and without further limitation on the Power Factor value, the angle φ can be conveniently optimized by minimizing the per-unit inductance so to reduce the size of the power converter and limit the load-dependent core saturation effects. Vice versa, when a wide constant power speed range is desired and the machine

flux weakening capability is improved making the rated current close to the short circuit one, the Power Factor angle is required to be around $\pi/4$ ($\tan\varphi = 1$) and again the achievable shear stress is maximized when the machine inductance is minimized. Anyway, in this case, a more severe limitation to the maximum shear stress might comes from the thermal limit on the feasible current loading.

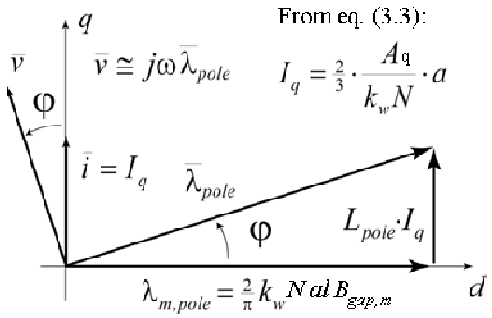

Figure 3.2 - Vector diagram of a SPM machine pole with the current vector in quadrature with the PMs flux linkage.

The considerations about the inductance minimization are of little importance with distributed windings, but it can become critical for fractional slot machines, especially the single layer ones, for which wrong design choices can lead either to impractical values of the Power Factor (at given shear stress) or, even if more rarely, to unsatisfactory shear stress levels (at given Power Factor and limited thermal current loading).

3.2. MINIMUM INDUCTANCE CONDITION

3.2.1. Normalized inductance and its minimization

The inductance L_{pu} (3.11) of the elementary block in Figure3.1 is the sum of the slot leakage component $L_{slot,pu}$ and the airgap inductance $L_{g,pu}$, which includes the overall harmonic content, besides the fundamental contribute.

$$L_{pu} = L_{g,pu} + L_{slot,pu} \tag{3.11}$$

The two terms in (3.11), normalized by (3.10), depend on the geometric variables defined in Figure 3.1 via expressions that are different for distributed (integer q) and concentrated (fractional q) windings, as it will be shown in the next subsections.

3.2.1.1. Distributed stator windings

As for distributed windings, the magnetizing inductance is given by (3.12), whereas the slot inductance expression is (3.13).

$$L_{g,pu} = \frac{\pi^2}{6 \cdot k_w^2} \cdot \frac{\frac{a}{g}}{k_c + \frac{l_m}{g}} \left[1 - \frac{(q-1)^2}{q^3} - \frac{n_{sp}}{4q} \left(1 - \frac{10q - 13 - n_{sp}(2q-1)}{2q^2} \right) \right] \quad (3.12)$$

$$L_{slot,pu} = \frac{\pi^2}{2k_w^2} \cdot \frac{\frac{l_t}{g}}{(1 - bk_t)} \cdot \left(\frac{a}{g} \right)^{-1} \cdot \left(1 - \frac{3n_{sp}}{16q} \right) \cdot k_{tip} \quad (3.13)$$

The factor k_{tip} (3.14) quantifies the inductance increase of a semi-closed slot with respect to an open one, due to the tooth tip shoe.

$$k_{tip} = 1 + \frac{b}{2} \cdot \frac{(1 - bk_t)^2}{k_{so}} \cdot \left(\frac{a}{g} \right) \cdot \left(\frac{l_t}{g} \right)^{-1} \cdot \frac{\left(1 - \frac{n_{sp}}{4q} \right)}{\left(1 - \frac{3n_{sp}}{16q} \right)} \quad (3.14)$$

The tooth tip shoe is as wide as the slot opening at the airgap is and as long as to guarantee that the steel is exploited locally according to the target flux density B_{fe}. The factor k_{so} stands for the slot opening at the airgap, expressed in per-unit of the slot pitch. Always with reference to the slot pitch, the normalized tooth tip length is defined via the expression $0.5 \cdot b \cdot (1 - b \cdot k_t)$.

Equations (3.12) and (3.13) are valid for any integer number of stator slots per pole per phase. They include the cases of both full-pitched and short-pitched coils, being n_{sp} the number of slots with conductors belonging to different phase windings.

Anyway, it is worth pointing out that, as evidenced by in the graphs of Figures 3.4-3.7, the results for q=2 (full pitch)are very similar to the ones obtained for q=1.Analogous conclusion can be drawn for all q values. Moreover, most of the machines with many poles (i.e. the ones are being mainly considered here) have a low number of stator slots per pole (namely, q=1).

In other words, for distributed windings machine, q is not a critical parameter with respect to the inductive behavior of the machine.

From (3.12) it sorts out that $L_{g,pu}$ is proportional to the ratio a/g. On the contrary, if the tooth length to airgap ratio l_t/g is fixed, $L_{slot,pu}$ (3.13) results inversely proportional to

a/g (3.13). Or better, since in (3.13) the airgap g can be simplified in the two terms l_t/g and $(a/g)^{-1}$, the slot inductance is actually proportional to l_t/a, whatever the airgap length is. The form of (3.13) was purposely chosen for having all the geometric dimensions normalized by the airgap g.

The dashed curves in Figure 3.3 show that the per-unit inductance, sum of (3.12) and (3.13), has a minimum for a precise a/g value.

The minimum inductance condition occurs when the pole pitch to airgap ratio is equal to $a/g|_{Lmin}$ (3.15):

$$\left.\frac{a}{g}\right|_{Lmin} = \sqrt{\frac{3 \cdot \frac{l_t}{g} \cdot \left(1 + \frac{l_m}{g}\right)}{1 - bk_t}} \tag{3.15}$$

It minimizes the overall pole inductance and the respective minimum inductance $L_{pu}|_{min}$, which includes both the magnetizing contribute and the slot leakage term, is defined via (3.16).

$$\left.L_{pu}\right|_{min} = \frac{1 + k_{tip}}{2} \cdot \frac{\pi^2}{\sqrt{3}k_w^2} \sqrt{\frac{\frac{l_t}{g}}{\left(1 + \frac{l_m}{g}\right) \cdot (1 - bk_t)}} \tag{3.16}$$

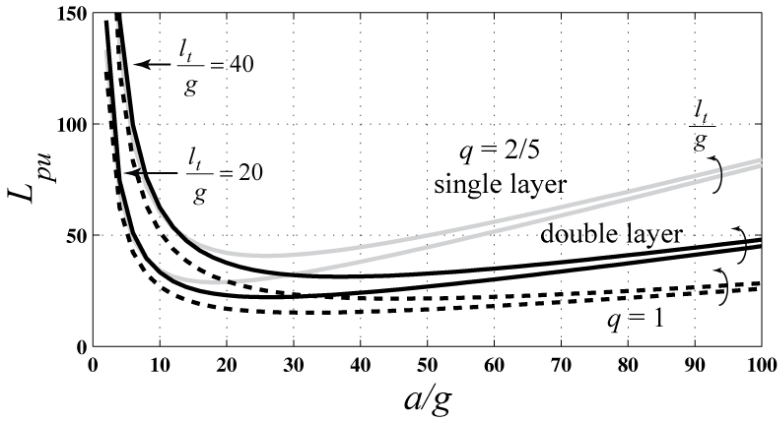

Figure 3.3 - Per-unit inductance versus pole pitch to airgap ratio. The examples refer to q=1 and q=2/5(single and double layer). l_m/g = 6 and l_t/g is a parameter.

The tooth to airgap length ratio l_t/g has effects on (3.15) and (3.16), as it can be seen also in Figure 3.3, and the optimal pole pitch (3.15) depends on l_m/g, besides the per-unit stator tooth length l_t/g.

3.2.1.2. Concentrated stator windings

Regarding fractional slots machines, the slot inductance is expressed by (3.17):

$$L_{slot,pu} = \frac{\pi^2}{2k_w^2} \cdot \frac{\frac{l_t}{g}}{(1 - bk_t)} \cdot \left(1 - \frac{3 \cdot (n_l - 1)}{4 \cdot Q_o}\right) \cdot \left(\frac{a}{g}\right)^{-1} \cdot k_{tip} \tag{3.17}$$

where n_l is the number of layers: it is equal to one in case of single layer configurations, whereas n_l = 2 stands for double layer stator windings. Obviously, if n_l =1, Expression (3.17) equals (3.13) and the factor k_{tip}, that accounts for the inductance increase of a semi-closed slot with respect to an open one due to the tooth tip shoe, needs to be modified as suggested by (3.18):

$$k_{tip} = 1 + \frac{b}{2} \cdot \frac{(1 - bk_t)^2}{k_{so}} \cdot \left(\frac{a}{g}\right) \cdot \left(\frac{l_t}{g}\right)^{-1} \tag{3.18}$$

In (3.17), Q_0 [25] is the number of slots corresponding either to half the "basic" periodicity of the machine, for those q where anti-periodic symmetry conditions apply, or to the full "basic" period, when they do not. In other words, the number Q_0, descending directly from q, represents the minimum number of slots to be simulated when symmetry boundary conditions (anti-periodic or periodic, respectively) are adopted.

The magnetizing inductance $L_{g,pu}$ of one SPM fractional slot pole is quantified by (3.19), for both single and double layer windings:

$$L_{g,pu} = \frac{1}{n_l} \cdot \frac{\pi^2}{12(qk_w)^2} \cdot \left(\frac{\frac{a}{g}}{k_c + \frac{l_m}{g}}\right) \tag{3.19}$$

Equation (3.19) says that the airgap inductance of a double layer machine is half the one of a single layer machine, having the same geometry, and this applies to any q values.

Expressions (3.12) and (3.13), that identify the airgap and slot leakage inductances of distributed winding SPM machines, were not derived, since they are currently available in the literature. Conversely, the general formulation, proposed by (3.17) and (3.19), is absolutely new and requires to be demonstrated.

The magnetizing phase inductance $L_{g,pole}$ of one machine pole accounts for self ($L_{g,aa,pole}$) and mutual coupling ($M_{g,ab,pole}$) contributions, as shown by (3.20)

$$L_{g,pole} = \frac{1}{2p} \cdot \left(L_{g,aa,pole} - M_{g,ab,pole}\right) \tag{3.20}$$

The two terms $L_{g,aa,pole}$and $M_{g,ab,pole}$come, in turn, from the integration of the winding functions N_a (phase a) and N_b (phase b) [26]. In formula:

$$L_{g,pole} = \frac{\mu_0 l \cdot a}{k_c g + l_m} \cdot \left[\frac{1}{2\pi} \cdot \left(\int_{-\pi}^{\pi} N_a^2 d\vartheta - \int_{-\pi}^{\pi} N_a N_b d\vartheta\right)\right] \tag{3.21}$$

All the feasible fractional stator winding configurations can be categorized, by grouping altogether the q values having exactly the same a and b winding functions over one "basic" periodicity of the machine.

TABLE 3-I
EXAMPLES OF WINDING FUNCTIONS INTEGRALS

q	BASIC SLOTS	BASIC POLES	LAYERS	$\frac{1}{2\pi}\int_{-\pi}^{\pi} N_a^2 d\vartheta$	$-\frac{1}{2\pi}\int_{-\pi}^{\pi} N_a N_b d\vartheta$	TOTAL
$^1/_2$	3	2	2	$\frac{N_{slot}^2}{18}$	$\frac{N_{slot}^2}{36}$	$\frac{N_{slot}^2}{12}$
$^1/_4$		4				
$^1/_8$		8				
$^1/_{10}$		10				
$^1/_2$	6	4	1	$\frac{5N_{slot}^2}{36}$	$\frac{N_{slot}^2}{36}$	$\frac{N_{slot}^2}{6}$
$^1/_4$		8				
$^1/_8$		16				
$^1/_{10}$		20				
$^3/_8$	9	2	1	$\frac{N_{slot}^2}{4 \cdot 81}$	$\frac{N_{slot}^2}{8 \cdot 81}$	$\frac{N_{slot}^2}{12}$
$^3/_{10}$		4				
$^2/_5$	12	10	1	$\frac{N_{slot}^2}{6}$	0	$\frac{N_{slot}^2}{6}$
$^2/_7$	12	14	2	$\frac{N_{slot}^2}{12}$	0	$\frac{N_{slot}^2}{12}$

The results of the classification are summarized in Table 3-I, where most of the commonly-used q values are reported. All the slot/pole examples have a winding factor equal or greater than 0.866, with the "basic slots" number limited to 12 for space

reasons. As evidenced in Table 3-I, the winding configurations that belong to the same group do differ for the number of "basic" slots and poles fitting into one elementary periodicity. However, all the q values, that are in the same category, lead to the same results, when integrating the two terms in square brackets in (3.21), since, as said, the respective winding functions are the same.

Moreover, it turns out that the sum of the two integrals in (3.21) is always equal to $N_{slot}^2/(6n_l)$, being N_{slot} the number of conductors per slot. Since N_{slot} is equal to N/q, the results of Table 3-I, together with (3.21), fully demonstrate the validity of (3.19). More in detail, by substituting the term in square bracket in (3.21) with the ratio $N_{slot}^2/(6n_l)$, Equation (3.22) is found:

$$L_{g,pole} = \frac{\mu_0 l \cdot a}{k_c g + l_m} \cdot \frac{1}{6n_l} \cdot \left(\frac{N}{q}\right)^2 \tag{3.22}$$

And, afterwards, the normalization of (3.22) by L_{base} (3.10) leads to (3.19).

Regarding the derivation of the slot inductance, the theory suggests that the leakage contribute corresponding to each stator slot is determined by the slot shape (supposed here to be rectangular, as an example) and its dimensions (namely, l_t and w_{slot}). In formula, if a slot is filled in with N_{slot} conductors, all belonging to the same phase, the respective leakage inductance L_{1slot} is (3.23).

$$L_{1slot}|_{n_l=1} = \frac{1}{3}\mu_0 \cdot l \cdot N_{slot}^2 \cdot \frac{l_t}{w_{slot}} \tag{3.23}$$

From the definition of the stator back iron dimensions (3.6)-(3.8), the slot width w_{slot} results to be equal to (3.24):

$$w_{slot} = \frac{a}{3q}(1 - bk_t) \tag{3.24}$$

So, if $n_l = 1$, the slot leakage inductance of one SPM pole ($L_{slot,pole}$) is defined by (3.25):

$$L_{slot,pole}\big|_{n_l=1} = \mu_0 \cdot l \cdot N^2 \cdot \frac{1}{1 - bk_t} \tag{3.25}$$

where both $N_{slot} = N/q$ and (3.24) have been substituted, taking into account that $L_{slot,pole}$ is q times L_{1slot}.

Eventually, the normalization of (3.25) by L_{base} (3.10) leads to (3.26), that is equivalent to both (3.13) and to (3.17), when $n_l = 1$.

$$L_{slot,pu}\big|_{n_l=1} = \frac{\pi^2}{2k_w^2} \cdot \frac{l_t}{a} \cdot \frac{1}{1 - bk_t} \tag{3.26}$$

However, in double layer windings (i.e. n_l=2), different phases share the same slot and the effect of mutual couplings reduces the resulting pole inductance, as well described in [26]. The mutual term acts differently according to the phase angle shift between the currents which flow into the conductors lying in the same slot. Again, by testing all the feasible fractional q combinations, it sorted out that concentrated stator windings can be grouped in a convenient way.

TABLE 3-II
VALUES OF Q_0 FOR EXAMPLE DOUBLE LAYER COMBINATIONS

"BASIC" SLOTS	3				9		12		15		18	
"BASIC" POLES	2	4	8	10	4	8	10	14	14	16	14	22
Q_0	3				9		6		15		9	

This time, all the possible q configurations ended up with showing the same behavior when the number of slots Q_0 is the same. That is, when the number of slots to be simulated in case of periodic or anti-periodic boundary condition is the same. Table 3-II condenses and categorizes all the possible situations.

According to the classification proposed by Table 3-II, it is possible to demonstrated that, in case of double layer windings, the normalized slot leakage inductance of one SPM pole is increased, with respect to the one of a similar pole with single layer concentrated windings, by a factor that is inversely proportional to Q_0.

$$L_{slot,pu}\big|_{n_l=2} = \left(1 - \frac{3}{4 \cdot Q_o}\right) \cdot L_{slot,pu}\Big|_{n_l=1} \tag{3.27}$$

In formula, Equation (3.27) quantifies this increase and the expression, proposed to evaluate the slot-leakage inductance of one block in normalized term, is then derived.

In Figure 3.3 the per-unit pole inductance, which includes both the components (L_g and $L_{slot,pu}$) that have just been calculated, is reported as a function of a/g for the example

winding q=2/5, in both single and double layer configuration. The curves corresponding to q=1 and q= 2 are plotted as well, for the sake of comparison.

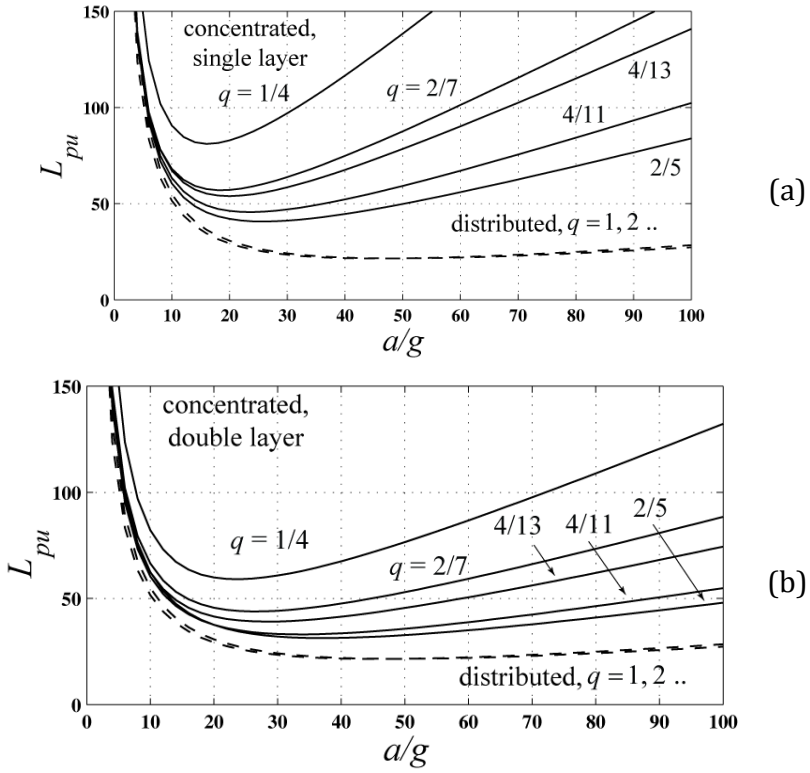

Figure 3.4 - Per-unit inductance versus pole pitch to airgap ratio (l_m/g = 6 and l_t/g = 40). a) Single layer machines compared to integral q ones; b) Double layer machines compared to integral q ones.

Double layer machines tend to have a lower inductance than single layer ones, as it is intuitive, and they have the minimum inductance condition at larger pole pitch values. The comparison between fractional machines having different q is reported in Figure3.4a, for single layer machines, and in Figure3.4b, for double layer ones. The two figures also show the curves for integral q, which, as said, are all very similar independently from q being 1, 2 or more.

The minimum inductance condition (3.28) and the minimum inductance value (3.29) can be quantified also for fractional slot machines.

$$\left.\frac{a}{g}\right|_{Lmin} = q\sqrt{\frac{6n_l \cdot \left(1-\frac{3\cdot(n_l-1)}{4\cdot Q_o}\right)\cdot\frac{l_t}{g}\cdot\left(1+\frac{l_m}{g}\right)}{(1-bk_t)}} \tag{3.28}$$

$$L_{pu}\big|_{min} = \frac{1+k_{tip}}{2}\cdot\frac{1}{q}\cdot\frac{\pi^2}{\sqrt{6}k_w^2}\sqrt{\frac{\frac{l_t}{g}\cdot\left(1-\frac{3\cdot(n_l-1)}{4\cdot Q_o}\right)}{n_l\cdot\left(1+\frac{l_m}{g}\right)\cdot(1-bk_t)}} \tag{3.29}$$

In this case, the minimum inductance pole pitch (3.28) is proportional to q, whereas it was insensitive to q in (3.15), for distributed winding machines, and also the minimum inductance value (3.29) varies a lot from one fractional q to another, as it is verified by Figure 3.4.

This accounts for how critical the choice of q can be when designing a fractional slot machine, if keeping the power factor within the limits (or maximizing the shear stress at given PF and cooling set up) is mandatory.

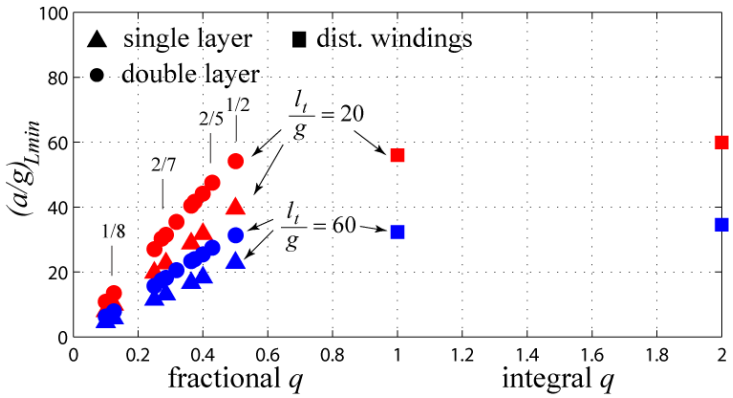

Figure 3.5 - Pole pitch factor that minimizes the machine inductance, as a function of the number of slots per pole per phase. l_t/g is a parameter

3.2.2. Minimum inductance machines

Machines having minimized inductance are compared in this subsection, meaning that their pole pitch satisfies (3.15), for integral q, and (3.28) for fractional q, at given stator tooth length l_t/g.

Figure 3.5 reports the optimal pole pitch as a function of the number of slot per pole per phase. In case of cylindrical machines all having the same rotor diameter, such a/g values represents a measure of the number of pole pairs, in inverse proportion. From Figure3.5, it sorts out that:

- fractional slot machines tend to have a smaller $a/g|_{Lmin}$ and then a higher number of poles, when the minimum inductance criterion is satisfied.

- minimum inductance double layer machines can be similar to integral slot ones, in terms of pole pairs number, for values such as q = 1/2 or 2/5.
- low q machines and single layer machines are forced to have a high number of poles (low a/g) for keeping the inductance low.

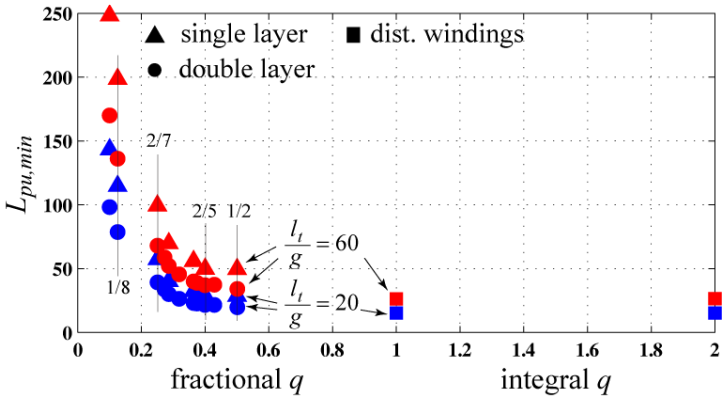

Figure 3.6 - Minimum pole per-unit inductance as a function of the number of slots per pole per phase and with the tooth length l_t/g as a parameter

Figure 3.6 reports the minimum values of the per-unit pole inductance (3.16) and (3.29), as function of the number of stator slots per pole per phase q and the normalized stator tooth length l_t/g. The plots give evidence of the considerations anticipated when Figure 3.3 and Figure 3.4 were discussed. To summarize, Figure 3.6 points out, once more, that:

- the behaviour of integral slot machines is insensitive to q, whereas the one of fractional slot ones is strictly dependant of q.
- the minimum inductance is inversely proportional to the fractional q, and is still very large for low values of q(such as 1/8 or 1/10).

3.2.2.1. Maximum Power Factor at given shear stress

As it was demonstrated, at given shear stress value, the per-unit inductance fully determines the Power Factor, once the rotor parameters are defined. Specifically, at given rotor geometry, all the "minimum inductance machines" are also the "maximum Power Factor machines".

In Figure 3.7, SPM machines, all having the same shear stress, are evaluated and their maximum Power Factor is reported for different q values, following the pole pitch

conditions of Figure 3.5 and considering the minimized inductances of Figure 3.6. The shear stress, chosen to produce the example plots of Figure 3.7, is a value typical of heavily loaded wind turbine generators. In fact, the more the shear stress (namely, the q-axis current loading) is increased, the more the Power Factor is critical. A demanding shear stress equal to 62.5 kN/m^2 was fixed and the magnetic loading (3.1) was evaluated, supposing to have rare-earths PMs in the rotor. That is, l_m/g = 6, B_r = 1.12 T and k_b = 1.15 were selected as indicative values. According to (3.4), also the electric loading was computed and its value, common to all the machines under comparison, turned out to be 55 kA/m. Eventually, the Power Factor came from (3.9), leading to the plots in Figure3.7.

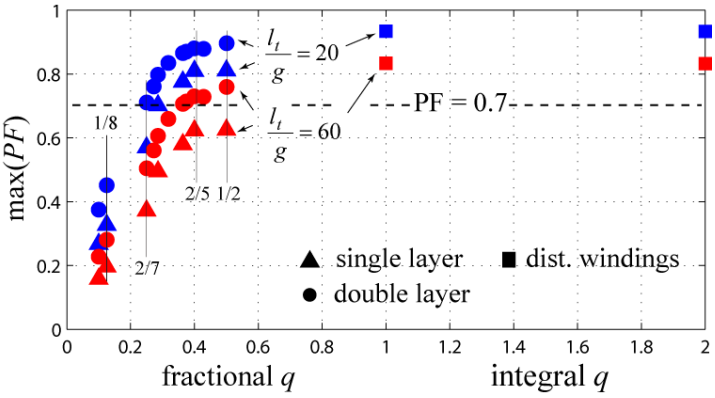

Figure 3.7 - Maximum power factor at given magnetic loading and fixed shear stress (σ = 62.5 kN/m^2). It is a function of the number of slots per pole per phase and the tooth length. l_t/g is a parameter

The results of Figure3.7 show that:

- with low fractional values of q (e.g. 1/8) there is no way of having an acceptable Power Factor, even if the pole pitch is chosen for PF maximization.
- popular slot per pole combinations such as 2/7 are at risk for this reason, with single layer windings.
- shortening the stator teeth improves the Power Factor, but it also directly increases the specific Joule loss (3.5).
- therefore, in many cases it is actually impossible to have an acceptable Power Factor with a low fractional q and single layer windings, due to the efficiency target.

- this becomes even more serious when the minimum inductance condition (3.28) is not respected.
- the Power Factor of integral slot machines is steadily high;
- depending on the stator tooth length, integral slot machines may have even a PF that is too high, with unwanted side effects such as high short circuit currents and PWM current ripple.
- thus, when dealing with distributed windings machine, it is not necessary to optimize the pole pitch, at least from this point of view.

3.2.2.2. Maximum shear stress at given Power Factor

When a wide Constant Power Speed Range is needed, one of the most convenient design strategy to enhance the flux weakening capability of the machine is to have the nominal current equal to the short circuit one and this will be fully demonstrated in Chapter 07. This condition relates univocally the magnetic loading at no load and the q-axis current. Or, in other words, it constrains the Power Factor angle to be around $\pi/4$. So, the minimum inductance condition is synonym of the maximum shear stress situation, at given Power Factor and PMs magnetic loading. Anyway, such situation corresponds also to the maximum current loading design and the thermal constraint could make the minimum inductance condition unfeasible.

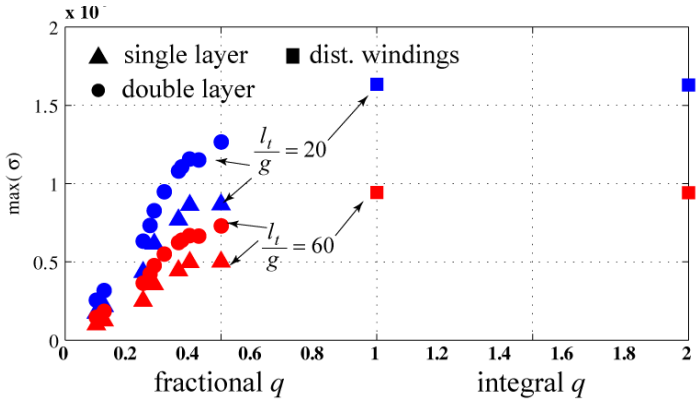

Figure 3.8 - Maximum shear stress at given magnetic loading and fixed PF (cosφ = 0.71) for having a Constant Power Speed Range theoretically unlimited. σ is shown as a function of the number of slots per pole per phase and with the tooth length. l_t/g as a parameter.

Figure 3.8 compares the behaviour of minimum inductance machines with different

q values, but all designed for having the same Power Factor, namely the one ($\tan\varphi = 1$) capable of guaranteeing a Constant Power Speed Range hypothetically unlimited. Also the magnetic loading (3.1) is supposed to be the same for all the machines, considering reasonable values for the rotor design parameters ($l_m/g = 6$, $B_r = 1.12$ T, $k_b = 1.15$). The shear stress, that can be theoretically achieve via minimum inductance machines when the Power Factor angle is close to $\pi/4$ and the thermal limit to the maximum current loading is disregarded, follows.

The results are shown in Figure 3.8 and lead to the following conclusion:

- according to the typical shear stress values, depending on the application fields and cooling setups, it occurs mainly with low fractional values of q and long stator tooth to have the need of fulfilling the minimum inductance condition for obtaining the willed shear stress level. In other words, the constraint introduced by the optimal flux weakening condition is more severe than the thermal one just in a few cases;
- in all the other situations, the plots suggest that the minimum inductance condition has not to be fulfilled. In fact, the choice of having the nominal current close to the characteristic one in order to make the Constant Power Speed Range as wide as possible does not limit the machine performance, in terms of torque density. It is rather the maximum current loading, imposed by the thermal constraint, to limit the achievable shear stress.
- fractional slot machines are even the most suitable candidates for many applications, where a wide Constant Power is required and the maximum current loading is strictly limited by thermal constraints, since they put into play a huge inductance and, thus, do not force the designer either to reduce the PM flux contribute or to exceed the upper current limits for equaling the nominal current to the short circuit one.

3.3. SPM ROTATING MACHINE INTO CONSTRAINED ENVELOPE

This section describes how a rotating machine can be designed via the linear per-unit model developed so far.

To start, it is convenient to remind both the relationship between the torque and the shear stress (3.30) and the expression that defines the number of poles (3.31), given the rotor radius r' and the pole pitch.

$$T = \sigma \cdot 2\pi \cdot r'^2 \cdot l \tag{3.30}$$

$$p = \frac{\pi \cdot r}{a} \tag{3.31}$$

It is also worth pointing out that the Joule loss density k_j of the final rotating machine can be easily computed as a function of the other design quantities, starting from the studies done on the reference block, via (3.32), that reasonably relates the heat power dissipation of the machine to its outer surface.

$$k_j = k_{j,block} \cdot \frac{r'}{r} \tag{3.32}$$

The design procedure aims at fitting into constrained outer dimensions a rotating machine capable of giving the desired torque and satisfying the PF and thermal constraint, at the same time. In the applications, for which it is mandatory to warrantee a wide Constant Power Speed Range at rated condition, the Power Factor angle is fixed by the need of having the nominal current close to the short circuit one. In the remaining situations, compatibly with the other design constraints, it is recommended to keep the Power Factor as high as possible, so neither the size of the converter nor the load-dependent core saturation phenomena get penalizing for the drive performance.

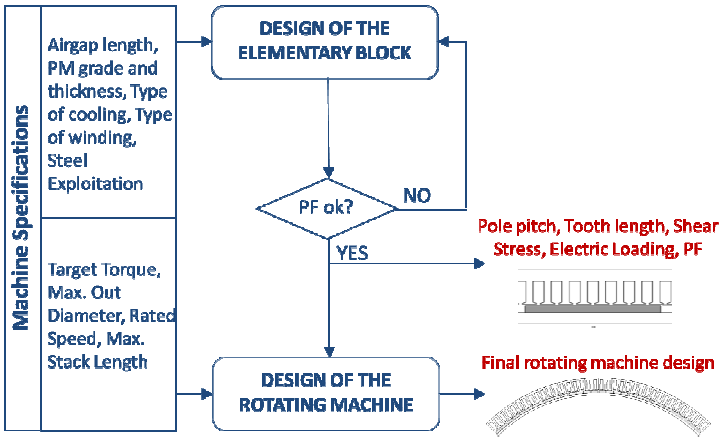

Figure 3.9 –Design flowchart of the final rotating machine

Whatever the nature of the PF limit is, the design tasks, schematically represented in Figure 3.9, can be organized as follows.

Firstly, the elementary block is determined, in terms of size and performance, via the per-unit model, introduced in Section 3.1. As it will be clarified, an iterative application of the formulas is needed because of the mutual dependence of the various design quantities. Then, the rotating machine is obtained as the assembly of a proper number of the just defined blocks.

As evidenced during the analysis of the rectified pole, sometimes the minimum inductance condition can orientate effectively the choice of the pole pitch and then the number of pole pairs (3.30). In that situations, such pole pitch will be the actual design choice. In other cases, it might be convenient to change the pole pitch for increasing and then optimizing the machines performance. The next subsections will explain how to deal with this challenge, depending on the application and the stator winding type. It will be shown that, in any cases, the modelling theory allows to deeply explore the design space and get immediate indications about the best design strategies.

3.3.1. Input data

The input data, needed to start the design procedure, are listed in the following.

- airgap length g
- q and type of winding
- PM grade (B_r) and thickness l_m/g
- steel exploitation B_{fe} (peak value)
- cooling and thermal constraint, represented by the target specific loss k_{j0}
- target shear stress σ_0
- target Power Factor PF_0

The target shear stress σ_0 is chosen with reference to typical figures of machines designed for similar applications and having analogous types of cooling and sizes.

As for the Power Factor, in case of flux weakening capability requirements, the goal value PF_0 imposes an equality constraint, whereas, in the remaining situations, the target

PF_0 suggests a lower limit to be respected for reducing conveniently the size of the power converter and making the load-dependent load saturation effects not too punishing for torque production.

Once the SPM pole is defined according to the parameters listed above, the rotating machine is designed for the following specifications:

- target torque T [Nm];
- rated speed n [rpm];
- maximum outer radius (r_0);
- stack length (l_0).

3.3.2. Design flowchart

3.3.2.1. Definition of the elementary block

1. The magnetic loading $B_{gap,m}$ is calculated via (3.1).
2. The electric loading is calculated from $B_{gap,m}$ and the σ_0 target, according to (3.4).
3. The tooth length is tentatively set according to the loss target k_{j0} and (3.5). The end connection factor is a tentative value in this case, to be recalculated once the active length and the pole pitch are finally done. This can require some iteration.
4. The pole pitch $a/g|_{Lmin}$ is calculated according to the minimum inductance condition, i.e. (3.15) or (3.27), respectively.
   a. The minimized Power Factor is evaluated and compared to its limit value.
   b. If the PF is compliant with the target value PF_0, then the block is completely defined.
   c. If the condition at point 4.b is not satisfied, then l_t is reduced and the flowchart is restarted from point 3. One of the two targets σ_0 and k_{j0} must be relaxed, in this case.

   The outputs of this stage are:
   - the pole pitch a/g;
   - the tooth length l_t/g;
   - the shear stress;

- the Power Factor;
- the Joule loss factor.

When optimizing the Power Factor without any strict constraints forced by the need of good quality flux weakening capability, sometimes a PF margin, with respect to a reasonable goal value, does exist and it is not convenient to stay on the minimum inductance pitch. If reducing the pitch still maintains an acceptable Power Factor, it is convenient to do it, because machines with a shorter pitch will have shorter end connections, a lighter back iron and a lower short circuit current. Having a PF margin is very likely with distributed windings; it happens less often with double layer, fractional *q,* also depending on the demanding shear stress and cooling setup, but it is, in general, quite rare with single layer windings.

This is to say that actually the procedure which defines the reference block limits properly the design space and outputs, alternative pole geometries to be fit into the final rotating machine, rather than one solution. Then, the performance achievable via the design of the final machine as the combination of each of these "concurrent" rectified blocks can be evaluated and the most convenient solution can be selected.

The next subsection (3.3.2.2) will describe how to build the final rotating machine into a constrained envelope, joining together defined pole geometries. Afterwards, Subsection 3.3.2.3 will compare the "concurrent" elementary blocks, suitable for defining the final rotating machine, taking into account that the performance of the motor will be influenced by:

- the geometry of each pole, of course;
- the key role played by the lever associated to the airgap shear stress, that is again determined indirectly by the pole shape, namely the stator tooth length and the pole pitch - see (3.7);
- the iron and PMs loss, up to now disregarded, that identifies an upper limit to the convenience of shortening the pole pitch.

3.3.2.2. Final rotating machine

On the basis of the input data T, r_0 and l_0 and given the analysis on the

elementary block, the steps suggested to define the ultimate SPM design are summarized in the following.

1. The product $r'^2 l$ is evaluated via (3.30), according to the target torque.
2. From $r'^2 l$, the rotor radius and stack length are chosen, within the maximum length limit.
3. The number of pole pairs (3.31) is calculated and truncated to the closest feasible number. Not all integers are feasible, when dealing with fractional slots.
4. The end connection length is corrected and the specific Joule loss is recalculated according to (3.5) and (3.32).
5. Also the machine inductance and the Power Factor are recalculated, after the pole pair truncation.
6. The stator outer radius is calculated and compared to its limit
   a. If the outer radius is ok, then the design is finished.
   b. If it is too large, the flowchart restarts from point 2 with a reduced r' and an increased l, where possible.
   c. If both l and r are over their limits (l_0 and r_0, respectively), some constraint must be relaxed.

3.3.3. Design maps at given torque and outer dimensions

TABLE 3-III
WIND TURBINE GENERATOR DESIGN EXAMPLE - SPECIFICATIONS

DEFINITION OF THE REFERENCE BLOCK - INPUT DATA		
Airgap g	4	mm
Magnet grade B_r	1.22	T
Per-unit PMs length l_m/g	5	
Slot/pole/phase q	2/5	
Slot filling factor k_{Cu}	0.4	
Core flux density B_{fe}	1.5	T
Upper limit for specific loss k_{j0}	7500	W/m^2
DESIGN OF THE ROTATING MACHINE – TARGET QUANTITIES		
Target Torque T	1273	kNm
Nominal speed n	15	rpm
Stack length l_0	1.5	m
Stator radius r_0	1.97	m

It is interesting to discuss the results of the design philosophy based on elementary blocks when moving to real world SPM rotating machines and especially to fractional slot ones.

At this purpose, a set of specification suitable for direct-drive wind power generators have been considered and the whole design space has been investigated. Namely, the main performance indicators of a family of SPM machines, all having the same stack cylinder and the same output torque, will be shown as functions of the number of pole pairs and the tooth length, since these are the last two design variable to be decided, once all the per-unit parameters have been properly fixed.

The example wind turbine generator (Table 3-III) is rated 2 MW at 15 rpm, that means 1273 kNm continuous torque. The stator diameter has to be lower than or equal to 4 m, and the stack length is expected to be 1.5 m. The specific loss target constrains k_{j0} to result lower than 7500 W/m^2, referring to direct ventilation from the wind. Anyway, it will be demonstrated that more performing designs, in terms of efficiency, can be achieved via distributed and concentrated windings SPM configurations.

Further design parameters have been fixed as suggested by Table 3-IV.

TABLE 3-IV
WIND TURBINE GENERATOR DESIGN EXAMPLE – DESIGN PARAMTERS

PER-UNIT DESIGN PARAMETERS	
Yoke per-unit width b	0.70
Tooth width factor k_t	0.76
Magnets shape factor k_b	1.15
Slot filling factor k_{Cu}	0.40

The performance charts in Figures 3.10-3.12 have been traced by means of the linear per-unit model, applied iteratively to obtain r = 1.97 m and the specified torque, while complying with the specific loss and PF targets. For each feasible (p, l_t) combination, the impact of the pole geometry on the airgap lever and the consequent effects on the performance achievable by the ultimate design have been considered. The class of machines having the per-unit pole inductance minimized have been identified and the respective locus will be highlighted by red dotted lines in the following figures.

All machines of Figure 3.10 and Figure 3.12a, including *design 1*, have q= 2/5, single

layer, whereas Figures 3.11 and 3.12b, together with *design 2*, refer to q= 2/5, double layer. The choice of having q equal to 2/5 comes from all the considerations about the Power Factor, summarized in Figures 3.5 to 3.7.

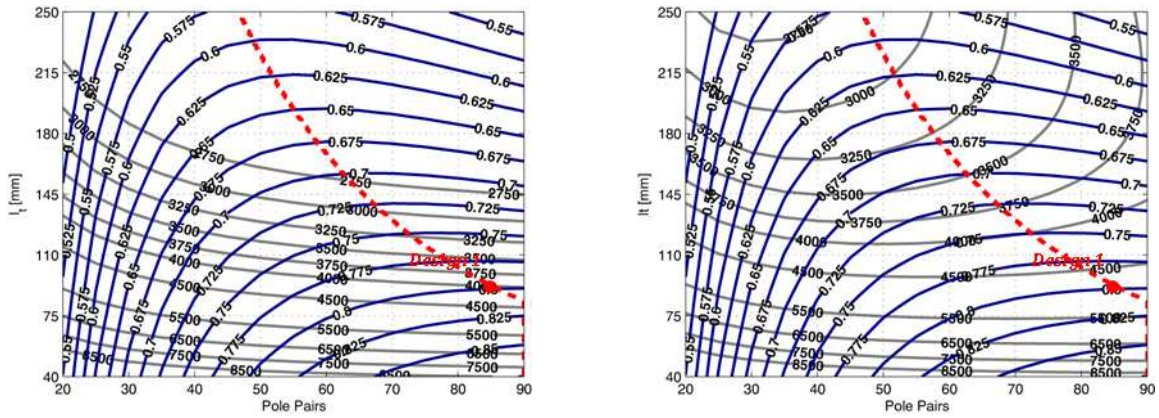

Figure 3.10 - PF (blue) and W/m² (grey) contour curves at constant outer dimensions (r = 1.97 m, l = 1.5m) and constant torque (1273 kNm) for q = 2/5, single layer. a) Specific Joule loss. b) Sum of specific Joule and Iron loss

Specifically, the plots in Figure 3.10a show the behaviour of the specific Joule loss (3.32), evaluated for all the single layer machines belonging to the chosen design space and defined according to the aforementioned specifications. The curves of Figure 3.11a have the same meaning, but they refer to double layer SPM machines.

Conversely, the plots in Figure 3.10b (Figure 3.11b, respectively) are representative of the total specific loss k_{j+i}, that includes the per-unit iron loss k_i (3.33), besides the Joule one k_j.

$$k_i = C_i \cdot B_{fe}^{\alpha} \cdot \left(\frac{n}{2\pi} \cdot \frac{p}{50}\right)^{\gamma} \cdot b \cdot \frac{1-\frac{l_t}{r}}{p+b} \cdot r \cdot \left(1 - \frac{b}{2} \cdot \frac{1-\frac{l_t}{r}}{p+b} + k_t \cdot \frac{l_t}{r} \cdot p\right) \qquad (3.33)$$

The specific iron losses are approximately quantified by (3.33) by taking into account the loss phenomena related to the fundamental electrical frequency (i.e. $p{\cdot}n/2/\pi$) only. In (3.33), C_i represents the iron loss per volume in correspondence of an electrical frequency equal to 50 Hz and a working flux density equal to 1 T. The coefficients α and γ come from the Steinmetz equation.

In Figure 3.10a *design 1* lays on the red line, has the Power Factor equal to a

reasonable value (explicitly, 0.8) and its Joule loss density is compliant with the specifications. The curves in Figure 3.10a show that the Joule loss of *design 1* can be reduced by increasing the number of poles and keeping the same tooth length. This "improvement area" indicates machines with a lower k_j and the Power Factor substantially unchanged, also due to the role played by the different lever associated to the airgap shear stress.

However, if the overall loss density is considered, the convenience of moving from the minimum inductance machine vanishes and *design 1* can be considered one of the best trade-off solutions, in terms of torque density, Power Factor and efficiency. Similarly, *design 2* is on the red line in Figure 3.11 and it turned out to represent one of the most suitable choice among all the feasible double layer concentrated winding designs.

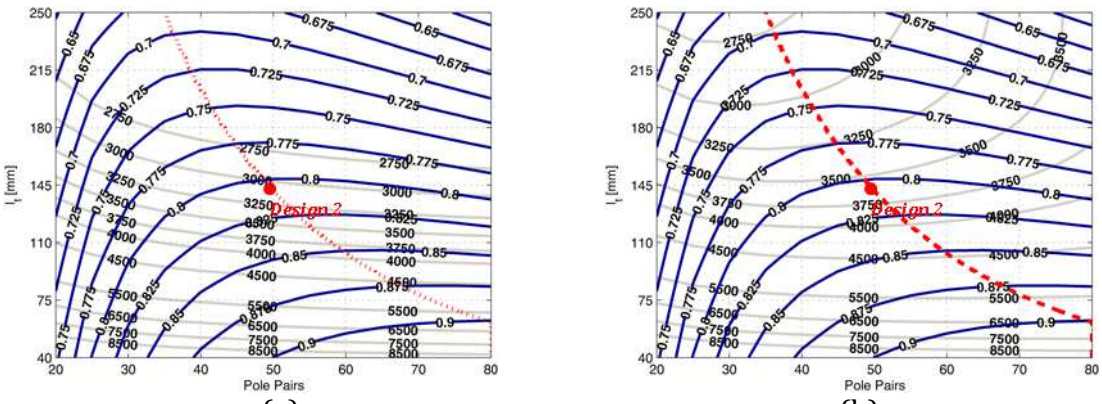

Figure 3.11 - PF (blue) and W/m² (grey) contour curves at constant outer dimensions (r = 1.97 m, l = 1.5m) and constant torque (1273 kNm) for q = 2/5,double layer. a) Specific Joule loss. b) Sum of specific Joule and Iron loss

To summarize, in general the red curve of minimum inductance splits the dominion of possible designs into a right-hand area of possibly convenient designs and a left-hand area of non-convenient designs. When dealing with direct-drive low speed machines, there are good reasons to choose to stay on the line or to move slightly rightwards. In the example case, the minimum inductance designs have revealed to be the most efficient, but for other low speed machines that are heavier loaded the Joule loss can get so preponderant that it might be convenient to move rightwards from the minimum inductance condition. Anyway, there are no reasons for moving leftwards, because all

figures of merit (PF, k_j, mass) would deteriorate in that case.

In particular, dealing with the mass of the active parts, moving horizontally both in Figure. 3.10 and 3.11 means to slightly reduce the total mass. This is confirmed by Figure 3.12 and it happens because machines with higher poles number and same tooth length have a thinner back iron both in the stator and in the rotor.

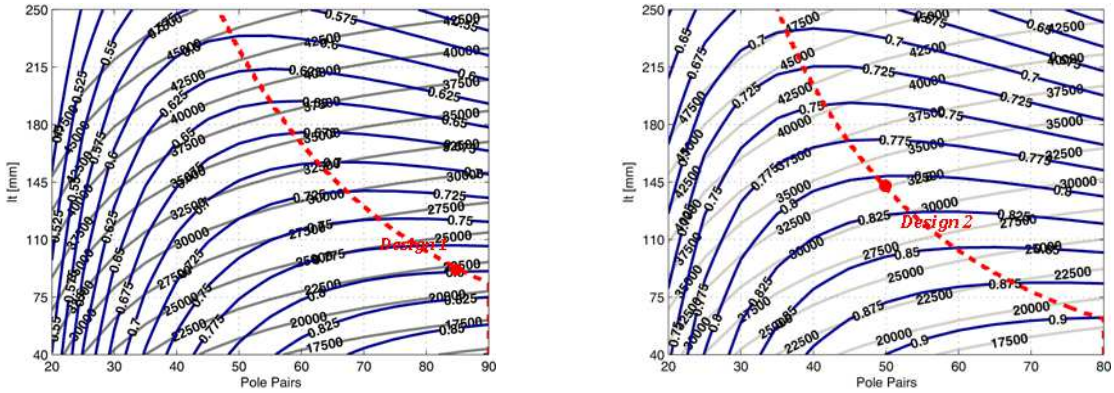

(a) (b)

Figure 3.12 - PF and weight contour curves at constant outer dimensions (r = 1.97 m, l = 1.5m) and constant torque (1273 kNm) for q = 2/5single layer (a) and double layer (b)

3.4. MODEL VALIDATION

This conclusive section aims at validating the developed theory and its generality, via meaningful design examples, purposely different in terms of both size and application.

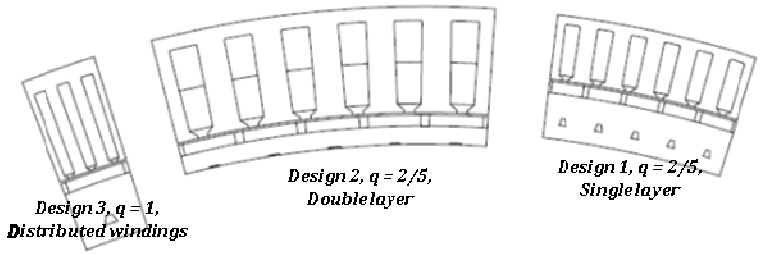

Figure 3.13 – Lamination of the three SPM machines, designed following the flowchart of Figure 3.9 according to the specifications listed in Table 3-III, 3-IV.

The first data, that will be presented, refer to the specifications listed in Tables 3-III and 3-IV, that are typical of large wind turbine generators.

As shown by Figure 3.13, the wind generators *design 1* and *design 2*, defined by

means of the design procedure summarized in Figure 3.9, are fractional slot winding SPM machines with single and double layer winding configurations, respectively.

TABLE 3-V
WIND GENERATOR EXAMPLE *design 1* (q=2/5, SINGLE LAYER)

GEOMETRICAL DESIGN OUTPUTS				
Pole pairs p	85			
Per-unit tooth length l_t/r	4.6			%
Rotor diameter $2r'$	3.7			m
STATOR WINDING AND SLOTTING EFFECT				
Slot per pole per phase q	2/5			
Winding factor k_w	0.97			
End connections factor k_{end}	1.06			
Carter coefficient k_c	1.08			
PERFORMANCE INDICATORS AND OTHER DESIGN QUANTITIES				
	Model	FEA		
Airgap flux density at no load $B_{gap,m}$	1.04	1.03		T
q-axis current loading A_q	37.8	37.8	(41.7)	kA/m
q-axis current I_q	2.62	2.62	(2.89)	kApk
Shear stress σ	39.3	36.2	(39.3)	kNm/m^3
Slot-leakage inductance L_{slot}	0.65	-		mH
Airgap inductance L_g	0.44	-		mH
Overall inductance L	1.09	1.14		mH
Power Factor	0.80	0.79	(0.76)	
Line Voltage	-	564	(577)	Vpk
Joule loss density k_j	4057	4037	(4914)	W/m^2
Iron loss density k_i	776	940	(961)	W/m^2
PMs loss density k_{pm}	-	650	(673)	W/m^2
Total loss density	4836	5627	(6548)	W/m^2

Design 3, also sketched in Figure 3.13 and designed according to the flowchart of Figure 3.9, is a distributed winding SPM machine with q = 1. The number of turns in series per phase of each example has been selected, on the basis of the FEA results, to have the line-to-line voltage equal to 1 kV. All he design outputs refer to the machine steady state operating temperature, that is 115°C.

Design 1, whose main performance indicators and geometric parameters are listed in Table 3-V, is a "minimum inductance" machine with a reasonable Power Factor value (that is, 0.8), that does not penalize too much the size of the power converter. Its

collocation in the design space is evident from the plots of Figures 3.10 and 3.12, where the red marker "*design 1*" lies in correspondence of the (p, l_t) combination: p= 85, l_t = 91 mm.

TABLE 3-VI
WIND GENERATOR EXAMPLE *design 2* (q=2/5, DOUBLE LAYER)

GEOMETRICAL DESIGN OUTPUTS				
Pole pairs p	50			
Per-unit tooth length l_t/r	7.5			%
Rotor diameter $2r'$	3.555			m
STATOR WINDING AND SLOTTING EFFECT				
Slot per pole per phase q	2/5			
Winding factor k_w	0.93			
End connections factor k_{end}	1.04			
Carter coefficient k_c	1.11			
PERFORMANCE INDICATORS AND OTHER DESIGN QUANTITIES				
	Model	FEA		
Airgap flux density at no load $B_{gap,m}$	1.04	1.05		T
q-axis current loading A_q	41.1	41.1	(44.8)	kA/m
q-axis current I_q	2.68	2.68	(2.93)	kApk
Shear stress σ	42.6	39.8	(42.6)	kNm/m^3
Slot-leakage inductance L_{slot}	1.09	-		mH
Airgap inductance L_g	0.68	-		mH
Overall inductance L	1.77	1.85		mH
Power Factor	0.80	0.80	(0.77)	
Line Voltage	-	568	(577)	Vpk
Joule loss density k_j	2984	2975	(3554)	W/m^2
Iron loss density k_i	553	974	(992)	W/m^2
PMs loss density k_{pm}	-	540	(555)	W/m^2
Total loss density	3537	4489	(5101)	W/m^2

Analogously, the example *design 2* (p= 50, l_t = 148 mm) was introduced in Figures 3.11 and 3.12. It represents again a "minimum inductance" machine and the number of pole pairs, together with the tooth length, was chosen in order to keep the Power Factor sufficiently high (namely, equal to 0.8). The machine performance are summarized in Table 3-VI.

Last, *design 3*, that is the distributed winding SPM wind generator described in Table 3-VII, has one slot per pole per phase, since higher q values would have made the stator

slots too slender to be feasible. The machine has 45 pole pairs, that leads to a pole pitch shorter than the one corresponding to the "minimum inductance" condition. In fact, in this case the Power Factor is not critical at all, as it is also confirmed by the results in Table 3-VII, and the respect of the maximum PF criterion would have caused a significant (and unwanted) increase of the active parts weight. The stator tooth length (l_t = 156 mm) has been fixed, so to obtain, according to the model, the same loss of *design 2*.

TABLE 3-VII
WIND GENERATOR EXAMPLE *design 3* (q=1)

GEOMETRICAL DESIGN OUTPUTS				
Pole pairs p	45			
Per-unit tooth length l_t/r	7.9			%
Rotor diameter $2r'$	3.552			m
STATOR WINDING AND SLOTTING EFFECT				
Slot per pole per phase q	1			
Winding factor k_w	1			
End connections factor k_{end}	1.30			
Carter coefficient k_c	1.06			
PERFORMANCE INDICATORS AND OTHER DESIGN QUANTITIES				
	Model	FEA		
Airgap flux density at no load $B_{gap,m}$	1.04	1.04		T
q-axis current loading A_q	40.9	40.9	(44.1)	kA/m
q-axis current I_q	2.35	2.35	(2.53)	kApk
Shear stress σ	42.6	40.2	(42.6)	kNm/m^3
Slot-leakage inductance L_{slot}	1.17	-		mH
Airgap inductance L_g	0.60	-		mH
Overall inductance L	1.77	1.74		mH
Power Factor	0.89	0.88	(0.86)	
Line Voltage		574	(577)	Vpk
Joule loss density k_j	3037	2981	(3481)	W/m^2
Iron loss density k_i	501	965	(979)	W/m^2
PMs loss density k_{pm}	-	110	(119)	W/m^2
Total loss density	3538	4056	(4579)	W/m^2

Another up-to-date application area that is worth including in the analysis is represented by traction drives, that are required to be efficient, deliver high torque levels in compact volumes, sustain significant overload transients and guarantee wide Constant Power Speed Ranges. Taking advantage of the analytical model described in

Section 3.1 and the conclusion drawn in Section 3.2, a double layer fractional slot winding SPM configuration has been selected to comply with the specifications listed in Table 3-VIII.

TABLE 3-VIII
TRACTION DRIVE DESIGN EXAMPLE - SPECIFICATIONS

DEFINITION OF THE REFERENCE BLOCK - INPUT DATA		
Airgap g	0.7	mm
Magnet grade B_r	1.22	T
Per-unit PMs length l_m/g	6.2	
Slot/pole/phase q	½	
Slot filling factor k_{Cu}	0.4	
Core flux density B_{fe}	1.55	T
Upper limit for specific loss k_{j0}	20000	W/m²
DESIGN OF THE ROTATING MACHINE – TARGET QUANTITIES		
Target Torque T_0	125	Nm
Nominal speed n	3500	rpm
Stack length l_0	0.170	m
Stator radius r_0	0.108	m

The motor, whose lamination is reported in Figure 3.14, is appropriate for automotive application. It is rated about 46 kW at 3500 rpm and has been designed, fixing the per-unit design parameters as shown by Table 3-IX and considering a steady state operating temperature equal to 130°C. A liquid cooled drive setup is provided for and, thus, the specific loss target is considered to be about 10000 W/m².

TABLE 3-IX
TRACTION DRIVE DESIGN EXAMPLE – PARAMETERS

PER-UNIT DESIGN PARAMETERS	
Yoke per-unit width b	0.72
Tooth width factor k_t	0.81
Magnets shape factor k_b	1.15
Slot filling factor k_{Cu}	0.40

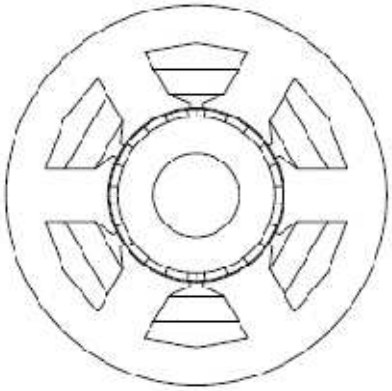

Figure 3.14 – Sketch of the traction drive design example (Tables 3-VII and 3-IX)

The number of pole pairs has been limited to two, not to penalize the efficiency of

the drive due to the iron and PMs harmonic losses, especially during operation at speed values higher than the nominal one. The magnet thickness l_m has been chosen to prevent demagnetization issue also in case of overload transients, determining univocally the available magnetic loading.

TABLE 3-X
AUTOMOTIVE DRIVE EXAMPLE – DESIGN OUTPUTS

GEOMETRICAL DESIGN OUTPUTS				
Pole pairs p	2			
Per-unit tooth length l_t/r	27.1			%
Rotor diameter $2r'$	0.0944			m
STATOR WINDING AND SLOTTING EFFECT				
Slot per pole per phase q	½			
Winding factor k_w	0.87			
End connections factor k_{end}	1.12			
Carter coefficientk_c	1.02			
PERFORMANCE INDICATORS AND OTHER DESIGN QUANTITIES				
	Model	FEA		
Airgap flux density at no load $B_{gap,m}$	1.10	1.07		T
d-axis current loading A_d	0	0	(6.7)	kA/m
q-axis current loading A_q	47.8	47.8	(50.3)	kA/m
Overall current loading A_q	47.8	47.8	(50.8)	kA/m
d-axis current I_d	0	0	(32)	Apk
q-axis current I_q	226	226	(238)	Apk
Overall current I	226	226	(240)	Apk
Shear stress σ	52.5	46.1	(52.5)	kNm/m^3
Slot-leakage inductance L_{slot}	0.678	-		mH
Airgap inductance L_g	0.233	-		mH
Overall inductance L	0.911	0.884		mH
Short circuit current I_{ch}	216	217		Apk
Power Factor	0.70	0.75	(0.77)	
Line Voltage	-	143	(153)	Vpk
Joule loss density k_j	10777	10825	(12208)	W/m^2
Iron loss density k_i	1541	2006	(2207)	W/m^2
PMs loss density k_{pm}	-	2573	(2709)	W/m^2
Total loss density	12318	15404	(17124)	W/m^2

Eventually, the tooth length has been computed to match the q-axis current loading, required to achieve the target torque, and the pole inductance so to approach the nominal current to the short circuit one and, thus, enhance the flux weakening capability

of the drive. The model results and the FEA one are reported in Table 3-X.

Whatever example is considered, the results shown in Tables 3-V, 3-VI, 3-VII and 3-X highlight that the accuracy of the analytical model is consistent with the performance commonly expected by a fast preliminary design stage.

This is verified also in case of machines with low pole pairs number, although their geometry is extremely dissimilar to the rectified one considered for modelling purposes.

In particular, the evaluation of the magnetic loading at no load is very accurate, when comparing the model data to the FEA one, and also the prediction of the phase inductance is quite reliable. In particular, this is confirmed, by the satisfactory matching between the short circuit current suggested by the analytical model and the one computed according to the FEA results, reported in Table 3-X for the traction drive.

Due to the iron saturation effects that are disregarded by the simplified model, the FEA data evidenced that the current loading identified by Equation (3.4) is not high enough to produce the willed torque. It occurs for all the design examples and the terms in brackets in the "FEA" columns of Tables 3-V, 3-VI, 3-VII and 3-X show the actual operating condition, in correspondence of the target shear stress, when the steel saturation effects are taken into account. In particular, the results of Table 3-X underline the opportunity of looking for the actual Maximum Torque per Ampere locus, that does not coincide exactly with the *q*-axis in presence of steel saturation.

3.4.1. Impact of steel saturation phenomena

The torque versus current curves in Figure 3.15, which are FEA calculated, show the progressive effect of core saturation with the *q*-axis current increasing for the three wind generators "*design 1*", "*design 2*" and "*design 3*" and they prove once again that the torque at rated current is lower than the one predicted by the per-unit model, which assumes magnetic linearity.

The factors that impact most on the divergence between the actual behavior of the machine and the linear one are:

- the harmonic content of the stator magneto motive force;

- the stator tooth length, which determines, together with the number of pole pairs, the distance run by the flux in the stator back iron;
- the stator core flux density at load, which is related to the target value B_{fe} at no load via the Power Factor.

Specifically, when at load, the stator core actually works at higher flux densities due to the armature flux and then progressively saturate as the current loading is increased (and, consequentely, the Power Factor is decreased).

This phenomenon is shown in Figure 3.16 for the three machines *design 1*, *design 2* and *design 3*, with reference to the rated condition. This highlights unequivocally the relationship between the Power Factor and the working flux density of the stator back iron when at load, since all the wind generators under comparison refer to the same no load target B_{fe} (i.e. 1.5 T).

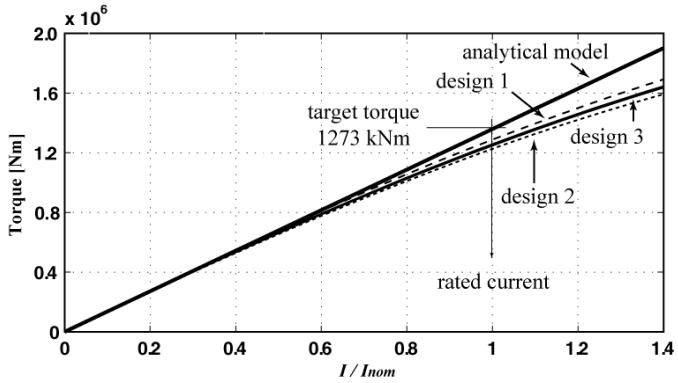

Figure 3.15 - Machine torque versus q-axis current curves, according to the linear model and the FEA. The plots put in evidence the effect of core saturation for all the design examples.!!

In general, up to a certain extent, at given stator geometry, those machines having higher armature flux linkage (i.e. a lower Power Factor) are more prone to torque reduction effects due to steel saturation. Also machines with long stator teeth and lower pole pairs number are vulnerable in this sense.

The model can be modified to include saturation or, alternatively, a possible countermeasure to reduce the torque overestimate, with no model complication, can be to oversize the yoke and tooth widths by a certain factor by setting a lower no-load peak flux density.

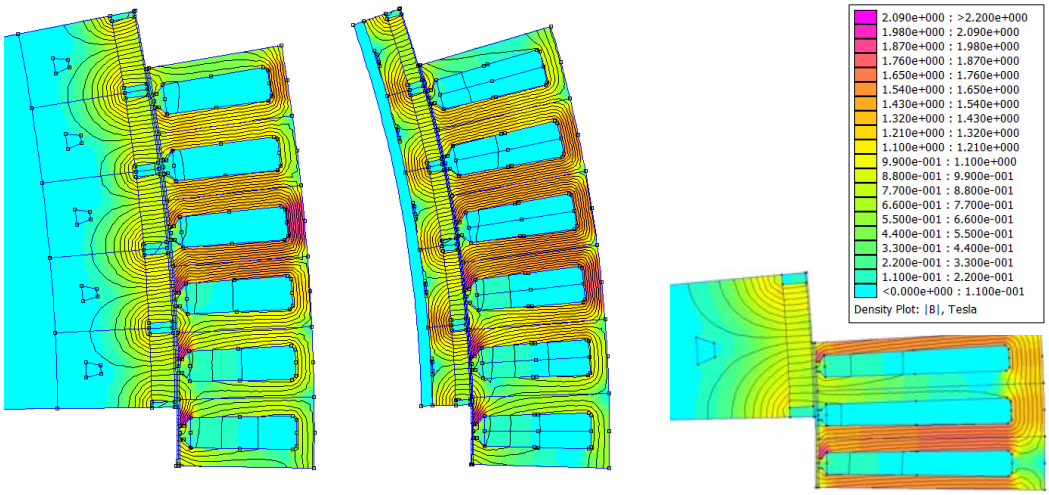

(a) (b) (c)

Figure 3.16 – FEA calculated flux density maps at rated condition. a) *design1*; b) *design 2*; c) *design 3*.

3.4.2. Joule, iron and PMs loss prediction

The discrepancy between the FEA and model evaluated Joule losses in Tables 3-V, 3-VI, 3-VII comes from the effect of curvature on the actual cross section of the stator slots. That is why this is less evident in *design 1*, which is the one with the shortest stator teeth and the highest pole pairs number (that is, the longest rotor radius).

In general, the linear model underestimates the copper area, thus overestimating the Joule loss, but the approximation can be tolerated in case of high pole numbers machines, also because it is conservative. Conversely, when dealing with smaller-sized and lower pole number motors, the overestimation of the Joule loss density is too penalizing and, thus, it is convenient to correct the estimated specific loss density by multiplying k_j (3.32) by the factor $0.5\cdot(1+r'/r)$. It was done in Table 3-X, effectively improving the prediction.

As for the specific iron loss, the analytical formulation (3.33) gives always an underestimated prediction: it occurs because the harmonic losses are not modeled and, above all, because the iron loss calculation is referred to the working flux density in the stator back iron at no load, instead of the respective load dependent value. As said, at this purpose some countermeasures can be adopted and, anyway, this modeling inaccuracy does not affect the design guidelines derived from the design maps of Subsection 3.3.3. In

fact, the locus corresponding to the minimum loss (maximum efficiency) machines in Figures 3.10 and 3.11, besides being determined mainly by the Joule contribute, is quite flat in the area that is of the main interest for the ultimate design, that is the one with shorter stator teeth and, consequently, feasible geometries in terms of weight.

Last, the PMs losses, which cannot be forecasted by fully analytical model in a reliable way, can be evaluated either via sophisticated numerical techniques or by means of the Finite Element Analysis, as it was done for the design examples discussed here. As it can be expected, the magnets losses are penalizing especially for fractional slot SPM machines, whose stator magneto motive force produces in the airgap a flux density waveform with a huge harmonic content.

3.5. FINAL DISCUSSION

The design of Surface Mounted Permanent Magnet motors has been approached by means of a per-unit analytical model, assuming magnetic linearity and a rectified geometry. The formulas cover distributed and concentrated windings, whose peculiarities are evidenced according to the aforementioned simple model. An original expression for the airgap and slot leakage inductance has been proposed, valid for fractional windings of all slot/pole/phase combinations in both single and double layer configurations. It has been verified that the airgap inductance of a double layer winding machine is exactly one half of that of a single layer machine, with equivalent stator and rotor geometry.

The analysis, that is based on per-unit geometrical parameters and normalized performance indicators, has general validity and applies to machines of all sizes, designed for various application fields. Practical design guidelines have been derived for machines required to have good properties in terms of flux weakening capability, but the reader is asked to refer to Chapter 07 for a deeper insight into this topic. In fact, the analysis focus has been represented here by direct-drive low-speed machines, with high number of poles. The Power Factor maximization criterion has been recognized as one of the most opportune design choice to reduce the size of the power converter and limit the load dependent saturation effects. From this point of view, single layer, concentrate

winding machines are at risk of an unfeasibly low Power Factor at given shear stress. Double layer ones are, instead, very flexible in setting the Power Factor at the designer's will and distributed winding machines are not critical at all.

The procedure to pass from the rectified geometry, introduced for modelling purposes, to the ultimate cylindrical design has been addressed. In particular, the actual convenience of the maximum Power Factor condition, found out via the per-unit analysis on the reference block, has been verified for the final design of direct-drive low speed rotating machines, taking into account all the performance indicators. It sorted out that the maximum Power Factor criterion, that coincides with the minimum inductance one, can effectively orientate the selection of the pole pitch and then the number of pole pairs. It has not always to be respected strictly, but it often splits bad designs from good designs.

Some meaningful examples have been presented, mainly for validation purposes. According to the results of the proposed design procedure and with respect to various up-to-date application fields, Chapter 07 will highlight pros and cons of choosing different stator winding configurations, when designing SPM machines. Moreover, a comprehensive analysis will be carried out, by comparing different PM machine types, also purposely thought for cost reduction.

Chapter 04

FASR machines robust towards demagnetization, as feasible starting designs

Standard SPM machines, as the ones examined in the previous section, have been recognized as reference designs in terms of torque density and efficiency for many up-to-date applications. However, as highlighted, they rely on rare-earth magnets for their high performance and, since the recent price volatility of such raw materials, designers and manufacturers of electric motors have been compelled to find out valuable alternative technologies.

An effective way to exploit lower energy density (and lower cost) magnets is to PM-assist Synchronous Reluctance machines, having multi-layer rotor structures, that is satisfactory starting design in terms of torque density. In this case, the magnet excitation is needed only as an additional contribute to the torque and an improvement for the Power Factor and the speed range of the drive. As a result, Ferrite Assisted Synchronous machines can provide satisfactory performances, despite the poor properties of ferrite materials in terms of both energy product and stiffness against demagnetization in low temperature environments.

This section and the next one will demonstrate how to design this kind of machines for optimizing their performance. According to the design approach that lies at the basis of this work, first reference is made to one rectified machine pole and general conclusions suitable for designs of all sizes and applications are derived. Then, multipolar rotating machines are designed as the combination of multiple rectified blocks and the results of the simplified model are validated.

In particular, the preliminary purpose of this chapter is:

- to propose geometric rules, easy to comply with, able to make the design of FASR rotor structures stiffer against demagnetization;
- to point out if the weakness of ferrite magnets towards demagnetization prevent or not FASR machines from being competitive with rare-earth based SPM and IPM counterparts.

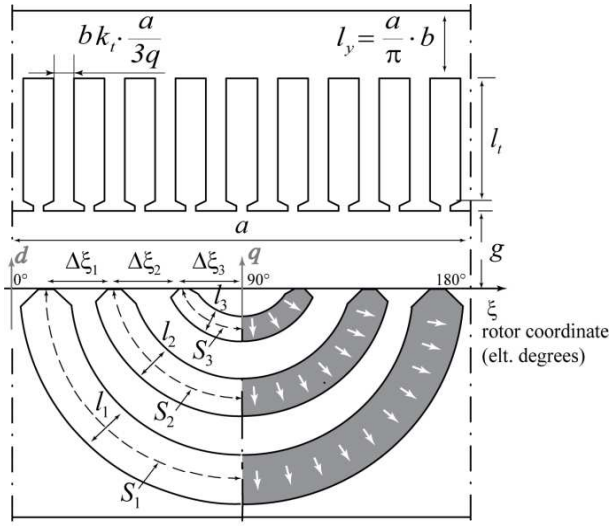

Figure 4.1 - Rectified pole of a FASR machine with a three-layer rotor and the PMs magnetized radial-wise. The dq axes follow the SR model approach.

In the following, the rotor geometry of one rectified machine pole (Figure 4.1) will be introduced, together with the equivalent circuit adopted to model its magnetic behavior along the quadrature axis, that is the one oriented against the PMs. The geometric rules needed for enhancing the starting SR design in terms of torque ripple, and the ones required for increasing the robustness towards demagnetization of FASR motors will be summed up. Figures of merit, such as the magnet flux density at no load and the maximum current loading according to irreversible demagnetization, will be quantified in equations, while discussing their dependence on the main design variables. Eventually, the severity of the demagnetization issue will be compared to the one of other well-known constraints, as for example the thermal limit and the one related to fault conditions. The comparison will allow to draw remarking conclusion about the feasibility of FASR designs in various application fields, demonstrating the opportunity of carrying on the analysis on this PM machines type, developing a comprehensive procedure to optimize the machine performance and speed up the

design stage.

4.1. MAGNETIC BEHAVIOR OF THE PMs-ORIENTED AXIS

4.1.1. Reference rotor geometry

The reference geometry in Figure 4.1 represents one rectified pole of a FASR machine with distributed windings.

The key geometric parameters in Figure 4.1 are:

- the airgap length g;
- the pole pitch a;
- the stator teeth length l_t;
- the pitch of the k-th rotor "slot" ($\Delta\xi_k$),
- half the width of the k-th layer (S_k) and its thickness (l_k);
- q is the slot number per pole per phase;
- b and k_t, that will be better addressed later, determine the size of the stator back iron.

l is the stack length of the reference block.

As for the number of rotor flux barriers and their shapes, different choices are possible. The number of layers (n) is three in the reference rotor of Figure 4.1 only as an example, since the theory has been developed to deal with any kinds of multi-layer rotor structures.

Moreover, round flux barriers are sketched in Figure 4.1 just for modeling purposes. In fact, actual rotor designs are always optimized to improve the saliency ratio between the d- and q-axis and usually they lead to more compact shapes of the rotor layers.

Since a PM-Assisted Synchronous Reluctance machine is analyzed here, the dq axes follow the SR model approach (that is, the d-axis is aligned to the maximum permeance direction).

4.1.2. Quadrature axis equivalent magnetic circuit

The circuit of Figure 4.2 shows the q-axis magnetic model of the rectified pole in

Figure 4.1, referring again to a 3-layer rotor structure as an example. The fluxes are the ones of half a pole.

- The m_{123} generators and the respective barrier permeances p_{b123} model the layers completely filled with ferrite magnets.
- The terms p_{g123} are the permeances of the rotor teeth at the airgap.
- The magneto-motive force generators f_{q123} stand for the effect of the q-axis stator current, oriented against the PMs.

The fundamental wave of the stator magneto-motive force, in per-unit of its peak value F_q, is averaged across each rotor tooth at the airgap and then modeled via the staircase f_{q123} reported in Figure 4.3. The model accounts for the polarization of the rotor flux guides into the potentials r_{123}, that are assumed to be uniform along the overall guides width and are always slightly lower than the respective values f_{q123}, as it will be recalled later.

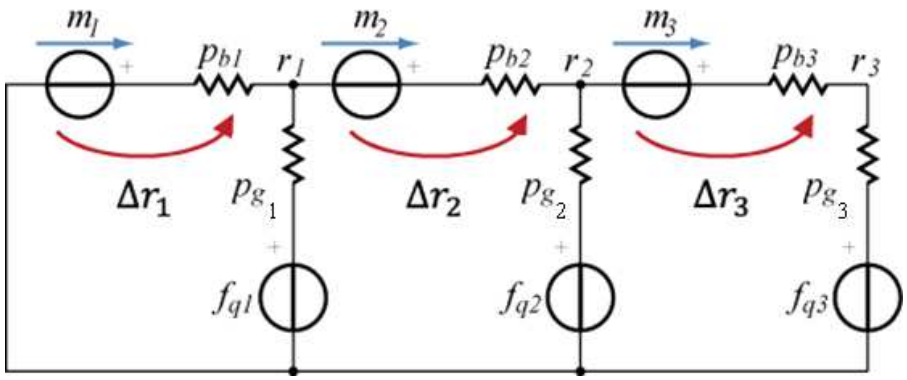

Figure 4.2 - The equivalent circuit represents the q-axis magnetic behavior of half a pole. It refers to the FASR example rotor in Figure4.1 (n=3).

Structural bridges have not been included in the magnetic equivalent circuit of Figure 4.2. Of course, their presence impacts the torque capability of the machine and its performances, for example in terms of Power Factor, but this will be taken into account in the following. In fact, the focus is now on demagnetization and magnetic ribs have a negligible influence in this sense. Or better, by disregarding their effects, the model turns out to be safer, since hen a demagnetizing current is applied against the magnets, the ribs shunt a portion of the flux crossing the barriers and release the PMs of a (small) part of their demagnetizing loading.

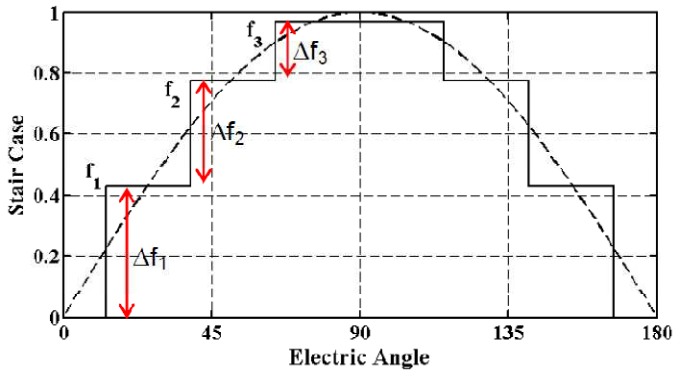

Figure 4.3 - Staircase distributions of the q-axis stator mmf f_{q123}, in per-unit of the peak value of the its fundamental waveform. It refers to the FASR example rotor in Figure 4.1 with n=3.

4.1.2.1. *Model normalization*

The magnetic behavior of the quadrature axis is examined here, expressing the magneto-motive force generators, magnetic potentials and permeances, that are included in the equivalent circuit of Figure 4.2, in normalized quantities.

The base values, corresponding to the main circuit components, are summarized in Table 4-I and discussed in the following.

The normalization factor used for magneto-motive forces and magnetic potentials is the peak value of the fundamental waveform, accounting for the q-axis stator mmf. Its expression is reminded for convenience by (4.1).

$$F_q = \frac{3}{\pi} \cdot k_w \cdot N \cdot I_q \tag{4.1}$$

I_q represents the q-axis current component, k_w is the winding factor, N is the number of conductors in series per pole.

The normalized magneto-motive force generators m_k, that model the ferrite magnets, are then identified by (4.2):

$$m_k = \frac{\frac{B_r}{\mu_0} l_k}{F_q} \qquad k = 1,2,\dots,n \tag{4.2}$$

where B_r stands for the remanence of the PMs and l_k symbolizes the k-th magnet thickness, as said.

Permeances are normalized such that they are given simply by the ratio between the

width and length of their respective flux tube. In other words, the base quantity of permeances is $\mu_0 \cdot l$, being l the machine stack length and μ_0 the permeability of free space.

So, Equation (4.3) and (4.4) follow, showing how to determine the barrier permeance p_{bk} and the airgap one p_{gk} as functions of the key geometric quantities put in evidence in the sketch of Figure 4.1.

$$p_{bk} \quad = \frac{S_k}{l_k} k = 1,2, \dots, n \tag{4.3}$$

$$p_{g,k} = \frac{a}{g} \cdot \frac{\Delta\xi_k}{\pi} k = 1,2, \dots, n \tag{4.4}$$

Last, it is pointed out that fluxes are normalized by the product $\mu_0 \cdot l \cdot F_q$.

TABLE 4-I
NORMALIZATION OF THE Q-AXIS MAGNETIC MODEL

QUANTITY	BASE VALUE
Magnetic potentials, mmfs	Peak F_q of the fundamental q-axis mmf waveform
Permeances	$\mu_0 l$
Fluxes	$F_q \mu_0 l$

4.1.2.2. *Solution of the q-axis magnetic circuit*

The relationship between the potential vectors $\boldsymbol{\Delta r}$, $\mathbf{m}$ and $\boldsymbol{\Delta f_q}$ (4.5), that have been introduced in the circuit of Figure 4.2 with reference to n=3, can be solved by means of the nodal-voltage method.

$$\boldsymbol{\Delta r} = \begin{bmatrix} \Delta r_1 \\ \Delta r_2 \\ \vdots \\ \Delta r_n \end{bmatrix} = \begin{bmatrix} r_1 \\ r_2 - r_1 \\ \vdots \\ r_n - r_{n-1} \end{bmatrix}, \boldsymbol{m} = \begin{bmatrix} m_1 \\ m_2 \\ \vdots \\ m_n \end{bmatrix}, \boldsymbol{\Delta f_q} = \begin{bmatrix} \Delta f_{q,1} \\ \Delta f_{q,2} \\ \vdots \\ \Delta f_{q,n} \end{bmatrix} = \begin{bmatrix} f_{q,1} \\ f_{q,2} - f_{q,1} \\ \vdots \\ f_{q,n} - f_{q,n-1} \end{bmatrix} \tag{4.5}$$

The process leads to the n-order system of linear equations, defined by (4.6).

$$\boldsymbol{A} \cdot \Delta \boldsymbol{r} = \boldsymbol{B} \cdot \boldsymbol{m} + \boldsymbol{C} \cdot \Delta \boldsymbol{f_q} \tag{4.6}$$

The matrices $\boldsymbol{A}$, $\boldsymbol{B}$ and $\boldsymbol{C}$ in (4.6) are given by (4.7)-(4.9) and they are all functions of the barriers width and length, as demonstrated by the presence of the permeances p_{bk}. The relationship between the various magnetic potentials depends also on the airgap length g and the airgap rotor "slot" pitches (namely, $\Delta\xi_k \cdot a/\pi$), since the terms p_{gk} are

involved in determining the matrices $\boldsymbol{A}$, $\boldsymbol{B}$ and $\boldsymbol{C}$, as well.

$$\boldsymbol{A} = \begin{bmatrix} p_{b1} + p_{g1} & -p_{b2} & 0 & 0 \\ p_{g2} & p_{b2} + p_{g2} & -p_{b3} & 0 \\ \cdots & \cdots & \cdots & \cdots \\ p_{gn} & p_{gn} & p_{gn} & p_{bn} + p_{gn} \end{bmatrix} \tag{4.7}$$

$$\boldsymbol{B} = \begin{bmatrix} p_{b1} & -p_{b2} & 0 & 0 \\ 0 & p_{b2} & -p_{b3} & 0 \\ \cdots & \cdots & \cdots & \cdots \\ 0 & 0 & 0 & p_{bn} \end{bmatrix} \tag{4.8}$$

$$\boldsymbol{C} = \begin{bmatrix} p_{g1} & 0 & 0 & 0 \\ p_{g2} & p_{g2} & 0 & 0 \\ \cdots & \cdots & \cdots & \cdots \\ p_{gn} & p_{gn} & p_{gn} & p_{gn} \end{bmatrix} \tag{4.9}$$

Given $\boldsymbol{A}$, $\boldsymbol{B}$ and $\boldsymbol{C}$, the solution of the system of linear equations (4.6), in terms of rotor potentials, is (4.10):

$$\Delta \boldsymbol{r} = (\boldsymbol{A}^{-1}\boldsymbol{B}) \cdot \boldsymbol{m} + (\boldsymbol{A}^{-1}\boldsymbol{C}) \cdot \Delta \boldsymbol{f_q} \tag{4.10}$$

4.2. GEOMETRIC RULES TO IMPROVE THE ROTOR DESIGN

Once the mathematical instruments that constitute the fundamentals of the proposed analysis are introduced, the strict relationship between the magnetic behavior of FASR machines and their rotor geometry is absolutely evident. It is then worth pointing out how the choice of the rotor geometric parameters can improve the FASR design, especially in terms of reduction of the overall harmonic content and stiffness against demagnetization.

4.2.1. Torque ripple minimization

When dealing with high-performance applications, such as electrical power steering, servo motors, and direct-drive wind power generators, it is essential to reduce the torque ripple for both low vibration and acoustic noise. Various studies have been carried out on this topic, demonstrating that torque ripple can be reduced by enhancements either in the machine design [30]-[48] or control methods [49]-[53].

In particular, the rotor design of Permanent Magnet Assisted Synchronous

Reluctance motors can be optimization for torque ripple minimization ripple via "regular" displacement of the flux barriers at the airgap [2], [54]-[55].

The equivalent number of rotor slots per pole pair n_r is introduced and the "regular" inter-barrier pitch Δξ (4.11) is defined:

$$\Delta\xi = \frac{2\pi}{n_r} \tag{4.11}$$

Depending on the number of stator slots, different choices of n_r are possible. The best strategy is to choose n_r as much as possible near to the number ($6 \cdot q$) of stator slots per pole pair, but excluding both $n_r=6 \cdot q$ and $n_r=6 \cdot q \pm 2$, which would lead to the direct interaction of stator and rotor harmonics. As a consequence, both $n_r=6 \cdot q+4$ and $n_r=6 \cdot$q-4 (if the number of stator slots is larger) are suggested, guaranteeing lower torque ripple designs.

Once the number of rotor slots per pole pair is fixed according to the just mentioned rule, the chosen number of rotor flux barriers n determines the rotor structure:

- If $n_r=4 \cdot n+2$, the rotor "slot" pitch $\Delta\xi_k$ (4.12) is kept constant, and equal to Δξ, along the whole periphery of the rotor. These are the most "regular" rotor topologies and they are called "complete" in [55].

$$\Delta\xi_k = \Delta\xi = \frac{2\pi}{n_r} k = 1,2,\dots,n \tag{4.12}$$

- If $n_r>4 \cdot n+2$, the rotor is addressed as a "non-complete" structure and a common choice (4.13) is to keep the inter-barrier pitch still uniform, with the general exception of the angle $\Delta\xi_n$ (between the smallest layer and the q-axis), that ends up with being larger than Δξ, according to the factor $k_{\Delta\xi n}$.

$$\begin{gathered} \Delta\xi_k = \Delta\xi = \frac{2\pi}{n_r} k = 1,2,\dots,n-1 \\ \Delta\xi_n = k_{\Delta\xi n} \cdot \Delta\xi \quad k_{\Delta\xi n} = \frac{n_r - 4n + 2}{4} \end{gathered} \tag{4.13}$$

The analysis will refer mainly to "complete" machine topologies, as the one proposed in the example rotor of Figure 4.1 (n=3, n_r=14). They allow a more convenient

accommodation of the flux barrier inside the rotor, without compromising too much the design of the iron rotor guides. They are characterized by having the permeances of the airgap flux tubes all equal to the same value, namely p_g (4.14).

$$p_g = \frac{a}{g} \cdot \frac{\Delta\xi}{\pi} \tag{4.14}$$

However, for the sake of generality, all the formulas will be adapted to include the cases of "non-complete" rotor types. When modeling the airgap flux tubes, reference will be made always to the "regular" permeance p_g, whatever the multi-layer rotor structure is, but, since in case of "non-complete" machines, the rotor "slot" pitch closest to the q-axis and, thus, the respective airgap permeance, are larger than their "regular" values, the parameter $k_{\Delta\xi n}$ will be involved in the formulas.

For "complete" rotor structures, it will be simply considered that $k_{\Delta\xi n}$ is equal to one.

4.2.2. Uniform PMs exploitation and harmonic content reduction

4.2.2.1. *Rotor barriers with constant thickness along their widths*

The first key design choice to preserve the magnets from the demagnetization risk is to have rotor flux barriers with constant thicknesses along their widths.

As said, the adoption of ferrite magnets constrains to have all the rotor layers full of PMs, in order to compensate for the lower B-H energy product of this magnet types. A non-constant thickness of a rotor flux barrier, that is a non-constant thickness of a ferrite magnets, would cause non-uniform flux density values for the PMs and the occurrence of weaker points, more prone to demagnetization, in their thinner sections.

It is then preferable to have uniform flux density working points for each magnet, by keeping their thickness constant, even if designing all the rotor layers with constant thickness along their spans does not represent a common practice, when dealing with PMASR machines. Actually, if rare-earth magnets are employed, only a portion of each rotor layers is required to be filled in with permanent magnet material and, consequently, the extremities of the flux barriers are usually made thinner, or better the middle area of the flux barriers is made thicker, so to optimize the saliency ratio between

the *d*- and *q*-axis. This way of shaping the rotor flux barriers denotes just an additional perfection to the anisotropic performance of the rotor and does not justify the adoption of such criterion also for FASR machines. In fact, with constant-thickness layers, multi-layer FASR rotors do still show satisfactory behaviors, in terms of saliency ratio (and this will be proved while presenting some design examples) and, further, they have the irrevocable advantage of a uniform exploitation of the ferrite magnets.

4.2.2.2. *Design of PMs permeance and mmf*

This last subsection aims at providing useful guidelines for the design of the rotor flux barriers, namely their lengths l_k and their widths S_k, so that:

- the overall harmonic content of the quadrature flux density is minimized;
- all the PMs filling the n rotor flux barriers work at the same flux density, whatever the q-axis current level is.

This two-fold purpose is pursued, if the rotor geometry is designed for having at the same time:

- the PMs mmfs $\boldsymbol{m}$ proportional to the per-unit stator mmf staircase $\boldsymbol{\Delta f_q}$
- the magnetic potential drops $\boldsymbol{\Delta r}$ proportional to the per-unit stator mmf staircase $\boldsymbol{\Delta f_q}$, as well.

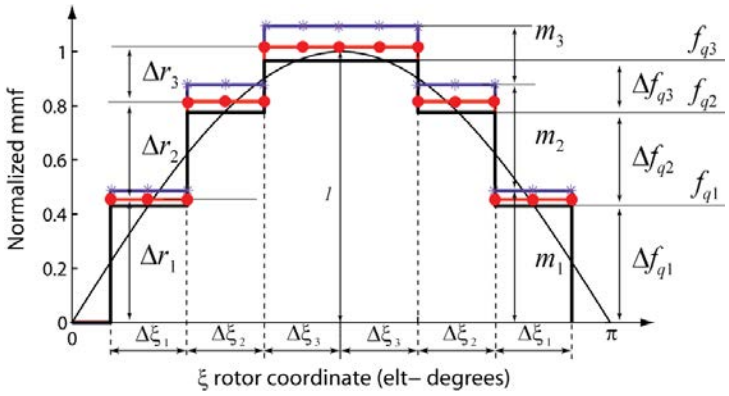

Figure 4.4 - Staircase distributions of the mmfs in the equivalent circuit of Figure 4.2, in per-unit of F_q. The plots are referred to the three-layer "complete" rotor of Figure 4.1. No markers: q-axis stator mmf f_{q123}. Star: PMs mmf m_{123}. Circle: iron guides magnetic potentials r_{123}.

As it will be demonstrated, the first condition determines the relationships to be respected between the magnets thicknesses l_k and the second constraints impose the

proportions to follow when choosing the PMs widths S_k.

The two conditions together allow both to reduce the overall harmonic content of the quadrature flux density, as it is intuitive, and to make all the PMs work at the same flux density. This is proved by the way the PMs flux density is determined. In fact, starting from the equivalent circuit of Figure 4.2, the flux $\Phi_{m,k}$ through half the k-th magnet, in per-unit, is quantified by (4.15).

$$\phi_{m,k} = (m_k - \Delta r_k) \cdot p_{bk} \tag{4.15}$$

The flux density in the magnet $B_{m,k}$, measured in Tesla, is then given by (4.16), where the per-unit flux has been de-normalized per $\mu_0 \cdot F_q \cdot l$.

$$B_{m,k} = \frac{\phi_{m,k} \cdot \mu_o \cdot l\, F_q}{l \cdot S_k} = \frac{(m_k - \Delta r_k) \cdot p_{bk}}{S_k} \cdot \mu_o \cdot F_q \tag{4.16}$$

Eventually, by manipulation of (4.16), (4.2) and (4.3), the flux density of the k-th magnet (4.17), divided by the PM remanence B_r, is determined via the division between the magnetic potential drop Δr_k and PM mmf m_k.

$$\frac{B_{m,k}}{B_r} = B_{m,pu,k} = 1 - \frac{\Delta r_k}{m_k} \tag{4.17}$$

It confirms that, if the rotor geometry is designed for having both the PMs mmf $\boldsymbol{m}$ and the magnetic potential drops $\boldsymbol{\Delta r}$ proportional to the stator mmf staircase, as in Figure 4.4, all the PMs work at the same flux density, at all current level. Reminding that m_k comes from the barrier thickness according to (4.2), if the staircase $\boldsymbol{m}$ needs to have the shape of $\boldsymbol{\Delta f_q}$, it follows that it is the PMs thickness distribution (4.18) that must copy once more the $\boldsymbol{\Delta f_q}$ distribution.

$$\frac{l_k}{\Delta f_{qk}} = const \qquad k = 1,2,\dots,n \tag{4.18}$$

In other words, the rotor magnetic insulation must be shared between the layers according to the stator mmf per-unit levels, as suggested by (4.19).

$$l_k = l_a \cdot \frac{\Delta f_{qk}}{f_{qn}} = l_{a,pu} \cdot \frac{a}{2} \cdot \frac{\Delta f_{qk}}{f_{qn}} \tag{4.19}$$

Where the total insulation l_a (sum of the n barriers thicknesses) or, better, its per-unit value $l_{a,pu}$ (normalized according to the pitch $a/2$), will reveal to be a key design parameter. In (4.19), f_{qn} is the top of the per-unit staircase $\boldsymbol{\Delta f_q}$ and, since it is given by the sum of the elements of $\boldsymbol{\Delta f_q}$, it is always close to one, whatever the number of layers is (for example, when n=3 and n_r=14, as for the plots in Figure 4.4, f_{q3} = 0.967)

Once all the elements of the vector $\boldsymbol{m}$ are made proportional to the respective levels $\boldsymbol{\Delta f_q}$, the matrix products $A^{-1}B$ and $A^{-1}C$ ought to be scalar numbers if also the magnetic potential drops $\boldsymbol{\Delta r}$ are required to be characterized by the same proportions. In fact, the relationship fixed by (4.10) is equivalent to (4.20):

$$\frac{\Delta \boldsymbol{r}}{\Delta \boldsymbol{f_q}} = (\boldsymbol{A}^{-1}\boldsymbol{B}) \cdot \frac{\boldsymbol{m}}{\Delta \boldsymbol{f_q}} + (\boldsymbol{A}^{-1}\boldsymbol{C}) \tag{4.20}$$

Where the element by element divisions $\boldsymbol{\Delta r}/\boldsymbol{\Delta f_q}$ and $\boldsymbol{m}/\boldsymbol{\Delta f_q}$ are put in evidence.

In order to fulfill the aforementioned condition:

- if the FASR rotor structure is “complete”, all the barrier permeances must be the same (4.21)

$$p_{bk} = \frac{S_k}{l_k} = p_b = const \quad k = 1,2,\dots,n \tag{4.21}$$

- if the FASR machine has a “non-complete” rotor type, all the barrier permeances must be the same, with the exception of the one corresponding to the smallest layer, which This is required to be larger than the others according to the factor k_{pbn} (4.22).

$$\begin{aligned} p_{bk} &= \frac{S_k}{l_k} = p_b = const \quad k = 1,2,\dots,n-1 \\ p_{bn} &= \frac{S_n}{l_n} = k_{pbn} \cdot p_b \qquad k_{pbn} = \frac{\Delta f_{q1}}{\Delta f_{qn}} \frac{\sin\left(k_{\Delta\xi n} \cdot \Delta\xi\right)}{\cos(\Delta\xi/2)} \end{aligned} \tag{4.22}$$

When all the barriers thicknesses respect condition (4.18) and the FASR rotor is “complete”, the constraint (4.21) says that also the layer widths S_k must be proportional to the steps of the stator mmf staircase (4.23).

$$\frac{S_k}{S_h} = \frac{\Delta f_{qk}}{\Delta f_{qh}} \quad \forall\, h,k \tag{4.23}$$

Analogously, given (4.18), condition (4.22) means that the barrier widths of "non-complete" rotor structures needs to be designed as suggested by (4.24):

$$\begin{aligned} &\frac{S_k}{S_h} = \frac{\Delta f_{qk}}{\Delta f_{qh}} \quad \forall\, h,k \neq n \\ &\frac{S_n}{S_1} = k_{pbn}\frac{\Delta f_{qn}}{\Delta f_{q1}} = \frac{\sin\left(k_{\Delta\xi n}\cdot\Delta\xi\right)}{\cos(\Delta\xi/2)} \end{aligned} \tag{4.24}$$

It is worth mentioning that the machine class that includes all "complete" rotor structures can be considered as a particular case of the more general topology, addressed here as "non-complete". In fact, when the number n_r is chosen to make the FASR rotor "complete", the factors k_{pbn} and $k_{\Delta\xi}$ are both equal to one and the relationships, fixed by (4.24), turn out to be equivalent to the one, expressed by (4.23).

To summarize, if the rotor layers (namely, l_k and S_k) are designed according to (4.18) and (4.23) or (4.24), then all the mmf staircases $\boldsymbol{\Delta f_q}$, $\boldsymbol{m}$, $\boldsymbol{\Delta r}$ have the same shape and all the PMs work at the same flux density. As said in 4.2.2.1, the flux density is homogeneous also throughout each magnet thanks to the constant thickness of the barriers. In conclusion, there are neither weaker magnets nor weaker local points inside the rotor flux barriers.

4.3. DEFINITION OF THE DEMAGNETIZATION CONSTRAINTS

If the FASR rotor geometry respects all the aforementioned rules, the simplest version of Equation (4.10) is valid and the PMs working point can be evaluated via (4.17) at all I_q load conditions, identifying the limit of irreversible demagnetization. In other words, it is possible to determine the condition which guarantees the magnet flux density to be higher than the demagnetization limit $B_{m,irr}$, whatever the temperature is and at all the feasible q-current levels, including rated operating condition, overload transients and fault conditions.

The demagnetization curves in Figure 4.5 show a typical behavior of ferrite materials in the B-H plane. At low temperatures, hard ferrites do demagnetize

irreversibly at disadvantageous values of flux density. For example, at -60°C, the magnet is safe if its working point B_m is larger than 0.27 T. In per-unit, at -60°C, of the respective remanence B_r, that is equal to 0.45 T, the lower limit $B_{m,irr,pu}$ to the PM working point is about 60%. Conversely, at 20°C, it is B_m>0.1 T, with B_r = 0.38 T, that guarantees the absence of demagnetization phenomena in the PMs (in normalized quantities, $B_{m,irr,pu}$ is required to be larger than 26%). For temperatures starting from +60°C on, all positive values of flux density are feasible when considering the example ferrite grade in Figure 4.5.

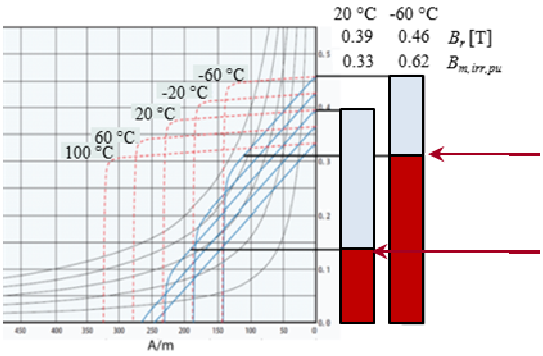

Figure 4.5 – Example magnetic curves of a ferrite material (Hitachi NMF-3C).The lower limitation $B_{m,irr,pu}$ is represented graphically in correspondence of different operating temperatures (namely, -60°C and 20°C).

The per-unit extent of the PM "dangerous" area, in terms of flux density, is indicated with colored bars in the example Figure 4.5, where the constraint $B_{m,irr,pu}$ is shown in correspondence of different operating temperature.

The limit $B_{m,irr,pu}$ will be compared to the PMs per-unit flux density at no load, which will be fully analytically determined and put in relationship with the rotor geometry in the following subsections. Besides, the maximum electric loading, that make the PMs work at their irreversible limit $B_{m,irr}$, will be quantified in equation, again as a function of the rotor design parameters.

4.3.1. Magnets flux density at no load

Starting from (4.10), the solution of (4.25) with $\Delta \boldsymbol{f_q}/\boldsymbol{m}$ equal to zero gives $\Delta \boldsymbol{r_0}/\boldsymbol{m}$ (4.26), which represents the vector distribution of the magnetic potential drops between the rotor flux guides at no load.

$$\frac{\Delta \boldsymbol{r}}{\boldsymbol{m}} = (\boldsymbol{A}^{-1}\boldsymbol{B}) + (\boldsymbol{A}^{-1}\boldsymbol{C}) \cdot \frac{\Delta \boldsymbol{f_q}}{\boldsymbol{m}} \tag{4.25}$$

As highlighted by (4.26), the ratio $\boldsymbol{\Delta r_0/m}$ is identified by a simple formulation and gets a scalar value, when the magnet mmfs $\boldsymbol{m}$ are designed to copy theper-unit stator staircase $\boldsymbol{\Delta f_q}$ (4.18) and both the airgap (4.14) and magnet(4.22-24) permeances are set to be "regular".

$$\frac{\Delta \boldsymbol{r_0}}{\boldsymbol{m}} = \frac{\frac{p_b}{p_g}\left(1 - \frac{\Delta f_{q2}}{\Delta f_{q1}}\right)}{1 + \frac{p_b}{p_g}\left(1 - \frac{\Delta f_{q2}}{\Delta f_{q1}}\right)} \tag{4.26}$$

So, by substituting (4.26) into (4.17), the uniform PM flux density $B_{m0,pu}$ (4.27) at no load is found.

$$B_{m0,pu} = \frac{1}{1 + \frac{p_b}{p_g}\left(1 - \frac{\Delta f_{q2}}{\Delta f_{q1}}\right)} \tag{4.27}$$

Equation (4.27) can then be re-written to put in evidence the influence of the key rotor design parameters.

The "regular" permeance p_g can be computed as in (4.14) and the permeance p_b, accounting for the magnets, can be calculated as suggested either by (4.23) if the rotor structure is "complete" or by (4.24) if the rotor structure is "non-complete"). All these substitutions lead to (4.28):

$$B_{m0,pu} = \frac{1}{1 + \frac{2\pi}{l_{a,pu}} \cdot \frac{S_1}{a} \cdot \frac{f_n}{\Delta\xi \cdot \Delta f_{q1}}\left(1 - \frac{\Delta f_{q2}}{\Delta f_{q1}}\right) \cdot \frac{g}{a}} \tag{4.28}$$

where the magnet thicknesses have been fixed according to (4.19). Moreover,. the per-unit steps of the stator mmf can be expressed as functions of the rotor "slot" pitch $\Delta\xi$ and (4.29) is obtained:

$$B_{m0,pu} = \frac{1}{1 + \frac{2\pi}{l_{a,pu}} \cdot \frac{S_1}{a} \cdot \frac{1}{k_{\Delta\xi n} \cdot \Delta\xi} \frac{\sin(k_{\Delta\xi n} \cdot \Delta\xi)}{\cos(\Delta\xi/2)} \cdot \frac{g}{a}} \tag{4.29}$$

Equation (4.29) points out that high a/g values (i.e. small per-unit airgaps), together

with large per-unit magnetic insulations $l_{a,pu}$, keeps $B_{m0,pu}$ close to one per-unit. So the PMs working flux density at no load stays close to the remanence value and it means that the magnets are not heavily loaded, at least at zero current.

4.3.1.1. *Effect of the rotor geometry on the no load PMs flux density*

Figure 4.6 and 4.7 show the behavior of B_{m0pu}, when the a/g ratio varies and in correspondence of different values of the main rotor design parameters, such as the number of layers and the total rotor magnetic insulation.

In order to put in evidence the influence of the aforementioned parameters, the no load per-unit flux density $B_{m0,pu}$ has been quantified supposing to have round shaped barriers. Under this exemplifying hypothesis (4.30), if the trigonometric functions involved in (4.29) are approximated by the first two terms of their respective Taylor series, a more suitable expression of $B_{m0,pu}$ (4.31) is found.

$$S_1 = \left(k_{\Delta\xi n} + n - 1\right)\Delta\xi\,\frac{a}{2} = \frac{\pi}{4}a\,\left(1 - \frac{2}{n_r}\right) \tag{4.30}$$

$$B_{m0,pu} = \frac{1}{1 + \frac{\pi^2}{2l_{a,pu}} \cdot \frac{1-\frac{2}{n_r}}{1-\frac{1\pi^2}{2n_r^2}} \cdot \frac{g}{a}} \tag{4.31}$$

In Figure 4.6, the $B_{m0,pu}$ characteristics (4.31) are reported as functions of the pole pitch to airgap ratio a/g, for both an adequate and an inadequate value of the per-unit rotor magnetic insulation. As an example, n_r has been chosen equal to 14, imaging to analyze the "complete" reference rotor of Figure 4.1, that has three rotor flux barriers. The two $B_{m,irr,pu}$ limits, indicated in Figure 4.6, represent typical demagnetization constraints for ferrite magnets, as discussed at the beginning of Section 4.3. According to the plots, demagnetization never occurs at 20°C, whereas, when dealing with very cold environments (e.g. -60°C) it is recommendable to have a good rotor magnetic insulation and an a/g ratio at least larger than 50 for the magnets of FASR rotors to be safe in terms of demagnetization.

Having small a/g ratios means that the airgap is thick with respect to the pole pitch and the PMs are loaded significantly even at no load conditions. Provided that the airgap

size and the rotor diameter are strictly related due to mechanical constraints [56], the lower limitation to a/g constitutes an upper limit to the number of poles of the rotating machine. In other words, if the airgap cannot be made smaller for a certain rotor size, the ratio a/g has to be increased choosing properly the number of poles: in fact, given the rotor diameter, designing more poles means having a smaller pitch a, and vice versa.

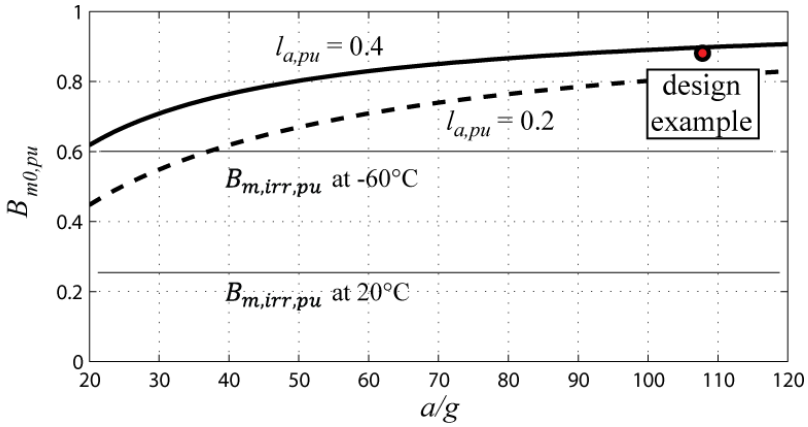

Figure 4.6 - No load per-unit flux density in the magnets for different values of the rotor magnetic insulation. For modeling purposes, the rotor flux barriers are supposed to be round shaped and, as an example, a "complete" rotor structure with three layers (n_r=14) has been considered. The demagnetization limits at -60°C and 20°C are indicated. The design example considered in Section 1.4 is put in evidence.

Equation (4.31) allows also to compare different rotor topologies and their behavior in terms of demagnetization at no load. According to the previous considerations, FASR rotors are required to have adequate magnetic insulation values. However, once the rotor magnetic insulation is fixed, FASR rotor can differ either for the number of rotor flux barriers or the choice of the equivalent number of rotor slots per pole pair. It means that it is possible to have either "complete" or "non-complete" rotor structures.

By comparing all "complete" FASR machine topologies, with different number of rotor flux barriers, it turns out that multi-layer rotor structures (i.e. $n \geq 3$, $n_r \geq 14$) are more convenient when it is needed to make the machine stiffer against demagnetization. In fact, case of "complete" Ferrite Assisted SR machines, the relationship between the number of layer n and the number of rotor slots per pole pair n_r is univocal and Equation (4.31) fully demonstrated the convenience of multi-layer rotor structures.

Conversely, if a fixed number of rotor flux barriers n and various n_r values are

considered, it is not possible to recognize significant advantageous either for "complete" FASR rotor topologies or "non-complete" ones, in terms of robustness towards demagnetization. This is because, given the chosen n, n_r cannot vary significantly.

The actual reason why "complete" rotor structure may be sometimes preferable depends rather on the more convenient way constant-thickness magnets can be arranged in the rotor without running up against a poor design of the iron flux guides and consequent saturation effects, that might compromise the FASR machine performance.

It can be concluded that, whatever the rotor structure is, provided a suitable number of rotor flux barriers, if the airgap is small enough (or vice versa the pole pitch is large enough) there is little or no risk of demagnetization at no load, even at arctic temperatures, such as -60°C. Nevertheless, it is mandatory to have a significant margin between the no load flux density and the limit $B_{m,irr}$: in fact, the parameter $B_{m0,pu}$ is a figure of merit of the machine robustness towards demagnetization also at load, as it will be explained in the next subsection.

4.3.2. **Feasible current loading according to demagnetization**

The purpose of this paragraph is to quantify the level of current loading that leads to irreversible demagnetization of the PMs at a given operating temperature.

Once again, it is the q-current loading (i.e., the one oriented against the PMs) to be of interest for demagnetization and the reader is reminded that the q-axis electric loading [Aturn/m] is related via (4.32) to the stator mmf modeled in the equivalent circuit of Figure 4.2.

$$A_q = \frac{\pi}{2} \cdot \frac{F_q}{a} \tag{4.32}$$

The relationship between the q-current loading and the irreversible demagnetization limit $B_{m,irr,pu}$ comes from manipulation of (4.25), this time with $\boldsymbol{\Delta f_q/m}$ different from zero. In this case, the rotor iron segments are polarized by the q-axis stator mmf, such that the vector potentials distribution $\boldsymbol{\Delta r/m}$ depends on F_q as shown by (4.33):

$$\frac{\Delta \boldsymbol{r}}{\boldsymbol{m}} = \frac{\frac{p_b}{p_g}\left(1 - \frac{\Delta f_{q2}}{\Delta f_{q1}}\right) + \frac{F_q}{M}}{1 + \frac{p_b}{p_g}\left(1 - \frac{\Delta f_{q2}}{\Delta f_{q1}}\right)} \tag{4.33}$$

Obviously, the ratio $\boldsymbol{\Delta r/m}$ depends also on M (4.34), which represents the peak value of the fundamental waveform accounting for the magnets mmf.

$$M = \frac{B_r}{\mu_0} \cdot \frac{l_{a,pu}}{f_n} \cdot \frac{a}{2} \tag{4.34}$$

Reminding that the PMs working flux density, in per-unit, is determined by (4.17), Equations (4.32) and (4.33-34) demonstrate that the maximum q-axis current loading according to irreversible demagnetization is (4.35).

$$A_{q,irr} = \frac{\pi}{4} \cdot \frac{B_r l_{a,pu}}{\mu_0 f_{qn}} \cdot \left(1 - \frac{B_{m,irr,pu}}{B_{m0,pu}}\right) \tag{4.35}$$

In fact, if the q-axis current loading is equal to $A_{q,irr}$, then all the PMs work at the flux density $B_{m,irr}$. Equation (4.35) is a key relationship, quantifying the electrical loading that can be tolerated by the magnets. The maximum current loading is proportional to the PMs remanence and to the per-unit magnetic insulation $l_{a,pu}$, as it can be intuitive. Moreover, the term in brackets says that $A_{q,irr}$ is a function of the margin between the material property $B_{m,irr,pu}$ and the no load flux-density $B_{m0,pu}$. If $B_{m0,pu}$ gets too close to $B_{m,irr,pu}$, then the feasible loading tends to zero and the feasible torque goes to zero along with.

4.3.2.1. *Effect of insulation and temperature on the current loading limit*

In (4.35), the presence of the per-unit magnetic insulation $l_{a,pu}$ and the no load PMs flux density $B_{m0,pu}$ summarizes the dependence of the limitation $A_{q,irr}$ on the rotor geometry. Conversely, the terms B_r and $B_{m,irr,pu}$ are involved in (4.35) to remind that $A_{q,irr}$ is determined also by the combination of the PM quality and operating temperature.

Figure 4.7 reports the applicable current loading (4.35) as a function of the a/g ratio, the insulation and the temperature. The curves are referred to the "complete" example rotor of Figure 4.1 (n=3, n_r=14). $A_{q,irr}$ grows very quickly, as the PM temperature passes from -60°C to more realistic temperatures such as 20°C or more. Nevertheless, it is still

possible not to limit the electric loading in a too severe way (e.g. under 30 kA/m or more), also when dealing with extremely cold environments, provided that both the magnetic rotor insulation and the pole pitch to airgap ratio a/g are high enough.

Values of a/g smaller than50 penalize the design, as it sorted out also during the analysis of the demagnetization risk at no load. Conversely, the effect of $l_{a,pu}$ is more relevant on $A_{q,irr}$ than it was on $B_{m0,pu}$. This happens because $l_{a,pu}$ counts twice in (4.35): explicitly in the formula and also implicitly through the term $B_{m0,pu}$ (4.29, 4.31). A weak insulation, besides compromising the reluctance torque of the machine, makes it more prone to demagnetization and more sensitive to the pole pitch to airgap factor.

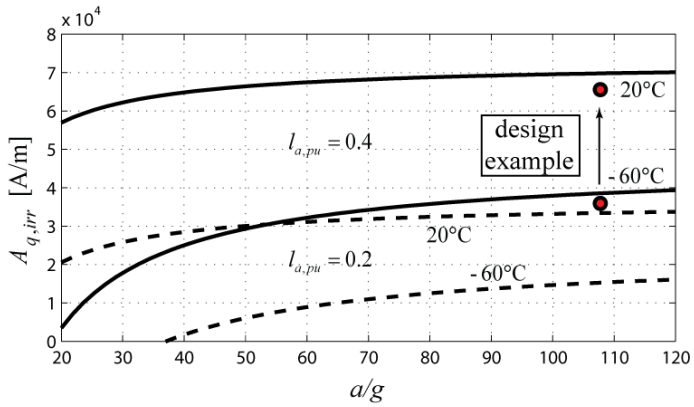

Figure 4.7 - Feasible electric loading $A_{q,irr}$, as a function of the pole pitch to airgap ratio. The effects of both the rotor insulation and operating temperature are shown. The curves are referred to the "complete" rotor example of Figure 4.1 (n=3, n_r=14).

It is interesting to notice that machines with significant insulation values (e.g. 0.4) and a properly designed pole pitch (e.g. a/g>50) have a robustness towards demagnetization at -60°C that is comparable to the one shown at 20°C by machines with weak insulation (e.g. 0.2). This stands for recalling once again the importance of maximizing the rotor magnetic insulation.

To conclude, with sufficient insulation and always at 20°C or more, the q-axis electric loading is allowed to be very high (80 – 90 kA/m) and the resulting torque density can get competitive with the ones obtainable via Nd-PMs excited machines. In the remaining cases, it is of key importance that the minimum temperature specified for transient overload operation is declared accurately, so wrong specifications cannot compromise the feasibility of FASR machines. In fact, although in many application fields

electrical machines are required to operate at ambient temperatures under 0°C (e.g. automotive, military, wind generation), yet it is thinkable that, when arctic temperatures such as -20°C or -60°C occur, a temporary de-rating can be accepted. It means that a warm-up stage at reduced current or even a pre-heating before operation may be conveniently scheduled.

4.4. DOES DEMAGNETIZATION LIMIT PERFORMING DESIGNS?

In the previous paragraphs, the demagnetization limit has been quantified in equations, pointing out how to design the rotor of FASR machines for obtaining good properties in terms of robustness towards demagnetization. The question that will be answered at the end of this conclusive section is: "Does the demagnetization constraint represent the most severe limitation to high performance applications, even for the presented optimized FASR designs?".

In other words, an exhaustive comparison between the demagnetization limit and other well-known constraints, as for example the thermal one, will be carried out. Moreover, different machine operating conditions, as overload and fault transients, will be investigated, so to highlight the actual limitations introduced by the adoption of ferrite magnets, known to be disadvantageous with respect to the demagnetization issue.

With reference to significant per-unit quantities, some general guidelines about the severity of the aforementioned constraints will be derived and meaningful results on different design cases, that have been studied with the two-fold purpose of validating the theory and better addressing the problem, will be described.

In particular, the data that will be presented as a summary of the developed work regard a direct-drive wind turbine alternator of small size (that is, 19 kW at 200 rpm), whose ratings are given in Table 4-II. The stator has three slots per pole phase and chorded windings, combined with a three-layer "complete" rotor, designed according to the rules described in Section 4.2.1 for torque ripple minimization. The rotor structure is then similar to the one sketched in Figure 4.1.

As shown by the lamination sketch in Figure 4.8, the rotor barriers have constant

thickness, but their shape is not round. In fact, the rotor saliency is maximized first via a sufficiently high rotor magnetic insulation and an adequate number of layers [57]-[58]. But, then, the anisotropy between the *d*- and *q*-axis is further increased by moving all the layers towards the airgap, radial-wise, instead of choosing round shaped barriers. The final design example has a saliency ratio equal to 5, at rated conditions. If the stator leakage inductance components (including the slot leakage term, the zig-zag contribute and end windings one) were negligible, the saliency ratio would be 8. If also the impacts of cross saturation and structural ribs were negligible, then the theoretical saliency ratio of the FASR design example would be 13. This is to address which factors affect negatively the FASR rotor saliency ratio, while confirming that the choice of having constant-thickness rotor magnets do not penalize considerably the reluctance torque component of FASR machines.

TABLE 4-II
RATINGS OF THE EXAMPLE DESIGN

MECHANICAL DATA		
Active length l	280	mm
Airgap g	0.75	mm
Stator diameter $2r$	380	mm
Rotor diameter$2r'$	304.5	mm
Pole pairs p	6	
Pole pitch to airgap ratio a/g	106	
Tooth length l_t	22	mm

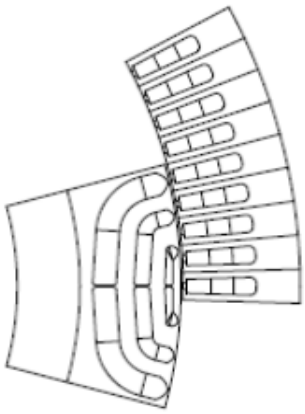

Figure 4.8 – FASR design example

The FASR motor, reported in Figure 4.8 and considered here as an example, has twelve poles. Given the airgap and the rotor diameter, that are closely related to the torque size, the number of poles have been chosen to produce a pole pitch to airgap ratio a/g as high as possible. In this case g is 0.75 mm and it is not negotiable due to mechanical constraints. The rotor diameter is 304.5 mm and a/g turns out to be equal to 106, having fixed p = 6. The per-unit rotor magnetic insulation is 0.375: this value comes from a tradeoff choice “air versus iron” between the room needed for the rotor layer and the one required by the flux guides. The ferrite grade is the one documented in Figure 4.5.

4.4.1. **Demagnetization and thermal constraints under comparison**

Regarding the comparison between the demagnetization limit and the thermal constraint at rated load, a significant figure of merit that summarizes the cooling properties of the machine can be introduced.

It is the power dissipation rate k_j at the outer surface, which can be defined as shown by (4.36), if the iron loss are disregarded as in case of low speed applications:

$$k_j = \frac{P_{Joule}}{2\pi \cdot r \cdot l} \tag{4.36}$$

P_{Joule} represents the copper losses and r is the outer radius of the stator stack. According to (4.36), the electric loading (4.37), corresponding to a given k_j, (i.e. corresponding to a given cooling set up) can derived.

$$A_{th} \approx k_w \sqrt{l_t} \sqrt{\frac{k_{cu}}{k_{end}\rho_{cu}(1 - bk_t)} k_j} \tag{4.37}$$

k_{cu} is the slot fill in factor (net copper area over slot cross section area), k_{end} is the total length of the conductors (including end connections) divided by the active length, ρ_{cu} is the copper resistivity, l_t is the tooth length and (1-b·k_t) accounts for the stator slots width. As highlighted by the operator "≈" in (4.37), the evaluation of A_{th} is proposed here in its approximated form, since the rotor radius, which determines in some way the copper area, has been confused with the outer stator radius, the power dissipation rate can be reasonably referred to. This point will be better addressed in the next Chapter. In fact, at this stage Equation (4.37) is sufficientely accurate to carry out an exhaustive comparison between the thermal and demagnetization limit.

Theoretically speaking, the demagnetization limit (4.35) and the thermal one (4.37) cannot be compared directly, because the first one refers to the q-axis current component only, while the latter one to the whole current, including the direct component. However, demagnetization occurs at high loads, in correspondence of which the current vector is close to the q-axis. Thus, assuming that (4.35) refers to the overall current amplitude would represent a conservative estimation of the machine current limit.

Under this hypothesis, Figure 4.9 compares the demagnetization and current limits, in terms of per-unit quantities, by means of (4.35) and (4.37).

In Figure 4.9, the continuous electric loading (4.37) is reported as a function of the tooth length in the two cases of k_j = 3500 and k_j = 10000 W/m^2. The lower k_j value (i.e., 3500 W/m^2) is representative of natural ventilation, while k_j=10000 W/m^2 stands for forced ventilation. Other parameters that have been fixed to compute the continuous thermal loading in Figure 4.9 are: k_{cu} = 0.4, k_{end} = 1.5,ρ_{cu} = 25·10^{-9} Ω/m (copper at 130°C) and k_w = 0.92.

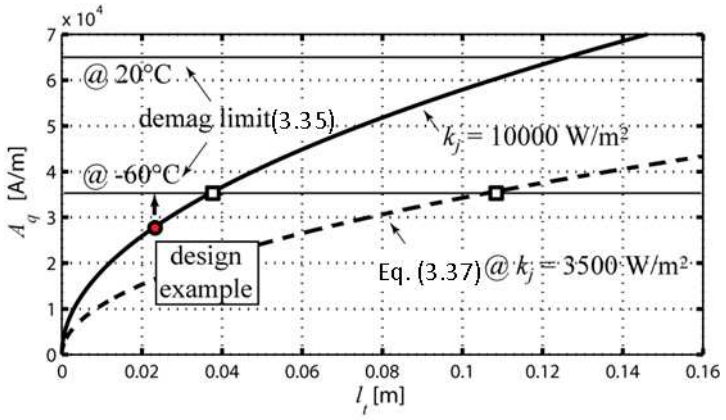

Figure 4.9 - Continuous electric loading versus tooth length, evaluated at 130°C (copper), for two types of cooling having k_j=3500W/m^2 and k_j=10000W/m^2. The demagnetization levels at-60°C and 20°C (magnet) indicate the transient overload limit.

In Figure 4.9, the demagnetization limits (4.35) at -60°C and +20°C are also shown, again referring to the geometry of the machine example of Figure 4.1. The upper limitation $A_{q,irr}$ is plotted in correspondence of the a/g area that has been revealing of main interest for the design: namely, a/g values greater than 50 have been considered, for which $A_{q,irr}$ is characterized by an asymptotic behavior (see Figure 4.7).

The current loading $A_{q,irr}$ (4.35) is a function of normalized quantities only and does not depend on the stator tooth length l_t. Conversely, the thermal limit A_{th} (4.37) is proportional to the square root of the actual length of stator teeth, and it is then related to the physical size of the machine, meaning that larger machines can withstand a lower current density, as known.

In other words, looking at Figure 4.9, it is possible to notice which machines are able

to withstand overload transients at a certain temperature, without running into irreversible demagnetization phenomena. These FASR machines are the ones with a stator tooth length which allows the rated loading (4.37) to be lower than $A_{q,irr}$ (4.35).

- With natural ventilation (k_j = 3500 W/m²) there is room for overload even when at -60°C with stator teeth up to 100 mm long. This is to say that FASR machines, that are naturally ventilated, do not suffer from demagnetization at any temperature, at least in the small and medium sizes.
- With forced ventilation (k_j = 10000 W/m²) the room for overload is smaller. Machines with stator teeth 40 mm long, or more, are at risk of demagnetization at -60°C, in this example. This is to point out that ventilated or liquid cooled machines are more at risk of demagnetization at very low temperatures, because they are more loaded. Yet, they have an abundant overload margin as the operating temperature approaches reasonable values, such as 20°C.

TABLE 4-III
EXAMPLE MACHINE OF FIG. 4.9:
REMARKABLE WORKING POINTS

POINT *a* - CONTINUOUS RATINGS		
Nominal speed	200	rpm
Continuous torque	910	Nm
Specific loss k_j	10000	W/m²
A_{th} at +130°C (4.36)	27.2	kA/m
Current amplitude	39	A
Phase angle (MTPA)	53°	
POINT *b* – OVERLOAD RATINGS, -60°C		
$A_{q,irr}$ at -60°C (4.34)	35.5	kA/m
Current amplitude	51	A
Phase angle (MTPA)	56°	
Overload torque	1240	Nm
OUT OF BOUNDS – OVERLOAD RATINGS, +20°C		
$A_{q,irr}$ at +20°C(4.34)	65.2	kA/m
Current amplitude	95	A
Phase angle (MTPA)	63°	
Overload torque	2330	Nm

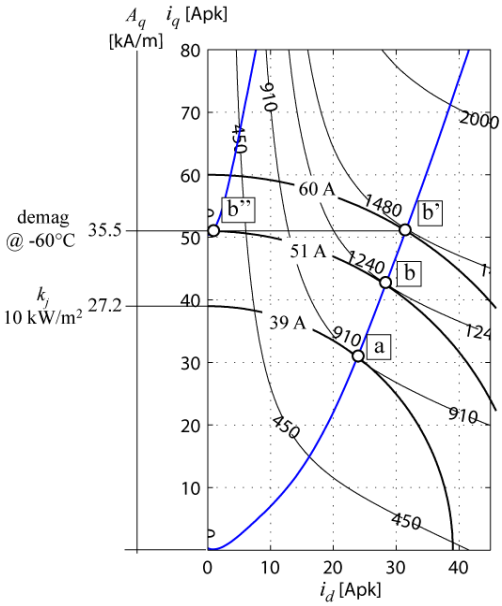

Figure 4.10 - Torque and current contour lines for the machine example of Figure 4.8 (see Table 4-II for details). The MTPA trajectory is FEA calculated at 130°C.

For those machines, that are characterized by a continuous loading limit higher than

the demagnetization one, a warm-up preparatory stage at reduced load might be needed before being able to apply full- and over-load currents.

In order to validate the general guidelines, that have just been derived, it is convenient to refer to the FASR design example of Figure 4.8. Its overload margin at -60°C is indicated with an arrow in Figure 4.9 and, more in details, the charts over the (i_d, i_q) plane of Figure 4.10 report the motor torque and current amplitude contours. The curves of Figure 4.10 have been FEA calculated at the rated temperature of 130°C. The maximum torque per Ampere (MTPA) control trajectory is also traced. So, rated- and over-load operating conditions can be deeper analyzed from both the thermal and demagnetization point of view. At the same time, it is possible to discuss the assumption of limiting the overall current loading (instead of the q-axis component, only) to the limit value $A_{q,irr}$, in order to make conservatively the PMs safe in terms of irreversible demagnetization.

The working points of interest that have been identified in Figure 4.10 are:

- *Point a* - According to the cooling set up of the machine example (k_j = 10000 W/m^2 - forced ventilation), the continuous thermal electric loading (4.35) is equal to 27.2 kA/mm. It is indicated with a red circle in Figure 4.9 and on the A_q scale of Figure 4.10. The working condition at continuous torque are then represented by *Point a*, that corresponds to an electric loading equal to 27.2 kA/mm and lies on the MTPA trajectory.
- *Point b*'' and *Point b*' - The irreversible demagnetization limit (4.35), calculated at -60°C, is 35.5 kA/m and it is reported in Figure 4.10. *Point b*'' is representative of this current loading level, fully oriented against the PMs, i.e. along the q-axis as assumed by the magnetic equivalent circuit model. *Point b*' should behave the same as *b*'', in terms of demagnetization, at least according to the model, since its quadrature component corresponds always to 35.5 kA/m. The direct component, associated to *point b'* is determined by the MTPA locus, as evidenced in Figure 4.10.
- *Point b* - Following the conservative approximation of limiting the whole current loading to demagnetization limit $A_{q,irr}$ without considering the actual

current phase angle, the maximum overload condition at -60°C is supposed to be *Point b*, that shows a certain margin with respect to *point b*'.

If compared to the continuous operating *Point a*, *Point b* is +30% current and +36% torque (see Table 4-III). It means that, even in the very disadvantageous (and unlikely) case of -60°C ambient temperature and a cold startup, there is still room for transient overload. As the temperature goes up to values larger than the zero, the demagnetization limitation gets out of the area represented in Figure 4.10. For example, the current loading limit at 20°C reported in Table 4-III (65.2 kA/m), and the corresponding current (95 A) and torque (2330 Nm) values are outside the range of Figure 4.10.

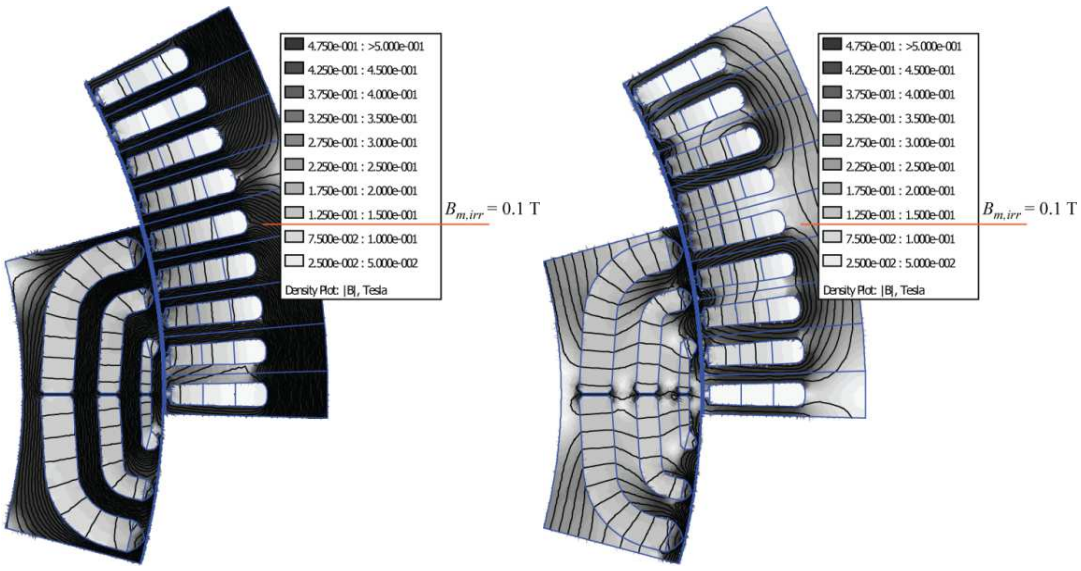

(a) (b)

Figure 4.11 - Flux density maps at maximum overload at 20°C($A_{q,irr}$= 65.2 kA/m, B_r= 0.38 T, $B_{m,irr}$= 0.10 T). a) 65.2 kA/m are applied along the MTPA angle (i_d = 43 A, i_q = 85 A) b) same situation, without the d-axis current (i_d = 0, i_q = 85 A), meaning a total current loading equal to 0.89 $A_{q,irr}$.

Figure 4.11a shows the Finite Element PM verification of this overload condition, that is 65.2 kA/m (95 A) applied along the MTPA locus and magnets at 20°C. Figure 4.11b refers to the same current on the *q*-axis (85 Apk), but has null *d*-axis current. This means, as said, that a safety margin with respect to the demagnetization limit $A_{q,irr}$ (4.35) output by the model does exist. At 20°C, the magnets are safe if their working flux density is larger than 0.10 T and the FEA verifications validate the developed theory, from this point of view. In Figure 4.11b the flux density is homogeneous over the width

of all the PMs and nearly the same for all the layers. In Figure 4.11a, although the overload *d*-axis current saturates the rotor iron, the flux density in the PMs is still fairly uniform, with the exception of the area that is closer to the tips of the barriers.

The tips area is represented more in detail in Figure 4.12: Figure 4.12a and Figure 4.12b are referred to the same operating conditions of Figure 4.11a and Figure 4.11b, respectively. In figure 4.12a, the flux lines in the tips do not follow the direction of magnetization of the ferrite, due to the deep saturation of the rotor flux guides, especially in points A and B. It is caused mainly by the *d*-axis flux, that is disregarded by the magnetic equivalent circuit model. When only the *q*-axis current component is present (see Figure 4.12b), the magnets work uniformly as expected.

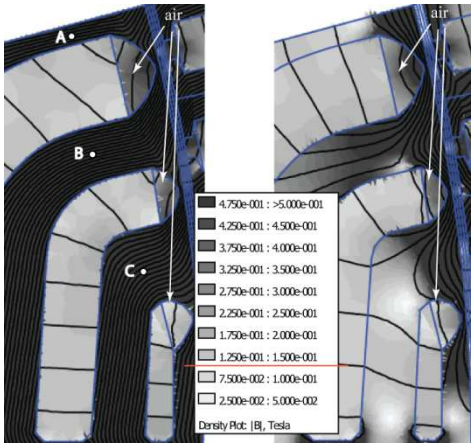

(a) (b)

Figure 4.12 - Enlarged view of Figures4.12a and 4.12b. The flux density in point A is 2.06 T, and in point B is 2.00 T.

The barriers tips have not been magnetized in the FEA model, since it is intended that they would not be in the ultimate design. Even when the tips are filled in with ferrite material (e.g. the plastic bonded one) and they are initially magnetized along the rest of the magnets, then the area tend to demagnetize very easily [9], [59]. In other words, in most of practical cases, the tips are either empty or magnetized poorly.

4.4.2. Discussion of the steady-state short circuit condition

Although it has been demonstrated that the current load capability of the machine is not seriously limited by demagnetization issue in operation, even at very low

temperatures, a particular care must be given to the short circuit condition.

The steady state short circuit current, aligned against the PMs, coincides with the machine characteristic current and is maximum at cold, due to the higher remanence of the magnets at low temperature. During normal operation, the PMs temperature is usually higher than the one registered at the start-up and the short circuit current turns out to be lower.

In practice, the unlikely event of a short circuit fault during start-up operations, in cold temperature environments, represents the riskiest occurrence in terms of demagnetization.

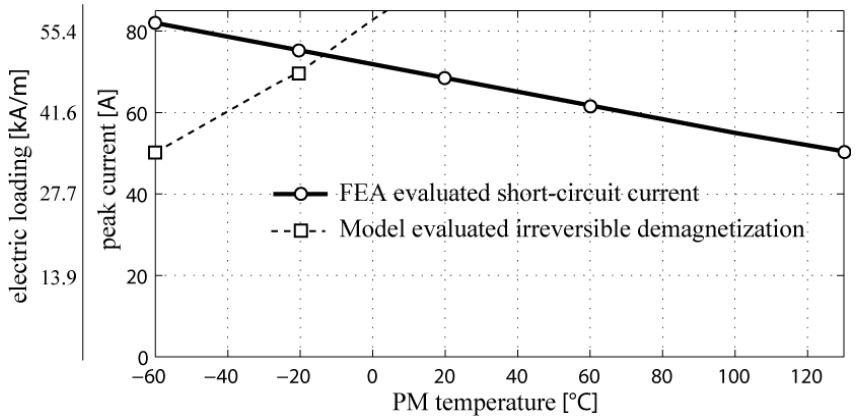

Figure 4-13 - Crossover temperature between short circuit current and steady state irreversible demagnetization limit for the FASR design example of Figure 4.9

Figure 4.13 reports the steady-state short circuit current of the FASR design example described in Table 4-II as a function of the PM temperature, that varies in the range (-60°C, 130°C). The comparison with the feasible continuous current loading (4.35) shows that, in case of fault, below -20°C, the machine is at risk in terms of demagnetization, if the rotor design has been arranged to be safe only with respect to the irreversible demagnetization limit (4.35) in normal operating condition.

To put in evidence this occurrence, Figure4.14a and Figure 4.14b show the flux density maps in case of short circuit, respectively at -20°C and +20°C. In both cases the flux density is uniformly distributed in the PMs and it is around 0.2 T. However, at -20°C, $B_{m,irr}$ is around 0.2 T and the PMs are then on the edge of irreversible demagnetization, whereas, at +20°C, the magnets are in the safe area, whose lower limit is 0.1 T in this

case.

To summarize, at rated temperature there are no practical limitations, and the margin with respect to irreversible demagnetization is so big that possible fault occurrences do not turn out to be dangerous in this sense.

However, the FEA results demonstrate that, although the machine example is safe at rated load at all temperatures and even at -60°C the motor can withstand a current overload of +44% without running against demagnetization issues, the short-circuit condition can get critical when dealing with very cold environments.

This makes necessary to pre-heat the machine up to (at least) zero degrees before starting non-zero speed operation. So the magnets are preserved also in case of fault, besides being absolutely secure at their steady state operating temperatures.

As an alternative, ferrite grades with higher coercivity values at low temperatures, which do exist [60], can be adopted for applications where low operating temperatures are extremely serious.

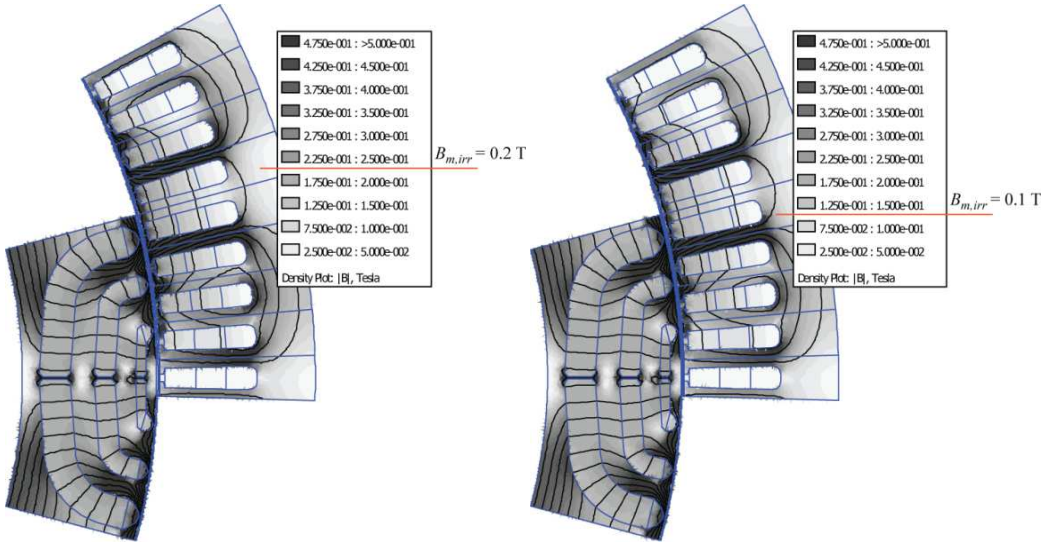

(a) (b)

Figure 4.14 - Design example of Table 4-II: flux density distribution at steady-state short circuit condition. a)PMs temperature = -20°C. B_r = 0.42 T, I_{sc} = I_q = 75.25 A; b) PMs temperature = +20°C. B_r = 0.38 T, I_{sc} = I_q = 68.5 A.

The transient magnetic behavior, in case of a short circuit fault, can worsen the figures presented in this steady state analysis. During the fault transient, in particular if

the starting current is much higher than the steady-state short-circuit current, the transient q-current loading can be very high and also the eddy current arising in the magnets must be considered as a cause of distortion of the uniform flux density distribution in the PMs.

This is demonstrated in [61] for a single layer Interior PM machine. A dedicated analysis might be required to account for transient behavior.

4.5. REMARKING CONCLUSION

This chapter introduced the main mathematical instruments for modeling the magnetic behavior of FASR machines.

It also formalized a set of design choices capable of improving the starting SR rotor design and the robustness against demagnetization of a Ferrite Assisted Synchronous Reluctance machine. The design criteria have been justified analytically and they lead to the uniform exploitation of the low energy density magnetic material, together with the reduction of the overall harmonic content.

To summarize, it is reminded that:

- the rotor “slot” pitch is regular (4.14);
- the rotor flux barriers have uniform thickness;
- the magnets thicknesses (4.18) and widths (4.21-4.24) follow the shape of the per-unit staircase, introduced to model the stator mmf.
- the total rotor magnetic insulation needs to be maximized, considering that real world machines can have a per-unit insulation up to 0.30–0.45, as a result of a tradeoff choice “air versus iron”.
- the airgap and the pole pitch are required to be matched correctly. In other words, the number of pole pairs must be chosen properly, given the airgap, or vice-versa.

The limit of safe current loading has been quantified analytically.

By comparison with the continuous thermal loading limitation, it turned out that larger machines are more at risk of demagnetization than smaller ones. Besides the

torque capabilities of FASR machines at rated load, overload operating conditions have been analyzed to draw significant conclusion about the severity of the demagnetization limit. In particular, very low ambient temperatures and cold starts have been considered, as they are major causes of demagnetization. The risks related to a short-circuit event when starting to operate the drive in very cold environments have been pointed out, as well.

The developed theory and FEA validation confirmed that the exploitation of the magnets is correct and that the estimation of the critical current loading is precise enough for being of practical use.

Moreover, it has been demonstrated that the demagnetization risk does not compromise the development of this technology, whose feasibility in many up-to-date applications will be discussed in detail in Chapter 07, after proposing a comprehensive design procedure to optimize the FASR machine performance in Chapter 05.

Chapter 05

A general approach to the optimal design of Ferrite Assisted SR machines

---

After introducing the basics for the modeling theory, a general approach to the optimal design of Ferrite Assisted Synchronous Reluctance machines will be formalized via a two steps procedure.

At first one rectified machine pole, as the one in Figure 5.1, will be analyzed. Reference will be made again to a schematic block with the rotor flux barriers having constant thickness along their widths and being completely filled in with ferrites, so to compensate for the lower B-H energy product of the magnets. As suggested in the previous chapter, the FASR rotor will be optimized for torque ripple minimization and its design improved for reducing the risk of demagnetization.

Regarding the evaluation of the machine performance, key figure of merits, such as shear stress, Power Factor and Joule loss density, will be identified and they will be expressed in equations, as function of both normalized quantities and significant geometric parameters, in order to derive general guidelines and tips for high performance designs. This preliminary per-unit analysis aims also at verifying if Ferrite Assisted Synchronous Reluctance machines can compete with rare-earth based SPM and IPM counterparts in terms of torque density and efficiency, despite the disadvantageous energy density of ferrite magnets. Machines of all sizes and applications of various kinds will be investigated throughout the analysis, highlighting pros and cons of the proposed technology with respect to different application fields and power density demands. Particular attention will be devoted to direct-drive low speed machines with high number of pole pairs.

Afterwards, the elementary blocks, which account for the magnetic behavior of each rectified FASR pole, will be assembled together in order to form a rotating machine fitting into fixed stack dimensions (stator diameter and stack length).

The design space will be identified according to the results of the per-unit analysis on the reference block and it will be clarified how to apply the key modeling equations to speed up the design stage. Moreover, the designer will be further oriented in his decision tasks, since it is possible to find out straightforward formulas to choose the pole pairs number of the machine in order to minimize either the Joule loss or the PM grade, at given torque.

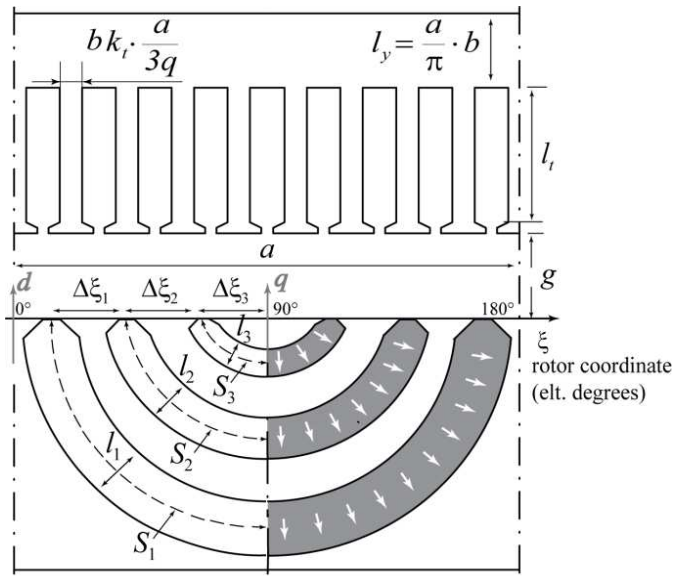

Figure 5.1 - Rectified pole of a FASR machine with a three-layer "complete" rotor (n=3, n_r=14) and the PMs magnetized radial-wise. The *dq* axes follow the SR model approach.

The proposed design procedure has been applied to several cases, with both FEA and experimental validation. Some results will be presented at the end of this Chapter, where the accuracy of the model will be discussed, and later on in Chapter 07, where the performance of FASR machines will be fairly compared to the ones of more standard (read, more expensive) solutions and other alternative technologies for PM-cost reduction. Experimental evidence of the validity of the proposed technology will be given as well: in Chapter 08, the reader will find some experimental data on a down-scaled FASR prototype and the respective SPM competitor.

5.1. KEY DESIGN EQUATIONS

This first section provides per-unit expressions for the design of both the magnetic loading B_{gap} and electric loading A of the rectified pole of Figure 5.1, distinguishing the different roles played by the components of B_{gap} and A along the direct and quadrature axis.

At this purpose, reference is made always to the simple geometry and symbols, introduced in Subsection 4.1.1. The magnetic behavior of the quadrature axis, that is the one oriented against the PMs, is analyzed via the equivalent circuit described in Subsection 4.1.2 and the same normalized model is adopted. The FASR rotor is intended to be optimized for both torque ripple minimization and stiffness against demagnetization, as suggested in Section 4.2.

The magnetic loading B_{gap} [T] is defined here as the peak flux density in the airgap.

The electric loading A [Apk/m] is proportional to the fundamental peak value F of the stator mmf waveform:

$$A = \frac{\pi}{2} \cdot \frac{F}{a} = \frac{\pi}{2} \cdot \frac{1}{a} \cdot \left(\frac{3}{\pi} k_w N I \right) \tag{5.1}$$

The reader is reminded that I is the peak value of the stator current, N is the number of conductors in series per pole per phase and k_w is the winding factor.

5.1.1. Direct axis magnetizing loading

A portion of the total electric loading has to be spent for generating the d-axis magnetizing loading $B_{gap,d}$, which is typically required to be around 0.75-0.9 T.

The value of $B_{gap,d}$ is strictly related to the size of the stator back iron and its exploitation in terms of flux density. In fact, if the q-axis flux is nearly zeroed by the PMs action, as it is the case with effective PM-Assisted designs, the stator yoke and teeth are interested mainly by the d-axis flux. Then, the chosen magnetizing loading in the airgap ($B_{gap,d}$) and the target flux density in the back iron (B_{fe}) determine the core dimension. As highlighted in Figure 5.1, the ratio b between $B_{gap,d}$ and B_{fe} represents:

- the yoke height, in per-unit of the pole pitch;
- the tooth width, in per-unit of the slot pitch, being k_t a scaling factor slightly lower than one.

b is usually between 0.5 and 0.65.

Once $B_{gap,d}$ (i.e. the product $b \cdot B_{fe}$) is fixed, the Ampere law defines the relationship (5.2) between the selected d-axis magnetizing loading and the required mmf F_d.

$$F_d = \frac{b \cdot B_{fe}}{\mu_0} g = \frac{B_{gap,d}}{\mu_0} g \tag{5.2}$$

Then, the d-axis electric loading A_d (5.3) is determined:

$$A_d = \frac{\pi}{2\mu_0} b \cdot B_{fe} \frac{g}{a} \tag{5.3}$$

A_d is proportional to the per-unit airgap g/a, to indicate that, when the airgap is too thick, a non-negligible part of the current loading is spent for d-excitation, with negative impact on the Joule loss and the Power Factor, as it will be recalled in the following.

5.1.2. "Natural compensation" of the quadrature axis flux linkage

When dealing with PM-Assisted motors, the magnets flux is designed for compensating either the whole q-axis flux of the basic SR machine or the majority of it [57]. In the former case, represented by the vector diagram of Figure 5.2, the FASR machine is "Naturally Compensated" [1]. It says that:

- the Power Factor is defined by the current argument only and just few poor design choices (i.e. the ones with large per-unit airgaps) lead to unsatisfactory PF values;
- the stator back iron is saturated primarily by the d-axis magnetizing flux and the cross saturation effects are definitely reduced.
- the flux weakening capability of the machine is improved, guaranteeing a Constant Power Speed Range theoretically unlimited.

So, the effect of the "Natural Compensation" condition on the machine Power Factor is twice beneficial, since with good PF values the size of the power converter can be

reduced and the flux weakening capability of the motor is increased. This point will be better addressed in the Chapter 07, when dealing with optimized designs devoted to automotive applications, for which having wide Constant Power Speed Range is mandatory. Moreover, the advantageous impact of having the FASR machine "Naturally Compensated" on the cross saturation phenomena guarantees improved performance of the motor in terms of torque production.

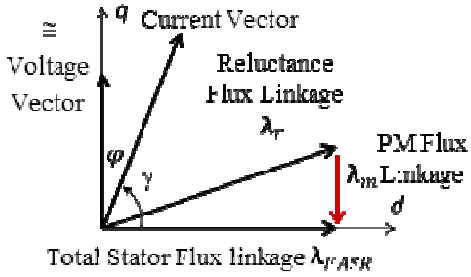

Figure 5.2 - Vector diagram of a "Naturally Compensated" PM-assisted machine.

"Natural Compensation" will be considered, from now on, as the rated design condition of the elementary block, even if some details about design choices, that are different from the "Natural Compensation" one, will be provided as well.

In order to fulfill the "Natural Compensation" condition, the PM flux linkage λ_m will be designed, so to have the q-axis rated current of the machine equal to the characteristic (or short circuit) one, namely I_{q0}[19]. In formula:

$$\lambda_m = L_q I_{q0} \tag{5.4}$$

Where L_q is the q-axis inductance.

The PM flux linkage λ_m of one rectified pole (5.5) is a function of the flux density $B_{gap,m}$, produced in the airgap by the magnets.

$$\lambda_m = \frac{2}{\pi} k_w N \cdot a \cdot l \cdot B_{gap,m} \tag{5.5}$$

Then, the characteristic loading A_{q0} follows from (5.5), according to the definitions (5.1) and (5.4):

$$A_{q0} = \frac{3\pi}{4\mu_0} \cdot \frac{B_{gap,m}}{L_{q,pu}} \tag{5.6}$$

where the normalization of the pole inductance $L_{q,pu}= L_q /L_{base}$ is based, as usual, on (5.7):

$$L_{base} = \frac{\mu_0 l}{2} \cdot \left(\frac{2}{\pi} \cdot k_w N\right)^2 \tag{5.7}$$

The key role played by A_{q0} has to do with the torque capability of the machine, as it will be demonstrated. Thus, it is worth pointing out its dependence on the main design parameters and it will be done by defining $B_{gap,m}$ and $L_{q,pu}$, in Subsection 5.1.2.1 and 5.1.2.2, respectively.

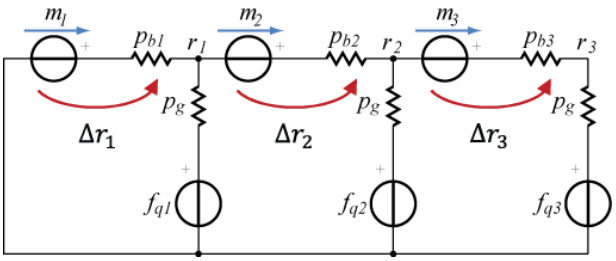

Figure 5.3 - The equivalent circuit represents the *q*-axis magnetic behavior of half a pole. It refers to the FASR example rotor in Figure5.1 (*n*=3).The airgap permeances p_{gk} are the same for all the rotor teeth at the airgap, as "regular" rotor structures, suitable for torque ripple minimization purposes, are considered here.

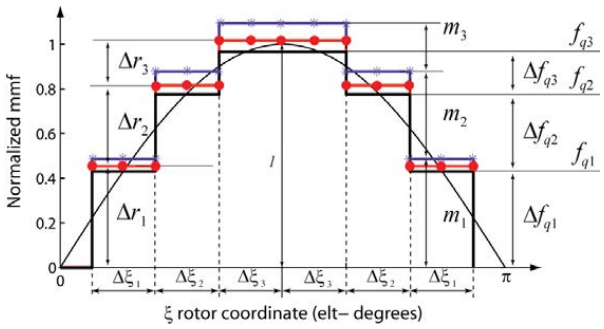

Figure 5.4 - Staircase distributions of the mmfs in the equivalent circuit of Figure 5.3, in per-unit of the peak value of the *q*-axis fundamental mmf. The plots are referred to the three-layer "complete" rotor example of Figure 5.1. No markers: *q*-axis stator mmf f_{q123}. Star: PMs mmf m_{123}. Circle: iron guides magnetic potentials r_{123}.

5.1.2.1. Airgap flux density produced by the PMs

At no load, the peak flux density in the airgap $B_{gap,m}$ and the flux density in the magnets B_{m0} are proportional to each other and are both obtained by solution of the magnetic circuit in Figure5.3, introduced in the Chapter 04.

The no load uniform flux density in the magnets, in per-unit of the PM remanence B_r, was derived in Section 4.3, under the hypothesis of designing both the PMs mmf $\boldsymbol{m}$ and the magnetic potential drops $\boldsymbol{\Delta r}$ proportional to the per-unit staircase $\boldsymbol{\Delta f_q}$, which models the effect of the q-axis stator mmf.

The same assumption, justified in Section 4.2.2 and summarized by the plots in Figure 5.4, will be adopted and recalled many times in the following.

Expression (5.8), that defines the PMs no load flux density, is reported here for convenience, reminding that $l_{a,pu}$, which is equal to $l_a/(a/2)$, represents the rotor per-unit magnetic insulation.

$$B_{m0,pu} = \frac{1}{1 + \frac{2\pi}{l_{a,pu}} \cdot \frac{S_1}{a} \cdot \frac{1}{k_{\Delta\xi n} \cdot \Delta\xi} \frac{\sin(k_{\Delta\xi n} \cdot \Delta\xi)}{\cos(\Delta\xi/2)} \cdot \frac{g}{a}} \tag{5.8}$$

In (5.8), the term S_1/a can be simplified and the PMs volume, in per-unit of the rotor one, can be introduced instead.

The substitution will produce a more useful formulation, since the normalized PMs volume $V_{m,pu}$ (5.9) is known to be an indicative design indicator, strictly correlated to the chosen $l_{a,pu}$.

$$V_{m,pu} = \frac{4(S_1 l_1 + .. + S_n l_n) \cdot l}{a^2 \cdot l} \tag{5.9}$$

The relationship between S_1/a and $V_{m,pu}$ is solved considering the geometrical constraints fixed on the magnets lengths l_k and widths S_k by (5.10) and (5.11).

They formalize the rules identified in Section 4.2.2 for pursuing at the same time the uniform exploitation of the PMs and the reduction of the overall harmonic content via the proportionality of both $\boldsymbol{\Delta r}$ and $\boldsymbol{m}$ to the per-unit steps $\boldsymbol{\Delta f_q}$.

$$l_k = l_{a,pu} \cdot \frac{a}{2} \cdot \frac{\Delta f_{qk}}{f_{qn}} \tag{5.10}$$

$$\frac{S_k}{S_h} = \frac{\Delta f_{qk}}{\Delta f_{qh}} \quad \forall\, h,k \neq n, \qquad \frac{S_n}{S_1} = k_{pn} \frac{\Delta f_{qn}}{\Delta f_{q1}} \tag{5.11}$$

Equations (5.10) and (5.11) lead to the univocal relationship (5.12) between the

term S_1/a and the normalized magnets volume $V_{m,pu}$, needed to carry on the analysis.

$$V_{m,pu} = \frac{n_r l_{a,pu}}{2} \frac{\tan(\Delta\xi/2)}{\cos(\Delta\xi/2)} \cdot \frac{S_1}{a} \tag{5.12}$$

So, Equation (5.13) is obtained by substituting (5.12) into (5.11) and by approximating the trigonometric function cos(Δξ/2) with the first two terms of the respective Taylor series.

$$B_{m0,pu} \cong \frac{1}{1 + \frac{4 \cdot V_{m,pu}}{l_{a,pu}^2}\left(1 - \frac{\pi^2}{n_r^2}\right)\frac{g}{a}} \tag{5.13}$$

In (5.13), the parameter n_r is put in evidence, keeping in mind its relationship (5.14) with the "regular" rotor "slot" pitch Δξ.

$$\Delta\xi = \frac{2\pi}{n_r} \tag{5.14}$$

The PMs flux density $B_{m0,pu}$ (5.13) at no load:

- determines the robustness of the machine towards demagnetization at any operating conditions, as it has been demonstrated in Section 4.3.2;
- defines the no load flux density in the airgap via a proportional relationship, that will be introduced in the following.

The maximization of B_{m0} has then a twofold purpose, that, according to (5.13), can be better pursued when dealing with multi-layer rotor structures ($n \geq 3$, $n_r \geq 14$), as the ones, this work focuses on. Equation (5.13) also suggests that designs with thick per-unit airgaps g/a and small rotor magnetic insulation $l_{a,pu}$ penalize the no load flux density in the magnets. Recommended values of $l_{a,pu}$ are around 0.30-0.45. With larger per-unit insulation, as it has already been pointed out, the design of the rotor flux guides would be poor and the consequent iron saturation effects might compromise the machine performance.

As said, a proportional relationship between the airgap flux density and the PMs one can be found from the q-axis magnetic circuit of Figure 5.3.

In fact, it has been demonstrated in Section 4.2.2.2. that the uniform PMs working

flux density $B_{m0,pu}$ (5.15) depend on the element by element division $\boldsymbol{\Delta r_0/m}$, between the magnetic potential drops at no load and the PM mmfs (both supposed to copy the shape of the per-unit steps $\boldsymbol{\Delta f_q}$).

$$B_{m0,pu} = 1 - \frac{\boldsymbol{\Delta r_0}}{\boldsymbol{m}} \tag{5.15}$$

The equivalent circuit of Figure 5.3 puts in evidence that, at no load, also the airgap flux density is proportional to the de-normalized potentials vector $\boldsymbol{\Delta r_0}$, according to the ratio μ_0/g.

Then, Equation (5.16) follows, showing that the peak flux density in the airgap $B_{gap,m}$ and the uniform flux density in the magnets B_{m0} are proportional to each other.

$$B_{gap,m} = \frac{V_{m,pu}}{l_{a,pu}} \frac{\Delta\xi \cdot \cos(\Delta\xi/2)}{\tan(\Delta\xi/2)} B_{m0} \cong 2\frac{V_{m,pu}}{l_{a,pu}}\left(1 - \frac{\pi^2}{n_r^2}\right) B_{m0} \tag{5.16}$$

The previous formula accounts for the flux concentration effect of this type of PM machines.

If the FASR rotor is designed with proper values of both $l_{a,pu}$ (e.g. 0.30-0.45) and $V_{m,pu}$ (e.g. 0.3-0.4), the airgap flux density $B_{gap,m}$ results to be roughly 2 times the flux-density in the magnets. The flux density in the magnets, in turn, can be optimized as previously described.

That is to say that low energy density PMs can still produce a valuable flux density in the airgap, thanks to the particular rotor topology.

Once more, multi-layer rotor structures (i.e. $n_r \geq 14$, $n \geq 3$) show noticeable advantages. In fact, in case of more standard IPM machines with one or two layers (that is, lower n_r values) the flux concentration is penalized by the terms in bracket in (5.16).

Figure 5.5, which puts together (5.13) and (5.16), shows the peak flux density produced by the PMs in the airgap, as a function of a/g and the magnets grade.

The plots are referred to the room temperature. However, of course, the actual temperature of the PMs and the law of degradation of their B-H characteristic with the temperature affect $B_{gap,m}$, and this dependence has to be taken into account in the design

procedure.

Whatever the magnets temperature is, the results in Figure 5.5 confirm and quantify the qualitative considerations, evidenced before, about the convenience of properly choosing both the pole pitch and the key rotor design parameters.

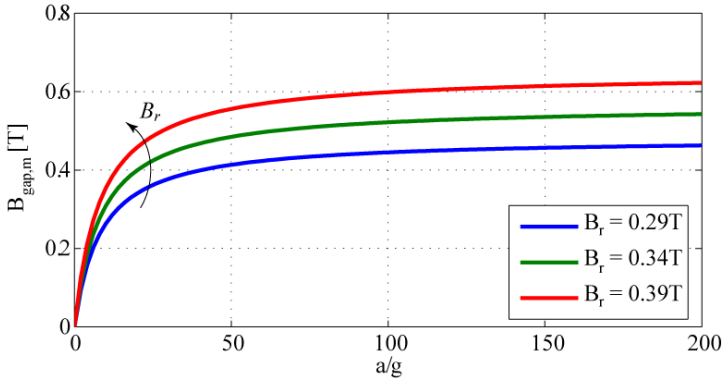

Figure 5.5 - Peak flux density in the airgap at no load (5.15), as a function of the pole pitch to airgap ratio. Ferrite grades with different remanence values are shown. The example is for l_{apu} = 0.4, $V_{m,pu}$=0.35, n = 3, n_r = 14.

5.1.2.2. q-axis inductance and its components

When designing PM-Assisted motors, the minimization of the q-axis inductance is one pivotal aspect, as it improves the rotor saliency of the basic SR machine. Besides, with low L_q values, the PM flux linkage needed to fulfill the "Natural Compensation" condition (5.4) can be reduced, or, if the PMs grade and volume are given, the characteristic current (5.6) can be increased.

The total q-axis inductance accounts for:

- the magnetizing term $L_{m,q}$;
- the slot leakage contribute $L_{\sigma,slot}$;
- the zig-zag inductance $L_{zz,q}$.

The magnetizing term $L_{m,\mathrm{q}}$ is representative mainly of the q-axis flux, flowing through the inner rotor, when the rotor iron segments are polarized by a stator mmf, oriented along the quadrature axis.

A quick and easy way to compute this contribute is to solve the equivalent magnetic circuit of Figure 5.3, while short-circuiting the mmf generators $\boldsymbol{m}$. With $\boldsymbol{m}$=0, if a q-axis

stator mmf F_q is applied, the flux linked by the stator windings depends on the peak flux density $B_{gap,q}$, produced in the airgap, by interaction between the rotor anisotropy and the q-axis stator mmf. Then, the respective magnetizing inductance $L_{m,q}$ is given by (5.17).

$$L_{m,q} = \frac{3}{2} \cdot \frac{B_{gap,q}\big|_{m=0}}{\mu_0} \cdot \frac{1}{F_q} \cdot L_{base} \tag{5.17}$$

The magnetic circuit of Figure 5.3 allows to evaluate the airgap flux density in the aforementioned condition. In particular, the peak value of the flux density in the airgap is determined as shown by (5.18) under the assumption that both the PMs mmf $\boldsymbol{m}$ and the magnetic potential drops $\boldsymbol{\Delta r}$ are designed to be proportional the mmf staircase $\boldsymbol{\Delta f_q}$ of Figure 5.4.

$$B_{gap,q}\big|_{m=0} = \frac{\mu_0}{g} \cdot \left(1 - \frac{\Delta r_1}{\Delta f_{q1}}\right) \cdot F_q \tag{5.18}$$

According to the same hypothesis, the term in round bracket in (5.18) turns out to be equal to (5.19):

$$\left(1 - \frac{\Delta r_1}{\Delta f_{q1}}\right)\Big|_{m=0} = \frac{\frac{p_b}{p_g}\left(1 - \frac{\Delta f_{q2}}{\Delta f_{q1}}\right)}{1 + \frac{p_b}{p_g}\left(1 - \frac{\Delta f_{q2}}{\Delta f_{q1}}\right)} \cong \frac{p_b}{p_g}\left(1 - \frac{\Delta f_{q2}}{\Delta f_{q1}}\right) \tag{5.19}$$

where an approximation has been introduced, considering that effective PM-Assisted designs are characterized by good rotor magnetic insulation and, thus, the ratio between the barrier permeance (p_b) and the airgap one (p_g) is small.

By substituting both (5.18) and (5.19) in (5.17), by reminding how the "regular" airgap permeance p_g (5.20) was defined, and by expressing the per-unit steps Δf_{qk} as functions of the rotor "slot" pitch $\Delta\xi$, Equation (5.21) is found:

$$p_g = \frac{a}{g} \cdot \frac{\Delta\xi}{\pi} \tag{5.20}$$

$$L_{m,q} = \frac{3\pi^2}{n_r} \cdot p_b \cdot L_{base} \tag{5.21}$$

Now, it is sufficient to recall the definition (5.22) of p_b, together with the ones of l_k

(5.10) and, if a reasonable modeling shape (e.g. rounded shape) is chosen for the rotor layers width S_k, as done in (5.23) for k = 1, the magnetizing quadrature inductance can be quantified.

$$p_b = \frac{S_k}{l_k} \tag{5.22}$$

$$S_1 = \left(k_{\Delta\xi n} + n - 1\right)\Delta\xi\,\frac{a}{2} = \frac{\pi}{4}a\,\left(1 - \frac{2}{n_r}\right) \tag{5.23}$$

In fact, by replacement of (5.22) and (5.23) in (5.21), the expression (5.24) of the flow-through q-axis inductance is obtained.

$$L_{m,q} = \frac{3\pi^2}{4l_{a,pu}}\left(1 - \frac{2}{n_r}\right)L_{base} \tag{5.24}$$

Regarding the other contributes to the overall q-axis inductance, Equation (5.25) suggests how to quantify the slot-leakage component.

$$L_{\sigma,slot} = \frac{\pi^2}{2k_w^2}\frac{1}{(1 - bk_t)}\cdot\frac{l_t}{g}\cdot\frac{g}{a}\cdot k_{tip}\cdot\left(1 - \frac{3n_{sp}}{16q}\right)\cdot L_{base} \tag{5.25}$$

In (5.25), l_t is the tooth length, (1-bk_t) is representative of the slot width, n_{sp} represents the number of slots with conductors belonging to different phase windings in case of chorded windings and k_{tip} (5.26) quantifies the inductance increase of a semi-closed slot with respect to an open one, due to the tooth tip shoe.

$$k_{tip} = 1 + \frac{b}{2}\cdot\frac{(1 - bk_t)^2}{k_{so}}\cdot\left(\frac{a}{g}\right)\cdot\left(\frac{l_t}{g}\right)^{-1}\cdot\frac{\left(1 - \frac{n_{sp}}{4q}\right)}{\left(1 - \frac{3n_{sp}}{16q}\right)} \tag{5.26}$$

Of course, the factor k_{tip} does depend on the stator slot opening at the airgap, which is symbolized by k_{so} in (5.26), taking into account its per-unit value with respect to the stator slot pitch.

$$L_{zz,q} = \frac{1}{8}\left[\left(\frac{\pi}{3q}\right)^2 + \left(\frac{2\pi}{n_r}\right)^2\right]\cdot\frac{a}{g}\cdot L_{base} \tag{5.27}$$

The zig-zag inductance [62], as highlighted by the squared terms in round brackets in (5.27), includes both the stator and rotor slots leakage effects, being q the number of

stator slots per pole per phase and n_r the equivalent number of rotor slots per pole pairs.

With reference to the FASR rotor structure in Figure 5.1, the curves reported in Figure5.6 show the per-unit q-axis inductance $L_{q,pu}$ as a function of the pole pitch to airgap ratio and with the normalized stator tooth length l_t/g as a parameter. $L_{q,pu}$ is shown in correspondence of both an inadequate (0.25) and an adequate (0.4) value of $l_{a,pu}$.

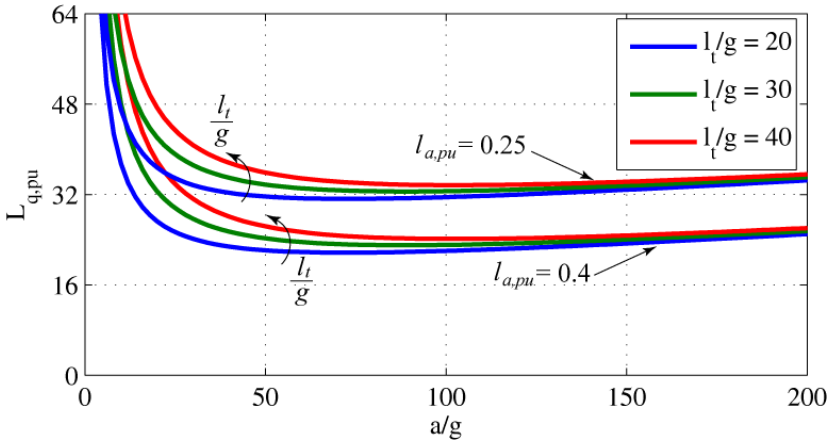

Figure 5.6 – Per-unit q-axis inductance $L_{q,pu}$ as a function of the pole pitch to airgap ratio and with the per-unit stator tooth length l_t/g as a parameter. $L_{q,pu}$ is shown in correspondence of both an inadequate (0.25) and an adequate (0.4) value of $l_{a,pu}$. Other parameters: q= 3, n=3, n_r = 14, k_w= 0.96, b= 0.55, k_t = 0.9, k_{tip} = 1.4

Figure 5.6 puts in evidence that for small values of a/g the slot leakage component dominates the total q-axis inductance with a bad impact on the achievable saliency ratio. Conversely, starting from a/g values roughly larger than 50, the term $L_{\sigma,slot}$, and thus the choice of l_t/g, get increasingly less important in affecting the total q-axis inductance. This overall value is definitely determined by the magnetizing component in the a/g area of main interest for the design, especially when the zig-zag one is limited thanks to high q and n_r values, as it is the case in the example rotor of Figure 5.6. It points out that both the per-unit. insulation $l_{a,pu}$ and the parameter n_r (read, the number of layers) are of crucial importance for the minimization of the overall q-axis inductance.

5.1.2.3. Characteristic electric loading

The characteristic electric loading is directly proportional to $B_{gap,m}$ (Figure5.5) and inversely proportional to $L_{q,pu}$ (Figure5.6).

As a result, the A_{q0} (5.6) curves in Figure 5.7 are flat in a wide range of a/g. In the same range (that is, $50 \leq a/g \leq 200$) the stator tooth length factor (l_t/g) is not of great importance, whereas the magnet grade, expectedly, is. Also the per-unit magnetic insulation in the rotor and the normalized PMs volume affect the characteristic current loading. As an example, the plots in Figure 5.7a show the behavior of A_{q0},referred to the outer values of typical $l_{a,pu}$ and $V_{m,pu}$ design spaces.

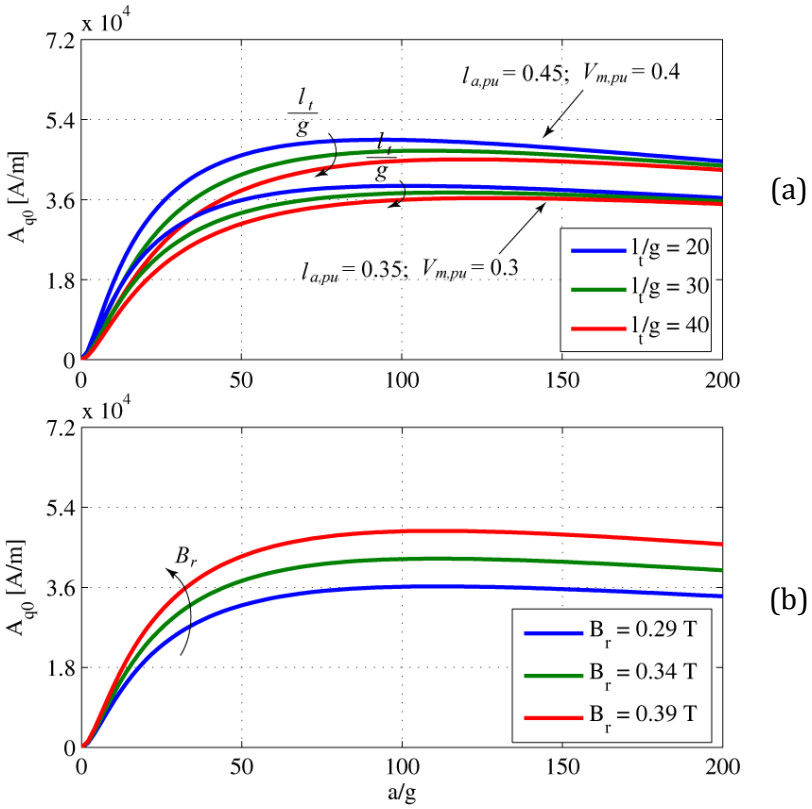

Figure 5.7 - Characteristic electric loading. Design inputs: q= 3, n=3, n_r = 14, k_w = 0.96, b= 0.55, k_t = 0.9, k_{tip} = 1.4. a) Effect of l_t/g, $l_{a,pu}$ and $V_{m,pu}$, with B_r = 0.34T. b) Effect of B_r with l_t/g= 30, $l_{a,pu}$ = 0.4 and $V_{m,pu}$ = 0.35.

It is worth highlighting that larger magnetic insulations and, consequently, larger PMs volumes are distinctive of multipolar machines, since the shape of their poles, closer to the rectified one, is more convenient to optimize simultaneously the design of the rotor flux barriers and iron guides.

5.1.3. Enhancements to the accuracy of the model

The accuracy of the proposed analysis can be improved as suggested in the next two

subsections:

- the first one (5.1.3.1) illustrates how to take into account the presence of rotor structural bridges, by quantifying the reduction of the PMs flux concentration effect (5.16).
- The second one (5.1.3.2) enlists the equations needed for modifying the definition of the *d*-axis current loading (5.3), so to compensate for the magnetic potential drops in the saturated stator back iron.

The effectiveness of the formulas reported in the following will be discussed at the end of this Chapter, by comparing the results of the proposed model to the FEA data for some relevant design examples.

5.1.3.1. Effect of structural ribs

Rotor structural bridges shunt a portion of the PM flux, weakening the no load flux density in the airgap.

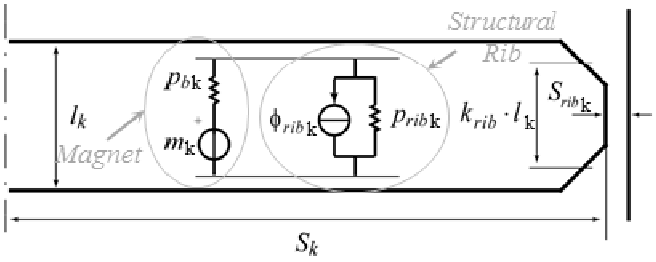

Figure 5.8 – Rotor barrier circuital model with structural bridges included.

Their magnetic behavior can be modeled by the Norton equivalent circuit of Figure 5.8. Starting from the model in Figure 5.8, the Thevenin equivalent circuit can be found out.

Specifically, the parameters $f_{rib,k}$, which stands for a mmf, and $p_{rib,k}$, which represents a permeance value, can be evaluated via (5.28) and (5.29), respectively.

$$f_{rib,k} = \frac{B_{rib0}}{\mu_{r,rib} \cdot \mu_0} l_{rib,k} \cdot \frac{1}{F_q} = \frac{B_{rib0}}{\mu_{r,rib} \cdot \mu_0} k_{rib} \cdot l_k \cdot \frac{1}{F_q} \tag{5.28}$$

$$p_{rib,k} = \mu_{r,rib} \frac{S_{rib,k}}{l_{rib,k}} = \mu_{r,rib} \frac{S_{rib,k}}{k_{rib,l} \cdot l_k} \tag{5.29}$$

The quantities, that identify the equivalent circuit of magnetic ribs, depend on:

- the rib working point on the saturated B-H curve of the rotor iron (namely, the flux density B_{rib0} and the respective relative permeability $\mu_{r,rib}$);
- the rib thickness $S_{rib,k}$ and length $l_{rib,k}$, which can be expressed in per-unit of the respective barrier length via the factor $k_{rib,l}$, as shown by (5.29).

The two factors B_{rib0} and $\mu_{r,rib}$ refer to the adopted steel grade and are derived from the saturated part of its magnetic characteristic, as suggested in Figure 5.9: The underlying assumption is that all the ribs are saturated at all working conditions (load and no load) of the machine. From experience and Finite Element Analysis verification, it turns out that the ribs of this type of PM-Assisted machines work all around 2 T, either at no-load or load condition.

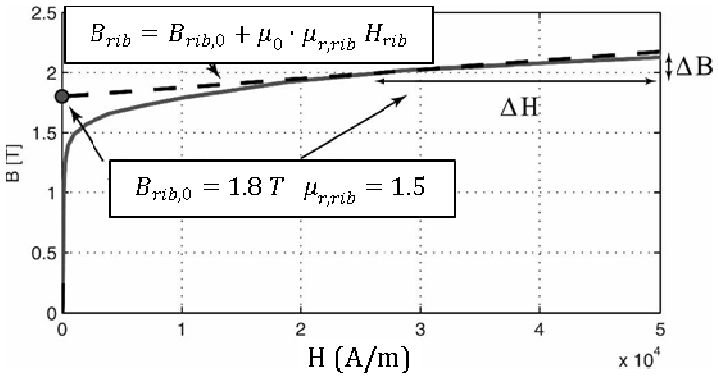

Figure 5.9 - Identification of the B_{rib0} and $\mu_{r,rib}$ parameters, for modeling the saturated iron ribs, from the magnetization characteristic of an example silicon steel. (Simboli!!)

With some manipulations, the superposition of the magnets model and the ribs one can be seen as its Thevenin equivalent, that has again the form of a PM-generated mmf m_k^* and an equivalent permeance p_{bk}^*, thus looking like the barrier circuit introduced in Figure 5.3. In other words, when it is needed to quantify the reduction of the PM flux due to the rotor structural ribs, it is sufficient to refer to the magnetic equivalent circuit of Figure 5.3, while substituting the n barrier permeances p_{bk} with p_{bk}^* (5.30) and the n mmfs m_k with m_k^*(5.31).

$$p_{bk}^* = p_{bk} + p_{rib,k} \tag{5.30}$$

$$m_k^* = \frac{1}{\mu_0 p_{bk}^*}\left(B_r \cdot S_k - B_{rib0} \cdot S_{rib,k}\right) \cdot \frac{1}{F_q} \tag{5.31}$$

It follows that the key design equations, derived in Subsection 5.1.2.1 for finding out the no load flux density $B_{gap,m}$, are still valid if S_1 is replaced byS_1^* (5.32) and B_r is replaced byB_r^* (5.33).

$$S_1^* = S_1 + \frac{\mu_{r,rib}}{k_{rib,l}} S_{rib,1} \tag{5.32}$$

$$B_r^* = B_r \frac{S_1 - \frac{B_{rib0}}{B_r} S_{rib,1}}{S_1^*} \tag{5.33}$$

5.1.3.2. Simple model of the iron saturation phenomena

As specified when the "Natural Compensation" condition was introduced, if the *q*-axis stator flux is zeroed by the PMs action, then the iron saturation effects come mainly from the flowing of the magnetizing *d*-axis flux. The magnetic potential drops associated to the *d*-axis flux in the stator back iron can be compensated, if the magnetizing current loading A_d (5.3) is increased by the multiple k_{sat} (5.34):

$$k_{sat} = 1 + \frac{1}{b} \cdot \frac{\frac{1}{k_t}\frac{l_t}{g} + \frac{1}{2}\left(1 - \frac{2}{\pi}\right)\frac{a}{g}}{\mu_0 \mu_{fe}} \tag{5.34}$$

μ_{fe} is the iron relative permeability in correspondence of the working flux density B_{fe}. B_{fe} is typically chosen to be around 1.5-1.7 T and the related μ_{fe} values are in the range of 600-800.

5.2. PERFORMANCE INDICATORS

5.2.1. Shear stress

The shear stress [Nm/m^3], averaged over one machine pole, is the cross product (5.34) of the airgap flux density by the electric loading [63].

$$\sigma = B_{gap,d} A_q - B_{gap,q} A_d \tag{5.35}$$

In the area that has been revealing of main interest for the design (i.e. $50 \le a/g \le 200$), if the machine is "Naturally Compensated", the second term of (5.35) is negligible, because both $B_{gap,q}$ and A_d are significantly smaller than the respective

counterparts on the other axis. Thus, the characteristic shear stress σ_0 is approximately defined as in (5.36):

$$\sigma_0 \cong B_{gap,d} A_{q0} = b B_{fe} \cdot A_{q0} \tag{5.36}$$

where the subscript *0* reminds of the reference to the "Natural Compensation" condition.

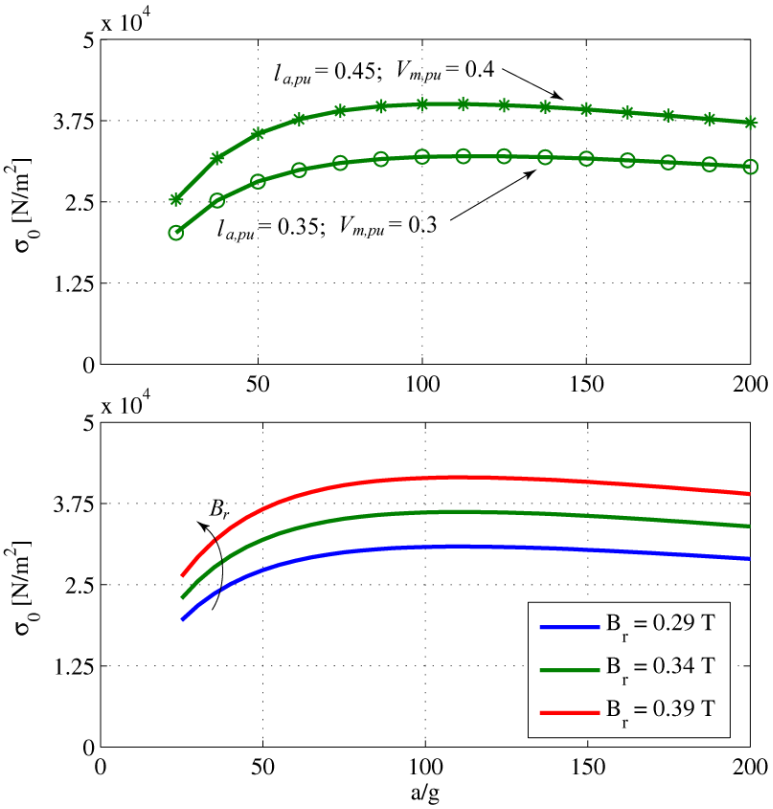

Figure 5.10 - Characteristic shear stress, for the same design inputs declared in Figure5.7. l_t/g is fixed and equal to 30. All the σ_0 curves are plotted starting from a/g=25, since for lower a/g values the approximation (5.36) is too imprecise. a) σ_0 is referred to the outer values of typical $l_{a,pu}$ and $V_{m,pu}$ design spaces. (B_r = 0.34T); b) Effect of B_r with $l_{a,pu}$=0.4 and $V_{m,pu}$=0.35.

Given the *d*-axis magnetic loading $B_{gap,d}$, the characteristic shear stress is decided by the characteristic loading only. As a consequence, it is influenced by: the pole pitch to airgap ratio a/g, the rotor per-unit magnetic insulation, the magnets volume and remanence.

The curves in Figure 5.10 quantify the impact of these four design parameters on the achievable performance, highlighting that the shear stress figures are competitive with

the ones of Nd-based machines [56], [63], especially for designs with large per-unit rotor insulation and multi-layer rotor structures. In that cases, A_{q0} is maximized thanks to the low q-axis inductance and the valuable concentration of the PMs flux in the airgap. This, associated to good ferrite grades improves the torque capability of the machine. Or, at given torque, it allows the employment of lower energy density magnets, since, being the layers completely filled with ferrite, their quantity is fixed.

To deal with shear stress values typical of very large liquid cooled machines, the analysis can be extended to "Non-Naturally Compensated" machines, taking advantage of the improved cooling system to put into play q-axis electric loadings larger than A_{q0} and thus increase the achievable σ.

In formula, if the q-axis current loading A_q is chosen to be larger than the characteristic one A_{q0} according to the factor x_{q0} (that is, $A_q = x_{q0} \cdot A_{q0}$), then σ is defined by (5.37) and the shear stress curves of Figure 5.10 are modified.

$$\sigma = x_{q0} \cdot \left(1 - \frac{2}{3} \left(1 - \frac{1}{x_{q0}} \right) \frac{L_{mq,pu}}{\frac{a}{g}} \right) \cdot \sigma_0 \tag{5.37}$$

If typical shear stress values corresponding to x_{q0} larger than one are calculated, the results indicate that FASR machines, which can withstand large thermal loadings, show satisfactory performances, in terms of torque density, if fairly compared to the ones of similar solutions based on rare-earth magnets.

5.2.2. Power Factor

Disregarding the resistive voltage drop as indicated in the vector diagram of Figure 5.2, the Power Factor angle φ_0 (5.38) at "Natural Compensation" is defined by the current phase angle only:

$$tan(\varphi_0) = tan\left(\frac{\pi}{2} - \gamma\right) = \frac{A_d}{A_{q0}} \tag{5.38}$$

The plots in Figure 5.11, that show the Power Factor behavior of "Naturally Compensated" FASR machines, point out the importance of a proper choice of the per-unit airgap g/a, confirming that the area that is recommended for high-performance

FASR designs is in the range $50 \leq a/g \leq 200$.

As shown in Figure 5.11, both A_d and A_{q0} penalize the PF in the low range of a/g. However, as a/g increases, the PF tends asymptotically to one, whatever the PMs. In other words, the per-unit airgap g/a (that is, the choice of the pole pairs in the final design) is the only variable to influence the PF of "Naturally Compensated" FASR machines.

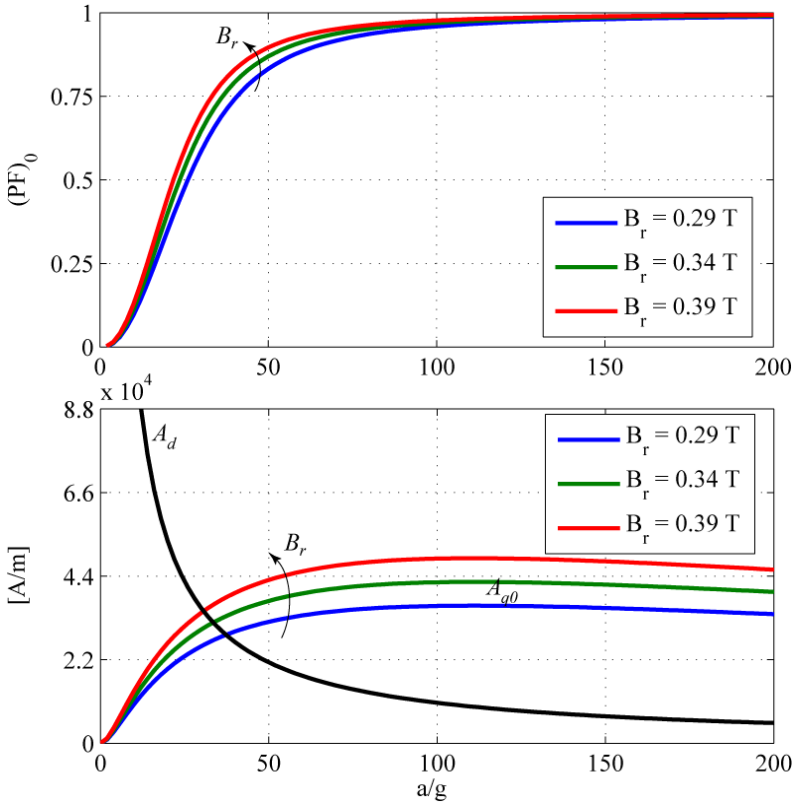

Figure 5.11–Power Factor (top) and current loading components (bottom) at "Natural Compensation". All the quantities are plotted as functions of the pole pitch to airgap ratio and with the PMs grade as a parameter. Same design parameters as in Figure5.7, 5.10, 5.11 (l_t/g = 30, $I_{a,pu}$=0.4 and $V_{m,pu}$=0.35).

5.2.3. Joule Loss density

The Joule loss density of the rectified pole in Figure 5.1 has already been computed in Chapter 04. It is defined by (5.39):

$$k_{j,block} = 2\rho_{Cu} \cdot \frac{k_{end}}{k_{Cu}} \cdot \frac{1 - bk_t}{l_t} \cdot \frac{A_d^2 + A_q^2}{k_w^2} \tag{5.39}$$

where the subscript "block" remarks that the power rate dissipation is referred to the surface ($a \cdot l$) of the rectified block. The reader is also reminded that ρ_{Cu} is the copper resistivity, k_{Cu} is the slot filling factor and k_{end} is the total length of one conductor, end connections included, in per-unit of the active length.

When core and PM losses can be disregarded, as it is the case of low speed multipolar machines, the Joule loss density is representative of both the efficiency and the type of cooling of the machine. Regarding the efficiency, the key role played by the tooth length will be described later. As for the type of cooling, since it identifies a maximum value for the heat rate density, Equation (5.39) can be used to find out the maximum electric loading A_{th} (5.40) at rated thermal conditions.

$$A_{th} = \sqrt{A_d^2 + A_q^2} = k_w \sqrt{l_t} \sqrt{\frac{k_{cu}}{k_{end}\rho_{cu}(1 - bk_t)} k_j} \tag{5.40}$$

Of course, this thermal limit must be compatible with the other key values of electric loading A_d, A_{q0}, $A_{q,irr}$, as deeply discussed in Chapter 04.

5.2.4. Summary of guidelines and tips for optimal FASR designs

From the analysis on the rectified FASR pole it turns out that:

- Designing multi-layer FASR rotor structures with good insulation properties allows to minimize the q-axis inductance and maximize the magnetic loading produced by the PMs by concentrating the flux in the airgap. This is twice beneficial for the shear stress. Besides, also the stiffness against demagnetization is enhanced.
- Given both n_r and $l_{a,pu}$, low pole pitch to airgap ratios a/g, meaning thick per-unit airgaps, make the machine prone to demagnetization and reduce the magnetic loading obtainable in the airgap thanks to the magnets. If a/g is too small, also the saliency ratio is unsatisfactory. In particular, the magnetizing d-axis inductance is low (requiring high excitation currents), whereas the q-axis one is high (badly affecting the characteristic electric loading).
- From the previous point, it follows that a low a/g ratio is a symptom of low

shear stress, low Power Factor and low efficiency (or more specifically increased Joule losses).

- The characteristic shear stress depends significantly on the PMs remanence, and very little on the stator tooth length, which will be handled as an important degree of freedom in the final design of the rotating machine. It impacts the machine weight, besides its efficiency.

5.3. FASR ROTATING MACHINE INTO CONSTRAINED ENVELOPE

A rotating machine, that is defined by the input data in Table 5-I, can be seen as an assembly of $2p$ elementary blocks, all having the rotor pitch equal to a. Thus, given the target torque T, the stack outer radius (r) and length (l), the machine can be designed via the closed form equations presented in the previous sections.

TABLE 5-I
DESIGN PROCEDURE: MAIN PARAMETERS, INPUT AND OUTPUT DATA

INPUT DATA	
Geometrical quantities	r, l, g
Performance target	Torque T
DESIGN PARAMETERS	
Magnetizing loading and sizing of the stator back iron	b, B_{fe}, k_t
Rotor design	n_r, n, $l_{a,pu}$, $V_{m,pu}$
Stator winding design	q, k_w, k_{Cu}, k_{end}
DESIGN VARIABLES	
Pole pairs p and stator tooth length l_t	
PERFORMANCE INDICATORS	
Power Factor, Joule loss density k_j	
OTHER DESIGN OUTPUTS	
Needed PM grade B_r, Electric loadings A_d and A_{q0}	

All the normalized parameters required to start the design have already been discussed and are briefly summarized in Table 5-I. The design variables are:

- the pole pairs number p
- the tooth length l_t.

Both p and l_t contribute to define the rotor radius r' (5.41).

$$r' = r - l_t - l_y \rightarrow \quad r' = r\frac{1 - \frac{l_t}{r}}{1 + \frac{b}{p}} \tag{5.41}$$

This is also due to the dependence, shown in Figure 5.1, of the stator yoke height on the rotor pole pitch a, which, in turn, is identified by (5.42), and thus again by p and l_t.

$$a = \frac{r'}{p}\pi \tag{5.42}$$

Given the torque, the relationship (5.41) allows to express univocally the required shear stress (5.43) in terms of the variables l_t/r and p and then start the design procedure.

$$\sigma = \frac{T}{2\pi \cdot (r')^2 \cdot l} \tag{5.43}$$

In fact, if the desired magnetizing loading $b \cdot B_{fe}$ is provided by a correct choice of the d-axis current loading (5.3), the characteristic q-axis electric loading follows directly from (5.43) by inversion of (5.36) or (5.37): the first equation covers the case of "Naturally Compensated" designs, whereas the latter regards "Non-Naturally Compensated" machines.

In the following, reference will be made mainly to (5.36), since in Subsection 5.1.2 the "Natural Compensation" condition has been identified as a convenient design choice: it guarantees good Power Factor values (see Figure 5.11), limits the cross-saturation effects and enhance the flux weakening capability of the drive. Anyway, the procedure, which will be proposed, can be easily adapted to design "Non-Naturally Compensated" machines. It might be necessary when an adequate cooling system is provided for and in case of very high demanding shear stress levels, since "Non-Naturally Compensated" FASR machines with $x_{q0} > 1$ has been revealed the most suitable solutions, as said in Subsection 5.2.1. The need of designing "Non-Naturally Compensated" FASR machines may occur also in other cases, since setting x_{q0} slightly lower than one helps to better exploit the drive in the "Torque versus Speed" plane, with satisfactory performance in terms of Constant Power Speed Range also in operating condition other than the rated one.

In general, on the basis of the equations listed above, both A_d and A_{q0} can be expressed and quantified as functions of the variables p and l_t/r. The same is for the Power Factor (5.38) and the PM grade needed for compensating the q-axis reluctance flux. The magnets remanence B_r can be derived via (5.6), (5.16), (5.24-27) starting from the A_{q0} value.

Also the Joule loss density k_j can be easily computed depending on the main design quantities, keeping in mind that the heat rate density is here reasonably calculated at the outside surface and is then related to the block one by (5.44).

$$k_j = k_{j,block} \cdot \frac{r'}{r} \tag{5.44}$$

The previous design steps can be iteratively applied in order to explore all the feasible combinations of l_t/r and p, that give the desired torque with the stack envelope constrained.

The design spaces of the two variables are identified in Subsection 5.3.1 and the concurrent designs are compared in Subsection 5.3.2, so to derive general guidelines for optimized solutions.

In particular, Subsection 5.3.3 shows how to simplify the design task, if the Joule loss density needs to be minimized. In this case, an analytical expression fixes the optimal pole pairs number, which does exist due to the different variation of the direct and quadrature current loadings with p.

In fact:

- as p increases, the rotor pitch a gets smaller and the d-axis current (5.3), needed to have the airgap flux density equal to $b \cdot B_{fe}$, increases;
- as p decreases, the bore radius decreases, as shown by (5.41)-(5.42). It means that the lever associated to the airgap shear stress is reduced and greater q-axis currents (5.43) are required. Also the end connections are longer if the bore radius is smaller, with a bad impact on the resulting k_j.

For machines, that are not designed for low speed applications, the optimal pole pairs number for the ultimate design does differ from the one that minimizes the Joule

loss only, due to the iron loss which obviously plays a considerable contribute in affecting the efficiency of the rotating machine. Even if the developed design procedure is devoted mainly to direct-drive low speed FASR motors, by means of simplified formulas, Subsection 5.3.3.1 will consider the impact of the iron loss on the machine performance, individuating the best design strategy in the whole design space.

5.3.1. Upper and lower limits to the design variables p and l_t/r

The choice of the tooth length factor l_t/r is a matter of trade-off, as it affects both the efficiency of the machine and the weight of its active materials. According to (5.39), too short stator teeth lead to unfeasible designs due to the increased Joule loss. On the other hand, having too long stator teeth impacts negatively the total weight, in addition to other unwanted side effects. In particular, with longer teeth and consequently smaller bore radius, the lever associated to the airgap shear stress is reduced and higher q-axis current loadings are required, at given output torque. Also the length of the end connection grows with l_t/r and it contributes to vanish the convenience of increasing the tooth length, over a certain extent, to reduce the Joule loss. As a result, effective l_t/r design spaces typically include values that vary from few percent to 30%, also depending on the machine size.

The analysis on the reference block suggests the presence of a lower limitation for a/g ($a/g \geq 50$) and thus an upper limit for the pole pairs number. In order to quantify it, Equation (5.45) is derived from (5.41) and (5.42).

$$p_{max} = \pi \frac{r}{g} \left(\frac{a}{g}\bigg|_{min} \right)^{-1} \left(1 - \frac{l_t}{r}\right) - b \tag{5.45}$$

In (5.45) the parameters b and l_t/r can be defined as discussed, then the minimum recommended a/g value univocally identifies the maximum number of pole pairs. This upper limitation, which is compliant with the core loss minimization purposes, depends on r/g. In turn, the ratio r/g, mainly related to constructional aspects, is a function of the machine size: it can be around 100, in case of small traction motors, and raise up to 500, for large wind turbine generators. A lower limit to the pole pairs number does also exist, because, as said, when p decreases, the yoke height increases and the bore radius, along

with the torque lever, decreases. It follows that machines with too few poles are heavier and less efficient, because of the augmented q-axis electric loading.

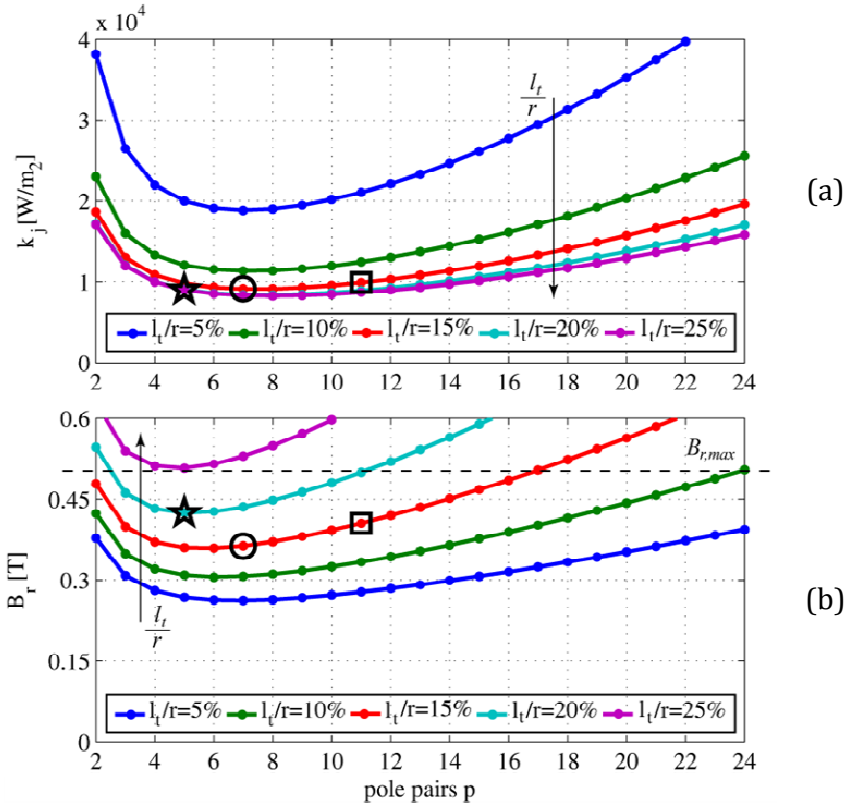

Figure 5.12 - Prototyped direct drive lift motor (T=795 Nm, r=0.19 m, l=0.25 m, b·B_{fe}=0.84 T). The plots show: the Joule loss density (a) and PM remanence (b) as functions of the number of pole pairs and with the tooth length as a parameter. The "circle" design is for Joule loss minimization; the "star" design is similar to the former one, but has longer stator teeth; the "square" design is for weight reduction.

5.3.2. Concurrent designs at given torque and outer stack

For finding out the best combinations of p and l_t/r with respect to the main design indicators, two examples are considered:

- the first one is the direct drive lift motor, that has been prototyped and tested to validate the proposed technology. It is rated 14 kW at 168 rpm; its outer radius is 0.19 m, its stack is 0.25 m, its airgap length is 0.75 mm. Experimental results on the drive performance will be discussed in Chapter 08.
- the other design example is a wind generator, rated 2 MW at 15 rpm. Its outer radius is about 2 m, its stack 1.5 m and its airgap length 4 mm. The

specifications are the same considered in Chapter 03 to validate the comprehensive approach to the design of multi-polar SPM machine for the sake of comparison.

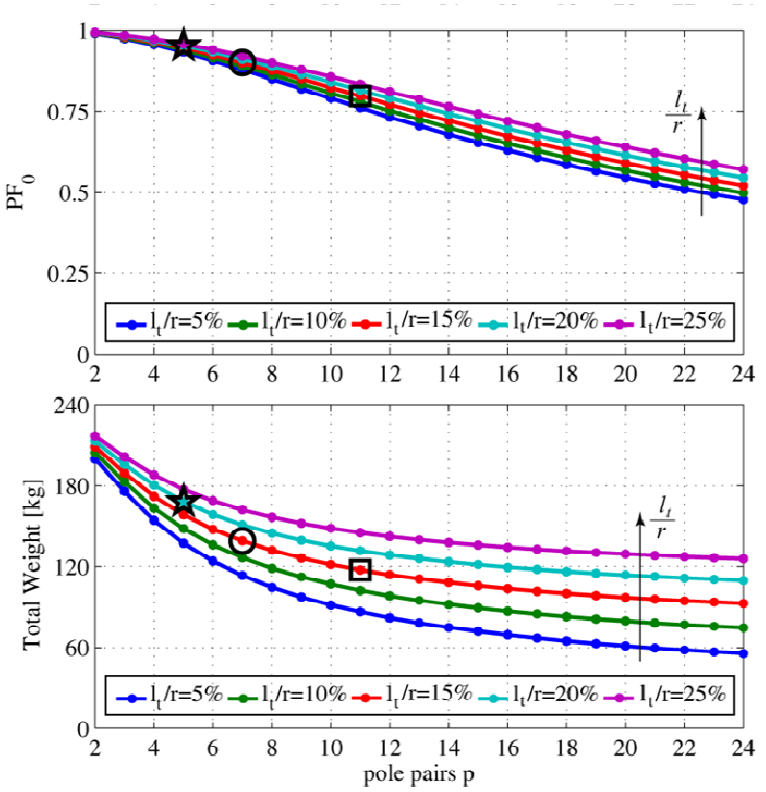

Figure 5.13 - Prototyped direct drive lift motor (T=795 Nm, r=0.19 m, l=0.25 m, b·B_{fe}=0.84 T). The plots show: the PF (a) and total machine weight (b) as function of the number of pole pairs and with the tooth length as a parameter. The "circle" design is for Joule loss minimization; the "star" design is similar to the former one, but has longer stator teeth; the "square" design is for weight reduction.

The two machines have been purposely chosen, since they are very different in terms of required shear stress, size and shape of the stack (specifically, the r/l ratio). As said, the final designs, defined for each of them, will be presented in Chapters 07, 08 and the performance of the two machines will be compared to the ones of rare-earth based motor types, designed according to the same specifications.

The curves in Figure 5.12 and Figure 5.13 refer to the prototyped motor, showing the charts of the Joule loss density, the needed PMs grade, the Power Factor and the total weight, as functions of the pole pairs number and with l_t/r as a parameter.

Figure 5.12a highlights that the Joule loss density is always minimum in correspondence of a specific number of pole pairs, that does not depend on the tooth length. It is also evident that the loss reduction obtainable by lengthening the stator teeth flattens with l_t/r beyond 15%. It says that, in this case, a machine with p equal to 7 and l_t/r lower than 15% (that is, the "circle" design in Figure 5.12 and Figure 5.13) results the most convenient in terms of Joule loss minimization.

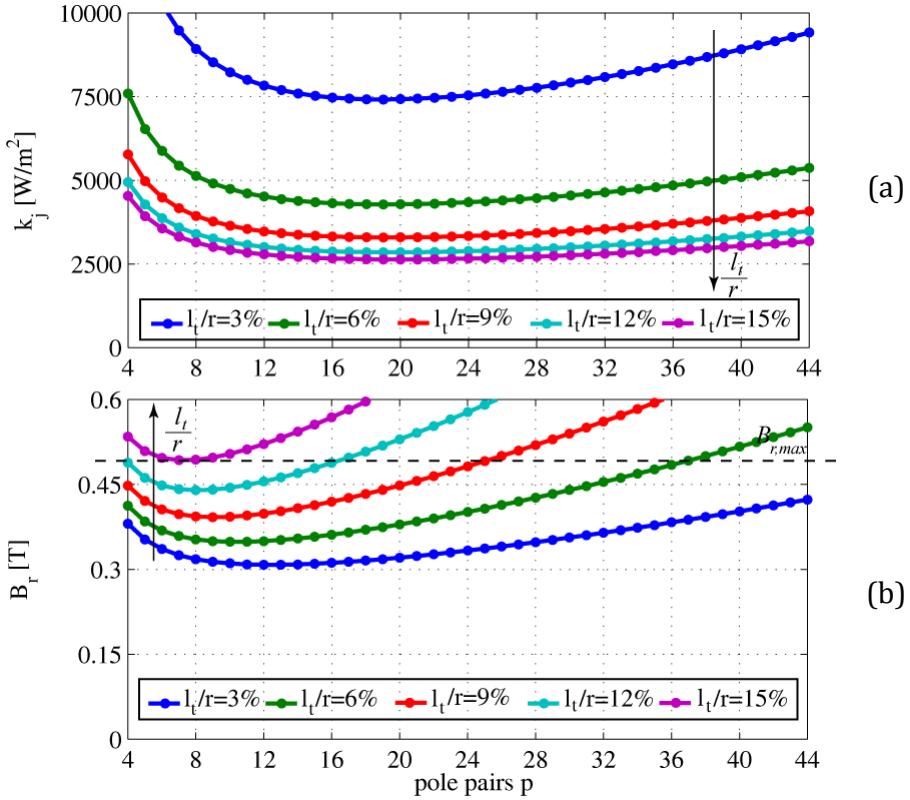

Figure 5.14 - Wind turbine generator (T=1273 kNm, r=2 m, l=1.5 m, b·Bfe=0.85 T). The plots show the Joule loss density (a) and PM remanence (b) as functions of the pole pairs number and with the tooth length as a parameter.

Conversely, the values of p that minimize the ferrite remanence needed to fulfill the "Natural Compensation" condition vary with respect to the tooth length, as shown by Figure 5.12b. In general, with longer stator teeth, the required PM grade is higher and more sensitive to the number of poles. For example, the "star" symbol in Figure 5.12 and Figure 5.13 indicates a design with p = 5 and l_t/r = 20%, that has nearly the same loss of the "circle" one but needs B_r = 0.43 T instead of 0.37 T.

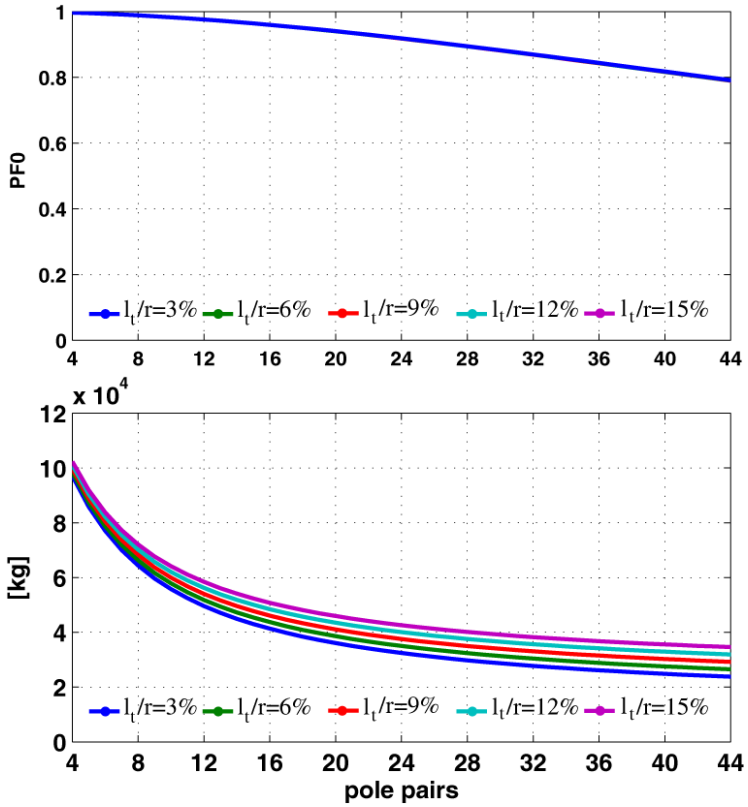

Figure 5.15 - Wind turbine generator (T=1273 kNm, r=2 m, l=1.5 m, b·Bfe=0.85 T). The plots show the PF (a) and total machine weight (b) as functions of the pole pairs number and with the tooth length as a parameter.

From Figure 5.13a and Figure 5.13b, it is highlighted that the choice of the pole pairs number is critical for both the Power Factor and the weight of the machine. However, the Power Factor is good (meaning, higher than 0.85) for both the "star" and "circle" designs. Mass reduction could lead to consider a number of pole pairs larger than 7, for example p=11 (that is, the "square" design), but it would require to accept a lower efficiency, a better PM grade, a poorer Power Factor and a higher fundamental frequency with the need of a proper check on the iron loss, up to now disregarded.

Figure 5.14 and Figure 5.15, that refer to a large wind generator, confirm the qualitative considerations presented for the prototyped lift motor, highlighting the generality of the proposed approach.

If the curves in Figure 5.14 and Figure 5.15 are compared to the ones corresponding to the prototyped direct-drive lift motor, it can be pointed out that the Power Factor is even less critical in this case.

However, the choice of the stator tooth length is more limited in this case, since for l_t/r ratios larger than 15% the slot leakage inductance gets too large for the low energy density ferrite magnets to be conveniently employed for fulfilling the "Natural Compensation" condition.

Moreover, the number of the pole pairs that minimizes the Joule loss density here is very different from the one found for the previous design example, since, as it will be demonstrated in the next subsection, this value is strictly related to the machine size and required torque.

5.3.3. Optimal poles number for Joule loss minimization

The number of pole pairs p_o, that does optimize the Joule loss, can be quantified, if (5.44) is minimized, reminding the expression (5.39) that relates the power loss dissipation rate to the whole machine current loading, to the actual length of the slot conductors (including the end connections) and to other per-unit parameters (quick to be set)

TABLE 5-II
DEPENDENCE OF THE POWER DISSIPATION RATE ON THE POLE PAIRS NUMBER

DIRECT AND QUADRATURE COMPONENTS OF THE STATOR CURRENT LOADING	
$A_d^2 = \frac{1}{r^2}\left(\frac{1}{2\mu_0}\cdot bB_{fe}\cdot g\right)^2 \frac{(p+b)^2}{\left(1-\frac{l_t}{r}\right)^2} \cong \frac{1}{r^2}\left(\frac{1}{2\mu_0}\cdot bB_{fe}\cdot g\right)^2 \frac{p^2}{\left(1-\frac{l_t}{r}\right)^2}$	(5.46)
$A_{q0}^2 = \frac{TSV^2}{4\left(1-\frac{l_t}{r}\right)^4}\cdot\left(1+\frac{b}{p}\right)^4\cdot\frac{1}{\left(bB_{fe}\right)^2}$	(5.47)
END-CONNECTION FACTOR	
$k_{end} = \left(1+2\frac{l_t}{l}\right)+\pi k_{sh}\cdot\frac{r}{l}\cdot\left(1-\frac{1}{2}\cdot\frac{l_t}{r}\right)\cdot\frac{1}{p}$	(5.48)
JOULE LOSS DENSITY	
$k_j \cong \frac{2\rho_{Cu}(1-bk_t)}{k_{Cu}k_w^2}k_{end}\left[\frac{\left(\frac{1}{2\mu_0}\cdot bB_{fe}\cdot g\right)^2}{r^2\left(1-\frac{l_t}{r}\right)}\cdot p^2+\frac{TSV^2}{4\left(bB_{fe}\right)^2\left(1-\frac{l_t}{r}\right)^3}\left(1+\frac{3b}{p}\right)\right]$	(5.49)

Table 5-II shows how the various factors, that contribute to influence the Joule loss density k_j, depend on the two design variables p and l_t. The expressions in Table 5-II have

been derived starting from the per-unit formulas on the rectified pole and relating the pole pitch a to the outer radius of the rotating machine by means of (5.41) and (5.42).

In particular, the d-axis current loading A_d (5.46) is computed as suggested by (5.3) and the q-axis characteristic current loading A_{q0} (5.47) is coherent with the two definitions (5.43) and (5.36). The end-connection factor k_{end} (5.48) is evaluated, taking into account the stator geometry and standard arrangements of distributed windings end connection.

As a result, an approximate expression (5.49) that quantifies the impact of both p and l_t on the Joule power loss density k_j has been found.

The minimization of (5.49), with respect to p, lead to number of pole pairs p_o (5.50), that minimizes the Joule loss:

$$p_o = \sqrt[3]{\frac{3}{2}\left(1+\frac{\pi k_{sh}}{3b}\frac{r}{l}\frac{1-\frac{l_t}{2r}}{1-\frac{2l_t}{l}}\right)\left(\frac{1}{1-\frac{l_t}{r}}\frac{\mu_0}{bB_{fe}}\frac{r}{g}TSV\right)^2} \tag{5.50}$$

In (5.49) and (5.50), the torque density TSV is referred to the stator volume and k_{sh} is the winding shortening factor, that is lower than one only in case of chorded windings.

Equation (5.50) can be simplified, obtaining (5.51), with very little loss of accuracy, especially when the factors l_t/r and l_t/l are small, as it is for large size generators.

$$p_o \cong \sqrt[3]{\frac{3}{2}\left(b+\frac{\pi}{3}k_{sh}\cdot\frac{r}{l}\right)\cdot\left(\frac{\mu_0}{bB_{fe}}\frac{r}{g}TSV\right)^2} \tag{5.51}$$

Equation (5.51) puts in evidence that p_o depends on:

- the outer radius to length ratio r/l, representative of the shape of the stack;
- the outer radius to airgap ratio r/g, accounting for the machine size and mechanical aspects;
- the torque density per stator volume TSV, again related to the machine size and to the type of cooling.

In general, pancake shape (i.e. $r/l >> 1$), small per-unit airgap and high TSV are all factors leading to increase the optimal number of poles for Joule loss minimization. This

is quantified by (5.51) and confirmed by the examples examined in the previous subsection. In fact, if compared to the prototyped lift motor, the wind generator has a *TSV* that is increased by 2.4 times, a double r/g value and a r/l ratio increased by 1.33. Then, also the optimal pole pairs number shifts from 7 to nearly 22, as graphically represented by Figure 5.12a and Figure 5.14a.

5.3.3.1. Iron loss impact on the optimal poles number for loss minimization

For direct-drive low speed machines, the Joule loss embodies the preponderant contribute in determining the efficiency of the machine and, as a consequence, choosing the number of pole pairs equal to p_o (5.51) represents one of the best design strategy.

Conversely, in many other applications, the iron loss affects significantly the efficiency of the machine and the convenience of fixing the pole pairs number to minimize only the Joule loss vanishes. In that cases, it is preferable to investigate the design space, considering as performance indicator in terms of efficiency the overall specific loss k_{i+j}, that is given by the sum of the Joule loss contribute k_j (5.44) and the iron loss one k_i (5.52).

$$k_i = C_i \cdot B_{fe}^{\alpha} \cdot \left(\frac{n}{2\pi} \cdot \frac{p}{50}\right)^{\gamma} \cdot b \cdot \frac{1-\frac{l_t}{r}}{p+b} \cdot r \cdot \left(1 - \frac{b}{2} \cdot \frac{1-\frac{l_t}{r}}{p+b} + k_t \cdot \frac{l_t}{r} \cdot p\right) \qquad (5.52)$$

As it was for SPM machines, Equation (5.52) helps predicting the iron loss, that are normalized by the machine outer surface when computing k_i. The specific iron losses (5.52) are approximately evaluated by taking into account the loss phenomena related to the fundamental electrical frequency (i.e. $p{\cdot}n/2/\pi$) only. The same assumption was adopted in Chapter 03, while dealing with the design of SPM machines, but with FASR machines, that generally have distributed stator windings, this approximation is even less penalizing with respect to the achievable accuracy. In (5.52), C_i represents the iron loss per volume in correspondence of an electrical frequency equal to 50 Hz and a working flux density equal to 1 T. The coefficient α and γ comes from the Steinmetz equation.

In order to show how the FASR design maps modify in case of applications, for

which the iron loss has considerable effects on the machine efficiency, actual specifications for an automotive drive have been considered. The motor must deliver about 46 kW at 3500 rpm; its outer radius is 0.108 m, its stack is 0.17 m and its airgap length is 0.7 mm.

Figure 5.16 reports the results of the iterative design procedure proposed in the previous sections, applied considering a compensation factor a little bit lower than one (x_{q0} = 0.8) because of the demanding specifications typical of traction drive train in terms of flux weakening capability at many operating conditions.

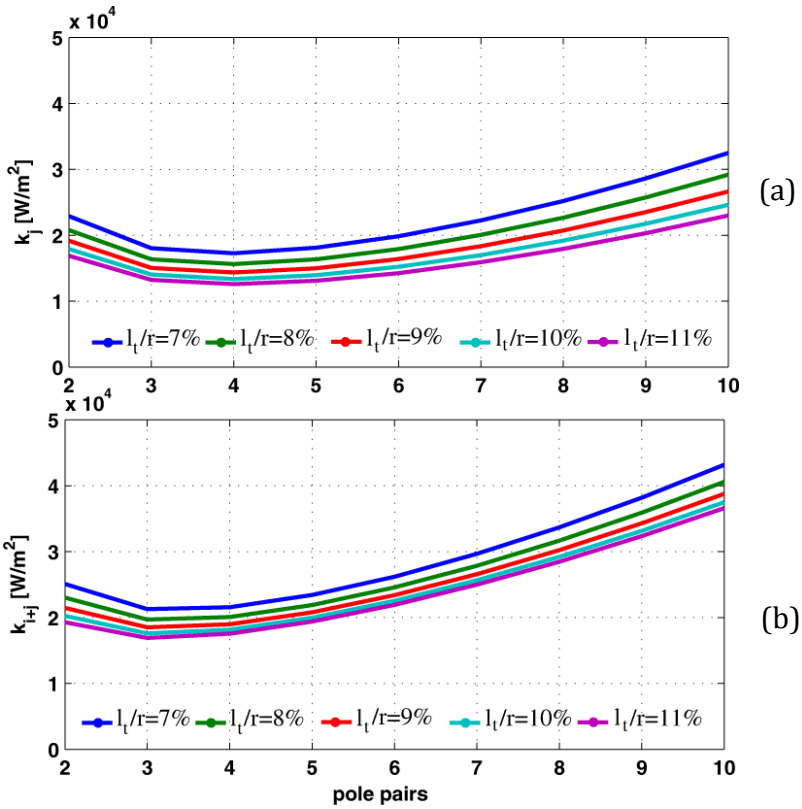

Figure 5.16 – Automotive drive (T=1110 Nm, r=0.108 m, l=0.170 m, b·Bfe=0.82 T). The plots show the specific Joule loss (a) and total specific loss of the machine (b), including the iron one, as functions of the pole pairs number and with the tooth length as a parameter.

Both the Joule specific loss k_j (Figure 5.16a) and the overall dissipation rate k_{i+j} (Figure 5.16b) are shown as functions of the pole pairs number and with the per-unit stator tooth length as a parameter. It is evident that, if the machine efficiency is required to be optimized, the pole pitch has not to be chosen according to (5.51), that would

suggest to design the FASR motor with a number of pole pairs equal to 5. In fact, the role played by the specific iron loss in determining the efficiency of the machine shifts the optimal pole pairs number, suggesting to select p=3. Moreover, the presence of a conspicuous contribute of iron loss makes the maximum efficiency area in the design space less flat and it does limit the opportunity of moving from this optimal condition, for example to find out a trade-off solution with respect to the other performance indicators, such as for example the mass (and cost) of active parts.

5.4. FEA VALIDATION OF THE PROPOSED DESIGN PROCEDURE

The feasibility of the proposed technology in many up-to-date applications, as power generation from renewable sources and automotive propulsion, will be deeply investigated in Chapter 07, showing various design examples, discussing and comparing their performance to the one of alternative PM-based solutions.

TABLE 5-III
FASR DESIGN EXAMPLES: SPECIFICATIONS, DESIGN PARAMETERS, GEOMETRICAL INPUTS

TARGET QUANTITIES				
	Design a	*Design b*	*Design c*	
Target Torque T_0	$1273 \cdot 10^3$	795	125	Nm
Nominal speed n	15	168	3500	rpm
Stack length l_0	1.5	0.250	0.170	M
Stator radius r_0	1.97	0.190	0.108	m
Airgap length g				
INPUT DATA AND PER-UNIT DESIGN PARAMETERS				
Yoke per-unit width b	0.55	0.54	0.63	
No-load back-iron flux density B_{fe}	1.55	1.55	1.30	T
Tooth width factor k_t	0.90	0.92	0.78	
Rotor slots per pole pair n_r	14	14	20	
Rotor flux barriers n	3	3	4	
Per-unit rotor insulation $l_{a,pu}$	0.40	0.42	0.30	
Per-unit magnets volume $V_{m,pu}$	0.35	0.30	0.22	
Slot filling factor k_{Cu}	0.4	0.4	0.4	
Slot per pole per phase q	3	3	4	
Winding factor k_w	0.96	0.96	0.92	
End connections factor k_{end}	1.33	1.53	1.61	
Carter coefficient k_c	1.05	1.11	1.10	
Operating temperature	115	100	130	

Now the focus is on providing evidence of the generality and accuracy of the proposed design procedure. At this purpose, FASR machines, different both in terms of size and application field, have been designed and FEA validated.

- *Design a* is the "usual" wind turbine generator rated 2 MW at 15 rpm, whose envelope is defined by the outer radius r, equal to 1.97 m, and the stack length l, equal to 1.5 m. It is supposed to be directly ventilated from the wind and the specific loss has to be lower than 8000 W/m^2.
- *Design b* delivers about 14 kW at 169 rpm, in a stack cylinder with r = 0.190 m and l = 0.250 m. It is a direct-drive lift motor, whose target specific loss is 10000 W/m^2. It was prototyped and its performance was experimentally tested.
- *Design c*, which is a machine for an actual traction drive train, is rated around 40 kW at 3500 rpm. Its outer radius is 0.108 m and its stack length is 0.170 m. Since it is intended to be liquid cooled, the specific loss can grow up to 20000 W/m^2 in this case.

The main input data, normalized parameters and operating temperature, the three example designs refer to, are reported in Table 5-III and the rotor and stator laminations of the traction motor *design c* are sketched in Figure 3.17, as an example.

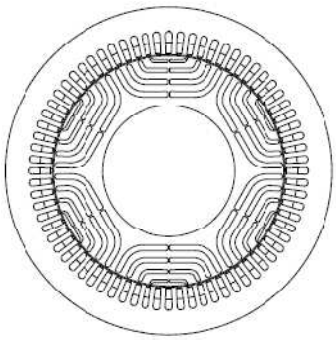

Traction motor "*design c*"

Figure 3.17 – Sketches of the three FASR design examples.

The best design strategy for each case has been identified via the performance charts in the (p, l_t) plane presented in the Subsections 5.3.2, 5.3.3, selecting the number of pole pairs in order to maximize the efficiency.

The wind generator *design a* and the lift motor *design b* (that is, the "circle" machine in Figures 5.12 and 5.13) are "Naturally Compensated" FASR motors with a number of

pole pairs equal to the value p_o (5.51) that does minimize the Joule loss, since, in this cases, the Joule loss represents the dominant dissipation contribute and, thus, this turns out to be the most convenient choice for satisfying the efficiency maximization purpose. The stator tooth length has been set for both machines, looking for a trade-off between weight and efficiency, also considering that, over a certain extent, it is worth anymore to lengthen the copper height for improving the machine efficiency. A detailed list of the results produced by the adopted model and the respective FEA data is reported in Table 5-IV for the large wind generator *design a* and in Table 5-V for the medium size lift motor *design b*.

TABLE 5-IV
WIND GENERATOR EXAMPLE *design a*

MATERIAL				
Ferrite magnet grade B_r	0.47			T
GEOMETRICAL DESIGN OUTPUTS				
Pole pairs p	24			
Per-unit tooth length l_t/r	7.0			%
Rotor diameter $2r'$	3.559			m
PERFORMANCE INDICATORS AND OTHER DESIGN QUANTITIES				
	Model	FEA		
Airgap flux density at no load $B_{gap,m}$	0.56	0.50		T
d-axis current loading A_d	21.4	21.4	(31.1)	kA/m
q-axis current loading A_q	49.6	49.6	(46.1)	kA/m
Overall current loading A	54.0	54.0	(55.6)	kA/m
d-axis current I_d	1.10	1.10	(1.60)	Apk
q-axis current I_q	2.55	2.55	(2.37)	Apk
Overall current I	2.78	2.78	(2.86)	Apk
Shear stress σ	42.5	39.2	(42.5)	kNm/m^3
q-axis inductance L_q	4.34	3.98		mH
Power Factor	0.92	0.99	(0.99)	
Line Voltage	-	508	(577)	Vpk
Joule loss density k_j	6713	6357	(6720)	W/m^2
Iron loss density k_i	490	533	(585)	W/m^2
Total loss density	7203	6890	(7305)	W/m^2

The automotive FASR motor, namely *design c*, has been defined so to guarantee a satisfactory behavior, in terms of flux weakening capability, at most operating condition. The q-axis current loading has been set to be 80% of the characteristic one. This design

strategy will be better addressed in Chapter 07. As suggested by the plots in Figure 5.16, the number of pole pairs of the final design is three and the stator tooth length is about 13% of the outer radius. The whole model outputs are summarized in Table 5-VI, together with the FEA validation data.

TABLE 5-V
LIFT MOTOR EXAMPLE *design b*

MATERIAL				
Ferrite magnet grade B_r	0.37			T
GEOMETRICAL DESIGN OUTPUTS				
Pole pairs p	7			
Per-unit tooth length l_t/r	14.4			%
Rotor diameter $2r'$	0.296			m
PERFORMANCE INDICATORS AND OTHER DESIGN QUANTITIES				
	Model	FEA		
Airgap flux density at no load $B_{gap,m}$	0.35	0.36		T
d-axis current loading A_d	15.0	15.0	(18.5)	kA/m
q-axis current loading A_q	27.1	27.1	(24.7)	kA/m
Overall current loading A	31.0	31.0	(31.0)	kA/m
d-axis current I_d	19.4	19.4	(23.9)	Apk
q-axis current I_q	35.0	35.0	(32.0)	Apk
Overall current I	40.0	40.0	(40.0)	Apk
Shear stress σ	46.0	44.6	(46.0)	kNm/m^3
q-axis inductance L_q	24.0	26.5		mH
Power Factor	0.87	0.86	(0.85)	
Line Voltage	-	225	(230)	Vpk
Joule loss density k_j	10500	8980	(8980)	W/m^2
Iron loss density k_i	950	996	(1005)	W/m^2
Total loss density	11450	9976	(9985)	W/m^2

For all the example designs, the magnet grade B_r needed to fulfill either the “Natural Compensation” or the “Non-Natural Compensation” condition has been evaluated taking into account the effect of the rotor structural bridges, that reduce the concentration of the PMs flux linkage in the airgap.

This effect is less relevant when dealing with large low speed machines, but it gets more penalizing in case of smaller motors, especially when structural ribs must be thick enough for the rotor lamination to be safe at all rotating speed levels, including the ones higher than the rated one. For example, magnetic bridges reduce by 5% the airgap PMs

flux density of the large wind generator *design a* and by 15% the PMs flux concentration effects of *design c*. In fact, *design c* is a traction motor designed to operate also at speed values, larger than the nominal one, up to 12000 rpm.

In general, whatever the size of the machine and its application area are, a good matching has been obtained between FEA and model results, except for the optimal current phase angle and the expected Joule loss.

TABLE 5-VI
TRACTION MOTOR EXAMPLE *design c*

MATERIAL				
Ferrite magnet grade B_r	0.38			T
GEOMETRICAL DESIGN OUTPUTS				
Pole pairs p	3			
Per-unit tooth length l_t/r	13.2			%
Rotor diameter $2r'$	0.076			m
PERFORMANCE INDICATORS AND OTHER DESIGN QUANTITIES				
	Model	FEA		
Airgap flux density at no load $B_{gap,m}$	0.43	0.48		T
d-axis current loading A_d	10.1	10.1	(15.5)	kA/m
q-axis current loading A_q	22.9	22.9	(20.4)	kA/m
Overall current loading A	25.0	25.0	(25.6)	kA/m
d-axis current I_d	94.7	94.7	(145)	Apk
q-axis current I_q	215	215	(191)	Apk
Overall current I	235	235	(240)	Apk
Shear stress σ	20.3	17.7	(20.3)	kNm/m^3
q-axis inductance L_q	0.153	0.165		mH
Power Factor	0.99	0.99	(0.99)	
Line Voltage	-	124	(153)	Vpk
Joule loss density k_j	14786	14950	(15593)	W/m^2
Iron loss density k_i	1637	1850	(2495)	W/m^2
Total loss density	16423	16800	(18088)	W/m^2

The former is underestimated by the model, as the core saturation effects contribute to modify the Maximum Torque Per Ampere (MTPA) locus in the (i_d, i_q) plane. However, it is worth pointing out that the current amplitude, needed to produce the willed torque, is predicted with an accuracy, good enough for being of practical use. This is also thanks to the corrective factor proposed in Subsection 5.1.3.2 for the d-axis current loading, which attempts to compensate for the stator back iron magnetic potential drops

increasing the current loading A_d. The discrepancy between the current phase angle suggested by the model and the one that is actually needed to make the FASR machine deliver the willed torque is evidenced by the results in the "FEA" columns of Tables 5-IV, 5-V and 5-VI: the terms in brackets show which working point corresponds to the target shear stress, according to the Finite Element investigation, whereas the other data analyzes the motor behavior in the design condition, proposed by the analytical model.

On the contrary, the model overestimates the Joule loss, because of the rectified geometry, which schematically models parallel side slots, referring their constant widths to the (shorter) bore radius. It occurred also when modeling the behavior of SPM machines in Chapter 03. Anyway, the model estimation results "safer" from this point of view and for small-sized FASR machines only, it is necessary to apply a corrective factor (i.e. $0.5 \cdot (1+r'/r)$) to obtain a reasonable estimation of the specific Joule loss, as pointed out also in Chapter 03.

5.5. CONCLUSION

A general approach to the optimal design of multipolar FASR machines has been discussed, with particular attention to direct-drive low speed applications.

The procedure, that has been described, is based on a fully analytical per-unit model, that has a twofold purpose. First, it aims at orienting the designers to the most convenient solutions by means of general guidelines, suitable for machines of all sizes and applications. Then, it provides closed-form equations to determine all the design variables and performance indicators of the machine.

As a result, the FEA is not mandatory, but just useful for final refinements. In particular, a simple formula suggests the optimal pole pairs number to be adopted if the Joule loss needs to maximized, greatly simplifying the design task. This pole pairs number does coincide with the optimal pole pairs number for efficiency maximization in case of low speed applications. In the remaining situations, the impact of the iron loss on the optimal pole pairs number for the overall loss minimization can be quantified.

In order to prove the generality of the design approach, the proposed method has

been applied to different cases, devoted to various application fields. Some FEA results, together with the model outputs, have been presented. The reader is asked to refer to Chapter 07 for the comparison of the proposed technology with alternative PM-based solutions for both wind generators and automotive applications, and to Chapter 08 for experimental verification on the FASR prototyped machine, introduced in the last subsections.

Chapter 06

An alternative to FASR motors for cost-reduction: magnets quantity minimization in rare-earth based PMASR machines

---

High-salient Synchronous Reluctance machines, Assisted via cheap ferrite magnets, have been selected as reduced-cost alternatives to high-performance (and high-cost) technologies, such as electrical machines of the Surface-Mounted type.

This chapter presents a technique to modify the rotor lamination of rare-earth based Permanent Magnet Assisted Synchronous Reluctance motors, in order to minimize the magnet volume with no side effect on performance, thus proposing another alternative technology for cost-reduction.

In general, SR designs, having multi-layer (i.e. high-salient) rotor structures and assisted with Permanent magnets of all kinds, have been extensively studied in recent years because of their potentially competitive torque density, efficiency, together with their inherent suitability to zero-speed sensorless control [64]–[72].

Moreover, it has been shown in the literature (and it will be proved later in this work) that maximizing the rotor saliency (i.e. reducing the PM flux linkage) is beneficial when a large Constant Power Speed Range is required [73], with further advantages welcome in many up-to-date applications, such as electric and hybrid traction.

These other pros are: lower overvoltage in case of inverter fault, larger overload capability [74] and smaller magnet quantity and cost.

A closed-form analysis, which is based on a lumped parameter model, will point out that the magnet quantity in case of rare-earth based designs can be optimized with a

significant (additional) saving of material volume and cost.

The basic idea behind the PM and rotor lamination modifications is shown in Figure 6.1. Given the starting PMASR rotor, optimized in terms of saliency between the direct and quadrature axes, an advantageous reduction in the PM volume of each layer can be obtained by reducing the thickness of the magnet pieces and filling in the space left free by the PMs with iron. Obviously, the tangential span of the magnets must slightly increase when the thickness decreases, but still the cross area of the PM gets smaller, up to a certain extent. When the shape of each magnet piece is modified, the two structural ribs at its sides accordingly move, as it is also evident from Figure 6.1.

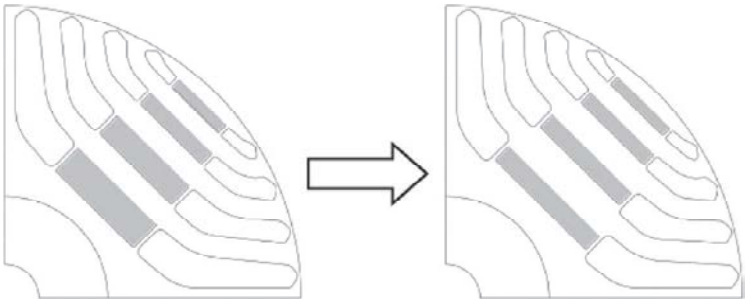

Figure 6.1 - Example of original and modified rotor geometry. Starting design (Left). Design with reduced PM volume, verified toward demagnetization at maximum overload (Right).

The rotor rearrangement has irrelevant practical impact on the machine performance and it is viable for all PMASR motors, where only a portion of the flux barriers is occupied by PMs, as it is often the case with rare-earth-based magnets.

The only factor that does intervene to constrain the opportunity of actually minimizing the magnet volume is represented by demagnetization issues. Thus, the risk of demagnetization will be evaluated in the following analysis, finding out an ultimate design, compatible with the worst case demagnetizing current condition, but still characterized by a noteworthy reduction of the PMs quantity and cost.

This chapter is organized as follows.

The PMASR machine design procedure is briefly summarized in Section 6.1 to point out how the starting SR motor is obtained and provide modeling basics of the procedure which optimizes the magnet volume and quantifies the demagnetization limit. Then, the rotor design modifications needed for PMs quantity reduction are analytically described

in Section 6.2, expressing the achievable volume saving in terms of per-unit quantities so to generalize the results. The limits related to the demagnetization risk will be also quantified in equations and discussed. Last, in Section 6.3, selected machines are Finite Element evaluated, to validate the analysis and highlight local field aspects.

6.1. DESIGN BASICS OF RARE-EARTH BASED PMASR MACHINES

When dealing with PM-Assisted SR machines, the first design step is to define the best possible SR rotor structure, given the size of the active parts (stack diameter $2r$ and length l) and the rate of heat removal at the outer stator surface, which is required to match the specific Joule, PMs and iron losses of the machine.

Afterwards, the magnets are added to the basic SR motor, so to improve the Power Factor and give an additional contribute to the torque.

Specifically, the magnets flux is designed for compensating either the whole q-axis flux of the basic SR machine or the majority of it [57]. If the q-axis rated current, that is one oriented against the PMs, is made equal to the short circuit (characteristic) one, the PMASR machine is "Naturally Compensated". It says that: only poor design choices lead to unfeasible Power Factor values, the cross-saturation effects are conveniently reduced and the Constant Power speed range of the drive at rated condition is theoretically unlimited. As an alternative, either the PM flux can be reinforced with respect to the "Natural Compensation" condition or the q-axis current put into play can be larger than the characteristic one. The first solution helps enhancing the flux weakening capability of the drive also at overload currents, whereas the latter is representative of machines that rely on an improved cooling system for increasing the achievable torque density. Anyway, both these design situations move just a little away from the "Natural Compensation" condition, also for preserving the overall machine performance from being penalized by cross-saturation effects. Thus, "Naturally Compensated" PMASR machines will be considered as main reference in the following, still providing a general procedure for the design of the PM flux in such Magnet ASR motors.

Throughout the aforementioned design procedure, the key design choices to be made are not dissimilar to the one discussed in the previous Chapter for the optimal

design of FASR motors. Thus, these criteria will be simply summarized here and in the following the focus will be on the design of the PM flux linkage, considering to start from "optimal" SR machines.

The crucial design points, that is worth recalling, deal with the definition of:

- the rotor geometry, namely its per-unit magnetic insulation and the flux barriers shape;
- the magnetizing *d*-axis airgap flux density *b*, expressed in per unit of the stator yoke exploitation target B_{fe}.
- the pole pairs number *p* and the stator tooth length factor, which both concur to determine the rotor diameter 2*r'*.

Designing multi-layer rotor structures with good insulation properties allows to minimize the *q*-axis inductance, thus reducing the magnets loading needed to fulfill the "Natural Compensation" condition. Specific geometric rules that allow to improve the PMASR rotor design in terms of uniform exploitation of the PMs and reduction of the overall harmonic content in the airgap flux density will be discussed in Subsection 6.1.3.

The design of the stator iron paths comes directly from the normalized flux density *b*, that represents both the yoke height (in per-unit of the pole pitch) and the stator tooth width (in per-unit of the slot pitch). Convenient *b* values are in the range 0.5-0.65, as trade-off choices. In fact, as the airgap flux density is increased, the shear stress is increased as well. But it occurs at the expense of larger *d*-axis currents (meaning larger Joule loss), larger stator back iron dimensions and larger recoil rotor iron paths, that lower the machine saliency.

As said, he number of pole pairs and the stator tooth length determine the airgap radius. The resultant pole pitch to airgap ratio needs to be sufficiently high not to make the machine prone to demagnetization and not to reduce the magnetic loading obtainable in the airgap thanks to the magnets.

If the per-unit airgap is too thick, also the saliency ratio is unsatisfactory. In particular, the magnetizing *d*-axis inductance is low (requiring high excitation currents), whereas the *q*-axis one is high (badly affecting the characteristic electric loading). The number of pole pairs has to be set accordingly, also considering the role played by the

airgap lever in the torque production mechanisms. Besides, the choice of the stator tooth length has to be handled as an important degree of freedom in defining the final design, as it impacts both the machine weight and efficiency.

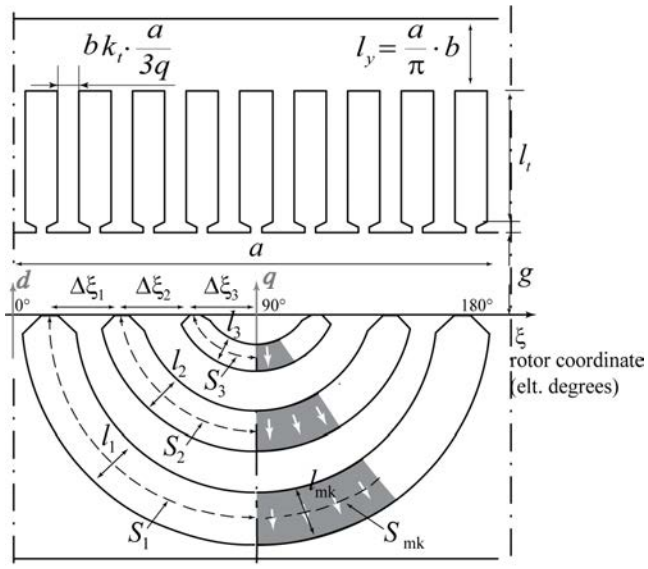

Figure 6.2 - Rectified pole of a rare-earth based PMASR machine with a three-layer rotor and the PMs magnetized radial-wise. The dq axes follow the SR model approach.

6.1.1. Reference pole geometry

The sketch in Figure 6.2 models one pole of a rare-earth based PM Assisted Synchronous Reluctance motor via a rectified geometry. Analogously to the analysis for the optimal design of FASR machines, the main geometric quantities are defined as follows:

- g is the airgap length
- a is the pole pitch;
- l_t is the stator teeth length;
- q is the slot number per pole per phase;
- b and k_t define the stator back iron dimensions;
- $\Delta\xi_k$ is the pitch of the k-th rotor "slot";
- S_k represents half the width of the whole k-th flux barrier;
- S_{mk} stands for half the width of the k-th magnets;
- l_k and l_{mk} are the thickness of the k-th flux barrier and the k-th magnet,

respectively.

- l is the stack length of the reference block.

As for the number of rotor flux barriers and their shapes, different choices are possible. The number of layers (n) is three in the reference rotor of Figure 6.2 only as an example, since the theory has been developed to deal with any kinds of multi-layer rotor structures.

Moreover, round flux barriers are sketched in Figure 6.2 just for modeling purposes. In fact, actual rotor designs are always optimized to improve the saliency ratio between the *d*- and *q*-axis, usually leading to more compact shapes of the rotor layers.

It is also worth specifying that, differently from FASR rotor topologies, which are required to have constant-thickness flux barriers, with this kind of rare-earth based PMASR structures, the extremities of the rotor layers can be made thinner again to optimize the saliency ratio between the *d*- and *q*-axis. More precisely, it is the middle area of the flux barriers that results slightly enlarged, while being kept constant in terms of thickness so to house in the magnets. When the thicknesses of the flux barriers' end-parts are non-constant, each S_k value is an equivalent width which takes into account that the respective length l_k varies along the rotor layer span.

Typical PM Assisted Synchronous Reluctance designs make use of magnet pieces, that are as long as the respective flux barriers are and as wide as to fill in a fraction of the layers span. In other words, as it is indicated in Figure 6.2, l_{mk} is usually equal to l_k and S_{mk} is smaller than S_k.

However, in order to minimize the magnet volume, here the magnets length l_{mk} will be made thinner than the respective length l_k, and the width S_{mk} will result a little bit larger than the ones that would have been needed, if l_{mk} had been made equal to l_k at same design condition.

The factor y_k (6.1) quantifies the chosen thickness ratio:

$$y_k = \frac{l_{mk}}{l_k} \qquad k = 1,2,\dots,n \tag{6.1}$$

According to (6.1), "$y_k = 1$" is representative of "standard" PMASR designs.

6.1.2. Quadrature axis equivalent magnetic circuit

The circuit of Figure 6.3 models the q-axis magnetic behavior of the rectified pole in Figure 6.2, considering a 3-layer rotor structure as an example.

The fluxes are the ones of half a pole.

TABLE 6-I
NORMALIZATION OF THE Q-AXIS MAGNETIC MODEL

QUANTITY	BASE VALUE
Magnetic potentials, mmfs	Peak F_q of the fundamental q-axis mmf waveform
Permeances	$\mu_0 l$
Fluxes	$F_q \mu_0 l$

As for the q-axis equivalent circuit proposed to examine the q-axis magnetic behavior of FASR rotors, all the magneto-motive force generators, magnetic potentials and permeances are expressed in normalized quantities. The base values, corresponding to the main circuit components, are summarized in Table 6-I for convenience.

The fundamental wave of the stator magneto-motive force, in per-unit of its peak value F_q, is averaged across each rotor tooth at the airgap and then modeled via the staircase f_{q123} reported in Figure 6.4 and indicated in the equivalent circuit of Figure 6.3 via mmf generators.

In this way, the model accounts for the polarization of the rotor flux guides into the potentials r_{123}, that are assumed to be uniform along the overall guides width and are always slightly lower than the respective values f_{q123}.

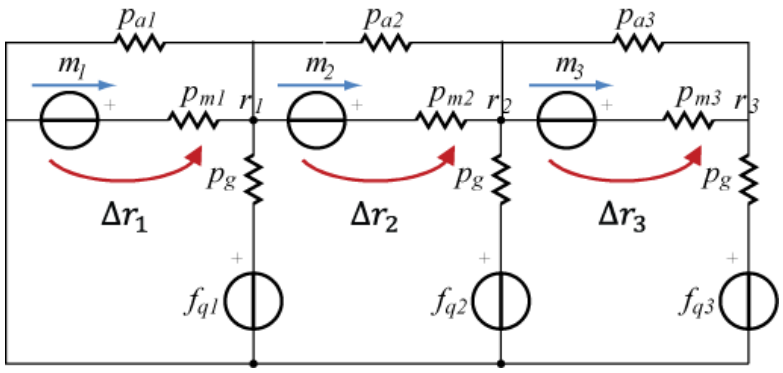

Figure 6.3 - The equivalent circuit represents the q-axis magnetic behavior of half a pole. It refers to the PMASR example rotor in Figure 6.1 (n=3).

The terms p_{g123}, which represent the per-unit permeances of the rotor teeth at the airgap, depend inversely on the airgap length and directly on the rotor "slot" pitches. A "regular" inter-barrier pitch $\Delta\xi$ (6.2) can be conveniently adopted for torque ripple minimization.

$$\Delta\xi = \frac{2\pi}{n_r} \tag{6.2}$$

In (6.2) n_r represents the equivalent number of rotor slots per pole pair. As said in Chapter 04, different choices of n_r are possible, in order to avoid the direct interaction between stator and rotor slot harmonics [55], [2]. If $n_r = 4n+2$, the rotor "slot" pitch $\Delta\xi_k$ is kept constant, and equal to $\Delta\xi$, along the whole periphery of the rotor. If $n_r > 4n+2$, the inter-barrier pitch is still uniform, with the general exception of the angle $\Delta\xi_n$ (between the smallest layer and the q-axis) that is larger than $\Delta\xi$, according to the factor $k_{\Delta\xi n}$. The most "regular" rotor topologies are called "complete" in [55] and have all the normalized airgap permeances equal to the value p_g (6.3).

$$p_g = \frac{a}{g} \cdot \frac{\Delta\xi}{\pi} \tag{6.3}$$

Conversely, in case of "non -complete" machines, (n-1) airgap permeances are still quantified by (6.3), but the n-th permeance p_{gn} is defined via (6.4).

$$p_{gn} = \frac{a}{g} \cdot \frac{\Delta\xi}{\pi} \cdot k_{\Delta\xi n} \tag{6.4}$$

The reader is reminded that $k_{\Delta\xi n}$ is equal to one if $n_r = 4n+2$, that is the rotor is "complete".

The m_{123} (6.6) generators and the permeances p_{m123} (6.7) stand for the presence of the magnets.

$$m_k = \frac{1}{F_q} \cdot \frac{B_r}{\mu_0} l_{mk} = y_k \cdot \frac{1}{F_q} \cdot \frac{B_r}{\mu_0} l_k \qquad k = 1, 2, \dots, n \tag{6.6}$$

$$p_{mk} = \frac{S_{mk}}{l_{mk}} = \frac{1}{y_k} \cdot \frac{S_{mk}}{l_k} \qquad k = 1, 2, \dots, n \tag{6.7}$$

In (6.6) and (6.7), the relative permeability of the PMs has been considered

approximately equal to one. B_r represents the remanence of rare-earth magnets and μ_0 is the free space permeability. Equations (6.6) and (6.7) are valid, whatever the value of y_k is.

The permeances p_{a123} model the remaining parts of the rotor layer that are not filled in with magnetic material. Namely, p_{a123} (6.5) represent the air flux tubes l_k long and (S_k - S_{mk}) wide.

$$p_{ak} = \frac{S_k - S_{mk}}{l_k} \qquad k = 1, 2, \dots, n \tag{6.5}$$

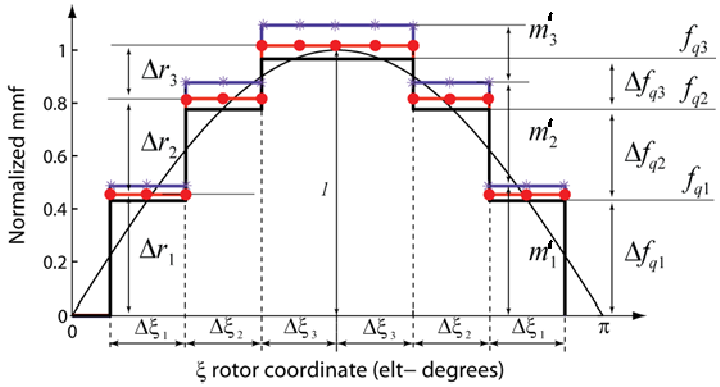

Figure 6.4 - Staircase distributions of the mmfs in the equivalent circuit of Figure 6.2, in per-unit of F_q. The plots are referred to the three-layer "complete" rotor of Figure 6.1. No markers: q-axis stator mmf f_{q123}. Star: equivalent mmf m'_{123}. Circle: iron guides magnetic potentials r_{123}.

Last, the normalized mmfs m'_{123} (6.8) and the permeances p_{b123} (6.9) are introduced in order to reproduce the magnetic behavior of the whole flux barrier (namely, "magnets" plus "air") via a unique Thevenin equivalent circuit.

$$m'_k = \frac{1/\mu_0}{\frac{S_k}{l_k} \cdot \left(1 + \frac{1-y_k}{y_k} \cdot \frac{S_{mk}}{S_k}\right)} B_r \cdot S_{mk} \qquad k = 1, 2, \dots, n \tag{6.8}$$

$$p_{bk} = \frac{S_k}{l_k} \cdot \left(1 + \frac{1 - y_k}{y_k} \cdot \frac{S_{mk}}{S_k}\right) \qquad k = 1, 2, \dots, n \tag{6.9}$$

6.1.3. Geometric rules to enhance the machine performance

Similarly to FASR rotor structures, also when dealing with rare-earth based PM Assisted SR machines, useful criteria can be found out for defining the shape of the rotor

flux barriers.

The design of Neodymium-Assisted SR rotors will be optimized in order:

- to minimize the overall harmonic content of the quadrature flux density;
- to guarantee a uniform exploitation of the PMs in terms of working flux density.

This two-fold purpose is pursued, if the rotor geometry is designed for having at the same time:

- the equivalent mmfs $\boldsymbol{m'}$ (6.10) proportional to the per-unit stator mmf staircase $\boldsymbol{\Delta f_q}$ (6.10)
- the magnetic potential drops $\boldsymbol{\Delta r}$ (6.10) proportional to the per-unit staircase $\boldsymbol{\Delta f_q}$, as well.

$$\Delta \boldsymbol{r} = \begin{bmatrix} \Delta r_1 \\ \Delta r_2 \\ \vdots \\ \Delta r_n \end{bmatrix} = \begin{bmatrix} r_1 \\ r_2 - r_1 \\ \vdots \\ r_n - r_{n-1} \end{bmatrix}, \boldsymbol{m'} = \begin{bmatrix} m'_1 \\ m'_2 \\ \vdots \\ m'_n \end{bmatrix}, \Delta \boldsymbol{f_q} = \begin{bmatrix} \Delta f_{q,1} \\ \Delta f_{q,2} \\ \vdots \\ \Delta f_{q,n} \end{bmatrix} = \begin{bmatrix} f_{q,1} \\ f_{q,2} - f_{q,1} \\ \vdots \\ f_{q,n} - f_{q,n-1} \end{bmatrix} \tag{6.10}$$

In other words, the designer is required to set the parameters that are in the equivalent circuit of Figure 6.3 so to make the shapes of both the mmfs $\boldsymbol{m'}$ and the potential drops $\boldsymbol{\Delta r}$ look like the curves in Figure 6.4.

The geometric rules that satisfy the aforementioned requirements can be derived following the same principles adopted for SR machines assisted by ferrite magnets. Thus, in the following the main design criteria will be schematically described and the reader is asked to refer to Chapter 04 for retracing all the demonstrations that are skipped here.

The rotor magnetic insulation l_a must be shared between the layers of the starting SR design according to the stator mmf per-unit levels Δf_{qk}, as suggested by (6.11):

$$l_k = l_a \cdot \frac{\Delta f_{qk}}{f_{qn}} = l_{a,pu} \cdot \frac{a}{2} \cdot \frac{\Delta f_{qk}}{f_{qn}} \tag{6.11}$$

where $l_{a,pu}$ stands for the total insulation, normalized by half the pole pitch $a/2$. f_{qn} is the top value of the per-unit staircase $\boldsymbol{\Delta f_q}$, which is always close to one, whatever the number of layer is.

Besides the layers thicknesses, also the magnets lengths must copy the shape of the

staircase distribution $\boldsymbol{\Delta f_q}$.

$$\frac{l_{mk}}{\Delta f_{qk}} = const \qquad k = 1, 2, \dots, n \tag{6.12}$$

It follows that, in case the magnets are made thinner than the respective barrier length in order to minimize the overall PMs quantity, a unique thickness ratio *y* valid for all the magnets is required.

The permeances p_{bk} (6.9) are needed to be "regular".

$$\begin{aligned} &p_{bk} = p_b = const \quad k = 1,2, \dots, n-1 \\ &p_{bn} = k_{pbn} \cdot p_b \qquad k_{pbn} = \frac{\Delta f_{q1}}{\Delta f_{qn}} \frac{\sin\left(k_{\Delta\xi n} \cdot \Delta\xi\right)}{\cos(\Delta\xi/2)} \end{aligned} \tag{6.13}$$

Specifically, it means that, starting from the first rotor flux barrier up to (n - 1)-th layer, the shape of both the magnets and the air gaps have to be set in order to make the p_{bk} permeances all equal to each other. Since for "complete" rotor structures k_{pbn} is equal to one, then all the permeances of such machines, including the n-th one, must result actually regular. Conversely, when the number of layer n matches the number of rotor "slot" so to make the machine "non-complete", the geometry of the flux barrier closest to the q-axis has to be arranged to fulfills the general condition reported in the second line of (6.13).

$$\begin{aligned} &\frac{S_k}{S_h} = \frac{\Delta f_{qk}}{\Delta f_{qh}} \qquad \forall\, h, k \neq n \\ &\frac{S_n}{S_1} = k_{pbn} \frac{\Delta f_{qn}}{\Delta f_{q1}} = \frac{\sin\left(k_{\Delta\xi n} \cdot \Delta\xi\right)}{\cos(\Delta\xi/2)} \end{aligned} \tag{6.14}$$

$$\begin{aligned} &\frac{S_{mk}}{S_{mh}} = \frac{\Delta f_{qk}}{\Delta f_{qh}} \qquad \forall\, h, k \neq n \\ &\frac{S_{mn}}{S_{m1}} = k_{pbn} \frac{\Delta f_{qn}}{\Delta f_{q1}} = \frac{\sin\left(k_{\Delta\xi n} \cdot \Delta\xi\right)}{\cos(\Delta\xi/2)} \end{aligned} \tag{6.15}$$

If (6.11) and (6.12) are respected, the requirements expressed by (6.13) lead to the need of designing the layer widths S_k according to (6.14). Analogous rules (6.15) have to

be followed when fixing the widths S_{mk} of the rare-earth magnet pieces.

To summarize, if the rotor layers (namely, l_k and S_k) and the magnets (namely, l_{mk} and S_{mk}) are designed according to (6.11)-(6.12), (6.14)-(6.15), then the magnet lengths l_{mk}, if different from the respective values l_k, can be chosen in a straightforward way via a unique scaling factor y, valid for all the PMs. Also the ratio S_{mk}/S_k, which fixes the portion of each rotor layer to be filled in with magnetic material, is a constant value for all the n rare-earth magnet pieces.

Moreover, thanks to according to (6.11)-(6.12), (6.14)-(6.15), all the magnets work at the same flux density, that turns out to be uniform also throughout each PM span thanks to the constant thicknesses l_{mk}.

6.1.4. Design of the PM flux

As said, the optimization procedure proposed for the design of rare-earth based PMASR machines deals with the minimization of the magnets volume and thus looks for the most suitable way of producing the desired PM flux.

The design tips proposed in the last subsection improve the performance achievable by the ultimate design and facilitate the computation tasks, since most of the design quantities to be handled are made more "regular".

The equivalent circuit reported in Figure 6.3 relates these design variables to the main geometric parameters, according to the system of linear equations (6.16) and together with the matrices **A** (6.17), **B** (6.18) and **C** (6.19).

$$\boldsymbol{A} \cdot \Delta \boldsymbol{r} = \boldsymbol{B} \cdot \boldsymbol{m}' + \boldsymbol{C} \cdot \Delta \boldsymbol{f_q} \tag{6.16}$$

$$\boldsymbol{A} = \begin{bmatrix} p_b + p_g & -p_b & 0 & 0 \\ p_g & p_b + p_g & -p_b & 0 \\ \cdots & \cdots & \cdots & \cdots \\ p_{gn} & p_{gn} & p_{gn} & p_{bn} + p_{gn} \end{bmatrix} \tag{6.17}$$

$$\boldsymbol{B} = \begin{bmatrix} p_b & -p_b & 0 & 0 \\ 0 & p_b & -p_b & 0 \\ \cdots & \cdots & \cdots & \cdots \\ 0 & 0 & 0 & p_{bn} \end{bmatrix} \tag{6.18}$$

$$\boldsymbol{C} = \begin{bmatrix} p_g & 0 & 0 & 0 \\ p_g & p_g & 0 & 0 \\ \dots & \dots & \dots & \dots \\ p_{gn} & p_{gn} & p_{gn} & p_{gn} \end{bmatrix} \tag{6.19}$$

Equations (6.16) can be exploited to select the magnets lengths and widths, so that a convenient relationship is fixed between the rated q-axis current and the PM flux linkage.

The PM flux linkage λ_m is usually chosen so that the q-axis rated current I_q is close to the short circuit or characteristic ($I_{q0} = I_{ch}$) one. Specifically, I_q will be intended equal to $x_{q0} \cdot I_{q0}$, with the factor x_{q0} properly set according to the considerations listed at the beginning of this section.

In formula, expression (6.20) has to be conveniently verified:

$$\lambda_m = L_q I_{ch} = L_q I_{q0} = L_q \frac{I_q}{x_{q0}} \tag{6.20}$$

In (6.20), the q-axis current corresponding to "Naturally Compensated" machines (i.e., $x_{q0} = 1$) is addressed as I_{q0}. The subscript "0" will be introduced again in the following, every time it will be needed to remind the reader of the "Natural Compensation" condition.

The stator mmf F_q and current loading A_q are determined via (6.21) and (6.22) as functions of the q-axis stator current I_q, depending on the number of conductors per slot N.

$$F_q = \frac{3}{\pi} \cdot k_w \cdot N \cdot I_q \tag{6.21}$$

$$A_q = \frac{\pi}{2} \cdot \frac{F_{q0}}{a} = \frac{\pi}{2} \cdot \frac{1}{a} \cdot \left(\frac{3}{\pi} k_w N I_q \right) \tag{6.22}$$

F_{q0} and A_{q0} stand for the characteristic stator mmf and current loading, respectively.

The term L_q (6.23), involved in (6.20), represents the overall q-axis inductance.

$$L_q = L_{m,q} + L_{\sigma,slot} + L_{zz,q} \tag{6.23}$$

As discussed in Chapter 05, it is given by three different contributes, namely: the magnetizing inductance L_{mq}, the slot-leakage term $L_{\sigma,slot}$ and the sum of the stator and rotor zig-zag contributes $L_{zz,q}$. These quantities are defined by (6.24), (6.25) and (6.26),

respectively, with reference to one machine pole and the same symbols adopted in Chapter 05.

$$L_{m,q} = \frac{3\pi^2}{4l_{a,pu}}\left(1 - \frac{2}{n_r}\right) \cdot L_{base} \tag{6.24}$$

$$L_{\sigma,slot} = \frac{\pi^2}{2k_w^2}\frac{1}{(1 - bk_t)} \cdot \frac{l_t}{g} \cdot \frac{g}{a} \cdot k_{tip} \cdot \left(1 - \frac{3n_{sp}}{16q}\right) \cdot L_{base} \tag{6.25}$$

$$L_{zz,q} = \frac{1}{8}\left[\left(\frac{\pi}{3q}\right)^2 + \left(\frac{2\pi}{n_r}\right)^2\right] \cdot \frac{a}{g} \cdot L_{base} \tag{6.26}$$

Further details about these equations can be found always in Chapter 05.

Provided that different phenomena intervene to determine the q-axis inductance, from (6.20), it follows that the flux produced by the PMs is compelled:

- to fully counteract the magnetizing flux (that is, $L_{m,q}{\cdot}I_q$) forced by the stator mmf to flow into the rotor, while making null the respective potential drop in the airgap;
- to pass through the airgap, so to compensate for the flux that the stator windings would still link due to slot and zig-zag leakage contributes.

This situation can be modeled by means of the equivalent circuit of Figure 6.3, saying that the potential drops Δr_k have to respect (6.27):

$$\Delta r_k = \left(1 + \frac{\phi_{leak}}{p_g}\right) \cdot \Delta f_{\mathrm{qk}} \tag{6.27}$$

being Φ_{leak} (6.28) the normalized flux required to flow towards the airgap for neutralizing the leakage stator fluxes.

$$\phi_{leak} = \frac{2\pi}{3} \cdot \frac{L_{m,q}}{L_{base}} \cdot \frac{\Delta\xi}{a} \tag{6.28}$$

The conditions that make true (6.27) can be found out by solving the equivalent circuit of Figure 6.3 via the nodal voltage analysis.

First, according to the system of linear equations (6.16), Expression (6.29) is derived.

$$\Delta r_k = \frac{1}{1+\frac{p_g}{p_b}\frac{\Delta f_{q1}}{\Delta f_{q1}-\Delta f_{q2}}} \cdot m'_k - \frac{\frac{p_g}{p_b}\frac{\Delta f_{q1}}{\Delta f_{q1}-\Delta f_{q2}}}{1+\frac{p_g}{p_b}\frac{\Delta f_{q1}}{\Delta f_{q1}-\Delta f_{q2}}} \cdot \Delta f_{qk} \tag{6.29}$$

Afterwards, by constraining (6.27) to coincide with (6.29), it turns out that (6.27) is verified by (6.29) when the flux barrier equivalent mmfs ***m'*** are related to the stator one via the factor k_{leak} according to (6.30)

$$m'_k = k_{leak} \cdot \Delta f_{qk} \tag{6.30}$$

Eventually, Equation (6.31) can be introduced to quantify k_{leak}.

$$k_{leak} = 1 + \frac{L_{\sigma,slot} + L_{zz,q}}{L_{m,q}} \tag{6.31}$$

Expression (6.31) can be demonstrated if it is reminded that the magnetizing q-axis inductance of Magnet-Assisted SR machines is correlated to the rotor permeances by means of (6.32), as it was pointed out in Chapter 05.

$$L_{m,q} = \frac{3}{2} \cdot \frac{\frac{p_b}{p_g}\left(1-\frac{\Delta f_{q2}}{\Delta f_{q1}}\right)}{1+\frac{p_b}{p_g}\left(1-\frac{\Delta f_{q2}}{\Delta f_{q1}}\right)} \cdot \frac{L_{base}}{g} \tag{6.32}$$

According to equations (6.24) - (6.26), the k_{leak} factor (6.31) varies depending on the pole pitch to airgap ratio, as shown in Figure 6.5, where the impact of both the zig-zag leakage contributes and the slot ones are highlighted.

Starting from (6.30), if the definition (6.8) is recalled, it is possible to compute the fraction S_{mk}/S_k (6.33) of each layer to be filled in with magnetic material for having the rate q-axis current equal to the chosen x_{q0} multiplied by the short circuit current.

$$\frac{S_{mk}}{S_k} = \frac{y}{\left[1+\frac{1}{k_{leak}}\left(\frac{1}{x_{q0}\cdot F_{q0}} \cdot \frac{B_r}{\mu_0}\frac{l_{a,pu}}{f_{qn}}\frac{a}{2}\right)\right]y - 1} \tag{6.33}$$

In other words, condition (6.30), which together with the definition of k_{leak} (6.31) leads to (6.33), identifies a family of PM Assisted SR designs, all having the same layer lengths l_k and the same properties in terms of compensation of the PM flux. For example, if x_{q0} is equal to one, Equation (6.33) gets representative of a specific class of "Naturally

compensated" machines.

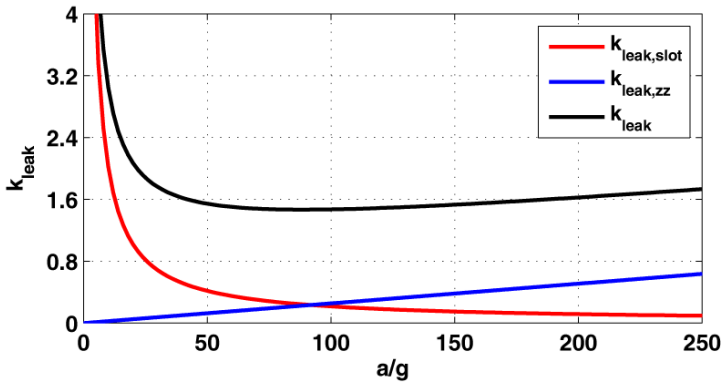

Figure 6.5 – The factor k_{leak} is reported as a function of the pole pitch to airgap ratio a/g in correspondence of two values of the normalized stator tooth length. Both the zig-zag contribute and the slot leakage one are put in evidence.

Equation (6.33) highlights also that the PM flux can be set at the designer will via different choices of the uniform parameter y.

The next section will show how to exploit the thickness ratio y as main degree of freedom to optimize the magnets volume without compromising the machine performance.

6.2. MINIMIZATION OF THE MAGNETS VOLUME

Given the flux barriers length (l_{mk}) and width (S_{mk}), the overall magnets volume $V_{m,pu}$, in per-unit of the rotor one, is expressed by (6.34):

$$V_{m,pu} = 4\frac{S_{m1}l_{m1} + S_{m2}l_{m2} + \cdots + S_{mn}l_{mn}}{a^2} \tag{6.34}$$

Each PM thickness l_{mk} (6.2) can be a fraction of the flux barrier one l_k, depending on the ratio y, which is a constant value for all the magnets.

Analogously, each PM span S_{mk} covers only a part of the whole layer width S_k. It occurs according to the compensation law imposed by (6.33), which fixes again a unique value of the ratio S_{mk}/S_k for the n magnets.

So, if the geometric rules put in evidence in Subsection 6.1.2 are respected, Equation (6.34) can be modified as shown by (6.35), pointing out that the required magnet volume

is a function of the thickness ratio y.

$$V_{m,pu} = \frac{y^2}{\left[1 + \frac{1}{k_{leak}}\left(\frac{1}{x_{q0} \cdot F_{q0}} \cdot \frac{B_r}{\mu_0} \frac{l_{a,pu}}{f_{qn}} \frac{a}{2}\right)\right] y - 1} \cdot \frac{4(S_1 l_1 + S_2 l_2 + \cdots + S_{mn} l_{mn})}{a^2} \tag{6.35}$$

If y is equal to one (that is, there is no difference between l_k and l_{mk}, as in case of "standard" PM-Assisted SR rotor designs), the magnets are required to occupy a portion S_{mk}/S_k of the respective flux barrier width equal to (6.36).

$$\left.\frac{S_{mk}}{S_k}\right|_{y=1} = \frac{1}{\left[\frac{1}{k_{leak}}\left(\frac{1}{x_{q0} \cdot F_{q0}} \cdot \frac{B_r}{\mu_0} \frac{l_{a,pu}}{f_{qn}} \frac{a}{2}\right)\right]} = k_{leak} \cdot \frac{x_{q0} \cdot F_{q0}}{\frac{B_r}{\mu_0} \frac{l_{a,pu}}{f_{qn}} \frac{a}{2}} = \frac{k_{leak}}{k_{M/Fq}} \tag{6.36}$$

When y = 1, the split ratio S_{mk}/S_k (6.36) depends directly on the factor k_{leak}.

Even if the relationship between S_{mk}/S_k and k_{leak} will not be so straightforward with y < 1, Equation (6.36) suggests that PMs quantity minimization purposes are more difficult to achieve with higher q-axis leakage fluxes to be compensated for.

Thus, according to the curves reported in Figure 6.5, machines with too thick per-unit airgaps (g/a > 2%) do not represent a convenient class of PMASR designs.

In (6.36), it has also been highlighted that, with "standard" rare-earth Magnet Assisted SR motors (i.e., y = 1), S_{mk}/S_k is decided mainly by the ratio between the stator q-axis mmf and the peak value M (6.37) of the magnets mmf.

$$M = \frac{B_r}{\mu_0} \frac{l_{a,pu}}{f_{qn}} \frac{a}{2} \tag{6.37}$$

This correlation has been (inversely) represented via the factor $k_{M/Fq}$ (6.38), that will be recalled many times in the following.

$$k_{M/Fq} = \frac{\frac{B_r}{\mu_0} \frac{l_{a,pu}}{f_{qn}} \frac{a}{2}}{x_{q0} \cdot F_{q0}} \tag{6.38}$$

When dealing with "Naturally Compensated" machines (i.e. x_{q0} = 1), the ratio $k_{M/Fq}$ introduces also an easy relationship between the required magnet heights S_{mk} and the target shear stress level σ_0, which depends on F_{q0} according to (6.39):

$$\sigma_0 = bB_{fe} \cdot A_{q0} = \frac{\pi}{2} bB_{fe} \cdot \frac{F_{q0}}{a} \tag{6.39}$$

As for "Non-Naturally Compensated" PMASR designs, the $k_{M/Fq}$ factor does still stand for a strict link between the willed shear stress and the PMs design, but the relationship is more complicated than (6.39).

Further information about this topic can be found in Chapter 05.

In any cases, depending on the compensation factor x_{q0} (implicitly represented by the ratio $k_{M/Fq}$) and the rotor geometry of the starting SR design (namely, S_k and l_k), the rare-earth magnet volume to be provided for with "typical" Magnet ASR machines that have $y = 1$ is (6.40):

$$V_{m,pu}\big|_{y=1} = \frac{k_{leak}}{k_{M/Fq}} \cdot \frac{4(S_1 l_1 + S_2 l_2 + \cdots + S_{mn} l_{mn})}{a^2} \tag{6.40}$$

Thinking about alternative solutions, the minimum value y_{min} (6.41) that might be associated to y is the one that makes the needed S_{mk} equal to S_k according to (6.33).

$$y_{min} = \frac{k_{leak}}{k_{M/Fq}} \tag{6.41}$$

This choice, that is designing thinner rotor layers completely filled in with rare-earth magnetic material, leads to an overall PMs volume $V_{m,pu}$ (6.42) that is equal to the one required by "standard" PMASR rotor structures, with no savings.

$$V_{m,pu}\big|_{y=1} = V_{m,pu}\big|_{y=y_{min}} \tag{6.42}$$

It follows that somewhere in between the two extreme designs, i.e. $y = 1$ and $y = y_{min}$, the PM volume figure does have a minimum.

By deriving (6.35) with respect to y, the optimum thickness ratio y_{opt} (6.43) is found.

$$y_{opt} = \frac{2}{1 + \frac{k_{M/Fq}}{k_{leak}}} \tag{6.43}$$

It minimizes the necessary PMs volume (6.44), at given $x_{q0} \cdot F_{q0}$, starting SR rotor geometry and stator design.

$$V_{m,pu}\big|_{y=y_{opt}} = \frac{4}{\left(1+\frac{k_{M/Fq}}{k_{leak}}\right)^2}\cdot\frac{4(S_1 l_1 + S_2 l_2 + \cdots + S_{mn} l_{mn})}{a^2} \tag{6.44}$$

If compared to "typical" rare-earth based PMASR machines (y = 1), designs which show $y = y_{opt}$ allow to reduce the magnets volume as quantified by (6.45).

$$\frac{V_{m,pu}\big|_{y=y_{opt}}}{V_{m,pu}\big|_{y=1}} = 4\cdot\frac{\frac{k_{M/Fq}}{k_{leak}}}{\left(1+\frac{k_{M/Fq}}{k_{leak}}\right)^2} \tag{6.45}$$

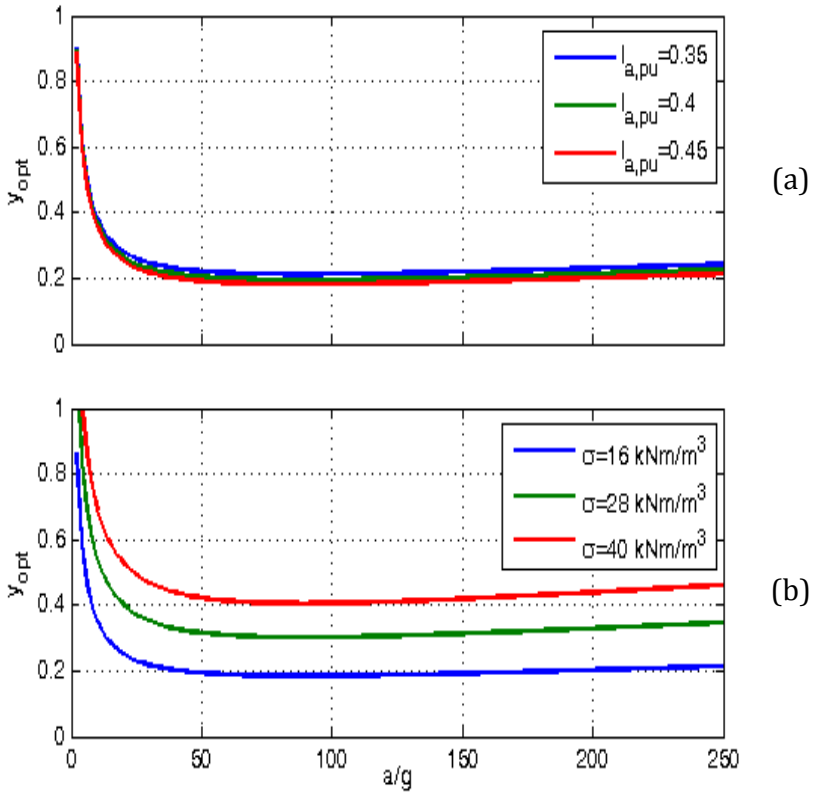

Figure 6.6 – Optimal thickness ratio y_{opt}, for PMs volume reduction, in "Naturally compensated" rare-earth based PMASR machines (n=3, n_r=14). The impact of the pole pitch to airgap ratio a/g (a, b), rotor magnetic insulation $l_{a,pu}$ (a), and target shear stress σ_0 (b) is highlighted. a) σ_0 is 28 kN/m²; b) $l_{a,pu}$ is 0.35.

In (6.43) and (6.45), the k_{leak} factor stands for the dependence of both the optimum y value and related volume saving on the pole pitch to airgap ratio a/g and further geometric variables, such as the stator tooth length factor l_t/r and the rotor magnetic insulation $l_{a,pu}$, that concur to determine the q-axis inductance.

Moreover, the presence of the $k_{M/Fq}$ ratio (6.38) in (6.41) and (6.43) points out that, in terms of PMs quantity reduction, the obtainable results vary according to the starting rotor geometry (namely, again $l_{a,pu}$), the magnet properties (read, B_r), the desired airgap shear stress and, thus, the selected mmf to be compensated for.

Figure 6.6 reports the optimal thickness ratio y_{opt} (6.43) for magnets volume reduction, as a function of the pole pitch to airgap ratio a/g, with reference to a family of "Naturally Compensated" PMASR machines with three rotor flux barriers and 14 rotor slots per pole pair. The impact of both the rotor magnetic insulation and target shear stress is addressed.

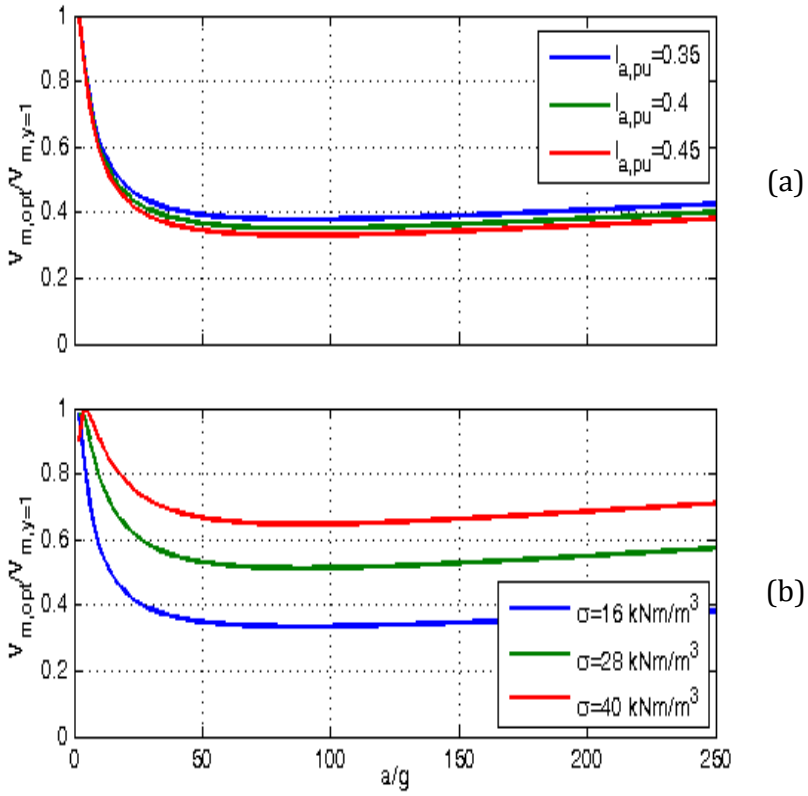

Figure 6.7 – Magnets volume saving in correspondence of the optimal thickness ratio y_{opt}. The plots are referred to "Naturally compensated" rare-earth based PMASR machines with n=3, n_r=14, as an example. The impact of the pole pitch to airgap ratio a/g (a, b) rotor magnetic insulation $l_{a,pu}$ (a) and target shear stress σ_0 (b) is highlighted. a) σ_0 is 28 kN/m²; b) $l_{a,pu}$ is 0.35.

Figure 6.7 puts in evidence the volume saving (6.44) obtainable by posing $y = y_{opt}$, while presenting the results in per-unit of the PMs volume that would have been needed if the same "Naturally Compensated" motor was designed in an "ordinary" way with the

PMs being as long as the respective flux barriers.

Once again, Figures 6.6 and 6.7 confirm the unfeasibility of Magnet Assisted SR designs with too thick per-unit airgaps, revealing that the area of main interest for the final design is in the range $50 \leq a/g \leq 150$. There, the stator slot leakage fluxes, the PMs are demanded to counteract, can be conveniently reduced.

In this area of practical use for the design, both the optimum y value and the consequent volume (and cost) saving show a nearly asymptotic behavior.

As it can be seen in Figures 6.6 and 6.7, the normalized rotor magnetic insulation $l_{a,pu}$ does not seem to affect the optimal designs in a significant way.

Conversely, the role played by the target shear stress is relevant.

The more the demanding shear stress is increased, the more the optimal thickness ratio y_{opt} grows up. The optimization procedure is more effective, leading to larger percent savings of magnetic material, when the optimized rare-earths Assisted SR machine is less heavily loaded. Yet, also in case of more competitive shear stress figures (e.g. 40 kN/m^2) the magnets volume can be reduced in a satisfactory way.

This is to say that the curves reported in Figure 6.7 do represent relevant results with respect to the optimization purposes of this analysis. However, the constraints introduced by demagnetization issues still have to be identified, together with their impact on the achievable saving of magnetic material.

6.2.1. Risk of demagnetization in case of overload currents

The demagnetization risk is now considered.

In fact, PMs with minimized area (that is, $y = y_{opt}$) are significantly thinner than the ones of respective "standard" designs with $y = 1$ and then are more prone to irreversible demagnetization.

Among all the possible rare-earths Assisted SR machines with reduced magnet volume (namely, the ones corresponding to $y_{min} \leq y \leq 1$), the feasible designs only will be selected, depending on the prescribed overload current that usually varies from one

application to another.

Taking advantage of the equivalent circuit of Figure 6.3, the linear equations (6.16) solve the relationship between the mmfs and parameters that are in the q-axis magnetic model. Accordingly, the PMs working flux density B_m (6.45) in correspondence of a fixed overload current ($k_o \cdot I_q$) oriented against the PMs can be predicted.

$$B_{m,pu} = \frac{B_m}{B_r} = \frac{1 + \frac{2\pi^2}{n_r} p_b \frac{g}{a}\left(1 - \frac{S_{mk}}{S_k}\right) - \frac{k_o}{k_{M/Fq}}}{1 + \frac{2\pi^2}{n_r} p_b \frac{g}{a}\left(1 - \frac{1-y}{y} \cdot \frac{S_{mk}}{S_k}\right)} \tag{6.45}$$

The magnets working flux density $B_{m,pu}$, expressed in per-unit of the remanence value B_r, results a uniform value for all the PMs thanks to the geometric rules introduced in Subsection 6.1.3.

For the derivation of (6.45), the reader is recommended to recall the procedure deeply described in Chapter 04.

$$B_{m,pu} = B_{m0,pu} - \frac{k_o}{k_{M/Fq}} \cdot \frac{1}{1 + \frac{2\pi^2}{n_r} p_b \frac{g}{a}\left(1 - \frac{1-y}{y} \cdot \frac{S_{mk}}{S_k}\right)} \tag{6.46}$$

In (6.46), it has been evidenced that the presence of a stator mmf $k_o \cdot F_q$ (= $k_o \cdot x_{q0} \cdot F_q$), oriented against the PMs, intervene to reduce the flux density of the magnets with respect to the working condition $B_{m0,pu}$ at no load.

Generally speaking, in presence of a certain q-axis overload current ($k_o \cdot I_q$), the PMs working flux density B_m depends on:

- the pole pitch to airgap ratio a/g;
- the starting SR rotor geometry, which decides p_b (via S_k and l_k) together with n_r;
- the ratio $k_{M/Fq}$ which embodies the dependence on the willed shear stress;
- the overload factor k_o;
- the selected thickness ratio y, which determines S_{mk}/S_k, besides being directly involved in (6.45)-(6.46).

As an example, Figure 6.8 considers “Naturally Compensated” machines designed via

a "typical" procedure that fixes y equal to one and shows how the design parameter affects the magnets flux density.

In Figure 6.8, the PMs working flux density $B_{m,pu}$ (6.45) is evaluated, with the ratio a/g varying.

The required span ratio S_{mk}/S_k is properly fixed by substituting the "Compensation" condition (6.33) in (6.45). In order to quantify $B_{m,pu}$, it is also supposed that an adequate magnetic insulation ($l_{a,pu}$ = 0.3) is provided for the starting SR rotor. Its flux barriers (n = 3, n_r = 14) are assumed to be circular, for modeling purposes.

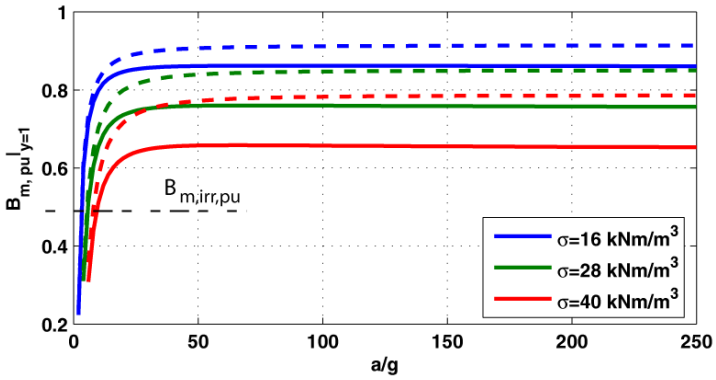

Figure 6.8 - PMs working flux density of "standard" (y = 1) "Naturally compensated" rare-earth based PMASR machines. n = 3, n_r = 14, $l_{a,pu}$ = 0.3. The impact of the pole pitch to airgap ratio a/g and target shear stress σ_0 is highlighted. Dashed curves refer to k_o = 1.2, continuous ones stands for k_o = 2.

In Figure 6.8, various shear stress target levels are considered and two different overload factors are taken into account. Continuous lines, which refer to k_o = 2, are typical of automotive applications, whereas having k_o close to one (as for dashed curves) is representative of common specifications for wind turbine generators.

From Figure 6.8, it is evident that the $B_{m,pu}$ curves tend to asymptotic values if the a/g ratio is larger than 50, whatever the overload current factor and rated shear stress levels are.

Analogous conclusions can be drawn also for PMASR machines designed with a reduced thickness ratio y. So, it is worth carrying on the analysis focusing only on this area, i.e. $50 \leq a/g \leq 150$, that has been revealing of main interest for the design also under many other points of view.

With $50 \leq a/g \leq 150$, the resulting relationship (6.45) between the selected thickness ratio y and the PMs working flux density $B_{m,pu}$ is plotted in Figure 6.9, where a class of "Naturally Compensated" machines designed for delivering different shear stress values at rated condition and withstanding different current levels at overload are compared.

The charts in Figure 6.9 help the designer to identify a lower limit (y_d) for the thickness ratio, capable of guaranteeing that the PMs working condition at overload is compliant with the flux density $B_{m,irr}$ which rare-earths grade can bear up without running up against irreversible demagnetization.

The constraint $B_{m,irr}$ is determined by the PM material datasheet, of course, and the worst case operating temperature has to be considered. Differently from ferrite magnets, as for rare-earth PMs, hot operating temperatures (e.g. 130°C) are the most critical in terms of demagnetization risk. By introducing a convenient margin, it can be considered that the only PMASR designs to be feasible are the ones that take the PMs flux density to 50% of the respective remanence value (namely, $B_{m,irr,pu} = 0.5$), in case of the worst case demagnetizing current and maximum operating temperature.

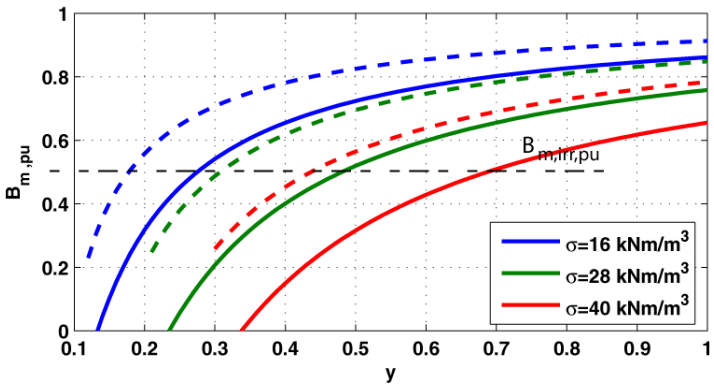

Figure 6.9 - PMs working flux density versus thickness ratio. "Naturally compensated" rare-earth based PMASR machines, designed with the a/g ratio larger than 50, are considered. n = 3, n_r = 14, $l_{a,pu}$ = 0.3. The rated shear stress σ_0 is a parameter. Dashed curves refer to k_o = 1.2, continuous ones stands for k_o = 2. The demagnetization limit $B_{m,irr,pu}$ is indicated.

According to this $B_{m,irr}$ constraint, the "conventional" machines of Figure 6.8 with the magnet pieces as long as the rotor flux barriers are always safe in the area of practical use for the design (namely, $50 \leq a/g \leq 150$). Conversely, Figure 6.9 highlights that, even

if the pole pitch to airgap ratio is selected properly, the y factor cannot be freely chosen, when the magnets must be preserved from irreversible demagnetization at overload.

In particular, Figure 6.10a reports the lower limit y_d that constrains the choice of the thickness ratio according to demagnetization issues as a function of the target shear stress at rated condition.

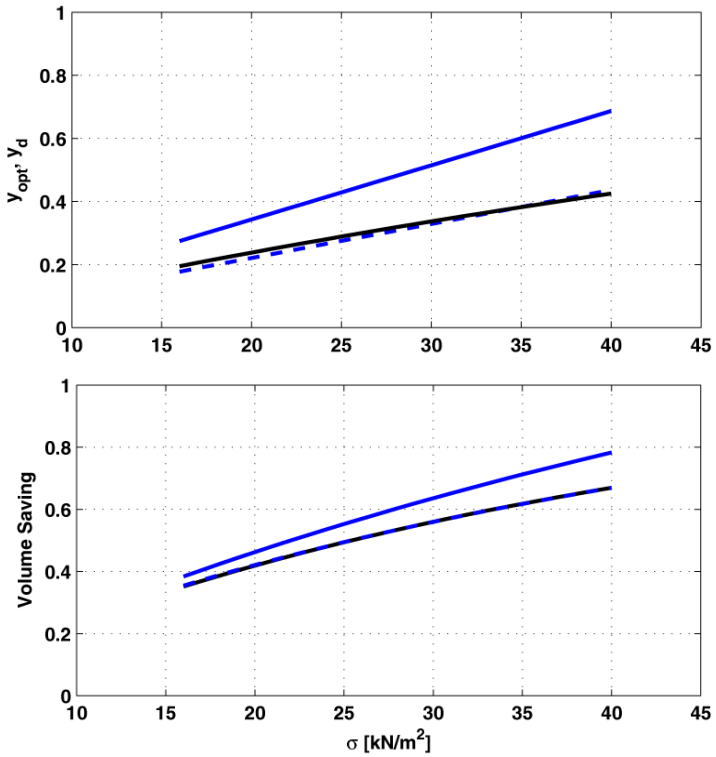

Figure 6.10 – Lower y limit for the magnets to be safe in terms of demagnetization (a, blue curves) and related volume saving with respect to "standard" PMASR designs (b, blue curve). Dashed curves refer to k_o = 1.2, continuous ones stands for k_o = 2. The black lines in (a) and (b) represent the optimal thickness ratio y_{opt} (6.43) and maximum volume saving (6.45), respectively. The plots are representative of "Naturally Compensated" PMASR machines.

In Figure 6.10, the PMASR machines are supposed to be "Naturally Compensated". The overload current factor is considered as a parameter. The plots in Figure 6.10a refer to pole pitch to airgap ratios larger than 50 and compare the limit y_d with the optimum thickness ratio (6.43) for PMs volume reduction, showing that the magnets quantity can be actually minimized only in some cases.

The PMs volume that can be saved by comparing both "y_d" designs and "y_{opt}" ones to common rare-earths Assisted SR machines having y = 1 is reported in Figure 6.10b. So

the severity of demagnetization constraints is quantified, depending on the overload factor. From Figure 6.10b, it turns out that the reduction in the PMs area with respect to "standard" rotor laminations is noteworthy even for PMASR machines designed to withstand very heavy overloads without having the magnets irreversibly demagnetized.

6.2.2. Effect of structural ribs

A more realistic model of the rotor flux barriers must include the mechanical ribs, as depicted in Figure 6.11.

The model gets formally more complicated, but the design of the PM flux to assist SR rotor structures cannot disregard the effect of magnetic bridges, since they shunt a significant fraction of the flux produced by the magnets.

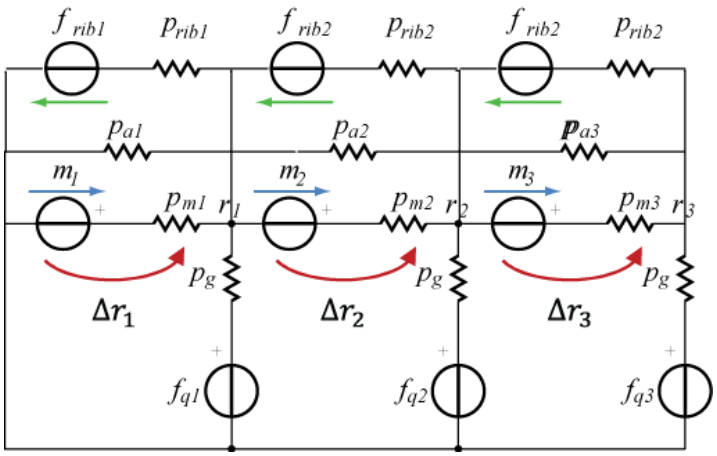

Figure 6.11 - The equivalent circuit represents the *q*-axis magnetic behavior of half a pole. It refers to the PMASR example rotor in Figure4.1 (*n*=3). The magnetic structural ribs are modeled and the whole flux barrier (namely, "magnet" + "air") is represented by a unique equivalent circuit (m'_{123}, p_{b123}).

As shown by Figure 6.11, the outer structural ribs and possibly the internal mechanical bridges of each layer are represented in the circuital model simply by the series of one equivalent mmf $f_{rib,k}$ (6.47) and an equivalent permeance $p_{rib,k}$ (6.48).

$$f_{rib,k} = \frac{B_{rib0}}{\mu_{r,rib} \cdot \mu_0} l_{rib,k} \cdot \frac{1}{F_q} = \frac{B_{rib0}}{\mu_{r,rib} \cdot \mu_0} k_{rib,l} \cdot l_k \cdot \frac{1}{F_q} \tag{6.47}$$

$$p_{rib,k} = \mu_{r,rib} \frac{S_{rib,k}}{l_{rib,k}} = \frac{S_k}{l_k} \cdot \frac{k_{rib,S}}{k_{rib,l}} \cdot \mu_{r,rib} \tag{6.48}$$

The rib thickness $S_{rib,k}$ and length $l_{rib,k}$ do represent actual geometrical quantities (that is, the width and length of the k-rib) when outer structural bridges only are designed. If also the internal ones are required, $S_{rib,k}$ and $l_{rib,k}$ get equivalent value, representative of the effects produced by both the mechanical ribs on the magnetic behavior of each barriers.

In any cases, as suggested by (6.47) and (6.48), it is convenient to express both the rib length $l_{rib,k}$ and width $S_{rib,k}$ in per-unit of the respective barrier length l_k and width S_k via the factors $k_{rib,l}$ and $k_{rib,S}$, since normalized quantities are always more useful when developing a general analytical theory.

B_{rib0} and $\mu_{r,rib}$ in (6.47) refer to the adopted steel grade and are derived from the saturated part of its magnetic characteristic, as suggested in Chapter 05 (Subsection 5.1.3.1) under the underlying assumption that all the ribs are saturated at all working conditions (load and no load) of the machine at a reasonable value (e.g. 2 T) coming from experience.

With some manipulations, the superposition of the flux barrier model (6.8) - (6.9) and the ribs one (6.47) - (6.48) can be seen as a Thevenin equivalent, that has again the form of a PM-generated mmf m_k^* (6.49) and an equivalent permeance p_{bk}^* (6.50).

$$p_{bk}^* = p_{bk} + p_{rib,k} = \frac{S_k}{l_k} \cdot \left(1 + \frac{k_{rib,S}}{k_{rib,l}} \cdot \mu_{r,rib} + \frac{1 - y_k}{y_k} \cdot \frac{S_{mk}}{S_k}\right) \tag{6.49}$$

$$m_k^* = \frac{1/\mu_0}{\frac{S_k}{l_k} \cdot \left(1 + \frac{k_{rib,S}}{k_{rib,l}} \cdot \mu_{r,rib} + \frac{1-y_k}{y_k} \cdot \frac{S_{mk}}{S_k}\right)} \cdot \left(B_r \cdot S_{mk} - B_{rib0} \cdot S_{rib,k}\right) \tag{6.50}$$

It follows that the effect of structural bridges is to modify the "Compensation" condition (6.30), compelling the designer to equal the product $k_{leak}\,\boldsymbol{\Delta f_q}$ to the equivalent mmfs $\boldsymbol{m^*}$ instead of the flux barriers ones $\boldsymbol{m'}$.

In formula, relationship (6.51) has to be matched:

$$m_k^* = k_{leak} \cdot \Delta f_k \tag{6.51}$$

As a consequence, each flux barrier is required to be filled in with a larger quantity (6.52) of magnetic material.

$$\frac{S_{mk}}{S_k} = \frac{y \cdot \left[1 + \frac{k_{rib,S}}{k_{rib,l}}\left(1 + \frac{1}{k_{leak}}\frac{1}{x_{q0} \cdot F_{q0}}\frac{B_{rib0}}{\mu_{r,rib} \cdot \mu_0}\frac{k_{rib,l} \cdot l_{a,pu}}{f_n}\frac{a}{2}\right)\right]}{\left[1 + \frac{1}{k_{leak}}\left(\frac{1}{x_{q0} \cdot F_{q0}} \cdot \frac{B_r}{\mu_0}\frac{l_{a,pu}}{f_{qn}}\frac{a}{2}\right)\right] y - 1} \tag{6.52}$$

Equation (6.52) says that, in order to compensate for the flux shunted by the saturated ribs and thus actually output the desired shear stress, the ratio S_{mk}/S_k has to augmented with respect to (6.33). Of course, it implies an increment of the overall magnets volume.

However, this does not change neither the value of the optimal thickness ratio for PMs quantity minimization nor the percent saving of volume when optimized PMASR machines ($y = y_{opt}$ or $y = y_d$) and "standard" PMASR ones ($y = 1$) are compared to each other.

Furthermore, it is not worth to evaluate the impact of magnetic ribs on demagnetization issues, since disregarding the role played by the additional branch ($f_{rib,k}$, $p_{rib,k}$) in the circuit of Figure 6.11 does represent a conservative approximation.

6.3. FEA COMPARISON OF ROTORS WITH DIVERSE PMs VOLUME

Starting from a common set of specifications typical of traction drive trains, three diverse rare-earths Assisted SR rotors have been designed with reshaped magnets, for evaluating the effect of the proposed design optimization on the achievable performance.

TABLE 6-II
TRACTION DRIVE DESIGN EXAMPLES - SPECIFICATIONS

DESIGN OF THE ROTATING MACHINE – INPUT QUANTITIES		
Target Torque T_0	125	Nm
Nominal speed n	3500	rpm
Stack length l	0.170	m
Stator radius r	0.108	m
Airgap g	0.7	mm
Upper limit for specific loss k_{j0}	20000	W/m^2
Operating temperature	130	°C

Table 6-II provides a detailed list of the design requirements, namely the geometric and performance ones, together with the operating temperature. All the concurrent designs are required to deliver the same torque, at comparable rated current levels, with

the stack envelope constrained. The input quantities of Table 6-II are similar to the ones used for testing the approach to the optimization of both SPM and FASR rotor configurations. So, an exhaustive comparison between all the alternative technologies analyzed in this work can be carried out. It will be done in the next Chapter.

In Figure 6.12, the three rotor (and stator) drawings that will be compared are presented.

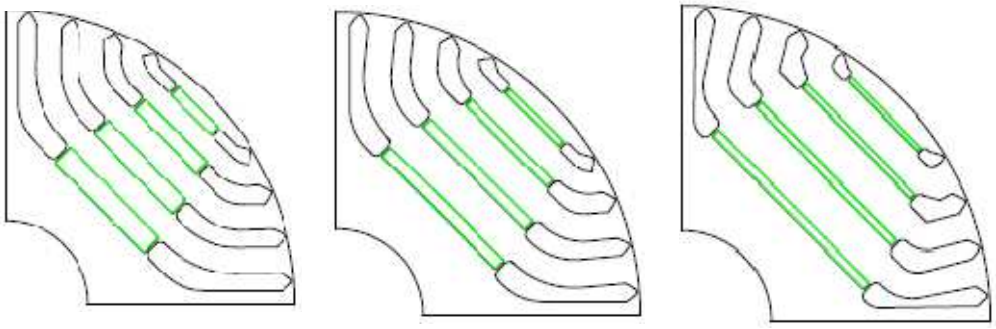

(a) (b) (c)

Figure 6.12 – Different rotor lamination derived from the same starting SR design. a) "Standard" configuration with y=1; b) "Safe" design with $y=y_d$; c) "Optimal" design for PMs quantity minimization ($y=y_d$).

They are all rare-earth based Magnet Assisted SR machines with two pole pairs, a four-layer rotor structure and a distributed stator winding with q = 4. The stator tooth length factor is about 15% of the outer stator radius. The PM grade is 1.12 T at 20°C. The data in Table 6-III put in evidence the whole set of parameters that associate the three machines under comparison.

Rather, the three PMASR designs of Figure 6.12 do differ for the rotor lamination.

Figure 6.12a is the most "standard" motor, which have the magnets as long as the respective flux barriers and will be addressed in the following as *design 1*. Conversely, for both the machines in Figure 6.12b and 6.12c, the thickness ratio is smaller than one. The rotor of Figure 6.12b (i.e., *design* y_d) has $y = y_d$ to say that y has been chosen to prevent the PMs to be irreversibly demagnetized at overload current and maximum operating temperature (130°C). Last, Figure 6.12c shows *design* y_{opt}, that is the optimal configuration in terms of PMs quantity minimization (in other words, y is chosen to be equal to y_{opt}).

Despite the differences in the rotor laminations of Figure 6.12, structural ribs have the same dimensions in all the machine configurations. In fact, no significant variation in mechanical stress arises from modifying the shape of the magnets and filling the free space with steel when using rare-earth PMs, that have nearly the same mass density of silicon steel.

TABLE 6-III
TRACTION DRIVE EXAMPLES – DESIGN PARAMTERS

STATOR DESIGN PARAMETERS				
	Design 1	*Design* y_d	*Design* y_{opt}	
Yoke per-unit width b	0.63			
No-load back-iron flux density B_{fe}	1.3			T
Tooth width factor k_t	0.78			
STATOR WINDING AND SLOTTING EFFECT				
Slot per pole per phase q	4			
Winding factor k_w	0.92			
End connections factor k_{end}				
Carter coefficient k_c	1.12			
ROTOR DESIGN PARAMETERS				
Rotor slots per pole pair n_r	20			
Rotor flux barriers n	4			
Per-unit rotor insulation $l_{a,pu}$	0.3			
MATERIAL				
Magnet grade B_r	1.12			T
GEOMETRICAL DESIGN CHOICES				
Pole pairs p	2			
Per-unit tooth length l_t/r	15.2			%
Rotor diameter 2r'	0.0702			m

In all cases (*design 1, design* y_d, *design* y_{opt}), the PM flux has been reinforced with respect to the "Natural Compensation" condition in order to enhance the flux weakening capability of the drive, also at overload condition. The just mentioned design strategy, which corresponds to a value x_{q0} smaller than one, will be deeply discussed in the next Chapter and has to be properly handled in order to arrange the design parameters so to make the ultimate design output the willed torque. At this purpose, useful formulas can be found out in Chapter 05.

The three designs under comparison, derived via the model developed so far, have

been FEA validated.

The results are in Table 6-IV.

From the data in Table 6-IV, it is evident that all the rare-earth Magnet Assisted SR machines are capable of providing for the willed torque. *Design* y_d and *design* y_{opt} do have the same rated current, whereas the most "classic" machine *design 1* requires a slightly higher current level to deliver the target shear stress. It occurs because the iron flux paths around the PM area are less loaded in machines with thinner magnets, thus preventing local field saturation effects that concur to deteriorate the machine torque capability. This phenomena is even more evident at overloads.

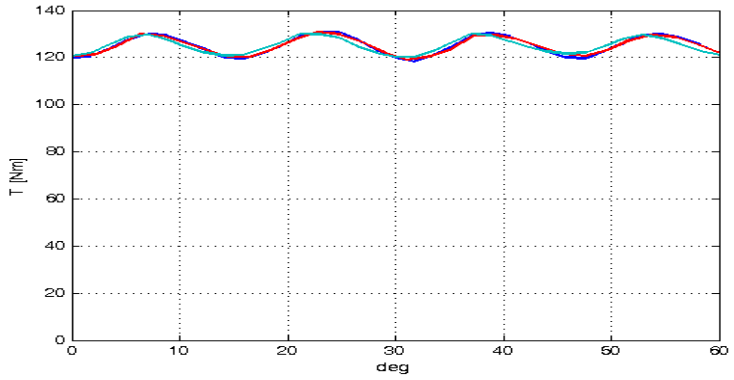

Figure 6.13 – Torque versus rotor angular position at rated condition. The three designs in Figure 6.12 are compared.

TABLE 6-IV
TRACTION DRIVE EXAMPLES – MAGNETS GEOMETRY AND FEA EVALUATED PERFORMANCE

MAGNETS GEOMETRY				
	Design 1	*Design* y_d	*Design* y_{opt}	
Thickness ratio y	1	0.39	0.34	
Magnet volume V_m	262	158	153	cm^3
FEA EVALUATED PERFORMANCE				
Rated torque T	125			Nm
Rated current I	246	240	240	Apk
PM flux linkage λ_m (130°C)	0.064	0.076	0.093	Vs
Short circuit current I_{ch}	268	266	260	Apk
Overload current I_o	415			Apk
PMs flux density (I_o, 130°C)	0.73	0.5	0.25	

Further notes about the machines performance at rated condition can be shortly

evidenced.

Torque ripple has been FEA evaluated (see figure 6.13): it is always small and substantially equal for all designs. Concerning iron losses, the FEA analysis did not show any appreciable variation among the various machines.

If demagnetization issues was disregarded, *design* y_{opt} would save a lot of magnetic material (−71%) without loss of performance, except for the no-load voltage increase. In fact, its PM flux is the highest one. The feasible machine *design* y_d still obtains a significant magnet saving (−66%), with a less penalizing increase in the no-load voltage, if compared to *design 1*.

Since all the compared motors have the same characteristic current according to the design assumptions and FEA validation in Table 6-IV, a higher back electromotive force (read, a higher no load flux linkage) indicates a higher *q*-axis inductance. This is to say that machines with less magnets (i.e. less magnetic insulation in the rotor structure) have a lower saliency and, consequently, a higher uncontrolled generator voltage for the same performance.

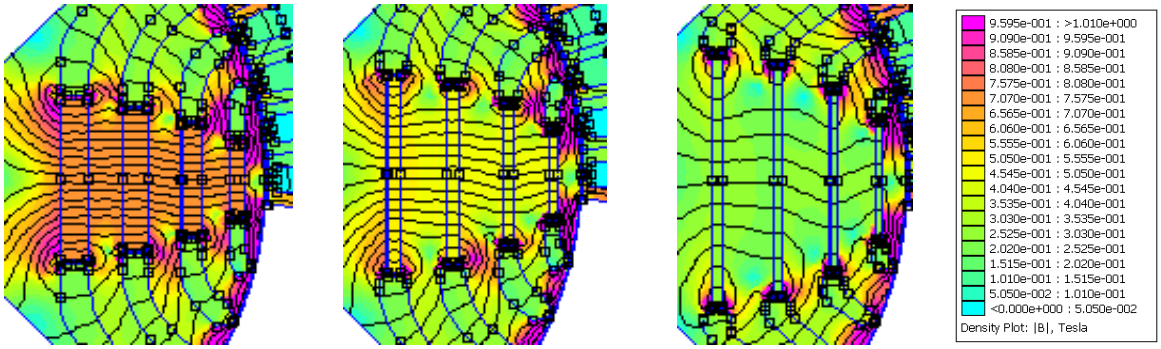

(a) (b) (c)

Figure 6.14 – Flux density maps of the three designs under comparison in worst case demagnetizing condition, that is: maximum operating temperature and maximum overload current (415 Apk) oriented against the PMs. a) *Design 1*; b) *Design* y_d; c) *Design* y_{opt}.

For the three considered designs, the magnets' working points are FEA evaluated at overload condition in correspondence of the maximum operating temperature. The chosen overload current vector, 415 Apk wide, means that Joule losses are three times larger than the nominal one. For the analysis, this current vector is oriented against the

magnets, as a worst case demagnetizing condition.

Table 6-IV reports the uniform flux density of the magnets in the four rotor layers and the maps in Figure 6.14 confirm that all the PMs work at very similar flux densities, with no weaker spots.

As forecast by the model, *design* y_d is safe, since it shows a uniform flux density around 0.5 T in each magnet (the PMs remanence B_r at 130°C is 1 T). Conversely, it can be seen from Figure 6.14 that the optimal solution *design* y_{opt} is definitively affected by demagnetization, for standard rare-earth magnet grades at 130°C.

6.4. RECAP

In this Chapter, an analytical procedure has been defined for reducing the magnet quantity in rare-earths Assisted Synchronous Reluctance machines without affecting the performances, at rated and overload condition.

The proposed solution introduces a new degree of freedom in the design of this kind of motors, making the rare-earth pieces thinner and taller, while coping with the same demanding shear stress at rated condition and compensation factor of the basic reluctance flux.

A minimum PM volume design does exist, but it is not always feasible due to the risk of demagnetization at overload. Still, a strong PM volume reduction can be obtained, even at heavy overloads.

The model adopted to demonstrate the feasibility of the proposed technology is based on closed-form equations, that help to relate straightforwardly the main design parameters to the obtainable performance. The modifications to be applied to the rotor geometry in order to minimize the magnet volume according to the demagnetization constraint are also easily addressed.

Machines with modified rotor laminations for PMs volume (and cost) reduction show mitigated local saturation in the rotor flux channels, leading to reduce cross-saturation and the needed *d*-axis magnetizing current. It results in better efficiency figures, especially at overload currents.

The PM modifications tend to increase the no-load voltage and reduce the saliency of the machine, which is anyway far larger than enough for sensorless control due to the SR-like rotor.

Practical design examples for a specified drive train have been discussed and FEA validated.

Chapter 07

Practical design examples in different application fields

It is widely recognized that Permanent Magnet Synchronous machines are attractive candidates for many up-to-date applications and a lot of efforts have been doing in the past 30 years for further enhancing this technology. The proposed work aims at fitting in this challenging scenario and, in the following, both the strengths and limitations of the machine configurations analyzed so far will be highlighted, remarking key engineering tradeoffs that are of practical use when developing such designs for different application fields.

In particular, the comparison will focus on direct-drive applications, that represents one of the broad areas in which PM machines have been achieving growing success during recent years. Direct-drive machines are distinguished by the fact that intermediate gears, belts, or other types of mechanical transmission components are eliminated between the machine and the connected load. It assures obvious benefits, such as the elimination of the weight, volume, cost, noise, and reliability risks associated to the speed-changing components. In exchange for these advantages, the electrical machine is typically required to output higher torque at a lower speed, resulting in a larger and heavier stack envelope. Anyway, PM machines are sufficiently attractive that the direct-drive configuration is getting the dominant solutions for a wide range of application fields. Among them, it is worth recalling appliance white goods, HVAC (heating, ventilating and air conditioning), power generation from renewable resources and electrified transportation.

In particular, in this Chapter, typical requirements for electrical motor drives for

both production from renewable (wind) energy and automotive applications will be summarized and practical design examples will be presented.

The results of the comprehensive approaches proposed to design SPM machines, Ferrite Assisted SR motors and Rare-earth PM-based ASR machines with a minimized magnets volume will be collected together and deeply discussed. An exhaustive comparison between the performance of such PM machines, with different rotor and stator configurations, will be carried out as well, looking for the most suited solution for each application, also in terms of cost reduction.

According to recent research works, PM machines of the Surface Mounted type are preferably equipped with non overlapping windings for better manufacturability, shorter end connections and potential flux weakening capability. However, it is recognized that concentrated windings reduce the saliency of any Magnet-Assisted rotor structures and thus the specific advantages, related to the reluctance torque component of this kind of motors, are partially compromised. For these reasons, the comparative analysis will focus primarily on SPM machines with concentrated windings and SR machines, having multi-layer rotor structures and assisted by either a minimized amount of rare-earth magnets or ferrite PMs, with distributed windings. In other words, the machine types that will be compared are at the opposite sides of the spectrum, in terms of manufacturing complexity. Even if many other combinations, such as for example simpler IPM rotor configurations equipped with fractional slots stators, stay in between the two machine types considered here, the selected examples are absolutely significant, while introducing state of art solutions (SPM machines), as reference competitors to reduced-cost alternatives, such as FASR motors and Rare-earth Assisted SR ones with a minimized volume of magnets.

7.1. LARGE WIND TURBINE GENERATORS

Wound-rotor induction machines represent an established technology, when dealing with wind power plants characterized by ratings of the installed generators greater than 1 MW. Anyway, there is a major technology thrust underway to adopt direct-drive PM generators for wind turbines, especially the larger one and with a focus on offshore

applications. Several international wind turbine manufacturers are actively developing new direct-drive PM generator technology, and one example is shown in Figure 7.1 [75].

Figure 7.1 – Typical structure of an offshore wind turbine. The example, that is a direct-drive PM generator rated 4.1 MW, refer to [75].

Direct-drive is appealing for wind turbine applications especially because the gearbox that is eliminated from conventional configurations has been a relevant source of reliability problems in current equipment. However, direct-drive PM configurations pose their own significant challenges when dealing with the design of such generators.

This issues will be schematically discussed in the next subsection, which will highlight typical requirements of large direct-drive wind generators and, thus, the main criteria, the comparative analysis that follows will refer to.

7.1.1. Main requirements for direct-drive wind power generators

In order to allow a higher penetration of direct-drive wind turbines in the marketplace, structural issues associated for example with maintaining small airgaps at large rotor diameters need to be addressed and, above all, three performance indicators must be optimized. They are:

- the torque per volume factor and the total mass of the generator;
- the ratio between torque and cost (read, operation and installation costs);
- the reduction of noise and torque oscillation at rated condition.

The first criteria, that have been identified as being of great importance for further enhancing this technology, say that designers and manufacturers are compelled to build

electrical PM generators for wind turbines able to deliver the willed torque in a compact volume and mass, so to facilitate transportation and installation problems. Torque density has been chosen as reference performance indicator, instead of power density, because it is independent on the choice of the rotating speed.

The second feature, that is the ratio between torque and cost, is particularly critical for the acceptance of direct-drive wind generators in the market. As for the installation cost, this issue is strictly related to the mass reduction purposes, and, in particular, solutions that make use of reduced-cost materials (e.g. ferrite magnets) instead of expensive ones (e.g. rare-earth based PMs) are preferable, especially when they do not lead to worse performance of the system. Regarding the operation costs, high efficiency levels are representative of low operation charges and are usually required in such applications.

Last, reducing torque pulsations in PM machines to be installed in wind turbines power plant has also received significant attention in recent years and sometimes severe specifications might be met when approaching this concern.

7.1.2. Design examples

The target performance, common to all the design examples presented here, is the one of a direct-drive wind power generator, rated 2 MW at 15 rpm. All the machine examples have been arranged to deliver the same continuous torque, that is 1273 kNm, in the same volume, defined by the stator diameter (1.97 m) and the stack length (1.5 m). Taking into account that the wind turbine is actually cooled by direct ventilation from the wind, the overall specific loss, including the Joule contribute, the PMs and iron loss, needs to be kept under the upper limit k_{j0} = 7500 W/m^2 not to exceed the maximum steady state operating temperature, intended to be 115°C.

All these specifications are collected in Table 7-I for convenience.

The three SPM example geometries, which are sketched in the left-hand side of Figure 7.2, have been designed following the flowchart proposed in Chapter 03 and they were first introduced, always in Chapter 03.

Different stator winding configurations are compared: *design 1* is a single layer concentrated winding SPM machine with a number of stator slot per pole per phase equal to 2/5; *design 2* is again a fractional slot winding PM machine of the Surface-Mounted type (q=2/5), but it is equipped with double layer stator windings; *design 3* is a SPM wind generator with distributed stator winding and the number of stator slots per pole per phase has been limited to one not to have too slender slots.

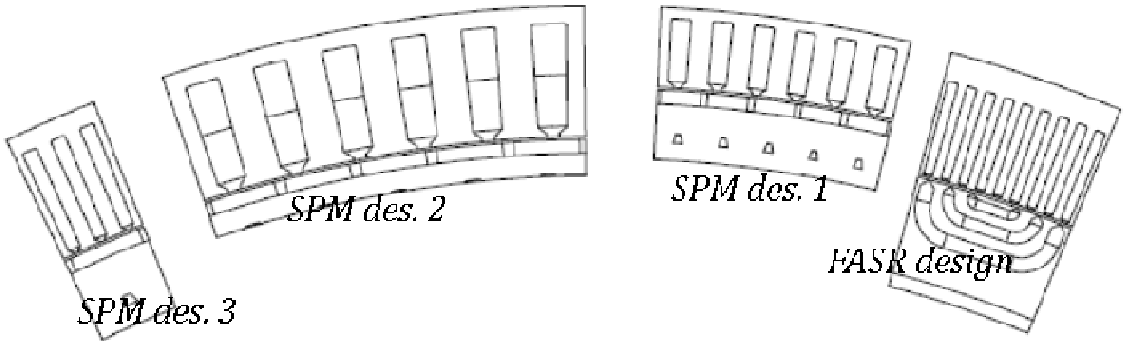

Figure 7.2 – Lamination of the four wind turbine generator design examples (r = 1.97 m, l = 1.5 m, Output power = 2 MW at 15 rpm,).

Also the FASR machine, designed according to the specifications listed at the beginning of this Subsection, has a distributed stator winding. This choice is justified by the need of fully exploiting the reluctance torque contribute, thus compensating for the low B-H energy products of ferrite magnets, since, in case of concentrated stator windings, the torque contribute, provided by the anisotropic rotor structure of PM Assisted SR machines, would be definitely compromised by the presence of a huge harmonic content in the stator mmf.

The ultimate design of the FASR wind generator, considered as an example in the following and reported in the right-hand side of Figure 7.2, has been defined according to the procedure developed in Chapters 04 and 05 for the optimal design of such PM machines.

Table 7-I summarizes the geometrical parameters and performances that distinguish the aforementioned design examples, namely the three SPM configurations and the FASR motor. The data come from the Finite Element Analysis, but it is worth recalling that, as it was demonstrated in the previous Chapters, the machine

performance can also be predicted by the proposed analytical formulas with little lack of accuracy, despite the simple nature of the closed-form model.

TABLE 7-I
WIND TURBINE GENERATOR DESIGN EXAMPLES

SPECIFICATIONS					
Target Torque T	1273				Nm
Nominal speed n	15				rpm
Stack length l	1.5				m
Stator radius r	1.97				m
Operating temperature	115				°C
STATOR WINDING AND SLOTTING EFFECT					
	SPM *des. 1*	SPM *des. 2*	SPM *des. 3*	FASR	
Slot per pole per phase q	2/5	2/5	1	3	
Winding factor k_w	0.97	0.93	1	0.96	
End connections factor k_{end}	1.06	1.04	1.30	1.33	
Carter coefficientk_c	1.08	1.11	1.06	1.05	
MATERIAL					
Magnet grade B_r	1.22	1.22	1.22	0.47	T
GEOMETRICAL DESIGN OUTPUTS					
Pole pairs p	85	50	45	24	
Per-unit tooth length l_t/r	4.6	7.5	7.9	7.0	%
Rotor radius r'	1.850	1.777	1.770	1.780	m
PERFORMANCE INDICATORS AT RATED CONDITION					
Current I	2.89	2.93	2.53	2.86	Apk
Line Voltage	577	577	577	577	Vpk
Power Factor	0.76	0.77	0.86	0.99	
Joule loss density k_j	4914	3554	3481	6720	W/m^2
Iron loss density k_i	961	992	979	585	W/m^2
PMs loss density k_{pm}	673	555	119	0	W/m^2
Total loss density	6548	5101	4579	7305	W/m^2
Efficiency	93.90	95.26	95.75	93.22	%
Stator mass	17.1	27.2	30.8	30.2	10^3kg
Rotor mass	2.00	4.14	3.46	7.27	10^3kg
Magnets mass	2.29	2.20	2.25	3.47	10^3kg
Total mass	21.4	33.6	36.5	40.9	10^3kg
Copper cost	61103	96580	125736	127460	USD
Iron cost	13103	21976	21414	24723	USD
Magnet cost	150476	144562	147847	17350	USD
Total cost	224682	263118	294997	169533	USD

Table 7-I reports also a price comparison for the four design examples. As a reference, the prices of the active materials have been fixed considering:

- copper 8.5 USD/kg;
- lamination 1.1 USD/kg;
- rare-earth PMs about 70 USD/kg;
- Ferrite PMs 7 USD/kg.

7.1.2.1. SPM machines with different stator windings configurations

As for *design 1*, as said, the number of slots per pole per phase is q = 2/5, since the analysis carried out in Chapter 03 put in evidence that this choice helps keeping the Power Factor of the machine within reasonable values, convenient in terms of size of the power converter and reduction of the load-dependent saturation effects in the stator back iron. *Design 1* is a "minimum inductance" machines, as it was better addressed in Chapter 03, and it has been designed for having a Power Factor value around 0.8. The design variables (p, l_t) have been properly combined to improve the machine efficiency, besides complying with the Power Factor target. As a result, the design output by the model, proposed in Chapter 03, results to have a satisfactory efficiency level, around 94%, while limiting both the mass and cost of active materials.

At the expense of an increased cost and weight of the active parts, *design 2*, that is a double layer concentrated winding machine again with q = 2/5, allows to achieve the Power Factor target (about 0.8) via a configuration, which is more efficient. *Design 2* is a "minimum inductance" SPM motor, always optimized in terms of efficiency, as it can be better understood by keeping in mind the design maps presented at the end of Chapter 03.

The distributed winding SPM example *design 3*, which has q = 1, has not been designed according to the "minimum inductance" condition, since the Power Factor is not critical at all, in this case. Rather, this SPM machine has been defined to obtain the same specific loss of *design 2* (i.e. the most efficient configuration, so far). Since the calculation was based on the model, which disregards the PMs loss and underestimates the iron one for the reasons evidenced in Chapter 03, eventually this distributed winding

machine turned out to be even more efficient than the "reference" one (*design 2*). This goal has been realized lengthening the stator tooth, that is the tallest one if compared this SPM machine to the other two SPM motors in Figure 7.2, having fractional slots winding.

This result, that is consistent with the literature and is synonym of both an higher mass and cost, remarks that fractional slot machines have lower Joule losses, due to their shorter end connections, with respect to distributed winding configurations. It is also confirmed by Table 5-I, where the end winding factors are reported for all the design examples.SPM machines are also appreciated for better manufacturability, as said.

Anyway, on the other hand, it remains true that the design of concentrated windings SPM machines has to be handled with care to keep the Power Factor in reasonable ranges of convenient values, especially when electrical machines are heavily loaded. Besides, the efficiency targets achievable via concentrated layer SPM designs are penalized in some way by the PMs loss, which arises due to the huge harmonic content in the stator mmf.

7.1.2.2. FASR machine

The FASR machine to be compared to the SPM designs described in the previous subsection is fully defined by the parameters and performance indicators, summarized in Table 5-I. Its characteristics have already been discussed in Chapter 05, where the main criteria that led to the definition of the ultimate design were also deeply discussed.

FASR machine topology, that exploits ferrite magnets instead of Nd-based ones, aims at representing a reduced-cost alternative to rare-earth based PM machine configurations and this compels the designers to look for a design strategy capable of maintaining satisfactory efficiency figures, even if it is anymore possible to rely on hard rare-earth PMs for the magnetizing contribute along the direct axis.

The analytical model, developed in Chapters 04 and 05, demonstrated that, at given output torque and stack envelope, a number of pole pairs that does minimize the loss of FASR machines does exist. Moreover, it turned out that the loss reduction obtainable by lengthening the stator teeth flattens with l_t/r beyond a certain extent. In other words,

since the selection of the stator tooth length is a matter of trade-off between cost, weight and efficiency, this l_t/r limit value can represent a good choice for the final design.

Starting from these considerations, the FASR wind generator, considered here as an example, has been designed with p = 24, for loss minimization, and l_t/r = 7%, not to "waste" extra copper (and thus weight and cost) when the consequent improvement in terms of efficiency starts to fall more steeply. This is because the FASR design example is intended, above all, to be representative of a reduced-cost solution for wind applications. As a result, the length selected for the stator tooth results to be shorter than the ones of two SPM design examples. This occurrence will be better addressed in the next subsection, while comparing all the proposed configurations.

7.1.2.3. Performance comparison at rated condition

The design examples, presented so far, highlight that the willed torque density level can be achieved both via high-performance (and high-cost) SPM designs and reduced-cost FASR machines, despite the lower energy density of ferrite magnets with respect to rare-earth raw materials.

The machines under comparison are all wounded for the same voltage and show similar current levels, at rated condition. The Power Factor is different from one design to the other, indicating that FASR machines allow to limit conveniently the size of the power converter.

Concentrated windings SPM designs help reducing the total mass of active materials, especially when a high pole pairs number is put into play. However, this degree of freedom needs to be considered carefully, since, by increasing the pole pairs number, the efficiency of the ultimate design may be seriously affected by the consequent increment of the iron loss and, above all, the eddy current loss in the PMs. Conversely, given the stack envelope and the output torque, the total mass of the distributed winding SPM machine (*design 3*) is comparable to the one of the FASR generator and, in this case, it is not possible to reduce it by further increasing the number of poles, since the stator slots would get too slender, even posing q = 1.

The mass increment of the FASR example, with respect to the SPM designs, does not

coincide with a cost increment because of the disparity between the specific cost of ferrite magnets (5 USD/kg) and rare-earth based PMs (around 70 USD/kg). In terms of active materials' cost, the biggest discrepancy (+73%) does exist between the distributed winding SPM design and the FASR one, since in these cases the copper volume is roughly the same. Always from the economical point of view, if compared to the FASR machine, *design 1*, that is the single layer concentrated winding SPM example, is more competitive than *designs 2* and *3*.

Anyway, the considerations and values, listed above and summarized in Table 5-I, refer to the current situation in the marketplace. If the price of rare-earth PMs were still the one (244 USD/kg) registered in the middle 2011, the active materials of *design 2* would cost 3.8 times the ones needed to build the FASR generator, whereas now the disparity between the two machines, in terms of cost, is "only" +53%. Analogous conclusion can be drawn for the other SPM examples. This is to say that FASR configurations are particularly attractive for not being dependent on possible monopolistic policies in the market and consequent price instability of rare-earth magnets.

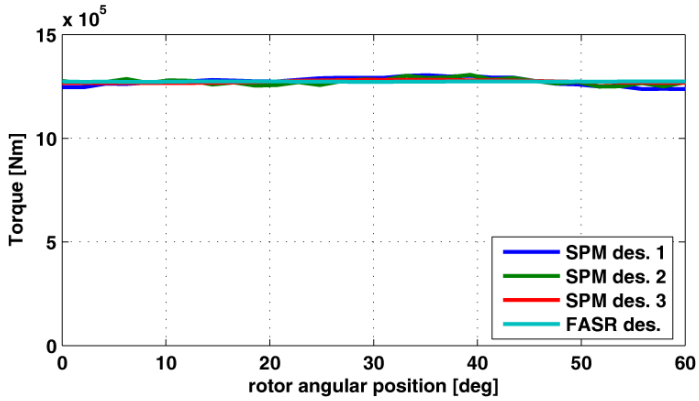

Figure 7.3 – Torque curves of the four wind generator examples of Figure 7.2, reported as functions of the rotor angular position.

As specified in Subsection 7.1.1, the operation costs, besides the installation ones, are also important when comparing alternative technologies for wind turbine generators. It means that efficiency does represent a relevant factor. As expected, the efficiency of SPM designs is higher than the one, achieved via the FASR machine example. This discrepancy varies from 1.5% up to 2.5%, depending on the SPM example taken as

reference for the comparison, and stands for a satisfactory result, if the concurrent machine types are fairly compared. Moreover, the distance between the two design topologies, in terms of efficiency, can be reduced by lengthening the stator tooth of the FASR design. It was not done because the goal is here to compare high-cost performing machines (namely, SPM generators) to solutions purposely thought for cost reduction, such as FASR machines. However, if needed, there is margin for reducing the total loss of the FASR design: for example, if its stator tooth was made as long as the one of *design 2*, the efficiency would be increased by 0.35 %, obviously at the expense of a slight increment of both weight and cost.

Last, the curves in Figure 7.3 compares the four generators of Figure 7.2, showing that the torque ripple does not represent a critical design issue and all the proposed configurations are suitable for being adopted in wind power plants.

7.2. ELECTRICAL MOTORS FOR AUTOMOTIVE APPLICATION

Another of the application areas where direct-drive PM configurations have drawn the most attention during the past several years has been hybrid-electric and battery-electric propulsion drives, combined either to chemical accumulators or fuel cells. The choice of the electric drive train most appropriate for this application is still a matter of discussion.

Induction motors and PM synchronous motors have been the alternative solutions considered in the past years [76]. The former are attractive for their ruggedness and availability, whereas the latter are generally preferable for their higher torque density and efficiency. Among PM motors, Surface-Mounted and Interior PM types are both considered [76]-[77].

For example, Honda, that was one of the first automotive manufacturers to introduce a production hybrid-electric vehicle into the marketplace in the late 1990s, chose for its first prototype a drive train based on a SPM machine. But, during the past years since selling its first hybrid-electric vehicle (namely, Honda Insight), it has evolved the configuration from using a Surface PM machine versions to adopting a form of Interior PM machine in more recent models [78].

Honda integrated motor assist drive (shown in Figure 7.4 [78]) mounts the electrical machine on the same driveshaft as the engine, comprising a classic parallel hybrid configuration. It generally falls into the category of mild hybrids in which the electric drive has torque and power ratings that are limited to approximately 25% or less of the engine's capabilities. The electric is used to assist with acceleration and regenerative braking, but the internal combustion engine is responsible for the majority of the propulsion effort.

Figure 7.4 - View of Honda Integrated Motor Assist (IMA) direct-drive PM configuration in CR-Z hybrid-electric power train [78]

Anyway, whatever the configuration of the electric or hybrid-electric vehicle (HEV, EV) is, an exhaustive comparison between the performances of electric drive trains based on different PM machine topologies has not been proposed yet.

Most of the more recent research in this field has being devoted to motors with non overlapping windings having the PMs either mounted on the rotor surface [18]-[21] or inserted inside the rotor [79], [80]. But such IPM machines are often very similar to SPM ones for magnets layout and, above all, for having a low saliency.

Here the comparison, which will be carried out at a given vehicle specification and inverter size since the whole drive train (that is, electric motor plus power converter) is taken into account, will consider:

- concentrated winding SPM configurations;
- distributed winding SR machines, having high-salient rotor structures, assisted

either by low-cost ferrite magnets or a minimized amount of more expensive rare-earth PMs.

In other words, PM machines with very different peculiarities will be compared so to highlight pros and cons with respect to the requirements typical of electrical drives for automotive applications.

7.2.1. Typical specifications of electrical drive trains for traction

The main criteria to be followed when designing electrical motors for traction come from the need of optimizing the performance of all the EV (or HEV) system components, that is, besides the electrical machine, the power converter and possibly the battery.

As for many other mass-production application, cost represents a significant factor in determining the most suited technology for automotive drive trains and, as for many other high-performance applications, efficiency has a particular importance. Efficiency plays a relevant role, especially when the regenerative braking is exploited, like in urban cycle, since for this type of workload a better efficiency of the motor drive can make the difference in terms of vehicle range.

The characteristics of a traction motor for EV are sketched in a general form in Figure 7.5: both at rated (continuous line) and overload (dashed line) condition, the curves show that constant-torque region at low speed and constant-power zones at high speed values are required.

The continuous torque at low speed is dictated by the maximum slope specified for hill climbing, whereas the continuous power determines the maximum cruising speed of the vehicle.

At overload, the electric motor is thermally safe at least for a couple of minutes, since the maximum ratings of both the inverter and the battery actually intervene to limit the output power: specifically, the inverter current determines the maximum torque, whereas in general it is the battery that constrains the maximum power.

This potential overload capability, which does represent a great advantage with respect to internal combustion engines, can be conveniently exploited. Intermittent

overload for short durations can be employed either for vehicle accelerations or possible power regeneration, at any rotating speeds. Overload is welcome also at large speed values, but the voltage limitation may prevent to match the specifications of Figure 7.5, also depending on the electric motor configurations.

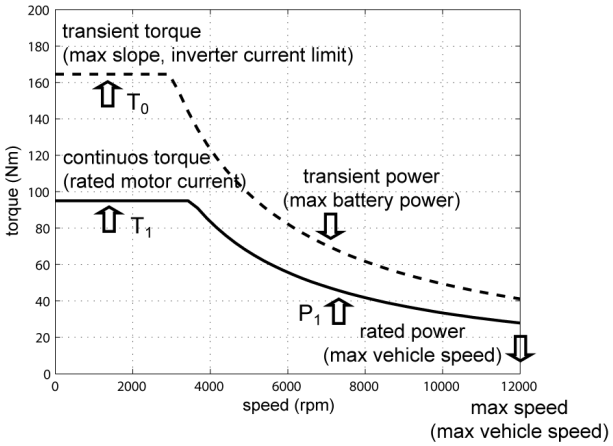

Figure 7.5 - Torque versus speed characteristics that schematically represent typical EV specifications at rated (continuous) and overload (dashed) condition.

This will be clarified by the models proposed in the next two subsections (7.2.1.1 and 7.2.1.2) that identify the best design strategy to approach the requirements of Figure 7.5 via SPM and PM-Assisted SR configurations.

7.2.1.1. Power curves of SPM motors at different current levels

Figure 7.6 shows the vector trajectories to be followed at rated current i_1 and at partial load i_{10} for making the SPM motor drive work in the flux-weakening regions. Figure 7.7 reports the power output by the drive at full- (i_1) and partial- (i_{10}) load with the speed increasing and voltage being limited by the inverter.

In the vector diagram of Figure 7.6, point A_1 represents the continuous working condition, in the low speed constant-torque zone. The current vector is in quadrature to the PM flux for maximum torque per Ampere (MTPA) operation.

At higher speed, for constant-power operation, the current vector is rotated to reduce the flux linkage and keep the voltage within the inverter limit. An ideal flat power curve is obtained if the current-dependent flux $L\ i_1$ equals the PM flux linkage λ_m [19]

$$\lambda_m = L \cdot i_1 \tag{7.1}$$

being L the SPM motor inductance. According to this design strategy, the power asymptotically tends to the limit value P_{lim} (7.2), determined by the rated current i_1 and the peak phase voltage amplitude V.

$$P_{lim} = \frac{3}{2} V \cdot i_1 \tag{7.2}$$

The per-unit continuous power curve plotted in Figure 7.7 summarizes the results. If power losses are disregarded, the output power curve has nearly the shape of the Power Factor. At base speed (point A_1), the per-unit power is nearly 0.7, since condition (7.1) leads to have the phase angle of the machine flux close to 45°. As the rotating speed is increased, the per-unit power, together with the Power Factor, approaches the unitary asymptotic value. In fact, the flux and current vectors tend to be in quadrature to each other (see Point C_1).

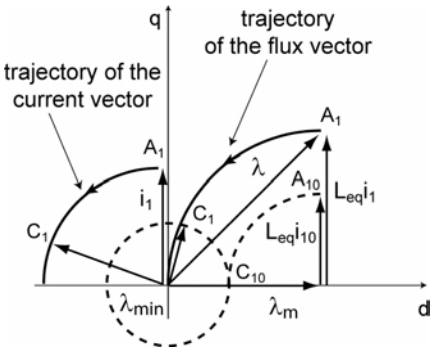

Figure 7.6 - SPM motor vector diagram at rated current (i_1) and at the no-load current amplitude needed at maximum speed (i_{10}).

So, the value P_{lim} coincides with the continuous power P_1, pointing out that the maximum output power of the drive is strictly correlated to the maximum operating speed value. Moreover, it highlights that, since the motor rated current i_1 must match the power dissipation allowed by the motor cooling and the PM flux λ_m has to be fixed to obtain an optimal torque to current ratio, the only parameter left to satisfy (7.1) is the motor inductance. In order to design the term L properly at this aim, the closed-form equations, provided for in Chapter 03 can be adopted. The most suited value of stator slots per pole can be selected and the geometric parameters can be conveniently set.

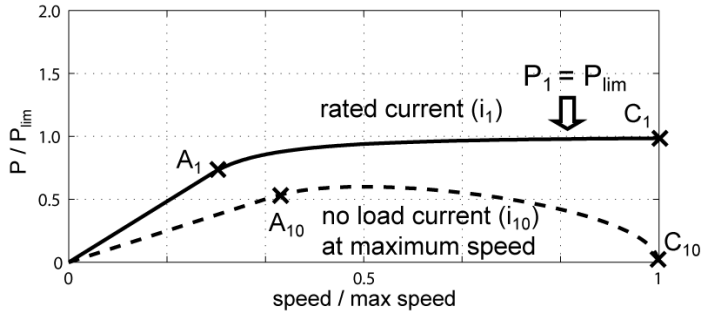

Figure 7.7 - SPM motor per-unit power curves versus speed at rated current (i_1) and no-load current maximum speed (i_{10}).

At partial and no load current levels, the obtainable power curves are penalized by the need of limiting the flux amplitude at high speed and thus cope with the voltage limit. In order to show typical power figures that can be achieved at partial load by SPM motors, in Figure 7.7, the worst-case de-magnetizing current i_{10} (< i_1) has been considered. It is given by (7.3):

$$i_{10} = \left(1 - \frac{\lambda_{min}}{\lambda_m}\right) \cdot i_1 \tag{7.3}$$

where λ_{min} is representative of the flux amplitude to be respected at maximum speed (ω_{max}) and it is quantified by (7.4) if the resistive drop is disregarded:

$$\lambda_{min} = \frac{V}{\omega_{max}} \tag{7.4}$$

The need for some flux-weakening current at light- and no-load is a general drawback of this kind of motors, because it implies more copper losses. Most of the time the drive is at partial load in the speed range above the base speed. In such cases only a small part of the motor current is actually giving torque while the most of Joule losses are spent just for flux weakening, as will be evidenced while analyzing the design example.

In Figure 7.8 a typical SPM motor vector diagram at overload is shown, with reference to a current i_0 that is 173% of the continuous current i_1 (i.e. 3 times the Joule losses).

At low speed, in the constant-torque region (A_0 in Figure 7.8), the Power Factor is

quite low and the voltage limit is met very soon, because of the larger flux amplitude.

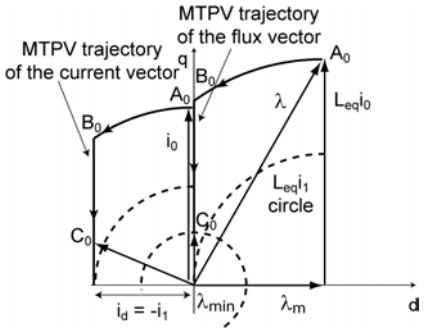

Figure 7.8 – SPM motor vector diagram at overload current i_0.

As for the power-constant region, the current is rotated until the flux vector is aligned to the q-axis (i.e. B_0 in Figure 7.8). For SPM motors, the q-axis represents the maximum torque per voltage (MTPV) flux condition [19]. According to the MTPV law, the i_d current (= $-i_1$) is spent to null the PM action along the d-axis, while progressively reducing the q-axis flux by regulating the i_q current component. In formula, the current i_{qMTPV} (7.5) is controlled so to make the respective flux amplitude λ_{MTPV} compliant with the voltage limitation V and the operating speed ω.

$$i_{q,MTPV} = \frac{\lambda_{MTPV}}{L} = \frac{1}{L} \cdot \frac{V}{\omega} \tag{7.5}$$

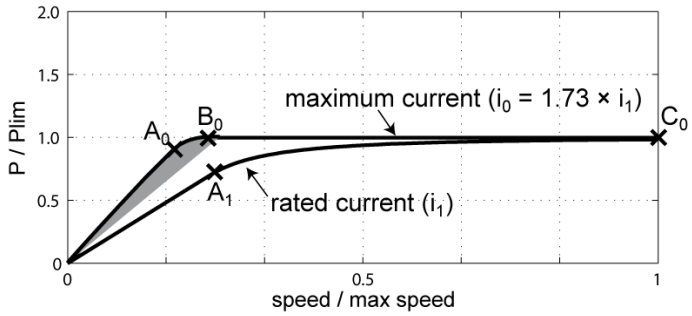

Figure 7.9 – SPM motor per-unit power curves versus speed at rated current (i_1) and 173% overload current (i_0).

At MTPV operating condition, also the torque (7.6), along with the q-axis current, varies inversely with speed.

$$T_{MTPV} = -\frac{3}{2} p \cdot \lambda_{q,MPTV} \cdot i_d = \frac{3}{2} p \cdot \frac{V}{\omega} \cdot i_1 \tag{7.6}$$

Consequently the output power (7.7) results to be constant with speed and, if the SPM machine has been designed according to (7.1) for having the nominal current close to the short circuit one, this power level is also equal to the P_{lim} value (7.2).

$$P_{MTPV} = \frac{3}{2} V \cdot i_1 = P_{lim} \tag{7.7}$$

In other words, once the MTPV limit is achieved, the output power is clamped to P_{lim}, independently of the available current overload.

For example, the 173% overload current i_0 produces an overload torque below the base speed, but the power overload vanishes as the speed increases beyond that point. This is evidenced in Figure 7.9.

In Figure 7.9, the curve corresponding to the overload current i_0 has a shaded area around the low-speed constant-torque zone, to remind that the power profiles have been derived via a linear model, that disregards steel saturation effects. The performance at rated current is correctly represented, because it can be assumed that the rated flux amplitude (MTPA flux at rated current i_1) coincides with the core saturation limit (λ_{sat}). But the overload capability of the motor is overestimated if steel saturation effects are not taken into account. Nevertheless, the simplified model is well representative of the behavior of the machine in the flux weakened region, where saturation effects are less evident. As a validation, FEA calculated power curves will be reported for the design examples, that will be discussed in Section 7.2.2.

7.2.1.2. Power curves of Magnet ASR motors at different current levels

In case of Magnet-Assisted SR designs, the rotor parameters (namely, the anisotropy ratio and magnet flux) can be conveniently set in order to meet the required specification in terms of power profiles at partial-, full- and also at over-load current levels.

At rated current i_1 and low speed, the continuous constant-torque is delivered making the drive work along the MTPA locus. According to the *dq* axes convention typical of SR and Magnet-Assisted SR machines, for MTPA operation both the *d*- and *q*-axis current components are positive and the optimal phase angle of the overall current

vector varies from motor to motor, depending on which contribute between the reluctance torque and the PM one is predominant.

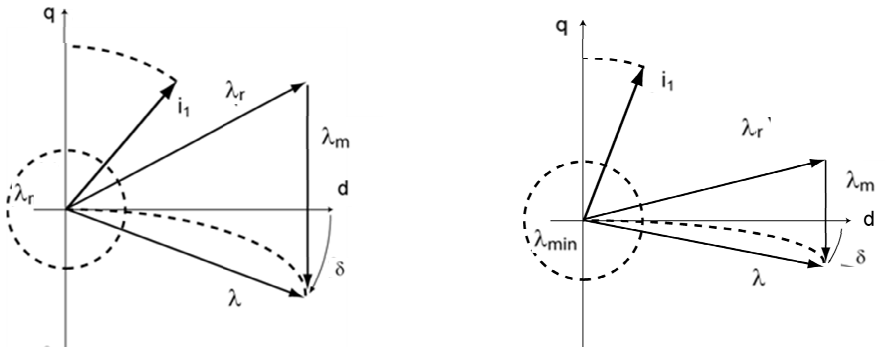

Figure 7.10 - Vector diagrams of two PMASR motor examples at rated current (i_1), in the respective MTPA conditions. The dashed curves are the trajectories of the flux and current vectors in flux weakening. The λ_r flux (where *r* stands for *reluctance*) is the one produced by the stator current. a) motor with low anisotropy. b) motor with high anisotropy.

The torque T (7.8), produced by Magnet-Assisted SR motors, show both PM flux and anisotropy terms.

$$T = \frac{3}{2} p\left[\lambda_m i_d + L_q(\xi - 1) i_d i_q\right] \tag{7.8}$$

At given thermal current, the larger the anisotropy ξ (= L_d/L_q) is, the lower the magnet flux λ_m needed to produce the willed torque is. This is shown by the vector diagrams of Figure 7.10 that compares two Magnet-Assisted SR motors, with same the flux and current but different saliencies. The lower saliency PMASR machine (Figure 7.10a) has a λ_m flux that is comparable, in per-unit of the rated one, to the SPM machine magnet flux. And the related side effects are also comparable, namely the overvoltage in case of uncontrolled generator operation [81] and the additional Joule loss for weakening the flux at high speed (even at reduced loads). The high anisotropy motor (Figure 7.10b), similar to the ones analyzed in this work, has much lower per-unit PM flux and side effects. In addition, the design with high-saliency and low λ_m improves the overload capability of the drive at large speed, as it will be demonstrated in the following.

For flux weakening (i.e. constant-power operation) at continuous load, the current

vector is rotated anticlockwise starting from the MTPA angle, as suggested by the dashed curves in Figure 7.10. As the flux is reduced, that is the speed is increased, the angle between the current and flux vectors always tends to 90°, as it was for the SPM motor. Analogously to the SPM motor, the MTPV locus is not met at rated current when the PMASR machine is "Naturally Compensated", meaning that its nominal current i_1 equals the characteristic one (I_{ch}), or if i_1 is slightly lower than I_{ch}.

As a result, the power profiles obtainable at rated current via such Magnet-Assisted SR designs are flat in a wide speed range, whatever the anisotropy ratio ξ and the PM flux linkage λ_m are. The plots in Figure 7.11 confirms the statement.

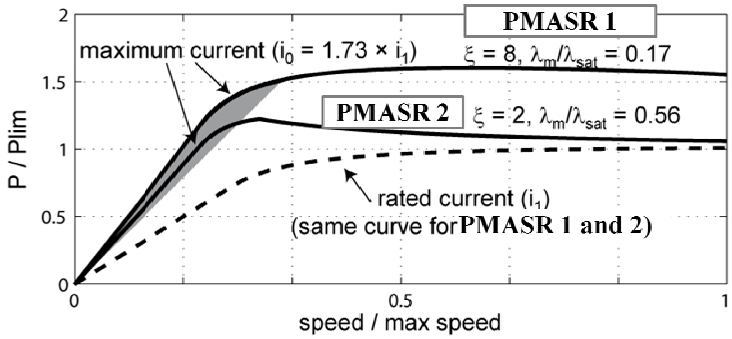

Figure 7.11 - Per-unit power versus speed for two PMASR motor drive examples with different saliency ratio and PM magnet flux, but designed for the same continuous torque and power (T1 , P1) according to (7.9), and with the same rated flux (λ_{sat}).

At overload current, in the constant-torque region, PM-Assisted SR motors are controlled along the MTPA locus. In the constant-power zone, that stands for higher speed values, the MTPV operation constraints the flux weakening trajectory. But, differently from the SPM case, the MTPV is no longer clamped to an upper limit value.

Nevertheless, the power curve of Magnet-Assisted SR motors tends to drop with speed in the MTPV area and specific design conditions have to be met for possibly having flat power curves at overload. Alternative design solutions are available, also depending on the specifications.

- The PMASR machine can be designed to fulfill the "Natural Compensation" condition (7.9) and the rotor parameters can be arranged so that the MTPV zone is encountered exactly in correspondence of the maximum speed and overload current.

$$\lambda_m = L_q \cdot i_1 \tag{7.9}$$

- As an alternative, if the overload capability of the PMASR motor needs to be further enhanced, the PM magnet flux can be reinforced with respect to the "Natural Compensation" criterion, as suggested by (7.10).

$$\lambda_m = L_q \cdot \frac{i_1 + i_0}{2} \tag{7.10}$$

The first design strategy was proposed in [82] and it is schematically represented in Figure 7.12, where the flux vector diagram at maximum speed is reported, with reference to the overload current i_0 (= 1.73·i_1). By solving the equation that describes the MTPV trajectory when $\lambda = \lambda_{min}$, i.e. when the flux amplitude equals its limit value at maximum speed (7.4), the respective flux phase angle δ_{max} (7.11) can be found.

$$\frac{L_q \cdot i_0}{\lambda_{min}} = \cos(\delta_{max}) + \frac{\lambda_m}{\lambda_{min}} \tag{7.11}$$

Then, by replacing the "Natural Compensation" condition (7.9) in (7.11), it results evident (7.12) that, given the overload ratio i_0/i_1, the ratio λ_{min}/λ_m, which guarantees to meet the MTPV locus at overload current only in correspondence of the maximum speed, is fixed.

$$\frac{\lambda_m}{\lambda_{min}} = \frac{1}{\cos(\delta_{max})} \cdot \left(\frac{i_0}{i_1} - 1\right) \tag{7.12}$$

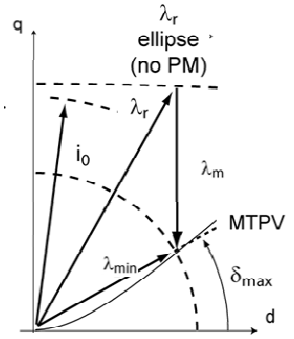

Figure 7.12 – Typical flux diagram of "Naturally Compensated" (7.9) PMASR motor at maximum speed and overload current i_0. The MTPV locus is supposed to be met exactly at maximum speed, maximum current.

The dependency on the motor saliency is little, as also shown by Figure 7.13. However, since, according to (7.8) and (7.9), the needed λ_m gets smaller with higher

saliencies (i.e. lower L_q), also the feasible maximum speed increases accordingly.

To point out this, in Figure 7.11, two PMASR machines are compared: one with high saliency (ξ = 8) and low PM flux ($PMASR_1$), and the other with low saliency (ξ = 2) and higher PM flux ($PMASR_2$). The two machines are designed to give the same continuous power curve (P_1), with the same current (i_1) and voltage (V). $PMASR_1$ can be designed to meet the MTPV at maximum speed, as explained, whereas $PMASR_2$ encounters the MTPV around 0.3 per-unit speed.

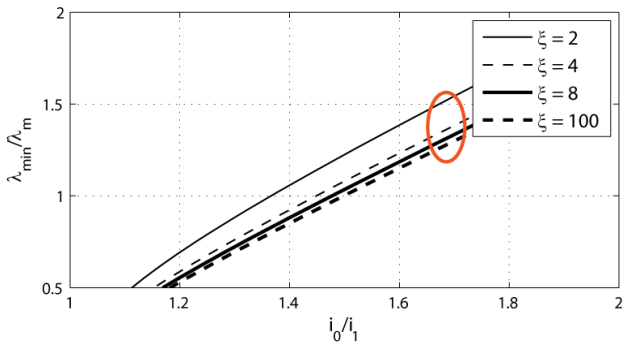

Figure 7.13 - Minimum flux as a function of current overload and anisotropy ratio, in case of "Naturally Compensated" PMASR motors.

In general, it can be concluded that "Naturally Compensated" PM-Assisted SR machines can be overloaded at low and high speed values, differently from the SPM case. The overload capability of such motors, designed according the "Natural Compensation" condition, is much higher when large saliency ratios are provided for.

Moreover, the overload capability of PMASR motors at high speed can be further improved if the PM flux is designed according to (7.10), that means increased by [0.5·(i_1+i_0)] with respect to the one that would fulfill the "Natural compensation" criterion (7.10).

Under this design hypothesis, in correspondence of the 173% overload current example, the PM flux should be increased by 36%. The minimum flux ratio (7.13) is then roughly reduced by 2.73 times with respect to (7.12).

$$\frac{\lambda_m}{\lambda_{min}} = \frac{1}{\cos(\delta_{max})} \cdot \left(\frac{i_0}{i_1} - 1\right) \cdot \left(\frac{i_0}{i_1} - 1\right)^{-1} \tag{7.13}$$

It follows that the maximum speed that is feasible with no MTPV limitation is two

times higher (2.73 / 1.36).

In Figure 7.14 the power versus speed curves are shown for the high anisotropy machine $PMASR_1$ ($\xi = 8$), both at rated and at overload current, with the PM designed according to the alternative strategies (7.9) and (7.10). Dotted lines are the $PMASR_1$ curves of Figure 7.11. As said, the rated performance has no practical modification, whereas the overload performance is improved.

Figure 7.14, together with the results shown in Figure 7.11, confirms that the design of the PM flux is not critical for high saliency motors and the comparison between Figure 7.14 and Figure 7.9 points out the dramatic difference between SPM and PMASR motors, as concerns the overload capability.

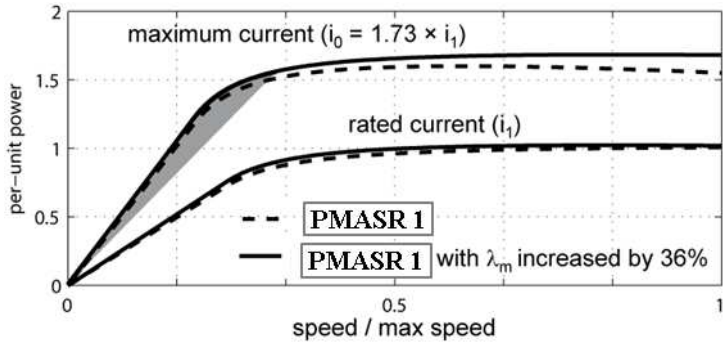

Figure 7.14 - Effect of increased PM flux on overload capability: per-unit power versus speed curves for $PMASR_1$, designed under according to the "Natural Compensation" condition (7.9) (same as Figure 7.11) and $PMASR_1$ (again $\xi = 8$) with the PM flux increased by 36% as suggested by (7.10).

The steel saturation effects, represented by a shaded area in the low speed region also for the PMASR designs of Figures 7.14 and 7.11, do not change the conclusion drawn in this paragraph about the advantageous flux weakening capability of Magnet-Assisted SR motors, since the adopted linear model is quite reliable in the constant-power zone.

7.2.2. Design examples

An exhaustive comparison necessarily deals with concrete design restrictions, such as thermal limits given by losses, current and voltage constraints determines by the inverter size, torque density target and efficiency maximization purposes. Thus, three machines with different rotor and stator configurations have been designed.

TABLE 7-II
TRACTION MOTOR DESIGN EXAMPLES

SPECIFICATIONS				
Target continuous torque T	125			Nm
Rated speed n	3500			rpm
Maximum speed	12000			
Stack length l	0.170			m
Stator radius r	0.108			m
Operating temperature	130			°C

STATOR WINDING AND SLOTTING EFFECT				
	SPM	Nd-PMASR	FASR	
Slot per pole per phase q	½	4	4	
Winding factor k_w	0.87	0.93	0.93	
End connections factor k_{end}	1.12		1.61	
Carter coefficientk_c	1.02		1.10	
MATERIAL				
Magnet grade B_r	1.22	1.12	0.38	T
Steel grade	M250-35A			
GEOMETRICAL DESIGN OUTPUTS				
Pole pairs p	2	2	3	
Per-unit tooth length l_t/r	27	12.5	13.2	%
Rotor radius r'	0.0472	0.071	0.0760	m
PERFORMANCE INDICATORS AT RATED CONDITION				
Continuous current I_r	240			Apk
Line Voltage	173			Vpk
Rated Power Factor	0.77	0.99	0.99	
Continuous Joule loss density k_j	12208	16952	15593	W/m^2
Continuous iron loss density k_i	2207	1957	2495	W/m^2
Continuous PMs loss density k_{pm}	2709	256	0	W/m^2
Continuous total loss density	17124	19165	18088	W/m^2
Efficiency at rated current	95.69	95.17	95.44	%
Overload current	415			Apk
Overload torque	175	220	230	Nm

The main design indicators (see Table 7-II) come from actual specifications:

- the outer diameter (216 mm) and stack length (170 mm) are fixed;
- the continuous current (240 Apk) and the line-to-line voltage (300 Vpk) are determined by the chosen inverter;
- the machine has to deliver about 50 kW continuous power in a wide Constant

Power Speed Range, up to the maximum speed 12000 rpm;

- the current overload can be 173% and a flat constant-power profile is desired also at overload.

All the machines are liquid cooled, allowing the specific loss to grow up to 20000 W/m^2, if needed. Due to the impact of iron loss at large speed values, a good quality steel (M250-35A) has been used, for all the designs.

A SPM based motor drive will be compared to two high-salient SR designs, assisted either by a minimized volume of rare-earth (Neodymium) PMs or ferrite magnets. Their geometric parameters are summarized in Table 7-II, together with some relevant quantities.

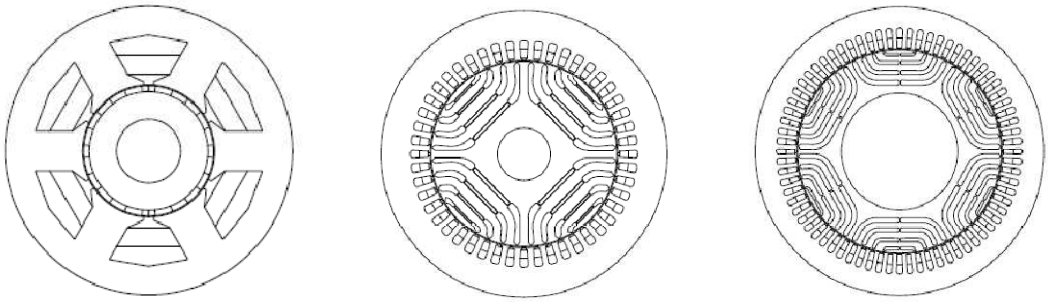

SPM Nd-PMASR FASR

Figure 7.15 - Example motors, sized for being combined with the same inverter, having the same continuous torque and power. The three motors have the same stator diameter and stack length.

7.2.2.1. SPM motor

In this case, the key point of the design is to satisfy the relationship (7.1), that suggests to match the short circuit current I_{ch} with the nominal one, since a wide Constant Power Speed Range is required at rated condition.

In turn, the nominal current, which has to comply with the constraint introduced by the inverter, must match the thermal and demagnetization limitations.

According to this aim, by taking advantage of the model proposed in Chapter 03, the SPM machine described in Table 7-II has been defined.

Due to the high value of the maximum operating speed, the pole number has been

maintained conveniently low (p = 2), so to limit the iron losses, together with the eddy current losses in the magnets.

The rotor parameters, namely the PMs ones, have been set to assure an adequate magnetic loading in the airgap at no load and prevent demagnetization issues. Then, the q-axis current loading, needed to produce the willed shear stress by interaction with the PMs, has been evaluated and the stator (i.e. the machine phase inductance) has been designed accordingly to approach condition (7.1).

After quantifying the inductive contribute to be put into play via the formulas presented in Chapter 03, fractional slots, that lead to higher magnetizing inductance, have been selected, also because of the additional benefit of shorter end connections. Eventually, the stator tooth length, which does decide the slot leakage inductance, was tuned in order to make the nominal current value close to the short circuit one.

As a result, the SPM motor, that will be used as a reference for the comparison, is a 6 slots, 4 poles machine, with a double layer winding and a stator tooth length equal to 27% of the outer radius (Table 7-II, Figure 7.15 - left-hand side). It was first analyzed in Chapter 03, where further details can be found.

7.2.2.2. High-salient SR motors, assisted by Nd-PMs and ferrite magnets

The high-salient Magnet-Assisted SR motors are intended to be reduced-cost alternative with respect to SPM configurations, since they are designed either with a minimized quantity of expensive rare-earth PMs or cheap ferrite magnets, without compromising the torque capability of the drive.

In case of automotive applications, besides cost reduction, this kind of rotor structures guarantees other welcome advantages, as for example lower back-emf value and satisfactory overload capabilities, as it has been theorized before and it will verified via the design examples.

At the aim of minimizing the q-axis inductance, thus reducing the need of a significant PM torque contribute, a multiple (four) barrier rotor structure has been chosen for both the Magnet-Assisted SR motors designed according to the specifications

listed at the beginning of this Section.

The mechanical robustness of the rotor at high speed is related to the proper design of the inter-layer iron ribs, in terms of placement and thickness. Both the rotors in Figure 7.15 have been verified against maximum centrifugal stress with reference to a maximum speed of 14000 rpm that is 20% higher than the maximum operating speed. Moreover, to reduce torque ripple [57] and high speed losses [83] the flux barriers have been displaced "regularly" (Chapter 04) at the rotor periphery, while properly matching the number of stator and equivalent rotor slots per pole.

The PM fluxes of both the Nd-Assisted SR motor and the Ferrite-Assisted one have been reinforced (7.10) with respect to the "Natural Compensation" condition, so to enhance the flux weakening capability of the drive, as it was suggested in Subsection 7.2.1.2.

The rare-earth PMASR motor has been designed for cost reduction with a minimized magnets volume, as said. Chapter 06 summarized the analytical theory behind the magnet volume optimization in Nd-based PM Assisted SR machines, showing that the procedure does not compromise the drive performance and can be conveniently adapted to avoid demagnetization issues.

The ultimate design of Figure 7.15, that will be considered as reference for the following comparison, is derived from the "Naturally Compensated" example proposed in Chapter 06 for validation purposes, by reinforcing the magnet flux λ_m according to (7.10).

The FASR design reported in Figure 7.15 has been defined, again according to the common specifications of Table 7-I, following the procedure described in Chapters 04, 05.

As it was better explained in Chapter 05, where the machine was first analyzed, the pole pairs number (p = 3) and stator tooth length (l_t/r = 13 %), together with the other design parameters, have been selected for maximizing the efficiency of the drive. Even if the optimization has been referred to the rated condition (i.e., T = 125 Nm, n = 3500rpm), the efficiency maps in Subsection 7.2.2.4 will show that the choice of

increasing the fundamental frequency with respect to the one of the other designs, that have both $p = 2$, has no drawbacks at higher speed values.

7.2.2.3. Drives comparison in terms of flux weakening capability

As shown in Figure 7.16, the three motors under comparison give the same continuous power curve, when supplied with the same continuous current, at the same inverter voltage.

Conversely, even if supplied with a 173% overload current, the SPM motor drive cannot deliver an incremented power at high speed value.

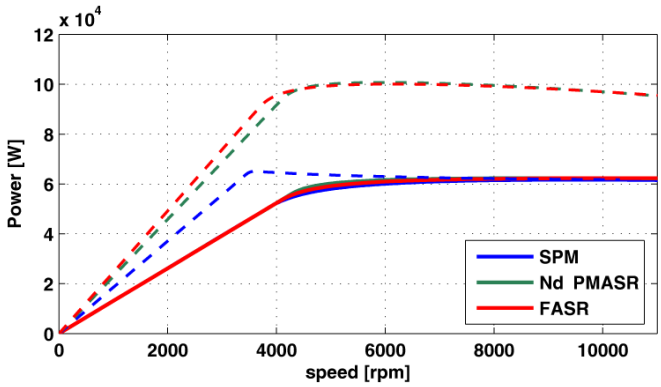

Figure 7.16 – Power curves of the drives under comparison at rated (continuous lines) and overload (dashed lines) condition.

The comparison between the plots in Figure 7.16 and the curves based on the linear model confirms the conclusion drawn in Subsection 7.2.1.1 and 7.2.1.2, while pointing out the effects of core saturation. The rated power curves are slightly affected by saturation, for all the motor examples. Though, the torque curves at overload are much different from the ones forecasted by the linear model, also at low speed. This is due to saturation and cross saturation effects. This phenomena is clearly heavier in the SPM case, which gives a definitely lower overload torque, also at low speed.

7.2.2.4. (T, n) efficiency maps of the concurrent drives

The efficiency comparison between different traction drives should refer to a specific vehicle cycle.

As a general basis for comparison, efficiency maps over the entire Torque – Speed

region are proposed here, for each motor topology, so that different driving cycles can be evaluated case by case.

The results are summarized in Figures 7.17, 7.18 and 7.19 for the SPM motor, the Nd-based PMASR machine with minimum magnet volume and the FASR design.

The motor efficiency is determined by:

- Joule loss;
- iron loss;
- eddy current loss in rare-earth PMs.

Depending on the machine topologies and the working load condition, the contribute that affects most the resultant efficiency level does vary.

The iso-efficiency and iso-loss curves in Figures 7.17, 7.18 and 7.19 have been traced by associating to each working point in the Torque versus speed plane a (i_d, i_q) combination, which, besides being compliant with the inverter current and voltage limitations, is able to minimize the overall losses, sum of the three contributes: Joule, iron, PMs.

The core losses over the whole torque and speed ranges have been calculated by means of transient Finite Element Analysis using MagNet (Infolytica). The iron loss model is based on the Epstein Frame loss measurements declared by the manufacturer and uses a modified Steinmetz equation augmented with an excess term to fit the loss manufacturer data. The accuracy of the model relies on the availability of loss curve data from the manufacturer at several frequencies, in particular at the highest ones. The M250-35A grade, adopted in the model, is characterized up to 2500 Hz and is of practical use for the analysis.

The harmonic losses of the rare-earth based PM-Assisted SR at high speed have been minimized by the specific 24-20 slot design [83]: with less rotor layers and less stator slots per pole higher core losses could be expected.

The PMs of the Surface Mounted machine are segmented tangentially and axially in 5 parts, for reducing the eddy current losses. Additional eddy current losses related to some kind of conductive retention devices are not considered, supposing that the PMs

are not constrained either into a conductive or non-conductive retaining sleeve.

The PM operating temperature is 130 °C in all cases.

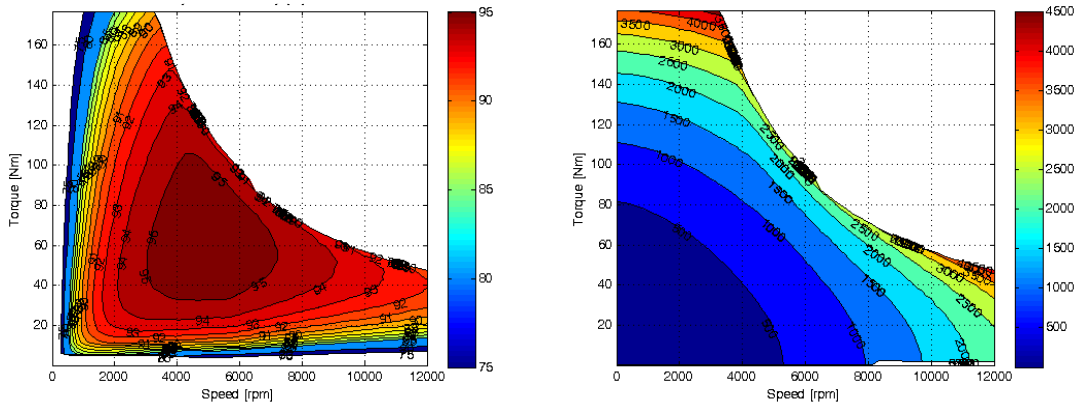

(a) (b)

Figure 7.17 – Efficiency (a) and loss (b) maps of the SPM example reported in Figure 7.15

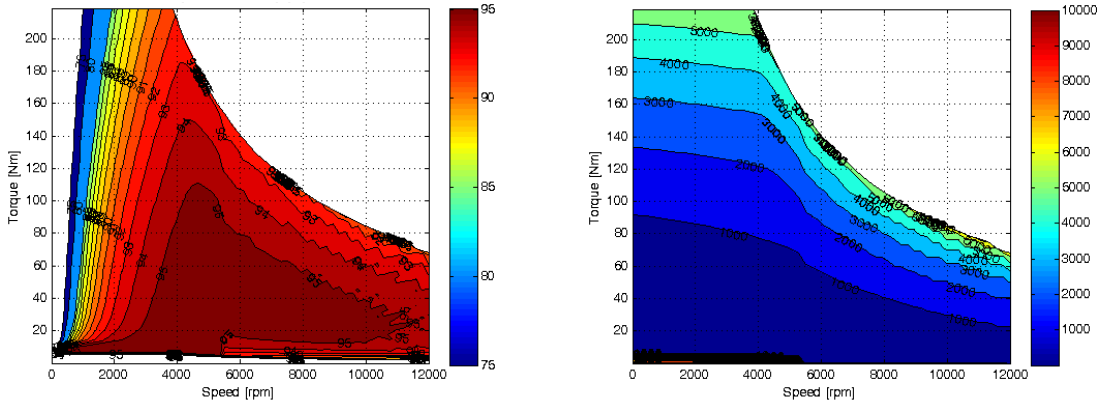

(a) (b)

Figure 7.18 - Efficiency (a) and loss (b) maps of the rare-earth PMASR example in Figure 7.15

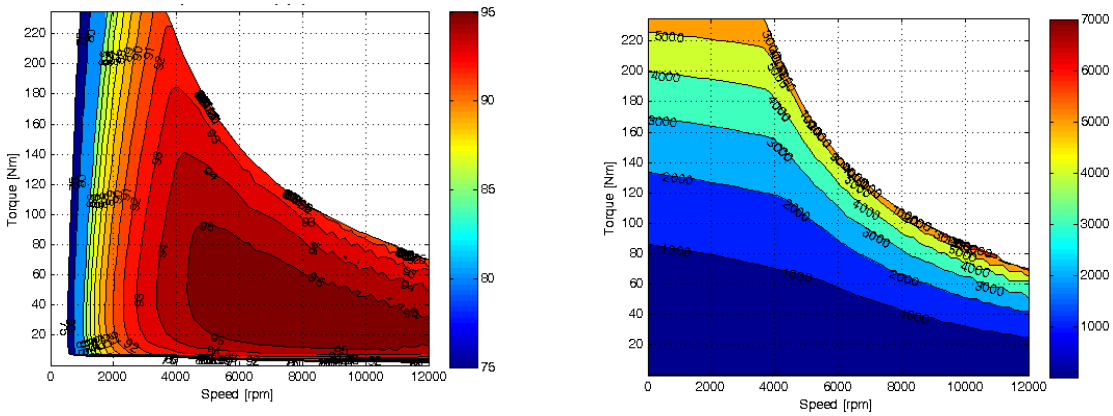

(a) (b)

Figure 7.19 - Efficiency (a) and loss (b) maps of the FASR example in Figure 7.15

In the loss maps of the three motors, the torque profile at rated current i_1, that is common to all the designs, is white lined, whereas the upper profiles of the maps, that are determined by the overload current i_0, are reported in black. The overload area of both the Magnet-Assisted SR motors is larger as said, if compared to the one of the SPM design example.

The maps of Figures 7.18 and 7.19 put in evidence that the losses of the Nd-PM Assisted SR motor and the FASR one are progressive with the load torque at all speeds, whereas the losses of the SPM drive (Figure 7.17) are not, except for very low speed. In fact, as soon as the speed increases, the SPM design suffers from two terms of losses that are independent of the torque. They are: the PM losses and Joule losses due to the de-excitation current component (that is, negative i_d). This explains the curled shape of the constant-loss curves in Figure 7.17a.

On the other end, both the Magnet-Assisted SR motors have little more copper losses (and then higher loss overall) at rated current due to the higher phase resistance. The SPM motor has shorter end-connections and a different copper area, resulting in a lower phase resistance. If the total slot cross section of the Magnet-Assisted ASR designs had been adjusted to make the respective resistances equal to the one of the SPM machine example, the motor would have still had the same continuous power with less Joule losses, but the overload capability would have been partially limited.

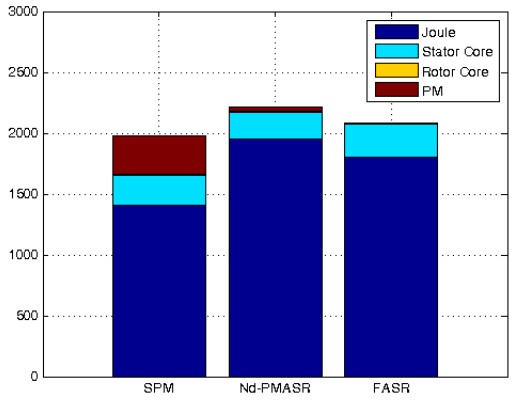

Figure 7.20 – Detail of the motor examples loss in point A (125 Nm, 3500 rpm, mild accelerations and decelerations in urban cycles)

The efficiency maps, reported in the left-hand side of Figures 7.17-7.19, show that all the machines are rather efficient on the entire area of operation: as for the losses, the

SPM motor is more efficient at low speed and much less at high speed.

Loss components are detailed for the three working points A and B put in evidence in Figures 7.17-7.19:

- Point A (125 Nm, 3500 rpm) is representative of mild accelerations and decelerations in urban cycles.
- Point B (20 Nm, 10000 rpm) is cruising power at 80% of the maximum speed.

Point A (Figure 7.20) coincides with the continuous rated condition, for which the three motors have been sized. The corresponding working point in the (i_d, i_q) have been considered along the MTPA locus, as it would be in case of common control techniques, that usually does not implement sophisticate algorithm for loss minimization. Losses have a dominant Joule term. The losses are mainly on the stator and the PM Assisted SR machines are slightly less efficient (≈-0.25%) in this area, also shown in Table 7-II.

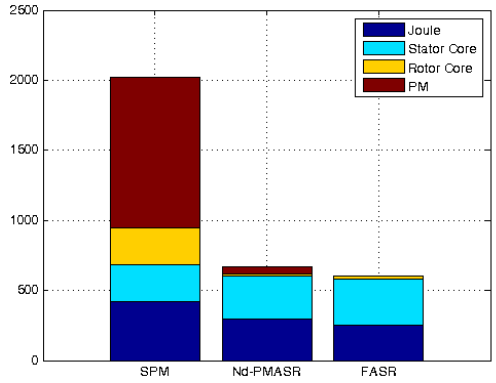

Figure 7.21 - Detail of the motor examples loss in point B (20 Nm, 10000 rpm, cruising power at maximum speed)

Losses at point B (Figure 7.21) show that the SPM Joule term is higher despite the lower resistance, due to the need of de-excitation current, and also the eddy current losses turn out to be penalizing for the overall efficiency.

In case the operating speed specification was lower, the SPM drive might have been helped by the possible adoption of a higher number of poles. If 10 or 14 poles are feasible, the continuous power density of the SPM motor can be higher [13], but still the PMASR machines would maintain a much higher overload capability. Nevertheless, the actual trend in traction is to increase the speed as much as possible for reducing the motor size, and this makes high pole numbers unfeasible.

Before concluding, it is worth highlighting that, in all cases, the two Magnet-Assisted SR machines show similar performance, with little advantages of the FASR configuration.

7.3. REVIEW ON PROS AND CONS OF VARIOUS PM DRIVE TYPES

Surface-Mounted PM and PM Assisted SR machines have been thoroughly compared, for challenging direct-drive applications, namely wind power generation and traction drive-trains.

The specific requirements, typical of each application area, have been put in evidence, together with common features, that are always welcome when dealing with the design of electric motors for high-performance drive.

Cost and mass reduction, as well as high efficiency targets and convenient matches with the power converter, plays a key role in determining the most suited motor technology for both wind power plants and automotive drives. In case of traction drive trains, the drive should meet also specific requirements in terms of both overload and flux weakening capability.

In general, whatever application is considered, it has been demonstrated that the willed torque density level can be achieved both via high-performance (and high-cost) SPM designs and reduced-cost FASR machines, despite the lower energy density of ferrite magnets with respect to rare-earth raw materials.

The achievable cost reductions are significantly high and, above all, rare-earth “free” technology makes the market of electric drives non-dependent on possibly monopolistic policies.

SPM motor configurations serve still as best concurrent solutions, in terms of lightness and efficiency (only at rated condition), even if the expense (i.e., weight and loss) to be paid with economically convenient Magnet-Assisted SR motor topologies is sustainable in most cases.

Specifically, if needed, high-salient PMASR motors have good overload capabilities over the entire speed range, whereas the output power of the SPM motor cannot overcome the continuous power rating independently of the applied current overload.

Dealing with losses and efficiency at high speed, the SPM motor is affected by extra-Joule losses for de-exciting the PM flux and magnets losses. Segmentation in both directions (circumferential and axial) is often required.

Chapter 08

Prototyped FASR lift motors: measurements and validation of the proposed technology

The following section complete the validation process of the modeling theory proposed in Chapters 04 and 05 for the design of Ferrite Assisted Synchronous Reluctance machines.

Two “twin” Ferrite Assisted SR motors were prototyped according to the specifications of an existing rare-earth based electrical machine of the Surface-Mounted type, intended for lift application. The FASR machines, purposely built and tested, serve as down-scaled prototypes of large wind generators, besides carrying out their prime function of direct-drive lift motor.

Chapter 05 dealt with specific features that concur to define the ultimate design of Ferrite Assisted rotor structures, putting in evidence major guidelines and key engineering tradeoffs for matching properly design parameters with strict requirements that are typical of many up-to-date applications.

In particular, the basic idea that led to the final design of the “twin” FASR prototypes is to realize a reduced-cost direct-drive lift motor, competitive with typical rare-earth PM based solutions, above all in terms of money and mass saving.

That is, again the purpose evidenced in the last chapter, where all the comparisons have been performed between machines having the same stack envelope (namely, outer diameter and active length). However, it can be said that starting rare-earth based SPM machines and definitive FASR motors are representative of opposite design philosophy: the first topology is devoted to efficiency maximization, the latter is purposely thought for limiting the mass production costs and making the motor technology independent on

the price instability of rare-earths in the marketplace.

As it can intuitive, one of the goal of this chapter is to quantify the impact of this choice on the drive performance, providing experimental evidences. The results obtained via experimental tests on the prototyped FASR motors will be presented also to evaluate the reliability of the FEA and model predictions.

The reference specifications and geometric parameters of the Ferrite Assisted SR motors, designed in Chapter 05 for the aforementioned direct-driven elevator, will be recalled in the first section of this Chapter. Further peculiarities concerning practical design aspects, skipped so far, will be addressed.

Afterwards, the test-bench setup for the experiments on the "twin" FASR machines will be described. The actual performances of the lift motors will be compared to the predicted ones and commented, with particular attention to the aspects correlated to the machine thermal behavior, that has not been studied via the analytical model. Typical power heat rate figures have been considered instead.

The impact of the operating temperature on the delivered torque will be shown as well.

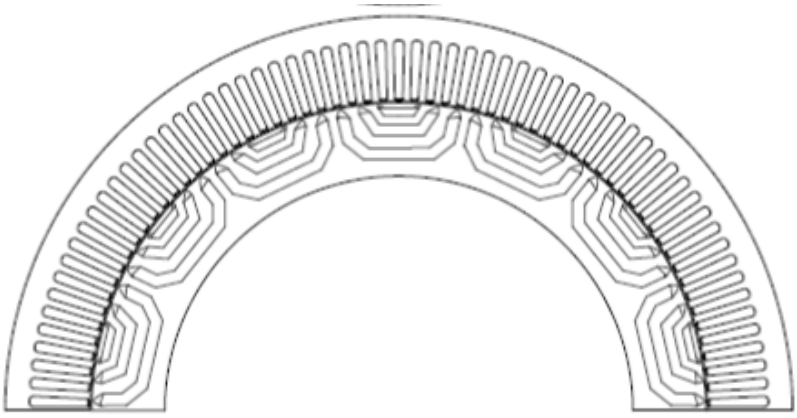

Figure 8.1 – Lamination sketch of the "twin" FASR prototypes built for lift application and tested in the shaft-connected configuration of Figure 8.

8.1. REFERENCE SPECIFICATIONS AND GEOMETRY

The prototype sketched in Figure 8.1 is a Ferrite Assisted SR machine with a multi-layer rotor structure and distributed stator windings. Related specifications are listed in

Table 8-I, where both full- and over-load working requirements are considered. In the same table, a useful set of data is added to remind the reader of the geometric parameters that define the design in Figure 8.1.

TABLE 8-I
MAIN DATA ABOUT THE PROTOTYPED FASR DESIGN

SPECIFICATIONS		
Target torque at rated condition	555	Nm
Required torque at overload	795	Nm
Rotating speed	168	rpm
Maximum steady state temperature for stator windings	125	°C
GEOMETRY - STACK ENVELOPE		
Airgap length g	0.75	mm
Stator outer radius r	0.19	m
Stack length l	0.25	m
Pole pairs number	7	
GEOMETRY – STATOR		
Stator yoke height l_y	0.011	M
Stator tooth width w_t	0.003	M
Stator tooth length l_t	0.013	M
GEOMETRY – ROTOR		
Rotor outer radius r'	148.25	M
Rotor inner radius	0.22	M
MATERIAL		
Ferrite magnets grade	0.37	T
Steel grade	M470-50A	Nm
Stator Winding	Copper	rpm

With a current vector as wide as the thermal limit is, the existing SPM competitor delivers about 9.8 kW, that is 555 Nm at 168 rpm. This working condition corresponds to a steady state operating temperature compliant with the maximum one (i.e. 125°C) tolerated continuously by the stator windings. In case of overload, the lift motor must provide for 795 Nm torque.

Without modifications in the stack envelope dimensions, the FASR prototype is demanded to match the same requirements.

Since in case of ferrite based electrical machines, the low energy density magnets make overload torque figures the most critical to achieve, the convenient “Natural Compensation” condition introduced in Chapter 05 has been referred to the overload

target torque. In other words, the prototypes show a typical "Naturally Compensated" vector diagram when working at overload, whereas at rated condition, they take advantage of a reinforced PM flux linkage to output the willed torque.

The number of pole pairs (that is, seven) has been chosen in order to minimize the Joule loss at overload. According to the analysis proposed in Chapter 05, it means that at given exploitation of the stator core and stator tooth length (i.e. copper area and cost), the efficiency is maximized by finding out an optimal equilibrium between the direct and quadrature current loading components needed to produce the target shear stress. The required *d*- and *q*-axis current amplitudes depend on the pole pitch with an inverse and direct proportional relationship, respectively, and it proves that a pole pairs number that minimizes the overall current loading (that is, the Joule loss) does exist. Additional information about this optimization procedure are reported in Chapter 05.

In particular, as for the prototyped FASR lift motors, the proposed design approach has been applied with the leading purpose of reducing the mass and, above all, cost of active materials. Thus, the copper area has been limited not to "waste" expensive conductive material without great improvements in the efficiency. In Chapter 05, it has been demonstrated that the Joule loss reduction that can be obtained by lengthening the stator tooth flattens over a certain l_t extent. In this case, l_t/r = 7% has been fixed.

TABLE 8-II
STATOR WINDING OF THE PROTOTYPED LIFT FASR MOTORS

STATOR WINDING		
	Prototype a	*Prototype b*
Slot per pole per phase q	3	
Shortening slots n_{sp}	0	1
Number of conductor per slot N	12	
Winding factor k_w	0.96	0.92
End connections factor k_{end}	1.53	1.33
Slot filling factor k_{Cu}	0.4	
Stator resistance (at 20°C)	0.82 Ohm	0.79 Ohm

8.1.1. Stator windings

The FASR prototypes have been addressed so far as "twins", since they do have the same stack envelope, the same stator and rotor lamination.

Moreover, both the machines have distributed stator windings with three slot per pole per phase and 12 conductors per stator slots. Each turn is built up with eight wires, that are put in parallel and have a diameter 0.8 mm long. It says that the slot filling factor, defined as copper area over net slot cross section, is 40%.

The two motors differ only for the layout of the stator windings:

- *Prototype a* has a full-pitched stator winding, as it is schematically shown in Figure 8.2. Its stator is not skewed.

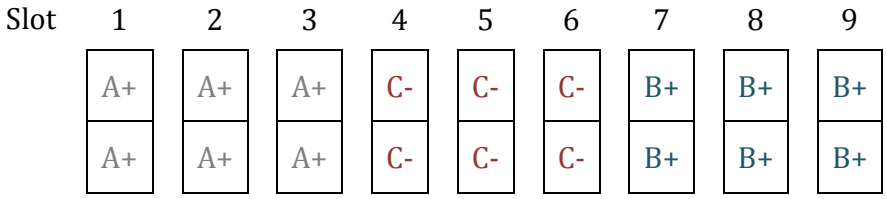

Figure 8.2 – Stator winding layout of *Prototype a* (one pole). The displacement of Phases A, B and C in the stator slots is indicated. The conductors are split in two layer, so both a series and parallel configuration can be adopted.

- If compared to *prototype a*, *prototype b* collocates at the opposite side of the spectrum including possible solutions for torque ripple reduction: the FASR machine has a short-pitched winding (see Figure 8.3) and the stator is conveniently skewed.

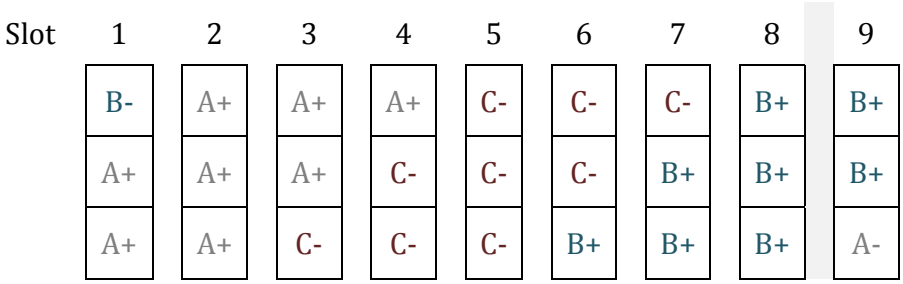

Figure 8.3 - Stator winding layout of *Prototype b* (one pole). The displacement of Phases A, B and C in the stator slots is indicated.

By shortening the stator winding, the torque waveform with respect to the rotor angle is characterized by a minor harmonic content and the end-connections are shorter, thus lighter and less penalizing in terms of Joule loss. As a consequence, the phase resistance of *prototype b* is 96% of the one shown by the "twin" *prototype a*. However, the winding factor of the short-pitched winding machine is less advantageous (about -

4%) than the one of *prototype b*, requiring a wider current vector to produce the willed magnetizing flux. It results on a slightly worse overall efficiency of *prototype b*, despite the lower resistance.

Table 8-II collects all the data concerning the stator windings of the prototyped SR machines, assisted via Ferrite magnets.

In the following, the discussion will focus on the full-pitch winding FASR motor *prototype a*, with no significant loss of information in terms of both validation and comparison purposes.

8.1.2. Fine tuning of the final design rotor lamination

The definition of the rotor and magnets geometry represents one of the most critical point, when dealing with the design of Magnet Assisted SR machines.

As suggested by the analysis developed in Chapters 04 and 05, a convenient multi-layer rotor configuration with three rotor flux barriers and good magnetic insulation properties ($l_{a,pu}$ = 0.42) has been provided for the prototyped lift motors. The layers have been displaced at the airgap regularly and the number of rotor slots per pole pairs (n_r = 14) has been matched suitably with the number of stator slots for torque ripple minimization [55], [57].

TABLE 8-III
RORROR LAMINATION OF THE PROTOTYPED LIFT FASR MOTORS

ROTOR GEOMETRY – PER UNIT DESIGN QUANTITIES		
Rotor slots per pole pair n_r	14	
Rotor flux barriers n	3	
Per-unit rotor insulation $l_{a,pu}$	0.42	
ROTOR GEOMETRY – ADDITIONAL PARAMETERS		
Anisotropy ratio	4	
Magnets volume	0.0023	m^3

The rotor layers are filled in with a ferrite material, whose BH characteristics are presented in Figure 8.4 in correspondence of different temperatures. The needed PM grade has been selected in order to fulfill the so called “Natural Compensation” condition at overload current, with reference to a temperature level (that is, 100 °C) representative

of worst case operating conditions.

Chapter 04 outlined some useful guidelines, capable of making the design of the rotor flux barriers (i.e. of the magnets) more straightforward, once the aforementioned per-unit parameters (recalled also by Table 8-III) are set.

- Specific rules were suggested to choose the constant length of each layer, according to the selected rotor magnetic insulation, sum of all the flux barriers thicknesses.
- Besides, practical tips were proposed so to fix proper proportions between the layer widths.

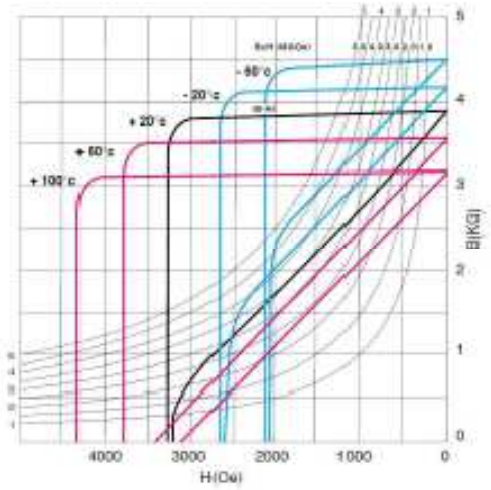

Figure 8.4 – Selected PM grade for the prototyped FASR lift motors, whose lamination is sketched in Figure 8.1.

However, when passing from an ideal geometry, as the one sketched till now for modeling one rectified FASR pole, to actual rotor designs, further features of practical relevance have to be taken into account.

Among the others, the following design aspects play a key role:

- the definition of the rotor lamination, meaning the most convenient balance “air versus iron”.
- the definition of the flux barriers shape, that stands also for the way of arranging the magnets inside the rotor with minimum manufacturing effort.
- the definition of the magnetic structural ribs according to the rotating speed of the machine.

Fixing a target value for the exploitation of the rotor core, in terms of flux density, represents a common and opportune practice to prevent that iron saturation effects impact too badly the achievable performance of Magnet Assisted SR machines in terms of torque density and Power Factor.

Similarly to the design of the stator yoke, if the *q*-axis flux is nearly zeroed by the PMs action, as it is the case with effective PM-Assisted designs like the prototyped FASR machines, the rotor flux guides are interested mainly by the *d*-axis flux. Thus, the goal flux density B_{fe} is respected in the rotor if the whole iron flux guides are as thick as the stator yoke is, namely as thick as decided by the product of the ratio b ($=B_{gap,d}/B_{fe}$) by the pole pitch a.

As for the FASR prototypes, this "rotor yoke" equivalent height has been conveniently divided up between the various iron flux guides, taking into account that each rotor flux guide is demanded to carry on a different portion of the overall magnetizing flux. As a result, the rotor lamination of the FASR prototypes shows iron flux guides, that are progressively thicker while getting close to the *d*-axis. As it is evidenced by the sketch in Figure 8.1, the lengths of the iron flux guides are kept as constant as possible throughout their spans, not to introduce local saturation phenomena.

Also the flux barriers, filled in with magnetic materials, are constant tubes, not to introduce weaker points prone to demagnetization. Moreover, the rotor layer are shaped so that the magnets, they house in, can be arranged in a convenient way also in case of large mass productions. The tip areas are not filled in with ferrite, since it would tend to be demagnetized very easily and thus the additional magnetic material would result wasted in some way.

Last, the relatively low speed level (168 rpm), fixed for this application, does not require to add in the rotor lamination of the prototyped FASR motors inner mechanical ribs, besides the outer inevitable ones. It has been verified that with airgap structural bridges, 0.5 mm wide and 0.5 mm long, the mechanical stress figures are compliant with the limit values typical of steel materials. So, inner magnetic ribs have not been provided for, not to penalize the electromagnetic design. In fact, FASR machines do show the advantage of having the PM flux concentrated in the airgap thanks to their multi-layer

rotor structure, but in case of thick mechanical bridges this effect is significantly reduced.

8.2. EXPERIMENTS

During the experimental tests, the "twin" FASR machines described in the previous section were shaft connected, as shown in Figure 8.5.

The respective converters were back to back connected, with the dc-link in common. Their prime control board, programmed via a FPGA device, is interfaced with an external dSpace control board, which actually regulates the machines' current vector and serves as main instrument for logging and storing the experimental data of interest.

The two Ferrite Assisted SR machines are equipped with standard encoders (VSF60A-BHP0-S02), which provide for an accurate measurement of the rotor angular position, estimated with an uncertainty of 0.077 electrical degrees.

Figure 8.5 – Two FASR "twin" prototypes, shaft connected on the test rig. A torque-meter is interposed between the two motors.

A torque-meter (HBM-T40B) was interposed between the two FASR prototypes and two power analyzers (Zimmer-LMG500) were used to log the electric quantities at the two machines' terminals. So, it was possible to carry out a precise evaluation of the power loss contributes.

Both continuous and overload operations were tested, with the direct measurement of the stator temperatures: namely, the chassis temperature and the winding temperature, verified in diverse points to look for possibly hot spots. The estimation of the PMs temperature is obtained via recurrent samples of the back electro motive force

and the comparison of this test value with a reference measurement got at the machine start-up (that is, when the magnets, together with the whole system, are as cold as the ambient is).

8.2.1. Flux linkage curves

The flux linkage curves (Figure 8.6) and the torque one (Figure 8.7) have been identified over the (i_d, i_q) plane, following the experimental procedure that will be introduced in Chapter 10.

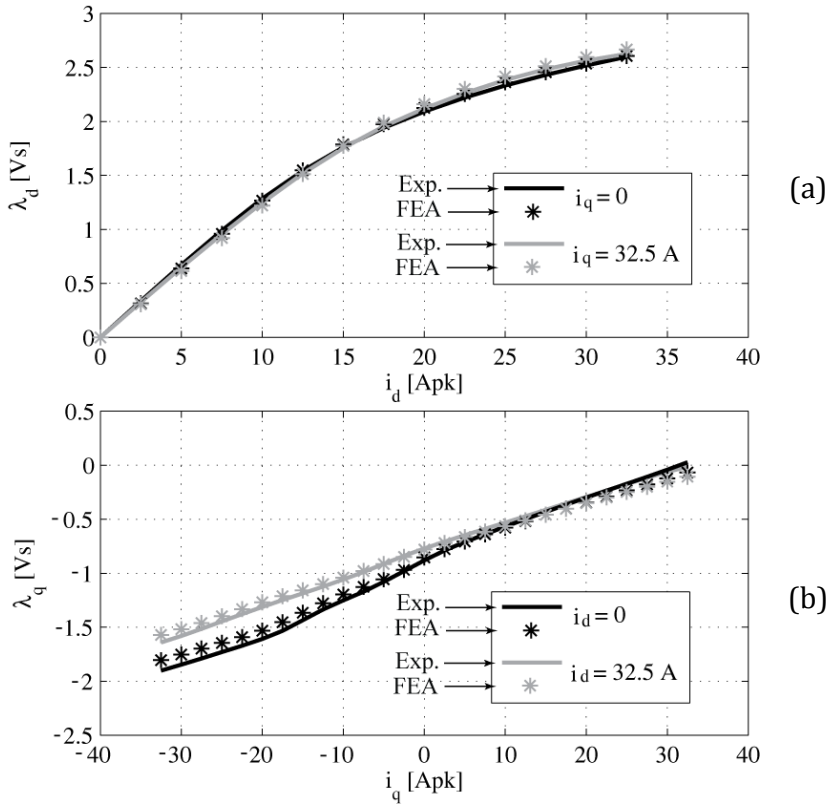

Figure 8.6 - *d*- and *q*-axis stator flux linkages of the twin prototypes of Figure 8.5. Both the FEA results and the experimental data refer to a stabilized value of the operating PMs temperature (that is, 84°C).

Both FEA and experimental data in Figures 8.6 and 8.7 refer to the same (constant) value of the PMs operating temperature. In fact, during the experimental identification of the magnetic model, the thermal conditions of the machine were conveniently stabilized. The copper temperature was maintained constant and equal to 100°C, meanwhile the

PMs operating temperature was around 84°C, as proved by the repetitive monitor of the back electro motive force.

In Figure 8.6, the 2D FEA flux linkages do match quite well the experimental ones. The leakage fluxes in the cast iron stator chassis are not negligible in this case and they were included in the FE model. Conversely, if compared to the other contributes, the end connections flux linkages are small and they were not modeled.

Anyway, since all the leakage fluxes do not contribute to produce the torque, the accordance between FEA and experiment is always good when comparing the torque, as done in Figure 8.7, at given current amplitudes and variable current arguments.

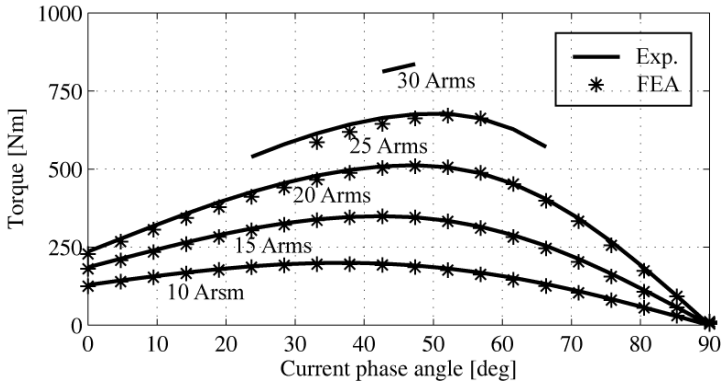

Figure 8.7 – Torque curves of the "twin" prototypes of Figure 8.5 at constant current amplitude and variable phase angle. Both the FEA results and the experimental data refer to a stabilized value of the operating PMs temperature (that is, 84°C).

The results of Figure 8.6 show also that both the *d*- and *q*-axis flux linkages are just merely affected by the current on the heteronymous axis, at least in the area of interest for the control (that is, $i_q \geq 0$). Especially for the *d*-axis flux linkages, it occurs thanks to the choice of "Natural Compensation". So the experimental results confirms the theoretical discussion.

8.2.2. Performance verification at rated and overload conditions

A detailed list of the experimental results got testing the overload capability of the FASR prototypes is reported in Table 8-IV, for a fair comparison to both analytical and FEA data.

As it can be seen, a very good matching has been obtained between all the experimental, FEA and model results.

According to the literature, FEA is confirmed to be a reliable method of analysis, capable of predicting with good accuracy the actual performance of the ultimate design.

TABLE 8-IV
COMPARISON OF EXPERIMENTAL, FEA AND MODEL DATA WITH THE "TWIN" PROTOTYPES OF FIGURE 8.5 WORKING AT OVERLOAD OPERATING CONDITIONS

PERFORMANCE VERIFICATION AT OVERLOAD				
	Exp.	*FEA*	*Model*	
Copper Temperature	100			°C
Estimated PMs Temperature	84			°C
Torque	791	799	795	Nm
Current	40	40		Apk
Current phase angle	53.3	61.0		deg
Line Voltage	230	-	-	Vpk
Power Factor	0.85	0.87	0.87	
d-axis flux linkage	2.34	2.36	2.33	Vs
q-axis flux linkage	-0.01	-0.015	0	Vs
Joule loss	2660	-	3134	W
Core loss (stator + rotor)	300	297	283	W
Efficiency	79.0	-	-	%

Finite element models serve also to conveniently refine the data obtained via the equations proposed in Chapters 04 and 05. As already discussed in the previous Chapters, the analytical model developed for the optimal design of Ferrite Assisted SR machines is very effective, since it does orient the designers to the most appropriate solutions by means of general guidelines, suitable for machines of all sizes and applications. Moreover, it provides for closed-form formulas to determine all the design variables and performance indicators of the machine. Table 8-IV shows that the design quantities are predicted by this simplified model quite satisfactorily, except for the optimal current phase angle and the expected Joule loss.

The former is underestimated by the model, since the rotor core saturation effects contribute to modify the Maximum Torque Per Ampere locus in the (i_d, i_q) plane. However, it is worth pointing out that the current amplitude, needed to produce the

willed torque, is predicted with good accuracy. This is also thanks to the corrective factor proposed for the *d*-axis current loading, that attempts to compensate for the stator back iron magnetic potential drops. A_d is increased by 14%, in case of the "twin" prototypes of Figure 8.5.

On the contrary, the model overestimates the Joule loss, because of the adopted rectified geometry, which schematically models parallel side slots referring their constant widths to the (shorter) bore radius. Anyway, the model estimation results "safer" from this point of view. This is valid for the prototypes under test, even if the additional core losses was disregarded by the model.

TABLE 8-V
EXPERIMENTAL RESULTS WITH THE "TWIN" PROTOTYPES OF FIGURE 8.5 WORKING AT RATED OPERATING CONDITIONS

MACHINE PERFORMANCE AT THERMAL RATED CURRENT			
	Cold	*Steady State Thermal Condition*	
Copper Temperature	20	125	°C
Estimated PMs Temperature	20	105	°C
Torque	572	544	Nm
Current	30	30	Apk
Current phase angle	49.3	49.3	deg
Line Voltage	275	266	Vpk
Power Factor	0.9	0.85	
d- axis flux linkage	2.00	2.05	Vs
q-axis flux linkage	-0.44	-0.26	Vs
Joule loss	1107	1595	W
Core loss (stator + rotor)	112	112	W
Efficiency	88.0	82.1	%

Table 8-V collects the experimental data, describing the thermal and electromagnetic behavior of the prototyped FASR lift motor at rated operating conditions. The continuous current amplitude is limited to 30 Apk (that is, -25% of the overload current level) by the maximum steady-state temperature allowed for the stator windings.

Before being warmed-up, at cold temperature (namely, 20°C), the FASR prototype delivers 572 Nm (that is, -38% of the overload torque), showing a Power Factor (0.9)

that is very convenient, since the PM flux linkage is "reinforced" with respect to the one that would fulfill the "Natural Compensation" conditions at this working load and temperature. The voltage vector phase angle and the current one are then extremely close to each other.

At steady state thermal condition, the copper temperature is around 125°C, thus compliant with the upper limitation imposed by the stator winding type. Conversely, the magnets temperature is estimated to be about 105°C from the back electro motive force monitoring. This causes a de-rating of the output torque, which decreases by 5% with respect to the one provided for at cold temperature. Even if the remanence of ferrite magnets varies along with the temperature according to a coefficient (e.g., -0.2%/°C) that is more disadvantageous if compared to the one (around -0.11%/°C) typical of rare-earth PMs, Ferrite Assisted SR machines, like the prototyped FASR motors in Figure 8.6, do not turn out to be penalized heavily by the temperature increase, in terms of torque production, because they do not rely completely on the magnets to produce the required shear stress and also because the magnets are not as close as the rare-earth PMs of SPM configurations are to the stator slots and thus work at lower temperature levels.

8.3. CONCLUSION

With reference to a direct-drive lift motor, this chapter presented some experimental results that validate the approach proposed in Chapters 04 and 05 for the optimal design of Ferrite Assisted SR machines.

The experimental data are in very good accordance with the results coming from the Finite Element Analysis and prove also the accuracy of the analytical model in predicting meaningful performance indicators of the ultimate design.

As a consequence, it can be said that the general conclusion drawn in the last Chapter when comparing competing motor topologies with respect to diverse application fields are absolutely valid, even if based on the analytical and FE results.

Chapter 09

Introduction to Part II: "Industry-friendly approach to the magnetic model identification and unified control of PM motor drives"

As it has been frequently recalled throughout this work, Permanent Magnet Synchronous motor drives are synonymous with high-performance for electric motion and energy conversion. Nevertheless, their deep penetration in practical application fields is strictly dependent on the ability of designers and researchers to comply with the requirements coming from the industrial world, that are, above all, cost-reduction and opportunities to adopt straightforward and universal design procedures.

The first part of this thesis dealt with the design of PM Synchronous motors, looking for reduced-cost machines, based on cheaper (and weaker) ferrite magnets, but still competitive with rare-earths based motor configurations. The design tasks have been approached via comprehensive procedures, capable of orienting manufacturers and designers, starting from few input data.

Anyway, when dealing with electrical drive trains, an integrated motor design and control design is mandatorily required for the whole technology to be accepted industrial-wise.

Besides the electrical motor, the other hardware components to be considered are: the power converter and the programmable microprocessor. The microprocessor runs a real-time algorithm that commands the inverter to supply (or absorb, in case of a generator) the proper 3-phase currents so to obtain the willed torque and speed evolution from the electrical machine.

The control process is based on few standard feedbacks (phase currents, DC voltage supplying the inverter, motor position) for all electrical motor drives, but sometimes it is necessary to optimise the control algorithm case by case, depending on the machine type. Moreover, the control does massively depend on the knowledge of the motor magnetic model [84] and it usually requires to be properly calibrated.

Accordingly, the industry's belief is that new drives generally need a tailored control software and cumbersome calibration involving test facilities, time and PhD-level expertise. This is unwanted.

During recent years, many authors, from academia and R&D environments, have worked towards a unified control version, suitable for PM motor drives of all kinds [85]-[86], with excellent results.

Still, the weak point of the knowledge of the motor model remains, in all the literature. There are two opposite philosophies: either to use a model that is too complicate [87] or one that is too simplified [86].

The former is not practical due to the following reasons:

- identification must reproduce operating conditions: inspection signals must involve power, requiring a proper test rig with an inverter, both adapted for each drive size.
- the measurement hardware and procedure are not standardized.
- the model is non linear, and its parameters vary with operating temperature and speed.

As an alternative to experimental identification, finite element calculation is not accurate enough and requires anyway software equipment, expertise and time. Simplified models can be achieved otherwise, e.g. from datasheets and impedance-meters, but the result might be unsatisfactory.

This research investigates a unified control strategy, suitable for PM motor drives of all kinds with minimum need of calibration and based on a simplified commissioning stage, which can be also performed automatically and on-site for the sake of standardization and industrialization. The results are collected in Chapters 10 and 11.

Chapter 10

Experimental approach to identify the magnetic model of PM Synchronous machines

As said, this research ends with the investigation of a unified control strategy suitable for Permanent Magnet synchronous motor drives of all kinds and a preliminary commissioning process for the automated identification of the machine magnetic model.

The project has been carried out working towards an industry-friendly version of the whole algorithm, possibly appropriate for commercialization.

According to this leading idea, the control technique has been made robust against machine parameter variation and usable with minimum need of calibration. On the other hand, the experimental approach for identifying the magnetic model of the electrical machine has been completely automated, while being made reliable, quick and repeatable with minimum hardware requirements.

The next Chapter will discuss the enhancements introduced to generalize and simplify the control tasks. This Chapter focuses on the automation of the procedure to identify the magnetic model of PM Synchronous machines.

The magnetic model is the relationship between the machine currents and stator flux linkages, in a specific reference frame. As known from the literature, the most convenient reference frame used to relate machine flux linkages and currents is the rotor synchronous frame (d, q).

Synchronous PM motors exhibit relationships between flux linkages and phase currents that can be highly non-linear, due to core saturation phenomena and cross-coupling effects between the direct and quadrature axis components. Interior PM

Synchronous motors and higher salient Magnet Assisted SR machines are renowned for being extremely non-linear, in terms of magnetic behavior [88]-[94]. However, nowadays even isotropic configurations, such as the ones of the Surface Mounted type, show similar non-linear output characteristics [95], [96]. This is because most of the currently adopted PM-based motor topologies are compact and heavily loaded designs, that face challenging and demanding up-to-date applications, such as traction, home appliances and power generation for renewable systems.

The relationships between flux linkages and phase currents of Synchronous PM motors are heavily influenced by the operating temperature, besides being highly non-linear.

As a result, a reliable identification procedure capable of stabilizing the PMs temperature during the test is required for both control and validation purposes.

With the machine magnetic model being available from experiments, the motor performance can be calculated with precision and the results can be exploited for control purposes. In particular, the Maximum Torque per Ampere (MTPA) and the Maximum Torque per Volt (MTPV) control trajectories can be identified in the (i_d, i_q) plane. Moreover, both analytical and Finite Element method can be validated. The comparison of motors provided by different manufacturers is also possible, without the need of insights about actual rotor and stator laminations.

This Chapter proposes an experimental method to evaluate the machine flux linkages, together with their relationship to the machine phase currents, using estimates of the phase voltages, so that no voltage measurements are needed. Stator resistance and inverter voltage drops are compensated for and the issue of the iron loss impact on the machine magnetic model is solved.

Alternative experimental setups, each of them distinguished by diverse hardware requirements, will be presented. Specifically, opportunities to perform the identification process as a quick one-time self-commissioning process with no lack of accuracy in the output characteristics have been pursued during this project and the results will be discussed in this Chapter.

Independently on the hardware configuration, it will be also suggested how to control the PMs temperature during the identification procedure by properly alternating active and idle states, since it is well known that the magnet temperature is a main cause of detuning of the motor model.

Throughout the following analysis, experimental results on various test machines will be provided for, in order to confirm the consistency of the approach.

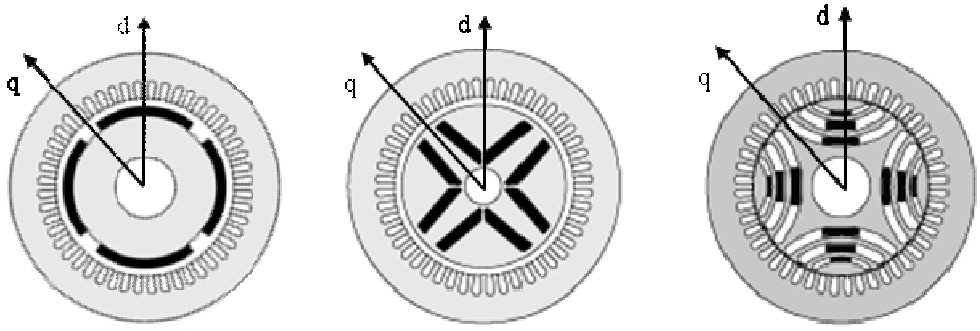

SPM IPM PMASR

Figure 10.1 – Different PM rotor configurations and related synchronous *dq* reference frames.

10.1. BASICS OF THE IDENTIFICATION METHOD

The prime goal of the identification test is to find out the functions (10.1) that relate the machine currents to the steady-state flux linkages.

$$\lambda_d = f_d(i_d,\, i_q)$$
$$\lambda_q = f_q(i_d,\, i_q) \tag{10.1}$$

In (10.1), both machine currents and stator flux linkages are conveniently expressed via the respective *d*- and *q*-axis components, synchronous to the rotor. In case of Permanent Magnet based Synchronous motor drives, the direct axis is oriented along with the PM flux linkage vector, as it can be seen in Figure 10.1 with reference to diverse rotor configurations. For the sake of generality, also Permanent Magnet Assisted SR machines will be indentified according to this PM-like *dq* axes, even though they are preferably analyzed with the *dq* axes following the SR approach in many applications.

The area of interest for the evaluation of the stator flux linkages in the *dq* current plane includes positive i_q values and negative flux-weakening i_d values, as in Figure 10.2.

However, for all PM machines, it is convenient to extend the identification area into the flux-intensifying region, colored in gray in Figure 10.2, for taking into account transient working points, such as, for example, the ones corresponding to torque reversal. This is helpful either for flux controlled drives or drives adopting a flux-observer [97], [98].

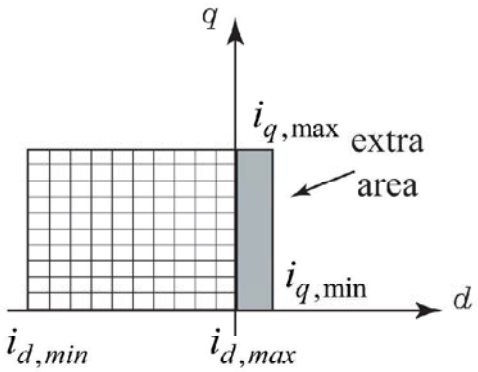

Figure 10.2 – Area of interest for the identification of the stator flux linkages in the (i_d, i_q) current plane.

The identification area must include all the operating conditions of the drive, that is partial-, full- and over-load current levels must be considered. Furthermore, the limits $i_{q,max}$ and $i_{d,min}$, highlighted in Figure 10.2, must be compliant with demagnetization issues and thermal constraints.

10.1.1. Evaluation of the stator flux linkages from the voltage vector

In correspondence of each (i_d, i_q) current vector belonging to the mesh grid of Figure 10.2, the *d*- and *q*-axis stator flux linkage can conveniently estimated from the quadrature and direct components of the voltage vector, respectively.

The procedures for the experimental evaluation of the stator flux linkages from the voltages can be divided into:

- standstill techniques;
- constant or variable rotating speed methods.

The standstill techniques are usually locked rotor methods, well known in particular for wound-field synchronous machines [99]-[100]. During the test, voltage pulses are applied to one axis (e.g. the direct one), while a constant current is controlled along the other axis (e.g. the quadrature one). This procedure is effective, but shows significant

drawbacks. The applied voltage vector needs to be integrated and this operation is prone to drift due to offsets, thus critical. Moreover, the voltage level to be handled by the inverter during the tests is very low and then potentially imprecise, especially for motors with a low per-unit resistance.

As an alternative, the stator flux linkages (10.2) can be evaluated starting from the voltages v_d and v_q with the machine being current controlled according to fixed (i_d, i_q) values and rotating at a certain speed level ω/p for having induced electromotive forces in the three phase stator windings.

$$\lambda_d = +\frac{v_q - R_s i_q}{\omega}$$
$$\lambda_q = -\frac{v_d - R_s i_d}{\omega} \tag{10.2}$$

The resistance voltage drops $R_s\, i_d$ and $R_s\, i_d$ are required to be compensated for, as it will be discussed in the next subsection.

In (10.2) the voltage components v_d and v_q can be either measured or estimated.

- Voltage measurement does represent a critical issue. The most accurate but difficult to tune solution is based on analog measurement of the motor terminal voltages, then analog rotational transformation, analog filtering of the PWM components and then analog to digital conversion of the obtained d- and q-axis components.
- A cheaper solution reconstructs the voltages from the inverter duty-cycle commands and the dc-link voltage measurement: a proper inverter dead-time compensation is mandatory in this case.
- An intermediate solution can be to measure the duty-cycles of the three phase voltages by means of three voltage comparators and a time capture unit.

10.1.2. Inverter dead-time and resistive voltage drops

In order to compensate for both the voltage drops on the stator resistance and the on-state and dead-time inverter voltage errors, motoring and braking mode can be conveniently alternated. It implies that the machine under test, and possibly the one that

serve as speed controlled servo motor drive, must be regenerative or have an adequate braking chopper.

If the machine is run first in motoring mode (meaning that the controlled current is $i_d + j \cdot i_q$) and then in braking conditions (that is, the complex conjugate current vector $i_d - j \cdot i_q$ is impressed), the average between the voltage vector in motoring and braking mode turns out to be independent on the dissipative voltage drops. Thus, the evaluation of the stator flux linkages from the voltage vector components in the synchronous reference frame gets straightforward and does not result affected by errors.

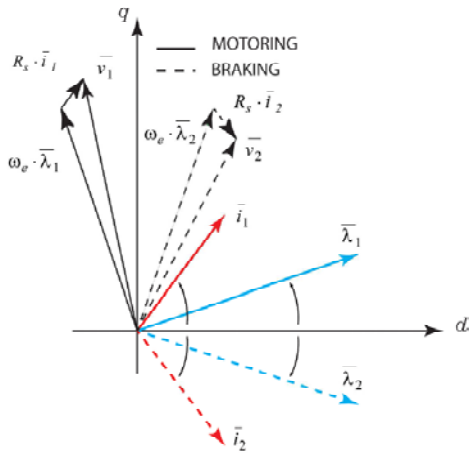

Figure 10.3 – Steady-state vector diagrams (current, flux linkage and voltage) of PM machine working in the flux-intensifying region in motoring (subscript 1) and braking (subscript 2) conditions: current vectors 1 and 2 are complex conjugates and also the respective flux linkage vectors are.

In Figure 10.3, with reference to a generic machine working for example in the flux-intensifying region, it is shown that two complex conjugate current vectors, namely 1 and 2, produce complex conjugates flux linkage vectors and the respective voltage vectors do differ only in the sign of the resistive drop.

In Section 10.3, it will be shown how to regulate the temperature during the identification test, attempting to maintain the temperature level substantially unchanged throughout the whole experiment. Anyway, as suggested in [101], an additional countermeasure can be adopted to avoid that temperature drifts affect the effectiveness of the compensation method for the resistive voltage drops.

Besides the two conjugate current pulses needed for alternate motoring and

braking, a third and final test pulse can be included, again in motoring, to eliminate possible resistance variations during the first two pulses, as represented in Figure 10.4.

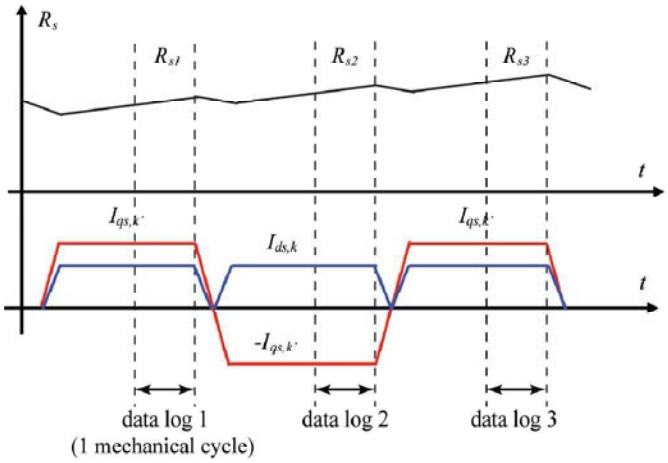

Figure 10.4 – Resistance variation due to temperature during the three-pulses evaluation of a generic point ($I_{d;k}$; $I_{q;k}$): the average of R_{s1} and R_{s3} equals R_{s2}.

In case the temperature varies during the current pulses, the average temperature of the two motoring tests (first and third pulses) will be equal to the average temperature of the braking test (pulse number two), and so it will be the stator resistance value, as represented in Figure 10.4.

10.1.3. Proper selection of the test speed

The choice of the test speed level represents a key issues. During the identification test, the speed should be:

- as high as to produce significant levels of v_d and v_q, with a good signal to noise ratio in case of voltage measurement.
- as low as needed for having a negligible contribution of the speed dependent loss, that is iron loss and PM loss.

A good tradeoff value can be conveniently identified, depending on the application.

10.2. IDENTIFICATION PROCEDURE WITH DIVERSE HARDWARE SETUPS

The machine stator flux linkages (10.2) can be identified in correspondence of the desired (i_d, i_q) inspection area, similar to the one in Figure 10.2, reconstructing the

voltage vector from the measured value of the dc-link voltage and the duty cycle commanded by the control. During the identification test, the machine under test is required to be controlled at constant (i_d, i_q) current values, while being kept in rotation, so that electro motive forces are induced in the stator windings.

The stator flux linkages can be evaluated via diverse hardware setups:

- The machine under test can be coupled to a servo drive, as shown in Figure 10.5, that serves as speed controlled machine.

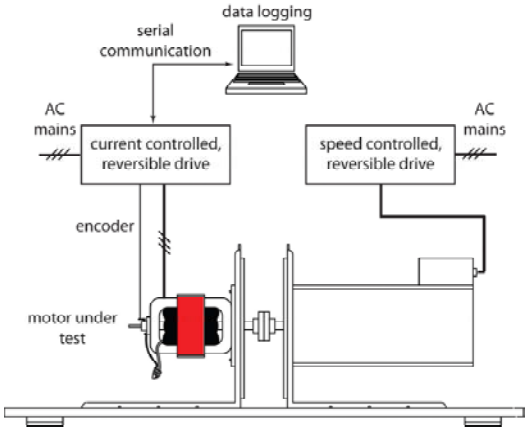

Figure 10.5 – Scheme of the test bench equipped with a speed-controlled servo drive, besides the motor under test

- As an alternative, the drive under test can duplicated. That is, a "twin" prototype is made accessible and shaft connected to the motor under test.

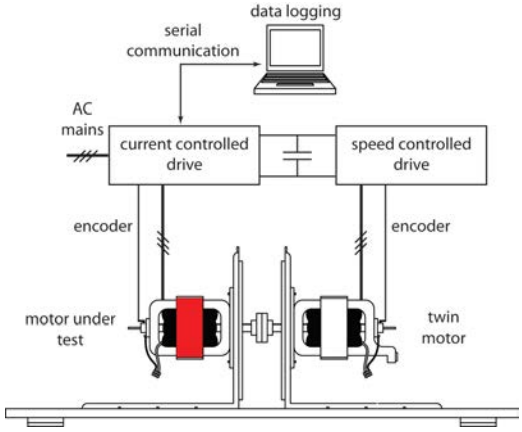

Figure 10.6 - Scheme of the test bench equipped with two "twin" prototypes shaft connected and the respective power converter back-to-back connected to a common dc-link.

The power converters of the two machines are back-to-back connected to a common dc-link. In this case, represented by Figure 10.6, the drive under test is current controlled, while the other one is speed controlled

- Only the machine under test, equipped with its power converter, is available, as it is pointed out by Figure 10.7.

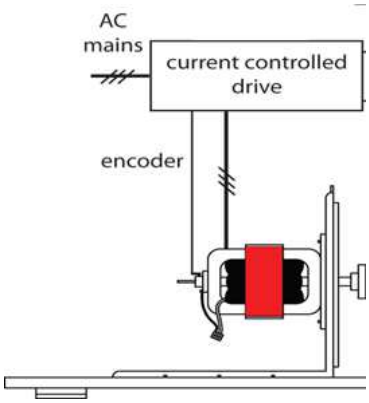

Figure 10.7 – Test of a single motor drive with no further components via a self-commissioning procedure, suitable to be performed on site.

In this case, the rotor has not to be locked, as for standstill methods. Rather, it is required to be left free to rotate. Motoring and braking modes have to be conveniently alternated, so to accelerate and decelerate the rotor. Meanwhile the estimation of the stator flux linkages via (10.2) can be performed.

In the following, the aforementioned hardware setups will be compared according to meaningful criteria, namely:

- reliability and accuracy of the results;
- requirements in terms of system components.

10.2.1. Test machine coupled to a speed-controlled servo drive

This former scheme is appropriate for identifying small- up to medium-size machines, when a suitable regenerative servo drive has been set up, as it is typically the case in test and research laboratories.

The torque rating of the servo drive must be redundant with respect to the maximum transient overload torque of the machine under test.

The Machine Under Identification (MUI) is driven at constant speed by the Speed-Controlled Machine (SCM). The MUI is current-controlled with proper patterns of the *dq* current references over the prefixed current mesh grid, alternating motoring and breaking mode, as said. The *dq* flux linkages are conveniently evaluated via the estimate of the phase voltages.

The active test time at each set of currents (i_d, i_q) should be as short as possible, to keep temperature variations under control and reduce the total duration of the identification procedure. On the other hand, current pulses should last as long as needed to guarantee that all unavoidable speed regulation transients are extinguished. Moreover, if the current pulses are sufficiently long, all the measures (voltages, currents, speed) involved in the identification of the stator flux linkages (10.2) can be conveniently logged over one or more mechanical period and then averaged to eliminate any signal component at electrical or mechanical periodicity, including motor space harmonics, inverter dead-time harmonics and defects of mechanical nature such as misalignments and eccentricities.

The robustness of the speed control during the identification of the stator flux linkages makes this evaluation method very precise. However, this procedure is expensive in terms of hardware requirements and this prevents the possibility of performing the experiments on-site.

10.2.2. Test of twin prototypes

The alternative solution of testing shaft connected "twin" prototypes is normally adopted for large machines, exceeding the torque size of typical servo drive based rig.

This dual identification scheme can be somehow preferable because it avoids the need for braking resistors or reversible AC/DC stages. The back to back configuration minimizes the power exchanged with the AC mains and makes it possible to monitor the aggregate loss of the two machines, while the flux linkages are being identified, via the dc-absorbed power.

However, if the two machines are actually identical, this procedure slightly limits the inspected overload current area, which has to be properly restricted so to make the

speed controlled drive capable of effectively regulating the speed at any operating conditions. In other words, with two identical machines there is no torque redundancy, though it would be still welcome.

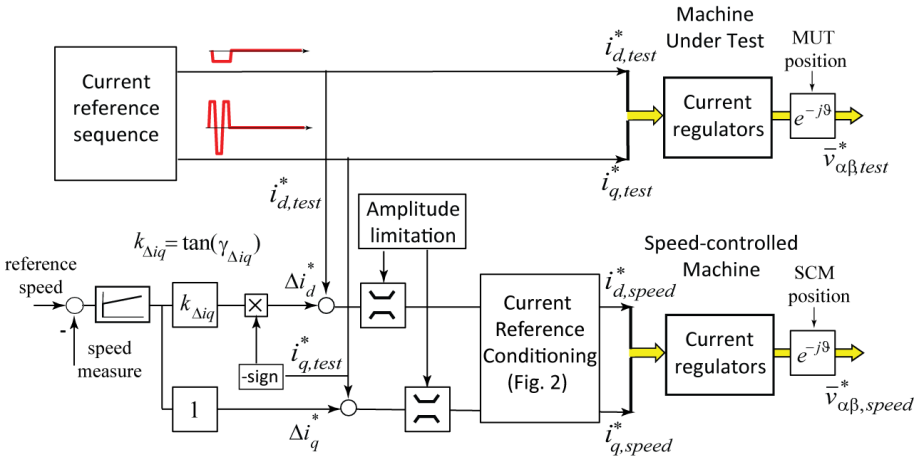

Figure 10.8 - Back to back, feed-forward assisted speed control scheme

Similarly to the standardized procedure implemented in presence of a servo drive running the machine to be identified, here the MUI is again current controlled, while the "twin" prototype, that serves as prime motor, is speed controlled. Each (i_d, i_q) test vector involves repetitive pulses, for alternating motoring, braking and possibly again motoring operation, so to compensate for series voltage drops with no uncertainties consequent to possible temperature drifts.

According to the scheme in Figure 10.8, the MUI references are feed-forwarded to the SCM, and added to the output of the closed loop speed regulator, meaning that a minimum set of data is required before setting up the experimental rig with the two identical prototypes.

In this way, the two machines work with complex conjugate currents at all times, and the speed controller is responsible of corrections only (that is, the vector components Δi_d and Δi_q in Figure 10.8).

The speed loop corrections (Δi_d, Δi_q) are conditioned for moving along a pre-determined phase angle $\gamma_{\Delta I}$, that is 60° in the example of Figure 10.9 which refers to PM Assisted SR machines. In case of SPM machines, the most suited $\gamma_{\Delta I}$ value is 90°; as for

IPM rotor topologies, an intermediate angle between 60° and 90° represents the most convenient choice. Both Δi_d and Δi_q are suggested by the speed loop of the prototyped, that serves as prime motor; then the resultant current references are saturated for complying with the maximum amplitude limitation and eventually conditioned for keeping the torque variations consistent with the sign of the speed regulator's output.

This SCM current conditioning strategy is graphically summarized in Figure 10.9.

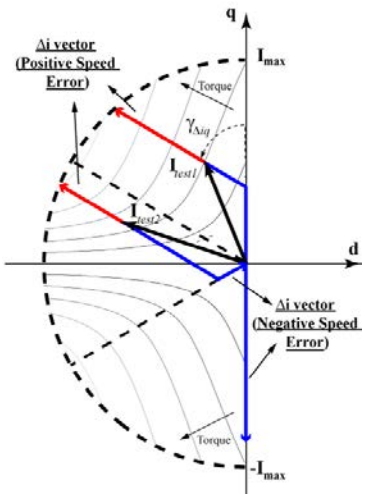

Figure 10.9 - Conditioning of the speed loop generated current reference Δi, starting from two different working conditions to correct speed errors with diverse sign.

Figure 10.10 – "Twin" traction PM Assisted Synchronous Reluctance motors, shaft connected and controlled by power converters having the dc-link in common.

Typical current paths impressed during the identification procedure are presented in Figure 10.11, with reference to the twin PMASR prototypes of Figure 10.10, as an example. The closed loop correction is very light, even during transients, and the speed regulation is scarcely affected by test current variations.

In general, this control and identification method show a stable behavior over the whole identification grid, independently on the drive motor type under test. This represents an obvious advantage.

Besides, since the two drives work at complex conjugate current points most of the time during the experimental test, the dc-measured power gets fairly representative of twice the losses of each one of the two machines. It means that, the efficiency maps of the drive in the (i_d, i_q) plane can be identified easily, while investigating the magnetic

behavior of the machine under test. This additional challenge is of practical relevance for many applications and stands also for a quick and reliable validation method if both analytical and Finite Element results need to be verified.

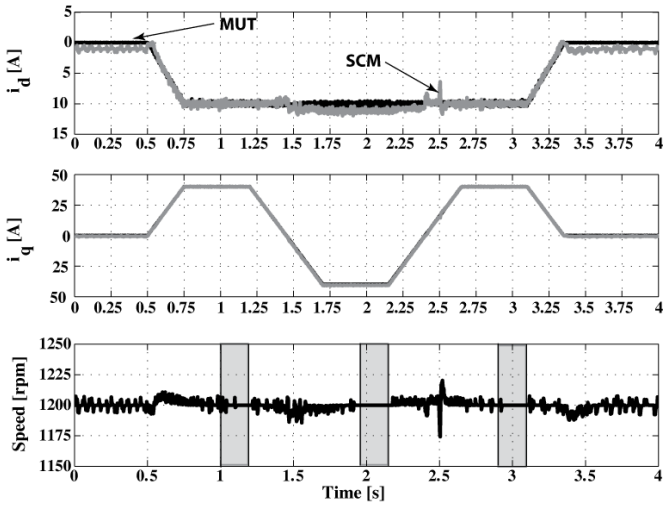

Figure 10.11 - Example of experimental results: identification of the working point Id = -10 A, Iq = 40 A for the "twin" machines of Figure 10.10. The i_q traces of both the MUI and the SCM are undistinguished. The grey boxes indicate data acquisition.

10.2.3. Test of a single motor drive with no further components

The magnetic model of PM synchronous machines can be conveniently identified also by means of a self-commissioning procedure with no further hardware requirements besides the drive to be tested, that is the "electrical motor" plus the "power converter", both available on site.

The MUI is current controlled alternating motoring and braking operating modes with proper timing, so to accelerate and decelerate the rotor between equal speed level, but opposite in sign.

As the rotating speed is increased sufficiently for having electro motive forces of significant amplitude induced in the stator winding, the stator flux linkage can be evaluated via (10.2).

Differently from the constant-speed identification methods, which are stiff towards noise and disturbances coming both from the mechanical setup and the power electronics components, in this case it is worth verifying the accuracy of the results.

At this purpose, the concentrated winding IPM machine in Figure 10.12 was first identified with a standard hardware setup, that is the servo drive reported in the same picture.

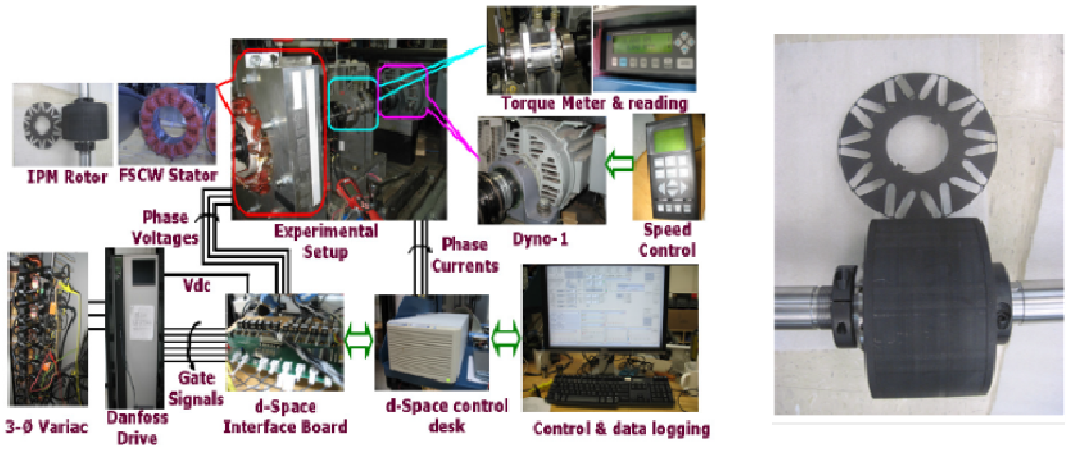

Figure 10.12 – Servo drive benchmark adopted for testing the fractional slots IPM motor, shown in the right-hand side of the picture.

Then, the stator flux linkages were identified over the same current mesh grid during consecutive acceleration and deceleration of the rotor, left free to rotate, following the procedure just described. The results, proving for by the constant-speed "standard" identification technique, and the ones, got via the self-commissioning process, are compared in Figure 10.13, showing very good agreement. In particular, the quadrature axis flux linkages are predicted with good accuracy, whatever the experimental identification procedure is.

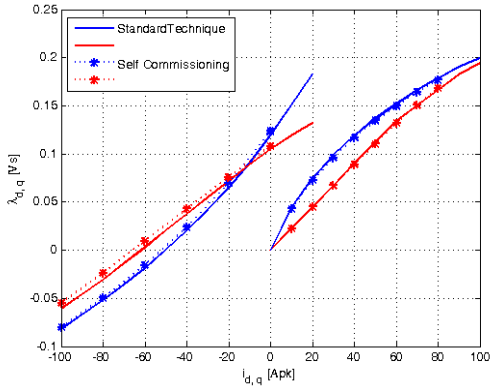

Figure 10.13 – Comparison of the magnetic models obtained by testing the IPM machine in Figure 10.12 (right-hand side) both coupled to a speed controlled servo drive and free to rotate to perform a brief self-commissioning process.

10.3. STABILIZATION OF THE PMS TEMPERATURE

One key contribution of this work is the stabilization and monitoring of the PM operating temperature during the identification of the stator flux linkages. It applies to all types of test rigs.

10.3.1. Control and monitoring of the magnets temperature

Given the target temperature Θ_{test} and the cooling setup, there is a one to one correspondence between the test current amplitude and the continuous operating temperature that this would produce at thermal steady-state. For each Θ_{test}, a circle of amplitude I_θ can be individuated, within the current grid, as represented in Figure . All the grid points outside the circle produce a temperature increase and, vice-versa, all the points inside the circle produce a temperature decrease, during the identification.

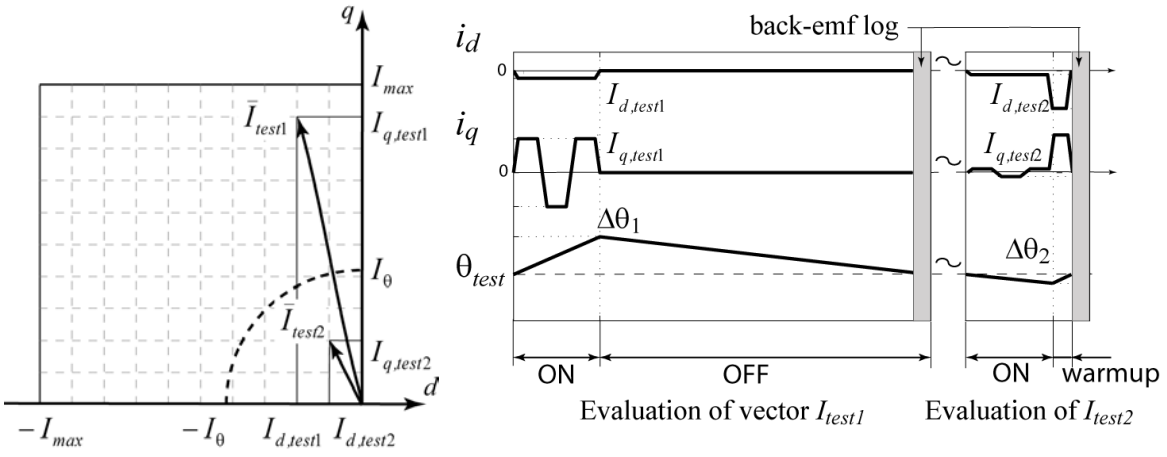

(a) (b)

Figure 10.14 - a) Identification grid. The dashed circle indicates the thermal current. b) current reference profiles for identification at constant temperature, referred to the two example vectors *test1* and *test2*, chosen as examples in the mesh grid depicted in a).

In Figure 10.14b, the pulse sequence of the generic current vector *test1* introduced in Figure 10.14a is shown, adding i_q reversal transients for alternating braking and motoring, as said.

The PM temperature is qualitatively plotted: it increases, while the current pulses are on (t_{on}), and then decreases at the following idle stage (t_{off}). The t_{on} duration is

constant for all the test points over the grid, whilst the zero-current time, t_{off}, has to be associated to the amplitude of *test1* according to (10.3) for recovering from the t_{on} heating completely, as in the figure:

$$t_{off} = \left(\frac{I_{test\ 1}^2}{I_\theta^2} - 1 \right) \cdot t_{on} \tag{10.3}$$

For points inside the circle, such as *test2* in Figure 10.14, the temperature is controlled via a warm-up interval at the highest available current I_{max}, whose duration is:

$$t_{wu} = \left(\frac{I_\theta^2 - I_{test\ 2}^2}{2 \cdot I_{max}^2 - I_\theta^2} \right) \cdot t_{on} \tag{10.4}$$

Both (10.3) and (10.4) assume that stator Joule loss is the only significant loss term, as it is the case here, with the test speed purposely chosen for having negligible core and PM losses.

The PM operating temperature is monitored on-line at the end of each test cycle, as indicated by the grey time windows in Figure 10.14b: in those time intervals, the current is controlled to zero, and the reference voltages account for the no-load back-emf, from which the PM flux linkage can be calculated. In case of PM temperature drift, the off-line calculated intervals (10.3) and (10.4) can be corrected by means of a very slow, integrative regulator.

10.3.2. Experimental validation

Figure 10.15 – Test motors identified at a stabilized temperature level. a) FASR prototypes presented in Chapter 08. b) Other motors for elevator with a Surface Mounted PM rotor configuration

In Figure 10.16 the PM flux linkage estimation is compared to measured

temperature values, either in the stator end-windings or on the motor chassis depending on the drive under test. The test machines, these experimental curves are referred to, are reported in Figure 10.15: the data in Figure 10.16a have been obtained via experimental tests on the FASR prototypes in Figure 10.15a; the results presented by Figure 10.16b correspond to the SPM "twin motors" in the photo of Figure 10.15b.

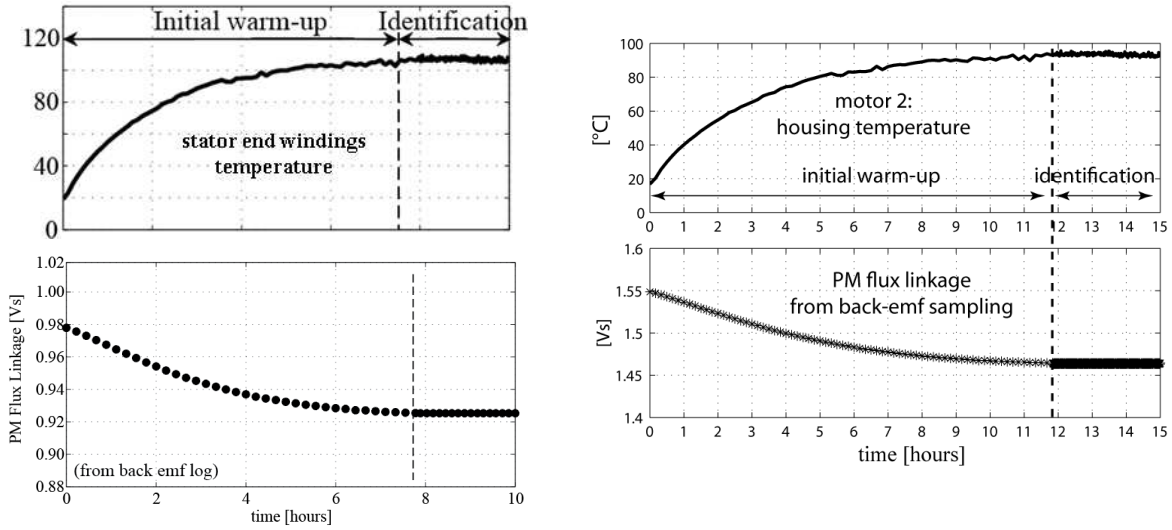

(a) (b)

Figure 10.16 - Correlation between PM flux linkage log and measured temperatures of test motor. a) FASR lift motors shown in figure 3.15a and described in Chapter 08. b) Smaller PM motors for elevator of the Surface Mounted type..

The plots in Figure 10.16 give evidence of the robustness of the PM temperature monitoring. Besides, both in Figures 10.16a and 10.16b, it is pointed out that after the initial warm-up, the PM flux linkage and the measured temperatures are constant during the identification. The initial warm-up takes hours in both examples because of the natural ventilation of all motors. Better cooling setups can reduce the thermal time constant and speed up the tests, as well as warming up at current overload.

Last, Figure 10.18 shows the flux linkage curves of the tested SPM motor, with the housing stabilized at 20°C and 90°C, respectively. Both the direct and quadrature axis stator flux linkages show different behavior at diverse temperature level, because of the role played primarily by the PM flux linkages in determining the flux density core exploitation and, thus, iron magnetic saturation of Permanent Magnet machines of the Surface Mounted type.

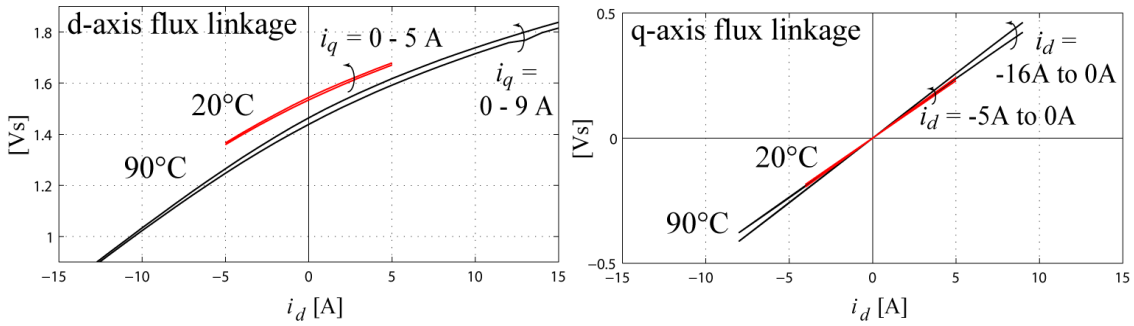

(a) (b)

Figure 10.17 - Flux linkage curves of the SPM motor of Figure 10.15b measured at 20°C and 90°C housing temperature.

Figure 10.19 refers to the prototyped FASR lift motor, comparing its magnetic model with the PM temperature stabilized at 20°C and 84°C. The Maximum Torque per Ampere locus is found out, starting from the experimental data estimated at both "cold" and "hot" operating conditions. The current vector providing for the same output torque is wider when the magnet temperature is hotter. Besides, the MTPA angle is slightly modified due to the ferrite magnets temperature variations.

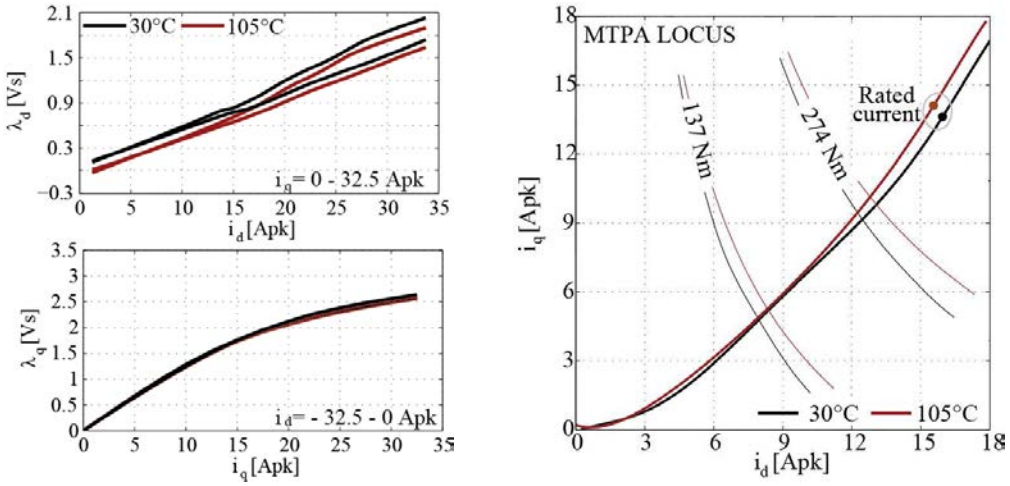

(a) (b)

Figure 3.18 – a) Flux linkage curves of the FASR motor of Figure 10.15a measured at 30°C and 105°C stator windings temperature. b) MTPA locus in the same thermal condition.

10.4. FINAL DISCUSSION

This paper formalized a procedure for the experimental identification of the magnetic model of PM synchronous electrical machines. The machine flux linkages are

represented as functions of the machine stator currents in the rotor synchronous reference frame. Once the magnetic model is identified, the motor control trajectories can be calculated and the motor performance can be defined in detail, possibly validating the results of either analytical or FE models.

Three different hardware setups have been compared, working towards a standardized identification process to be performed on-site with:

- no further hardware requirements, besides the drive train to be identified;
- no lack of accuracy in predicting the relationships between the phase currents and stator flux linkages of the electrical machine under test.

Main issues related to the stabilization and monitoring of the PMs temperature during the experimental identification of the flux linkages over a prefixed current mesh grid, including partial- full- and over- thermal loads, have been addressed.

Chapter 11

Unified version of a predictive direct flux control scheme for PM-based motor drives

This chapter investigates a direct flux vector control strategy, suitable for Permanent Magnet Synchronous Motor drives of all kinds with minimum need of calibration and minimum requirements in terms of knowledge of the magnetic behavior of the electrical machine.

Direct Torque Control (DTC) is widely adopted for AC motor drives thanks to its fast dynamics and easy implementation. It should be better addressed as Direct Torque and Flux Control, since the flux amplitude is usually controlled as state variable, complementarily to the airgap torque.

The direct control of the estimated flux magnitude has been conveniently introduced to facilitate the full exploitation of the inverter voltage limit, especially during flux-weakening operation [102].

However also the maximum current limit must be handled with care, as suggested in [103]. Common DTC algorithms can be adapted at this purpose, by making the controller operate in stator flux coordinates. So, the current component in quadrature with the flux linkage vector can be regulated on behalf of the torque.

In particular, the so called Direct Flux Vector Control (DFVC) proposed in [104] combines the main features of direct-flux control schemes along with the ones of *dq* current vector controllers, taking advantage of two simple closed-loop Proportional-Integral (PI) regulators. The first one controls the flux magnitude via the direct component of the voltage vector, as many DTC schemes do, and, differently from standard DTC algorithms, the second one is used to regulate the quadrature stator

current on behalf of the torque, as said.

Starting from [104], the research field has been extended working towards a unified DFVC strategy, that aims at:

- still guaranteeing the full exploitation of the inverter current and voltage limits via compact on-line computations;
- being suitable for all Permanent Magnets synchronous motor drives with no modifications and being insensitive to motor parameter variations;
- assuring good control performances, while demanding a minimum need set of tuning operations to the end user.

The predictive version of the DFVC algorithm proposed in [104] is basically a control scheme where the PI-Based stator vector control has been replaced by simple linear equations, able to relate the desired torque to the reference voltages without requiring preliminary commissioning efforts.

The basics of this novel control algorithm will be presented and the main challenges related to the control implementation will be highlighted as well. The mathematics behind the stator vector control will follow, together with important notes about the countermeasures needed to make the algorithm robust towards motor parameters variations.

Then, the predictive stator current and flux observer will be introduced as key enabling technology for this closed-form control scheme, that has to cope with the problems consequent on the unavoidable delays of digital implementation.

To conclude, experimental and simulation results will be provided. The tests reported here refer to a PM-assisted Synchronous Reluctance (PMASR) motor drive, purposely chosen for its extremely non linear magnetic behavior. That makes the machine the most challenging example in terms of sensitivity to motor parameters variations.

For the sake of generality, the performances of the proposed control algorithm will be compared to the ones of more standard PI-Based control techniques, namely the Current Vector Control (CVC) [105] and the DFVC scheme introduced in [104].

11.1. BASICS OF THE PROPOSED CONTROL

The proposed control operates in stator flux coordinates (d_s, q_s): the direct voltage component regulates the amplitude of the flux linkage vector λ, whereas the quadrature one controls the stator quadrature current i_{qs} by acting on the load torque angle δ.

Figure 11.1 introduces the angle δ, the position ϑ_s of the stator flux coordinates, the rotor position ϑ and the angular frequency ω, showing different PM rotor configurations.

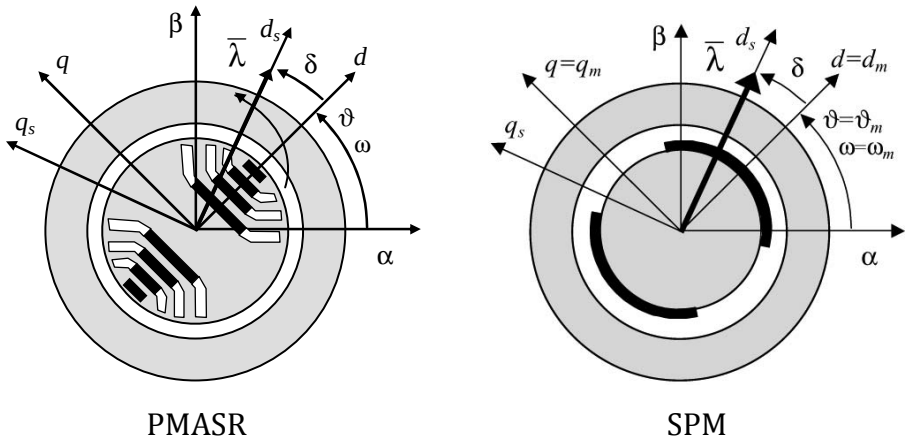

PMASR SPM

Figure 11.1 - Reference axis frames and phase angles: stationary frame (α, β), rotor synchronous frame (*d*, *q*), stator flux synchronous frame (d_s, q_s); load torque angle δ, rotor position ϑ, stator flux synchronous frame position ϑ_s. Different PM rotor structures are considered.

The various reference frames are put in evidence. Since the control theory has been developed for PM machines of all kinds, the direct axis *d* is made coincident with the PM flux direction, also in case of Permanent Magnet Assisted SR machines, even though they are preferably analyzed with the *dq* axes following the SR approach in many applications.

11.1.1. Digital implementation of predictive controllers

The predictive control algorithm, which is being presented here, takes advantage of the inverse machine model to relate via explicit equations the required command values (namely, the voltage vector components) to the ones selected as references (that is, the input torque and flux amplitude), while possibly improving the control dynamics under the inverter voltage and current limitations.

The main technical challenges associated with the design of such a control technique are represented by:

- the typical non-linear model of PM machines, also sensitive to motor parameters variations;
- the unavoidable delays introduced by digital controllers.

In particular, it is known that digital controllers can update the voltage command only one switching period (T_{sw}) later than the corresponding sample time t_k, due to the computation tasks. In literature [106], [110], it has also been pointed out that the knowledge of the machine states at the actuation time (namely t_{k+1}) is absolutely required when dealing with closed-form control strategies, as it is the case here. In other words, for this topology of control algorithms, programmers are compelled to process the data available at the sample time t_k to predict the machine states, needed for control, at the execution time t_{k+1}.

Thus, a predictive observer is mandatory. If it is omitted, the controlled variables turn out to be characterized by an intrinsic oscillatory behavior [107], [108]. Only in few cases, this unwanted side effect can be mitigated by corrective factors [109] and always at the expense of a worst dynamics.

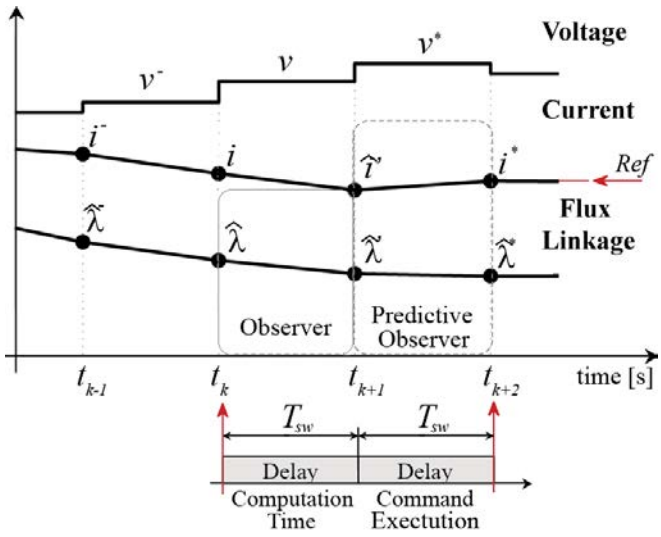

Figure 11.2 - Sequence of events in consecutive sample instants and unavoidable delays of digital implementation. The flux linkages at t_k are estimated by a standard observer, while currents and flux linkages at t_{k+1} are given by a predictive observer (see Section 11.4 for further details).

Figure 11.2 provides a graphical representation of the sequence of events occurring in successive sample instants, putting in evidence the main consequences to the unavoidable delays introduced by digital controllers.

Figure 11.2 serves also as a reminder of the notations adopted in the rest of the document.

If reference is made to a generic sample time t_k, as for flux linkages and currents:

- the superscript " – " indicates a past value;
- the superscript " ' " stands for a predicted quantity;
- If no symbols are added, the considered variable coincides with its current value.

The "hat", if present, specifies that the quantity is output by the observer.

Again with reference to a generic sample time t_k, as for voltages:

- the superscript " – " indicates that the command is executed between the instants t_{k-1} and t_k;
- the voltage vector latched during the computation time is reported with no additional marks.

Reference quantities are always indicated with a "star" as superscript: the reference voltage vector, evaluated during the computation time, is executed between the instants t_{k+1} and t_{k+2}, meaning that the controlled current and flux can achieve their respective reference value two switching period later than t_k, or even more if the available Volt-seconds are not sufficient.

11.1.2. Control scheme

The main control blocks of the proposed algorithm are reported in Figure 11.3 and an overall description of the control sequence is provided here, even if more details can be found in the next sections.

Starting from the reference torque T^* (most likely output by a speed regulator), the Maximum Torque Per Ampere (MTPA) law determines the flux linkage reference λ^* and the required quadrature current i_{qs}^* follows from the torque equation (11.1):

$$T = \frac{3}{2} p \cdot \lambda \cdot i_{qs} \tag{11.1}$$

At this point, the reference quantities, limited according to the current and voltage constraints, are manipulated via linear equations, together with the outputs of the predictive observer, and the reference voltage vector is obtained.

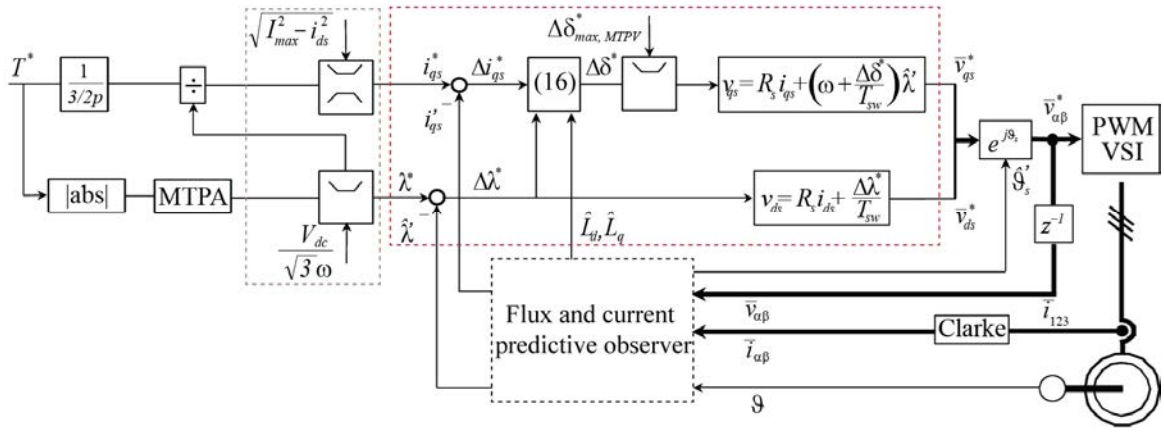

Figure 11.3 – Predictive Direct Flux Vector Control scheme. (Dotted grey block: inverter current and voltage limitations; Dotted black block: predictive stator flux and current observer; Dotted red block: closed-form stator vector control)

It is worth highlighting that the state variable directly controlled by the quadrature component of the voltage vector is the load torque angle δ: its value depends both on the flux linkage reference and the quadrature current one and it is properly constrained for limiting the machine operating area according to the Maximum Torque Per Voltage (MTPV) trajectory [104].

11.1.2.1. Maximum current and voltage limitations

The upper value $i_{qs,max}$ that constrains the amplitude of the reference quadrature current, coming from (11.1) and the reference torque T^*, can be quantified as suggested by (11.2):

$$i_{qs,max} = \sqrt{I_{max}^2 - i_{ds}^2} \tag{11.2}$$

In fact, both the direct component i_{ds} of the current vector and the quadrature one concur to determine the amplitude of the stator current, that cannot exceed the upper

limit I_{max} according to the inverter specifications.

As for the magnitude of the flux linkage vector, the upper limit λ_{max} depends on the electrical operating speed ω. In formula:

$$\lambda_{max} = \frac{\left|V_{max} - R_s i_{qs}^* sign(\omega)\right|}{\omega} \tag{11.3}$$

where V_{max} is a function of the dc-link voltage V_{dc} and has to be set according to the choice of exploiting or not the over modulation region. The resistance voltage drop, expressed in terms of the stator resistance R_s, can be neglected, depending on the motor power rating.

11.2. CLOSED-FORM STATOR VECTOR CONTROL

11.2.1. Magnetic model

The magnetic model of PM Synchronous machines in rotor coordinates is defined by (11.4).

$$\begin{cases} \lambda_d = L_d(i_d, i_q) \cdot i_d + \lambda_m \\ \lambda_q = L_q(i_d, i_q) \cdot i_q \end{cases} \tag{11.4}$$

The torque expression is reported in (11.5) for convenience.

$$T = \frac{3}{2} p(\lambda_d i_q - \lambda_q i_d) \tag{11.5}$$

In the modeling equations (11.4), the d- and q-axis stator flux linkages (λ_d, λ_q) are defined via the PM flux linkage λ_m and the inductances L_d and L_q, which are both functions of the stator currents i_d, i_q. It occurs in general because of saturation and cross saturation effects and Figure 11.4a shows, as an example, the non-linear relationships between the flux linkages and currents of the motor, that will be considered as a reference in the last section of this Chapter for validation purposes (see Table 11-I for details).

In the following, when addressing the stator inductances, the terms in bracket in (11.4) will be omitted for a shorthand notation, but their dependency on the operating

condition will be taken into account as described in the next subsection.

Specifically, the cross-coupling between the *d*- and *q*-axis will be adaptively included in the estimation of the self-inductances L_d and L_q instead of employing at the same purpose two extra parameters, namely the mutual terms L_{dq} and L_{qd} conventionally adopted in literature, as for example in [111].

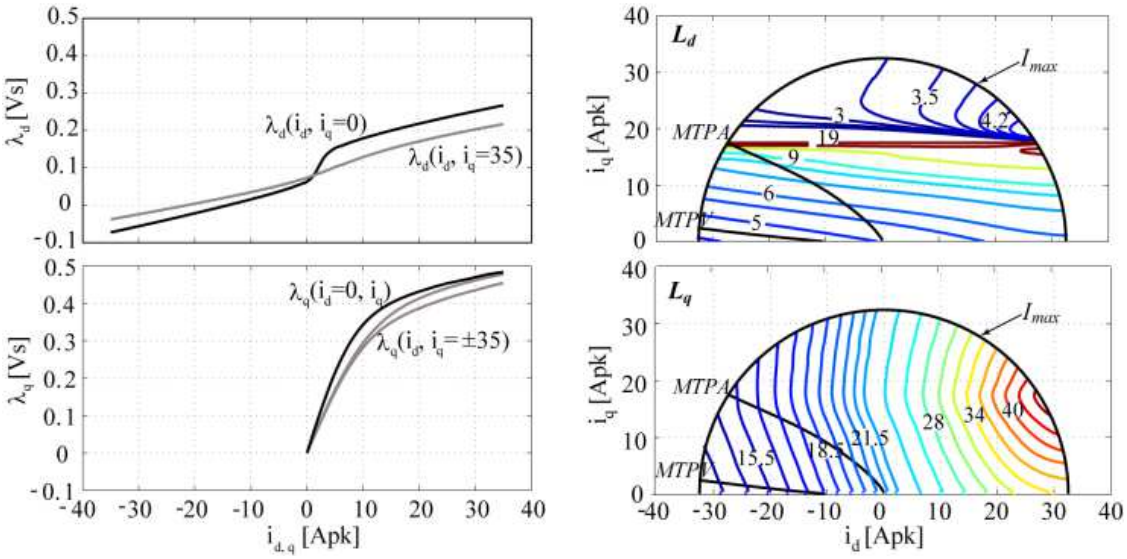

(a) (b)

Figure 11.4 – All plots are referred to the PMASR motor, considered as an example for validation purposes (see Table I for details); a) Machine magnetic model in the rotor reference frame; b) Variations of the inductances L_d (top) and L_q (bottom) in the *d*-, *q*-axis current plane.

Provided (11.4), a coordinate rotation leads to (11.6), that represents the model of PM synchronous machines in the stator field oriented reference frame (d_s, q_s).

$$\begin{cases} \lambda = L_{ds} \cdot i_{ds} + L_{dqs} \cdot i_{qs} + \lambda_m \cos(\delta) \\ 0 = L_{dqs} \cdot i_{ds} + L_{qs} \cdot i_{qs} - \lambda_m \sin(\delta) \end{cases} \tag{11.6}$$

The direct and quadrature components of the stator current vector are i_{ds} and i_{qs} respectively; the inductances defining both the d_s-and q_s-axis magnetic behavior vary between L_d and L_q along with the position δ of the flux linkage vector, as shown by (11.7) and 11.(8).

$$L_0 = \frac{L_d + L_q}{2} \qquad \Delta L = \frac{L_q - L_d}{2} \tag{11.7}$$

$$\begin{bmatrix} L_{ds} & L_{dqs} \\ L_{dqs} & L_{qs} \end{bmatrix} = \begin{bmatrix} L_0 - \Delta L\cos(2\delta) & \Delta L\sin(2\delta) \\ \Delta L\sin(2\delta) & L_0 + \Delta L\cos(2\delta) \end{bmatrix} \tag{11.8}$$

Equation (11.9) follows from (11.5) and it expresses the torque in terms of the stator flux linkage magnitude and phase, instead of its *d*-, *q*-axis components.

$$T = \frac{3}{2}p\left(\frac{\lambda\lambda_m}{L_d}sin(\delta) - \frac{\lambda^2}{2L_q}(\xi - 1)\,sin(2\delta)\right) \tag{11.9}$$

In (11.9) both the magnets and the reluctance torque contributes are put in evidence, introducing the saliency ratio ζ that is given dividing the inductance L_q by L_d.

11.2.2. Adaptive evaluation of the *d*- and *q*-axis inductances

The magnetic model represents the basis of many predictive control algorithms, included the one proposed here, and that is why inaccuracies in the parameters estimation may heavily affect the capability of deriving and performing optimal control laws [108].

To overcome this problem, instead of time consuming off-line estimation tests, the presented control scheme takes advantage of simple operations (11.10), that are performed on-line at each sample time for deriving the stator inductances from the observed flux components $\hat{\lambda}_d$ and $\hat{\lambda}_q$.

$$\begin{cases} \hat{L}_d = \dfrac{\hat{\lambda}_d - \lambda_m}{i_d} \\ \hat{L}_q = \dfrac{\hat{\lambda}_q}{i_q} \end{cases} \tag{11.10}$$

The effect of magnetic saturation and cross saturation is adaptively included in the estimated inductances, that turn out to be dependent on the operating condition.

This improves the capability of modeling the magnetic behavior of the motor.

In fact, as shown in Figure 4b with reference to the PMASR machine considered here as an example, both L_d and L_q vary significantly in the *d*-, *q*-axis current plane, even along the MTPA locus.

11.2.3. Direct and quadrature reference voltage equations

In the stator reference frame (d_s, q_s), the voltage equations are expressed as described in (11.11).

$$\begin{cases} v_{ds} = R_s \cdot i_{ds} + \dfrac{d\lambda}{dt} \\ v_{qs} = R_s \cdot i_{qs} + \left(\dfrac{d\delta}{dt} + \omega\right) \cdot \lambda \end{cases} \tag{11.11}$$

If the sampling period T_{sw} is small enough to hypothesize negligible variations of the electrical speed ω, the voltage equations (11.11) can be easily transposed in the discrete time domain, leading to (11.12).

$$\begin{cases} v_{ds}^{*} = R_s \cdot \hat{\imath}_{ds}^{'} + \dfrac{\Delta\hat{\lambda}^{*}}{T_{sw}} \\ v_{qs}^{*} = R_s \cdot \hat{\imath}_{qs}^{'} + \left(\dfrac{\Delta\hat{\delta}^{*}}{T_{sw}} + \omega\right) \cdot \hat{\lambda}' \end{cases} \tag{11.12}$$

In (11.12), it is put in evidence that the reference voltages to be computed at a generic sample time t_k depend on the predicted machine states at the delayed actuation time t_{k+1}. In particular,$\Delta\lambda^{*}$, as well as $\Delta\delta^{*}$,are given by the difference between the respective reference and predicted values (11.13).

$$\begin{aligned} \Delta\hat{\lambda}^{*} &= \hat{\lambda}^{*} - \hat{\lambda}' \\ \Delta\hat{\delta}^{*} &= \hat{\delta}^{*} - \hat{\delta}' \end{aligned} \tag{11.13}$$

The voltage model, or better its discrete-form, fits well for the main purpose of the present work, as it relates analytically the direct voltage component v_{ds} to the desired flux variation, while pointing out that the quadrature voltage component v_{qs} regulates the torque by acting on the load angle δ. It follows that the next step to be pursued is to define the load torque angle variation, required for achieving the reference torque, in terms of the control variables i_{qs} and λ.

11.2.4. Desired load torque angle variation

The non linear relationship (11.9) between the torque and the load angle δ can be solved manipulating the d_s-, q_s-axis magnetic model.

By differentiating both the equations reported in (11.6) over a small time interval, equations (11.14) and (11.15) are found.

$$\frac{di_{ds}}{dt} = \Lambda_{ds}\frac{d\lambda}{dt} + I\Theta_{ds}\frac{di_{qs}}{dt} + \Delta_{ds}\frac{d\delta}{dt}$$

$$\begin{aligned} \Lambda_{ds} &= +\frac{1}{L_0 - \Delta L\, cos(2\delta)} \\ I\Theta_{ds} &= -\frac{\Delta L\, sin(2\delta)}{L_0 - \Delta L\, cos(2\delta)} \\ \Delta_{ds} &= -\frac{2\Delta L\big(sin(2\delta) i_{ds} + cos(2\delta) i_{qs}\big) - \lambda_m\, sin(\delta)}{L_0 - \Delta L\, cos(2\delta)} \end{aligned} \tag{11.14}$$

$$\frac{\mathrm{di_{ds}}}{\mathrm{dt}} = \Lambda_{\mathrm{ds}}\frac{\mathrm{d}\lambda}{\mathrm{dt}} + \mathrm{I}\Theta_{\mathrm{ds}}\frac{\mathrm{di_{qs}}}{\mathrm{dt}} + \Delta_{\mathrm{ds}}\frac{\mathrm{d}\delta}{\mathrm{dt}}$$

$$\begin{aligned} \mathrm{I}\Theta_{\mathrm{qs}} &= -\frac{L_0 + \Delta L\cos(2\delta)}{\Delta \mathrm{L}\sin(2\delta)} \\ \Delta_{\mathrm{qs}} &= -\frac{2\Delta \mathrm{L}\big(\cos(2\delta)\mathrm{i_{ds}} - \sin(2\delta)\mathrm{i_{qs}}\big) - \lambda_{\mathrm{m}}\cos(\delta)}{\Delta \mathrm{L}\sin(2\delta)} \end{aligned} \tag{11.15}$$

Since the direct component i_{ds} of the stator current is the only variable not to be directly related to the torque, the right sides of both equations (11.14) and (11.15) can be equaled, so that the derivative of the angular position δ becomes a function of the other two derivatives, namely the quadrature current and the flux linkage magnitude ones.

Then, if the continuous-form equations are referred to the discrete-time domain and the evolution in time of currents and flux linkages is taken into account, equation (11.16) is obtained.

$$\Delta\hat{\delta}^* = \frac{\Delta\hat{\mathrm{i}}^*_{\mathrm{qs}} + \frac{(\hat{\xi}-1)}{2\hat{\mathrm{L}}_{\mathrm{q}}} \cdot \Delta\hat{\lambda}^*}{\frac{\cos(\hat{\delta}')}{\hat{\mathrm{L}}_{\mathrm{d}}} \cdot \lambda_{\mathrm{m}} - \frac{(\xi-1)\cos(2\hat{\delta}')}{\hat{\mathrm{L}}_{\mathrm{q}}} \cdot \hat{\lambda}'} \tag{11.16}$$

At this point, the goal of computing via linear equations the command voltages

needed to achieve the reference torque is completely fulfilled.

$$\Delta\hat{\imath}_{qs}^{*} = i_{qs}^{*} - \hat{\imath}_{qs}^{'} \tag{11.17}$$

In fact, once i_{qs}^{*} and $\lambda^{*}$are derived, as described in Section 11.1, and the observer outputs the predicted values of the quadrature current and the flux linkage amplitude, $\Delta\hat{\lambda}^{*}$ (11.13) and $\Delta\hat{\imath}_{qs}^{*}$ (11.17) are univocally determined. Equation (11.16) can then be applied, since $\hat{\delta}'$ is provided by the predictive observer and the estimated inductances are supposed to be approximately constant in one sample period. Eventually, the discrete-form voltage model (11.12) leads to the reference voltages v_{ds}^{*} and v_{qs}^{*}.

As a result, the quadrature control channel and the direct one turn out to be coupled only in presence of diverse inductances along the *d*- and *q*-axis, that means having $\zeta \neq 1$ in Equation (11.16). It confirms a well known concept coming from the theory, that is, when dealing with highly salient machines, the achievable torque variation depends on both the flux amplitude variation and the quadrature current one, making the limited available Volt-seconds the main constraint to the feasible dynamics.

Conversely, when the saliency ratio is close to one, according to (11.16), the load angle required to achieve the desired torque derives from the quadrature current reference only and the *ds*- and *qs*-control channels are independent. It is the case of concentrated winding interior PM machines and surface PM machines, which can be both modeled by means of (11.4) - (11.11)and then controlled with the proposed algorithm: as for the first ones, the saliency ratio is limited by the harmonic content, whereas for the latter ones the parameter ζ is always close to one, provided that only saturation effects concur to diversify the *d*- and *q*-axis magnetic behavior.

11.2.5. MTPV operation

The MTPV operation, or voltage-limited operation, occurs in the flux-weakening region at high speed, when the pull-out torque has been reached and the torque is no longer maximized by exploiting the full inverter current.

This condition occurs by definition when the partial derivative of the torque with respect to the load angle is equal to zero and the MTPV constraint is translated into an

upper limitation (namely δ_{max}) for the load torque angle [104].

In formula, according to (11.9), the MTPV condition is quantified as shown in (11.18).

$$\left.\frac{dT}{d\delta}\right|_{\lambda=cost} = \hat{\lambda}' \cdot \left(\frac{\cos(\hat{\delta}')}{\hat{L}_d} \cdot \lambda_m - \frac{(\xi - 1)\cos(2\hat{\delta}')}{\hat{L}_q} \cdot \hat{\lambda}' \right) = 0 \tag{11.18}$$

It is worth highlighting that the above expression determines also the validity domain of the proposed control law, since the algorithm is based on equation (11.16) and that expression is undetermined when its denominator is null (11.19).

$$\frac{\cos(\hat{\delta}')}{\hat{L}_d} \cdot \lambda_m - \frac{(\xi - 1)\cos(2\hat{\delta}')}{\hat{L}_q} \cdot \hat{\lambda}' = 0 \tag{11.19}$$

This result represents an important challenge, since it gives the opportunity to make the algorithm detect the MTPV operating condition autonomously and adapt the control accordingly, without requiring specific off-line computations.

The correct exploitation of the MTPV control trajectory is able to maintain the quadrature control channel stable over the whole speed range.

11.3. PREDICTIVE CURRENT AND FLUX OBSERVER

At teach sample time t_k, the observer serves as real-time model of the physical system, to estimate the flux linkages, that cannot be measured directly, but also to predict the machine states at the instant t_{k+1}, that is when the commands are executed. The observer operates in two consecutive steps, schematically described in Figure 11.5:

- the first one estimates the stator flux linkages at the sample time t_k, while providing the expected inductances $\hat{L}_d$ and $\hat{L}_q$;
- the second one manipulates the results of the first block to predict the stator currents and flux linkages at the instant t_{k+1}.

11.3.1. Observed flux at the sample time t_k

The control blocks, needed for estimating the flux linkages at the sample time t_k, are

based on the current-to-flux model at low speed and on back-electromotive force integration at high speed, as schematically described in the following.

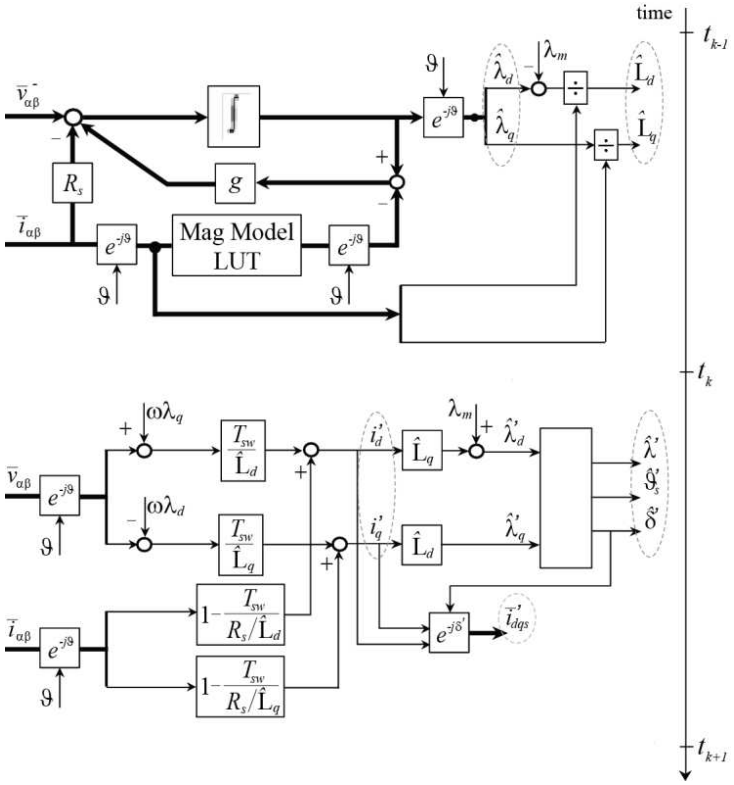

Figure 11.5 - Predictive stator flux and current observer. The scheme is divided in two separate blocks, whose outputs are put in evidence for convenience. The first block estimates the flux linkages at the sample time t_k, whereas the latter one predicts the values of flux linkages and currents at the execution time t_{k+1}.

Back-electromotive force integration. Figure 11.5 shows how to take advantage of the voltage model (11.20) in the stationary reference (α, β) for estimating the stator flux linkages at the sample time t_k, pointing out that they are determined by the voltage command v latched between the instants t_{k-1} and t_k.

$$\begin{cases} v_\alpha = R_s i_\alpha + \dfrac{d\lambda_\alpha}{dt} \\ v_\beta = R_s i_\beta + \dfrac{d\lambda_\beta}{dt} \end{cases} \tag{11.20}$$

Current-to-flux model. The magnetic model relates the measured stator currents at the sample time t_k to the corresponding flux linkages in the (d, q) rotor frame: thus, as reported in Figure 11.5, coordinate rotations are needed to insert the computation in the

flux observer scheme. A simple magnetic model (11.4) with constant values of the stator inductances can be adopted in those applications where very low speed operation is not required and/or the starting torque is moderate; otherwise a more accurate modelis preferred.

Crossover of the alternative estimation methods. The α, β flux linkages estimated by the two alternative schemes just mentioned are combined by means of the gain g, which is expressed in radians per second and represents the crossover angular frequency between the low- and high-speed estimation methods.

Estimated d-, q-axis inductances. Since the proposed procedure estimates the flux linkages in the stationary frame (α, β), a coordinate rotation is needed for obtaining $\hat{\lambda}_d$and $\hat{\lambda}_q$, and then evaluating the stator inductances applying (11.10).

At this point, the observer outputs are:

- the *d*,*q* stator flux linkages at the sample time t_k;
- the estimated inductances $\hat{L}_d$ and $\hat{L}_q$.

11.3.2. Predicted current and flux at the sample time t_{k+1}

Starting from the results of the scheme described in the previous subsection, the steps required to predict the machine states at the actuation time t_{k+1} are listed in the following:

Coordinate rotation of $i_{\alpha\beta}$ and $v_{\alpha\beta}$. The measured rotor position (or the estimated one in case of sensorless controllers) is used to refer to the *d*-, *q*-axis frame both the currents measured at the sample time t_k and the voltage settings, updated at the same instant.

Prediction of the stator d-, q-axis currents. The voltage model (11.21) in the *d*, *q* synchronous frame leads to the predicted values of the stator currents (i'_d, i'_q) at the execution time t_{k+1}.

$$\begin{cases} v_d = R_s i_d - \omega\lambda_q + \dfrac{d\lambda_d}{dt} = R_s i_d - \omega\lambda_q + L_d \dfrac{di_d}{dt} \\ v_q = R_s i_q + \omega\lambda_d + \dfrac{d\lambda_q}{dt} = R_s i_q + \omega\lambda_q + L_q \dfrac{di_q}{dt} \end{cases} \tag{11.21}$$

In fact, under the hypothesis that the *d*- and *q*-axis inductances are constant during one sample period, the first-order differential equations (11.20) can be solved and the discrete-form expressions (11.22) follow.

$$\begin{cases} i_d' = i_d e^{-\frac{R_s}{\hat{L}_d}T_{sw}} + \dfrac{v_d + \omega\lambda_q}{R_s}\left(1 - e^{-\frac{R_s}{\hat{L}_d}T_{sw}}\right) \\ i_q' = i_q e^{-\frac{R_s}{\hat{L}_q}T_{sw}} + \dfrac{v_q - \omega\lambda_d}{R_s}\left(1 - e^{-\frac{R_s}{\hat{L}_q}T_{sw}}\right) \end{cases} \tag{11.22}$$

They can be simplified, as in the diagram of Figure 11.5, if all exponentials are approximated with the first two terms of the corresponding Taylor series.

Prediction of the stator d-, q-axis flux linkages. Again under the assumption of negligibleness of the stator inductances variations in one sample period, the values i_d' and i_q' calculated via (11.22) can be replaced in (11.4) giving the predicted flux linkages λ_d' and λ_q' at the actuation time t_{k+1}. At this purpose, $\hat{L}_d$ and $\hat{L}_q$ have to be considered instead of $L_d(i_d,i_q)$ and $L_q(i_d,i_q)$ respectively.

As for this second stage, the outputs needed for control are highlighted in Figure 11.5 and listed here for convenience:

- the predicted amplitudeλ' of the stator flux linkage vector at the execution time t_{k+1};
- its position, referred both to the stationary frame α, β (ϑ_s') and the synchronous frame *d*, *q* (δ').
- the predicted quadrature stator current i_{qs}'.

11.4. VALIDATION

Experimental tests and simulations on a voltage supplied inverter PMASR motor drive have been carried out for validating the proposed control scheme and comparing its performance to the ones of more standard PI-Based control techniques.

Similar tests have been repeated on other PM based motor drive, obtaining analogous performance. A high-salient Magnet Assisted SR motor has been purposely chosen for presenting this validation section because of its extremely non-linear

magnetic behavior.

Table 11-I summarizes the main data of the drive. The PMASR motor under test has been designed for traction and its multi-barrier rotor lamination, which guarantees a good saliency ratio between the *d*- and *q*-axis, is shown in Figure 11.6. The response of the system to the proposed control has been tested both in simulation, with the assistance of Matlab toolboxes, and on an experimental bench, equipped with a dSpace board and a standard incremental encoder with 512 pulses per revolution.

TABLE 8-I
DRIVE DATA

MOTOR DATA		
Continous power	7	kW
Peak power	10	kW
Base Speed	2200	rpm
Maximum speed	10000	rpm
Stator resistance	0.3	Ohm
Rotor inertia	$4.6\ 10^{-3}$	kgm^2
INVERTER DATA		
Switching Freq.	10	kHz
DC voltage	350	V
Maximum current	33	Apk

Figure 11.6 – Rotor lamination of the motor under test, whose main data are listed in Table 11-I.

11.4.1. Torque step response and torque reversal

The torque step response and the more demanding case of torque reversal are presented first to investigate the dynamic behavior of the proposed control.

The plots, reported in Figure 11.7, compares the experimental and simulation results for a 5 Nm torque step.

Expectedly, the torque observed on the experimental rig is noisier, if compared with the one obtained in simulation, because of the sensitivity of the control to the disturbances coming from the currents measures. This undesired effect can be still mitigated, as shown in (11.23), by means of the attenuation coefficient k_a.

$$v_{qs}^{*} = R_s \cdot \hat{i}_{qs}^{'} + \left(k_a \cdot \frac{\Delta\hat{\delta}^{*}}{T_{sw}} + \omega \right) \cdot \hat{\lambda}' \tag{11.23}$$

If the attenuation coefficient is close to one (e.g. 0.8), as it is the case of the results in Figure 11.7, it is possible to attenuate satisfactorily the noisy behavior of the torque, without compromising the dynamic performance of the control.

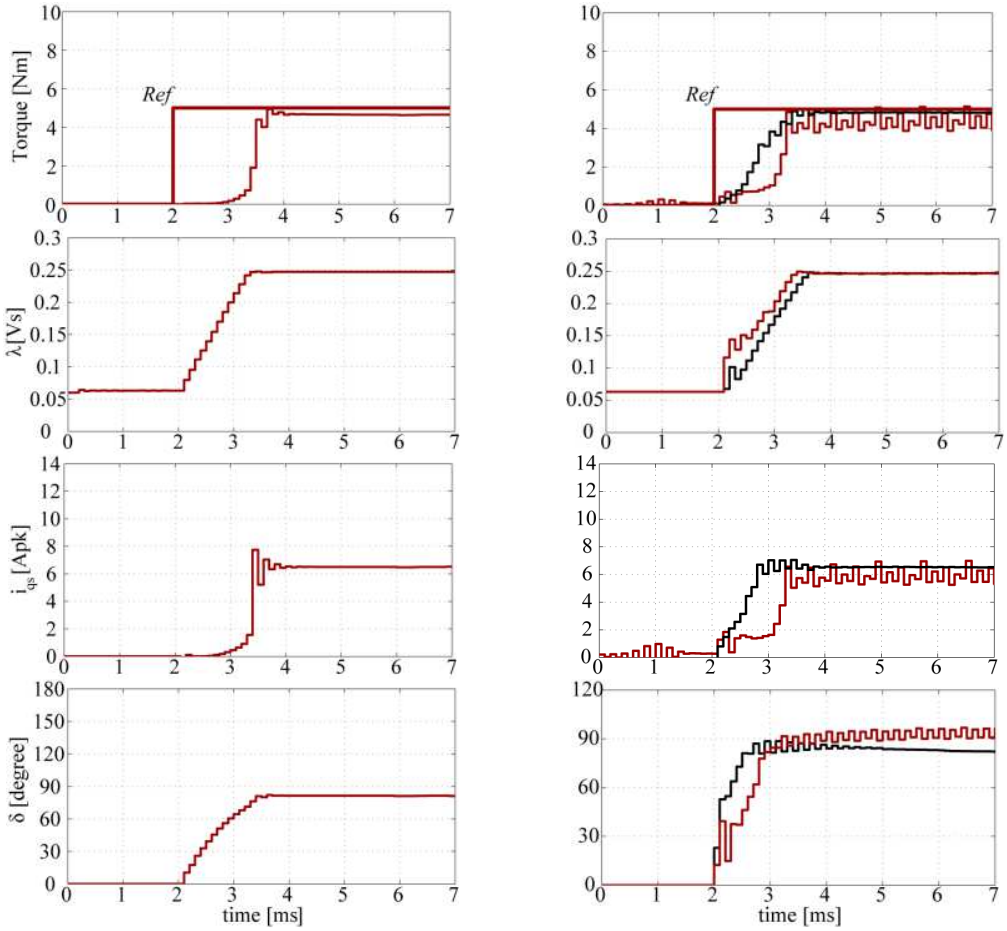

Figure 11.7 - Simulation (left) and experimental (right) results for a 5 Nm torque step. From top to bottom, the reported signals are: the torque, the observed flux magnitude, the quadrature current and the load torque angle. As for the experimental results, the black curves are referred to k_a=0.8, whereas the red ones to k_a=1. In simulation, k_a is equal to one. The y-axis limits have been chosen for a fair comparison with the results in Figure 11.11.

This result is confirmed by the curves reported in Figure 11.8, that shows again a 5 Nm torque step, reporting the experimental results of Figure 7, referred to k_a=0.8, together with the ones obtained controlling the machine with a standard Current Vector Control and with the PI-Based version of the DFVC presented in this paper. The different controllers lead to performances that are almost comparable: in particular the predictive algorithm guarantees the best dynamics, even if the steady state error seems to be a little

bit greater.

As for the torque reversal test, Figure 11.9 highlights that analogous conclusion about the dynamic response of the three control schemes can be drawn. In this case, the flux vector has to rotate from a positive load angle to the same angle with opposite sign (or vice versa) and the available Volt-seconds represent the main limitation to the feasible dynamics, regardless the adopted control scheme.

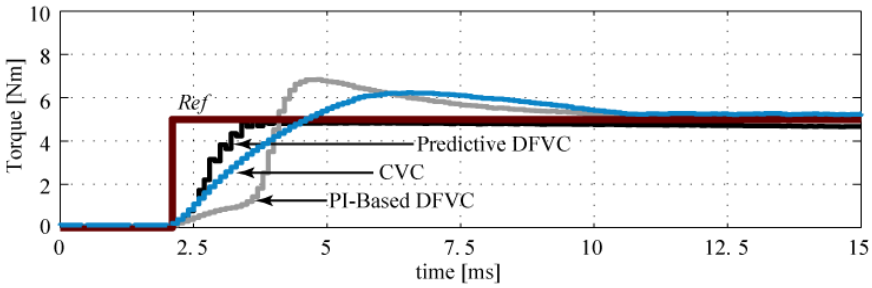

Figure 11.8 - Experimental results for a 5 Nm torque step. The reader is reminded that for the predictive DFVC the attenutation coeffcient k_a is equal to 0.8.

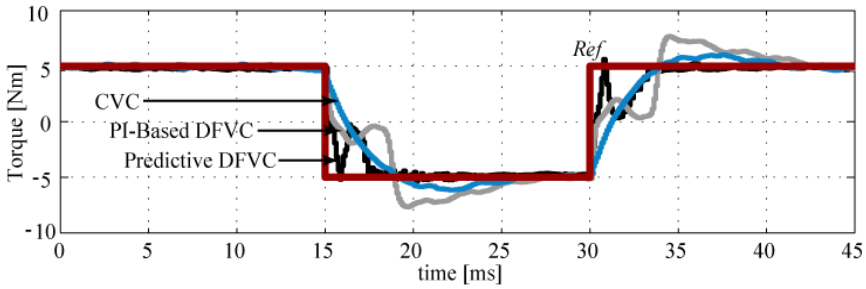

Figure 11.9 - Experimental results for a 5 Nm torque reversal. The reader is reminded that for the predictive DFVC the attenutation coeffcient k_a is equal to 0.8.

Besides being one of the most challenging conditions in terms of dynamic response, torque reversal can be critical and lead to unacceptable overcurrent transients. It happens, when dealing with highly salient machines and direct-flux controllers, if the demanding torque is close to the nominal one and the flux is not properly weakened during the reversal transient.

In fact, while rotating, the flux linkage vector gets close to *d*-axis position, and in that condition a large flux magnitude is also synonym of a large current value due to the small *d*-axis inductance.

As an example, a maximum torque reversal is shown in Figure 11.10, where the

trajectories of the current and flux linkage vectors are reported to put in evidence the consequences of improper control actions.

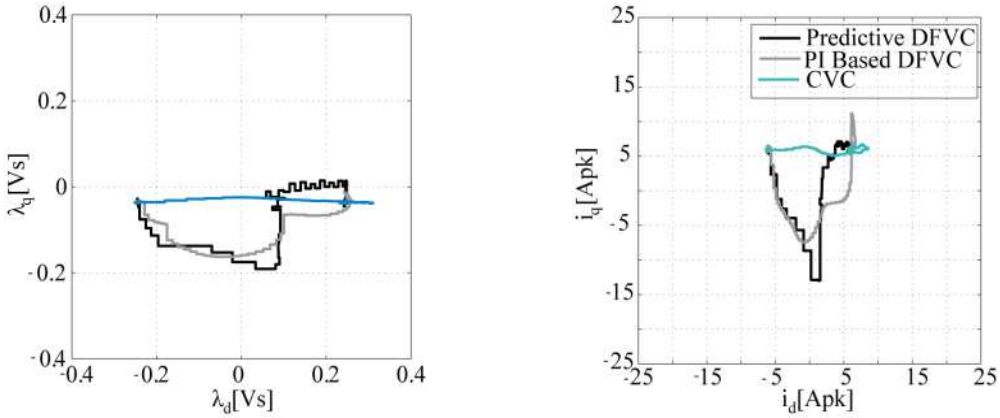

Figure 11.10 - Simulation results: trajectories of the flux linkage and current vectors in the *d*, *q* plane during maximum torque (30 Nm) reversal. In case of direct flux controllers, flux-weakening (FW) turns out to be a mandatory countermeasure against undesirable over current transients.

It is worth noticing that the curves in Figure 11.9 have been obtained weakening correctly the flux magnitude during torque reversal: this demonstrates that the countermeasure proposed against undesired over current transients does not compromise the achievable dynamics. In fact, as said, the performances of the two DFVC scheme are similar to the ones of the CVC, that is not affected by the same problem and that, during the reversal transient, forces both the flux linkage vector and the current one to a completely different trajectory.

11.4.2. Predictive observer as key-enabling technology

The experimental and simulation results have pointed out the key role played by the predictive observer.

In particular, Figure 11.11 demonstrates that the predicted flux linkages and currents computed by the observer forecast with good approximation the machine states at the execution time, whereas additional experimental tests have been performed purposely to put in evidence the consequences of an incorrect implementation of this enabling block.

If the values of currents and flux linkages at the actuation time t_{k+1} are not predicted

and if they are approximately confused with the ones at the instant t_k, the controlled quadrature current and thus the torque are affected by an intrinsic oscillatory behavior, which cannot be satisfactorily attenuated either as suggested by (11.23), also because large values of the attenuation factor k_a definitely compromise the feasible dynamics. This is shown in Figure 11.12, with reference to a 5Nm torque step for a fair comparison with the results reported in Figure 11.7.

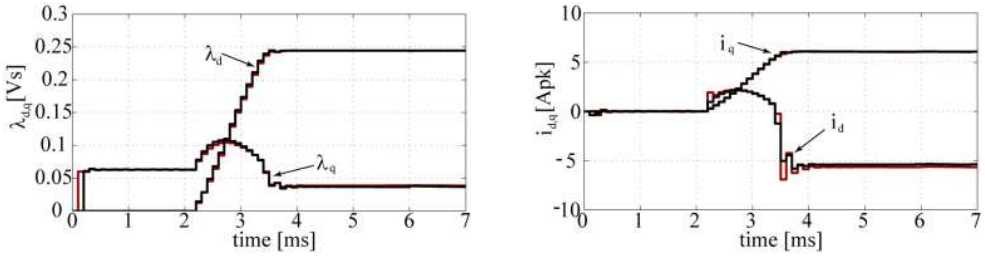

Figure 11.11 - Simulation results for the 5 Nm torque step of Figure 11.7. Left: the predicted stator flux linkages (red) are compared with the actual ones (black), obtained simulatingthe magnetic behavior of the motor; Right: the predicted values of the stator currents (red) are compared with the measured ones (black).

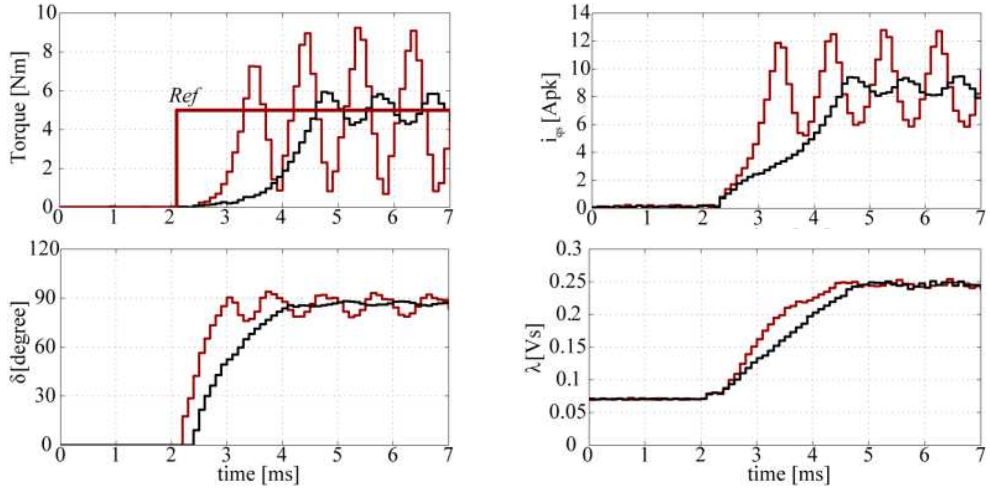

Figure 11.12 – Experimental results: a 5 Nm torque step is applied to the controlled drive, as in the case of Figure 7, but the predictive flux observer is not implemented here. The reported signals are: the torque, the quadrature current, the observed flux magnitude and the load torque angle. The red curves refer to k_a=1, while the black ones to k_a=0.4

11.4.3. Effectiveness of the adaptive evaluation of L_d, L_q

Simple tests have been carried out in simulation to verify the effectiveness of the adaptive calculation of the stator inductances and the plots in Figure 11.13 summarize the results.

If the *d*- and *q*-axis inductances are considered as constant values, referred for example to the nominal operating condition, the torque response turns out to be noisier and affected by greater steady state errors.

11.5.

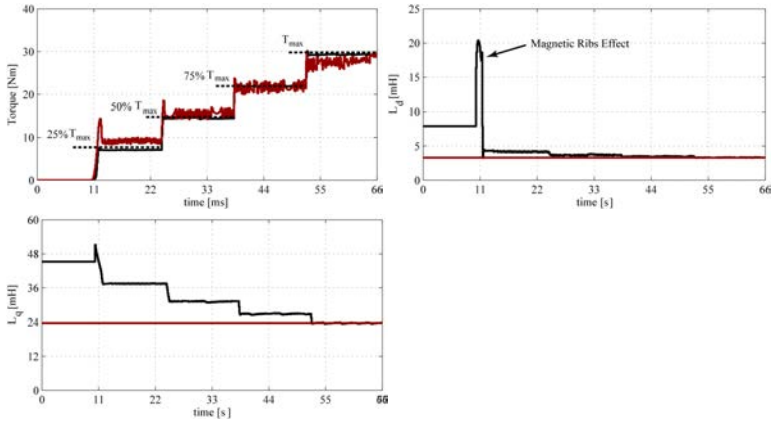

Figure 11.13 – Simulation results: torque response with (Black) and without (Red) the adaptive calculation of the stator inductances. Plotted quantities: torque, estimated inductances. When the inductances are not adaptively estimated, their values are assumed to be the "nominal" ones (or better they are referred to the maximum torque and the operating point is determined by the MTPA trajectory).

11.5.1. Speed step response

The simulation results for speed step response are reported in Figure 11.14 and 11.15 to show the control performances in the deep flux weakening region.

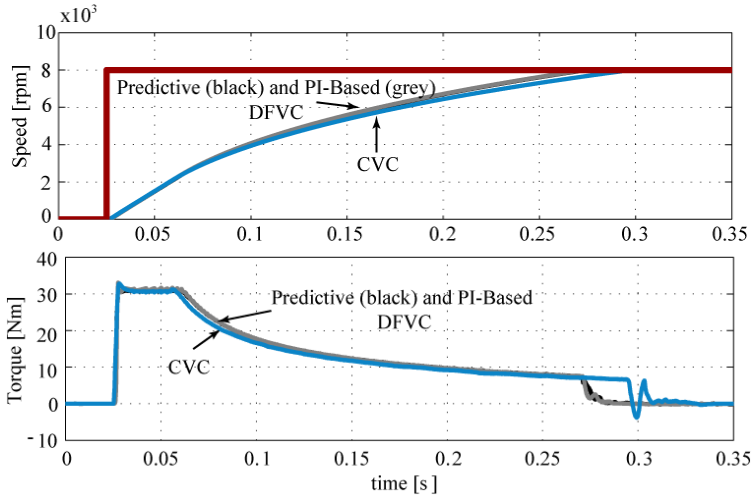

Figure 11.14 - Simulation results: 8000 rpm speed step response.

The reported signals are: speed and torque (Figure 11.14) and the common control variables (i_{qs}, λ, δ) of the DFVC schemes (Figure 11.15). The MTPV operation mode and the current limitation region are put in evidence.

Again, at least in simulation, it is not possible to identify significant differences between the performances of the two DFVC schemes, namely the predictive algorithm and the PI-Based one. However the CVC does not seem to fully exploit the inverter voltage and current limits, besides being disadvantaged by the additional on-line and off-line computations required for including the flux-weakening operation mode.

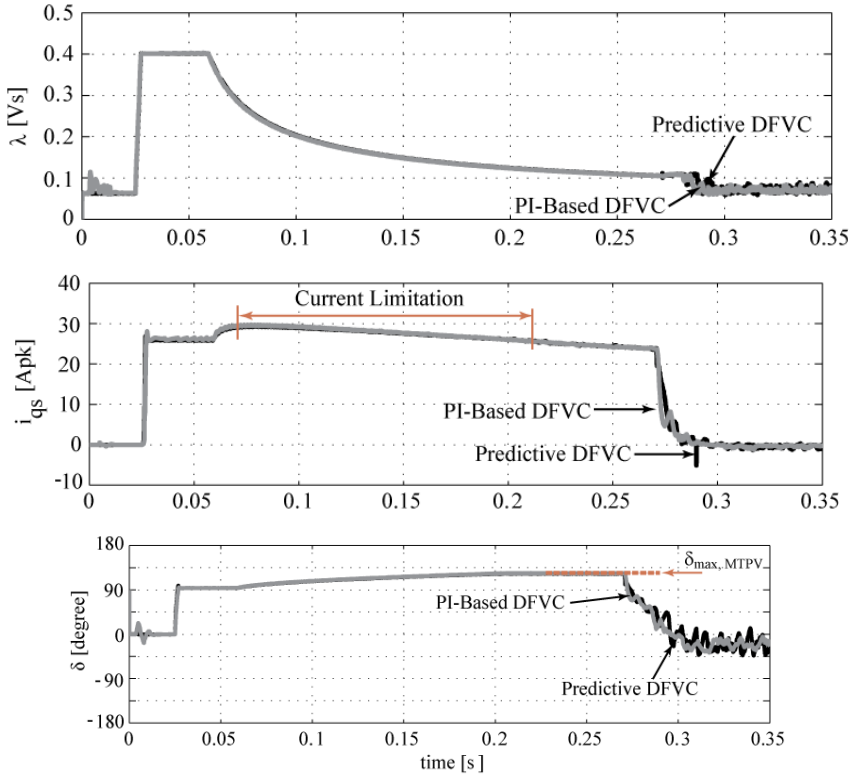

Figure 11.15 - Simulation results: variables regulated by the Direct Flux Vector controllers during the speed transient reported in Figure 11.14. Top to bottom: stator flux linkage amplitude, quadrature current and load torque angle. The black curves refer to the predictive DFVC, while the grey one to the correspondent PI-Based version.

11.6. CONCLUSIVE OBSERVATIONS

The design of a predictive control algorithm based on closed form equations and insensitive to motor parameter variations has been discussed, providing experimental and simulation results to test the control performances on a PMASR motor drive.

The straightforward exploitation of the inverter voltage and current limits guarantees maximum torque production under all operating conditions, including flux-weakening and MTPV operations, without requiring specific off-line computations. The adaptive evaluation of the stator inductances at each sample time improves the achievable dynamics and precision. The implementation of a predictive observer mitigates the typical oscillatory behavior of this kind of controllers.

As a result, the discussed control strategy leads to performances that are pretty close to the ones of more widely adopted PI-Based techniques. The predictive-adaptive scheme has still the additional key advantage of being universally suitable with minimum need of calibration for different PM machines, that is for PM machines of all kinds (as demonstrated by the mathematics behind the stator vector control) regardless their saturation and cross saturation characteristics.

Conclusion

According to the original purposes, this research has been focused on the design, identification and control of Permanent Magnet Synchronous motor drives.

An integrated motor and control design has been provided for, as it is mandatorily required for conveniently exploiting such high-performance drive-trains. Besides, the project has been carried out working via industry-friendly approaches, compelled to face cost-reduction issues and standardization requirements in terms of both design and control procedures.

The first part of the thesis was devoted mainly to the design of reduced-cost Permanent Magnet machines, together with their comparison to state of art performing technologies.

- A general approach to the optimal design of multipolar PM Synchronous electrical actuators has been discussed.
- The proposed procedure is based on closed-form equations, that allow to identify the most convenient design choices and the main design variables in a straightforward way. The resulting guidelines do not refer to a specific case, but to a whole class of electric machines suitable for many up-to-date applications.
- The analytical models, that have been developed, predict the performance indicators of the final design with good accuracy despite their simplified nature. This makes the Finite Element Analysis not mandatory, but just useful for few refinements.
- Different machine topologies have been considered, proposing a novel approach

to design most of the up-to-date machine configurations and exploring innovative technologies or reevaluating older ones to face the recent price volatility of rare-earth raw materials.

- In particular, the possibility of reducing the magnets volume needed to PM-assist SR machines and the exploitation of lower cost (and lower energy density) ferrite magnets have been explored.
- The design of FASR machines, robust against demagnetization and optimized for Joule loss minimization, have been formalized and experimental results give evidence of the consistency of the proposed solution.

This work concludes with the investigation of a unified control strategy suitable for Permanent Magnet (PM) synchronous motor drives of all kinds, improved by a preliminary commissioning process for the automated identification of the machine magnetic model.

- A novel control technique universally suitable for PM motor drives has been proposed, addressing the issues related to the knowledge of the machine magnetic model.
- The predictive-adaptive Direct Flux Vector control scheme, that has been presented, turned out to have the key advantages of:
    - being applicable without modifications to PM motor drives of all kinds;
    - requiring no calibration to the user.
- The robustness of the control algorithm against model parameters variation has been optimized and the need of having the non-linear magnetic model of the PM machine identified has been limited to the implementation of the flux observer at low speed.
- Both an accurate modeling procedure and a quick self-commissioning one have been tested for the identification of the machine magnetic model and the impact of the PMs temperature on the performance of the drive has been considered stabilizing the thermal conditions during the identification process.
- Experimental tests on diverse PMs machines have been performed to validate the consistency and the generality of the approach.

Bibliography

[1] Moghaddam, R.R.; Magnussen, F.; Sadarangani, C.; , "Theoretical and Experimental Reevaluation of Synchronous Reluctance Machine," Industrial Electronics, IEEE Transactions on , vol.57, no.1, pp.6-13, Jan. 2010.

[2] RR Moghaddam, “Rotor for a Synchronous Reluctance Machine”, US Patent App. 13/230,543, 2011.

[3] Barcaro, M.; Bianchi, N.; Magnussen, F., "Permanent-Magnet Optimization in Permanent-Magnet-Assisted Synchronous Reluctance Motor for a Wide Constant-Power Speed Range," Industrial Electronics, IEEE Transactions on , vol.59, no.6, pp.2495,2502, June 2012.

[4] Guglielmi, P.; Boazzo, B.; Armando, E.; Pellegrino, G.; Vagati, A.; , "Permanent-Magnet Minimization in PM-Assisted Synchronous Reluctance Motors for Wide Speed Range," Industry Applications, IEEE Transactions on , vol.49, no.1, pp.31-41, Jan.-Feb. 2013.

[5] Chino, S.; Ogasawara, S.; Miura, T.; Chiba, A.; Takemoto, M.; Hoshi, N.; "Fundamental characteristics of a ferrite permanent magnet axial gap motor with segmented rotor structure for the hybrid electric vehicle," Energy Conversion Congress and Exposition (ECCE), 2011 IEEE , vol., no., pp.2805-2811.

[6] Sekerak, P.; Hrabovcova, V.; Pyrhonen, J.; Kalamen, S.; Rafajdus, P.; Onufer, M., "Comparison of Synchronous Motors With Different Permanent Magnet and Winding Types," Magnetics, IEEE Transactions on , vol.49, no.3, pp.1256,1263, March 2013.

[7] Eriksson, S.; Bernhoff, H.; , "Rotor design for PM generators reflecting the unstable

neodymium price," Electrical Machines (ICEM), 2012 XXth International Conference on , vol., no., pp.1419-1423, 2-5 Sept. 2012.

[8] Barcaro, M.; Bianchi, N., "Interior PM Machines using Ferrite to Replace Rare-Earth Surface PM Machines," Industry Applications, IEEE Transactions on , vol.PP, no.99, pp.1,1, 0.

[9] Ooi, S.; Morimoto, S.; Sanada, M.; Inoue, Y.; , "Performance evaluation of a high power density PMASynRM with ferrite magnets," Energy Conversion Congress and Exposition (ECCE), 2011 IEEE , vol., no., pp.4195-4200, 17-22 Sept. 2011.

[10] Armando, E.; Guglielmi, P.; Pastorelli, M.; Pellegrino, G.; Vagati, A., "Performance of IPM-PMASR Motors with Ferrite Injection for Home Appliance Washing Machine," Industry Applications Society Annual Meeting, 2008. IAS '08. IEEE , vol., no., pp.1-6.

[11] Sanada, M.; Inoue, Y.; Morimoto, S.; "Rotor structure for reducing demagnetization of magnet in a PMASynRM with ferrite permanent magnet and its characteristics," Energy Conversion Congress and Exposition (ECCE), 2011 IEEE , vol., no., pp.4189-4194.

[12] Vagati, A.; Boazzo, B.; Guglielmi, P.; Pellegrino, G., "Design of Ferrite Assisted Synchronous Reluctance machines robust towards demagnetization," Industry Applications, IEEE Transactions on , vol.PP, no.99, pp.1,1. (Respective Conference Paper: Vagati, A.; Boazzo, B.; Guglielmi, P.; Pellegrino, G., "Ferrite assisted synchronous reluctance machines: A general approach," Electrical Machines (ICEM), 2012 XXth International Conference on , vol., no., pp.1315,1321, 2-5 Sept. 2012)

[13] El-Refaie, A.M.; Jahns, T.M., "Comparison of synchronous PM machine types for wide constant-power speed range operation," Industry Applications Conference, 2005. Fourtieth IAS Annual Meeting. Conference Record of the 2005 , vol.2, no., pp. 1015- 1022.

[14] Pellegrino, G.; Vagati, A.; Guglielmi, P.; Boazzo, B.; , "Performance Comparison Between Surface-Mounted and Interior PM Motor Drives for Electric Vehicle Application," Industrial Electronics, IEEE Transactions on , vol.59, no.2, pp.803-811, Feb. 2012.

[15] P. L. Alger, "The Nature of Polyphase Induction Machines", New York, Wiley, 1951.

[16] J. Haataja, "A comparative performance study of four-pole induction motors and synchronous reluctance motors in variable speed drives", Ph. D., Lappeenranta University of Technology, ISBN 951-764-772-7, ISSN 1456-4491, Lappeenrannan teknillinen yliopisto, Digipaino, 2003.

[17] Mecrow, B.C.; Jack, A.G.; Haylock, J.A.; Coles, J.; , "Fault-tolerant permanent magnet machine drives," Electric Power Applications, IEE Proceedings - , vol.143, no.6, pp.437-442, Nov 1996

[18] El-Refaie, A.M.; Jahns, T.M.; , "Optimal flux weakening in surface PM machines using concentrated windings," Industry Applications Conference, 2004. 39th IAS Annual Meeting. Conference Record of the 2004 IEEE , vol.2, no., pp. 1038- 1047 vol.2, 3-7 Oct. 2004

[19] W.L. Soong, T.J.E. Miller, "Field-weakening performance of brushless synchronous AC motor drives", Electric Power Appl. , IEE Proceedings, Vol. 141, Issue 6, Nov. 1994, pp. 331-340.

[20] T. M. Jahns, "The expanding role of PM machines in direct-drive applications," in Proc. ICEMS, Aug. 20–23, 2011, pp. 1–6.

[21] A. M. EL-Refaie, "Fractional-slot concentrated-windings synchronous permanent magnet machines: Opportunities and challenges," IEEE Trans. Ind. Electron., vol. 57, no. 1, pp. 107–121, Jan. 2010.

[22] J. Cros and P. Viarouge, "Synthesis of high performance PM motors with concentrated windings," IEEE Trans. Energy Convers., vol. 17, no. 2, pp. 248–253, Jun. 2002.

[23] F. Magnussen and C. Sadarangani, "Winding factors and Joule losses of permanent magnet machines with concentrated windings," in Proc. IEEE IEMDC, Jun. 1–4, 2003, vol. 1, pp. 333–339.

[24] P. Salminen, "Fractional slot permanent magnet synchronous motors for low speed applications," Ph.D. dissertation, Dept. of Elect. Eng., Lappeenranta Univ. of Technol., Lappeenranta, Finland, 2004, 150.

[25] N. Bianchi and M. Dai Pre, "Use of the star of slots in designing fractional-slot single-layer synchronous motors," Proc. Inst. Elect. Eng.––Elect. Power Appl., vol. 153, no. 3, pp. 459–466, May 1, 2006.

[26] A. M. El-Refaie, T. M. Jahns, and D. W. Novotny, “Analysis of surface permanent magnet machines with fractional-slot concentrated windings,” IEEE Trans. Energy Convers., vol. 21, no. 1, pp. 34–43, Mar. 2006.

[27] Q. Ronghai and T. A. Lipo, “General closed-form analytical expressions of air-gap inductances for surface-mounted permanent magnet and induction machines,” in Proc. IEEE IEMDC, Jun. 1–4, 2003, vol. 1, pp. 443–448.

[28] D. W. Novotny and T. A. Lipo, Vector Control and Dynamics of AC Drives. Oxford, U.K.: Calderon, 1998.

[29] Guoxin Zhao; Lijian Tian; Qiping Shen; Renyuan Tang, "Demagnetization Analysis of Permanent Magnet Synchronous Machines under Short Circuit Fault," Power and Energy Engineering Conference (APPEEC), 2010 Asia-Pacific , vol., no., pp.1,4, 28-31 March 2010

[30] T. M. Jahns and W. L. Soong, “Pulsating torque minimization techniques for permanent magnet AC motor drives—A review,” IEEE Trans. Ind. Appl., vol. 43, no. 2, pp. 321–330, Apr. 1996.

[31] Z. Q. Zhu and D. Howe, “Influence of design parameters on cogging torque in permanent magnet machines,” IEEE Trans. Energy Conv., vol. 15, no. 4, pp. 407–412, Dec. 2000.

[32] N. Bianchi and S. Bolognani, “Design techniques for reducing the cogging torque in surface-mounted PM motors,” IEEE Trans. Ind. Appl., vol. 38, no. 5, pp. 1259–1265, Sep./Oct. 2002.

[33] L. Zhu, S. Z. Jiang, Z. Q. Zhu, and C. C. Chan, “Analytical methods for minimizing cogging torque in permanent-magnet machines,” IEEE Trans. Magn., vol. 45, no. 4, pp. 2023–2031, Apr. 2009.

[34] T. Li and G. Slemon, “Reduction of cogging torque in permanent magnet motors,” IEEE Trans. Magn., vol. MAG-24, no. 6, pp. 2901–2903, Nov. 1988.

[35] M. F. Hsieh and Y. S. Hsu, “An investigation on influence of magnet arc shaping upon back electromotive force waveforms for design of permanent-magnet brushless motors,” IEEE Trans. Magn., vol. 41, no. 10, pp. 3949–3951, Oct. 2005.

[36] Y. Li, J. Xing, T. Wang, and Y. Lu, “Programmable design of magnet shape for permanent-magnet synchronous motors with sinusoidal back EMF waveforms,”

IEEE Trans. Magn., vol. 44, no. 9, pp. 2163–2167, Sep. 2008.

[37] Y. Pang, Z. Q. Zhu, and Z. J. Feng, "Cogging torque in cost-effective surface-mounted permanent-magnet machines," IEEE Trans. Magn., vol. 47, no. 9, pp. 2269–2276, Sep. 2011.

[38] S.-M. Jang, H.-I. Park, J.-Y. Choi, K.-J. Ko, and S.-H. Lee, "Magnet pole shape design of permanent magnet machine for minimization of torque ripple based on electromagnetic field theory," IEEE Trans. Magn., vol. 47, no. 10, pp. 3586–3589, Oct. 2011.

[39] S. Lee, Y.-J. Kim, and S.-Y. Jung, "Numerical investigation on torque harmonics reduction of interior PM synchronous motor with concentrated winding," IEEE Trans. Magn., vol. 48, no. 2, pp. 927–930, Feb. 2012.

[40] Z. Q. Zhu, S. Ruangsinchaiwanich, N. Schofield, and D. Howe, "Reduction of cogging torque in interior-magnet brushless machines," IEEE Trans. Magn., vol. 39, no. 5, pp. 3238–3240, Sep. 2003.

[41] C. S. Koh, H. S. Yoon, K. W. Nam, and H. S. Choi, "Magnetic pole shape optimization of permanent magnet motor for reduction of cogging torque," IEEE Trans. Magn., vol. 33, no. 2, pp. 1822–1827, Mar. 1997.

[42] R. Lateb, N. Takorabet, and F. Meibody-Tabar, "Effect of magnet segmentation on the cogging torque in surface-mounted permanent-magnet motors," IEEE Trans. Magn., vol. 42, no. 3, pp. 442–445, Mar. 2006.

[43] D. G. Dorrell and M. Popescu, "Odd stator slot numbers in brushless DC machines—An aid to cogging torque reduction," IEEE Trans. Magn., vol. 47, no. 10, pp. 3012–3015, Oct. 2011.

[44] M. Lukaniszyn, M. JagieLa, and R. Wrobel, "Optimization of permanent magnet shape for minimum cogging torque using a genetic algorithm," IEEE Trans. Magn., vol. 40, no. 2, pp. 1228–1231, Mar. 2004.

[45] L. Dosiek and P. Pillay, "Cogging torque reduction in permanent magnet machines," IEEE Trans. Ind. Appl., vol. 43, no. 6, pp. 1565–1571, Nov.-Dec. 2007.

[46] C. S. Koh and J. S. Seol, "New cogging-torque reduction method for brushless permanent-magnet motors," IEEE Trans. Magn., vol. 39, no. 6, pp. 3503–3506, Nov. 2003.

[47] Z.Q.Zhu, J.T.Chen, L. J.Wu, andD. Howe, “Influence of stator asymmetry on cogging torque of permanent magnet brushless machines,” IEEE Trans. Magn., vol. 44, no. 11, pp. 3851–3854, Nov. 2008.

[48] W. Fei and P. Luk, “Torque ripple reduction of a direct-drive permanent magnet synchronous machine by material-efficient axial pole pairing,” IEEE Trans. Ind. Appl., vol. 59, no. 6, pp. 2601–2611, Jun. 2012.

[49] M. Aydin, Z. Q. Zhu, T. A. Lipo, and D. Howe, “Minimization of cogging torque in axial-flux permanent-magnet machines: design concepts,” IEEE Trans. Magn., vol. 43, no. 9, pp. 3614–2622, Sep. 2007.

[50] J. Holtz and L. Springob, “Identification and compensation of torque ripple in high-precision permanent magnet motor drives,” IEEE Trans. Ind. Appl., vol. 43, no. 2, pp. 309–320, Apr. 1996.

[51] N. Matsui, T. Makino, and H. Satoh, “Autocompensation of torque ripple of direct drive motor by torque observer,” IEEE Trans. Ind. Appl., vol. 29, no. 1, pp. 187–194, Jan./Feb. 1993.

[52] J.X.Xu, S.K. Panda,Y. J. Pan, T. H. Lee, andB.H. Lam, “Amodular control scheme for PMSM speed control with pulsating torque minimization,” IEEE Trans. Ind. Appl., vol. 51, no. 3, pp. 526–536, Jun. 2004.

[53] Z. Q. Zhu, Y. Liu, and D. Howe, “Minimizing the influence of cogging torque on vibration of PM brushless machines by direct torque control,” IEEE Trans. Magn., vol. 42, no. 10, pp. 3512–3514, Oct. 2006.

[54] A. Vagati, “Synchronous Reluctance Electrical Motor having a low torque ripple design”, US Patent 5,818,140 – Oct.6,1998.

[55] A. Vagati, M. Pastorelli, G. Franceschini, and S. Petrache, "Design of low-torque-ripple synchronous reluctance motors," Industry Applications, IEEE Transactions on, vol. 34, no. 4, pp. 758 -765, jul/aug 1998.

[56] T. Lipo, “Introduction to AC Machine Design”, University of Wisconsin Power Electronics Research Center, 1993.

[57] A. Vagati and P. Guglielmi et al., "Design, analysis and control of Interior PM synchronous machines". Tutorial Course notes of IEEE Industry Applications Society Annual Meeting (IAS), CLEUP, Padova (Italy), ISBN 88-7178-898-2, pp. 6.1-

6.35, 2004.

[58] R.R. Moghaddam, "Synchronous Reluctance Machine (SynRM) in Variable Speed Drives (VSD) Applications". ISBN 978-91-7415-972-1, PhD Doctoral Thesis, edited by KTH, Stockholm, SWEDEN, 2011.

[59] Sanada, M.; Inoue, Y.; Morimoto, S.; "Rotor structure for reducing demagnetization of magnet in a PMASynRM with ferrite permanent magnet and its characteristics," Energy Conversion Congress and Exposition (ECCE), 2011 IEEE , vol., no., pp.4189-4194.

[60] Hitachi, "High Energy Ferrite Magnets – NMF Series", http://www.hitachi-metals.co.jp/

[61] J. D. McFarland and T. M. Jahns, "Investigation of the rotor demagnetization characteristics of interior PM synchronous machines during fault conditions," in Energy Conversion Congress and Exposition (ECCE), 2012 IEEE, 2012, pp. 4021-4028.

[62] G. Franceschini, A. Fratta, C. Petrache, A. Vagati, and F. Villata, "Design comparison between induction and synchronous reluctance motors," in ICEM 1994, Paris, France, Sept. 6-8, 1994.

[63] T. J. E. Miller Brushless PM and Reluctance Motor Drives, 1989 :Clarendon

[64] E. Lovelace, T. Jahns, and J. Lang, "A saturating lumped-parameter model for an interior PMsynchronous machine," IEEE Trans. Ind. Appl., vol. 38, no. 3, pp. 645–650, May/Jun. 2002.

[65] N. Bianchi, S. Bolognani, D. Bon, and M. D. Pre, "Rotor flux-barrier design for torque ripple reduction in synchronous reluctance and PM assisted synchronous reluctance motors," IEEE Trans. Ind. Appl., vol. 45, no. 3, pp. 921–928, May/Jun. 2009.

[66] C. Jo, J.-Y. Seol, and I.-J. Ha, "Flux-weakening control of IPM motors with significant effect of magnetic saturation and stator resistance," IEEE Trans. Ind. Electron., vol. 55, no. 3, pp. 1330–1340, Mar. 2008.

[67] G. Foo and M. Rahman, "Sensorless direct torque and flux-controlled IPM synchronous motor drive at very low speed without signal injection," IEEE Trans. Ind. Electron., vol. 57, no. 1, pp. 395–403, Jan. 2010.

[68] M. Barcaro, N. Bianchi, and F. Magnussen, "Rotor flux-barrier geometry design to reduce stator iron losses in synchronous IPM motors under FW operations," IEEE Trans. Ind. Appl., vol. 46, no. 5, pp. 1950–1958, Sep./Oct. 2010.

[69] S.-H. Han, W. Soong, T. Jahns, M. Guven, and M. Illindala, "Reducing harmonic eddy-current losses in the stator teeth of interior permanent magnet synchronous machines during flux weakening," IEEE Trans. Energy Convers., vol. 25, no. 2, pp. 441–449, Jun. 2010.

[70] A. Consoli, G. Scarcella, and A. Testa, "Industry application of zero-speed sensorless control techniques for PM synchronous motors," IEEE Trans. Ind. Appl., vol. 37, no. 2, pp. 513–521, Mar./Apr. 2001.

[71] H. Kim, M. Harke, and R. Lorenz, "Sensorless control of interior permanent-magnet machine drives with zero-phase lag position estimation," IEEE Trans. Ind. Appl., vol. 39, no. 6, pp. 1726–1733, Nov./Dec. 2003.

[72] P. Guglielmi, M. Pastorelli, G. Pellegrino, and A. Vagati, "Position sensorless control of permanent-magnet-assisted synchronous reluctance motor," IEEE Trans. Ind. Appl., vol. 40, no. 2, pp. 615–622, Mar./Apr. 2004.

[73] M. Barcaro, N. Bianchi, and F. Magnussen, "Design considerations to maximize performance of an IPM motor for a wide flux-weakening region," in Proc. 19th ICEM, Sep. 2010, pp. 1–7

[74] G. Pellegrino, A. Vagati, and P. Guglielmi, "Design tradeoffs between constant power speed range, uncontrolled generator operation, and rated current of IPM motor drives," IEEE Trans. Ind. Appl., vol. 47, no. 5, pp. 1995–2003, Sep./Oct. 2011.

[75] K. Williamson, "GE Returns Offshore with New Turbine", Renewable Energy Focus.com, Apr. 2011. http://www.renewableenergyfocus.com/view/17427/ge-returns-offshore-with-new-turbine/

[76] Z. Q. Zhu and C. C. Chan, "Electrical machine topologies and technologies for electric, hybrid, and fuel cell vehicles," in Proc. IEEE VPPC, Sep. 3–5, 2008, pp. 1–6.

[77] K. T. Chau, C. C. Chan, and C. Liu, "Overview of permanent-magnet brushless drives for electric and hybrid electric vehicles," IEEE Trans. Ind. Electron., vol. 55, no. 6, pp. 2246–2257, Jun. 2008.

[78] http://www.crzforum.com/forum/engine-battery-discussion/777-hondasima-

breakdown.html

[79] J. J. Germishuizen and M. J. Kamper, "IPM traction machine with single layer non-overlapping concentrated windings," IEEE Trans. Ind. Appl., vol. 45, no. 4, pp. 1387–1394, Jul./Aug. 2009.

[80] L. Chong and M. F. Rahman, "Saliency ratio derivation and optimization for an interior permanent magnet machine with concentrated windings using finite-element analysis," IET Elect. Power Appl., vol. 4, no. 4, pp. 249–258, Apr. 2010.

[81] T. M. Jahns and V. Caliskan, "Uncontrolled generator operation of interior PM synchronous machines following high-speed inverter shutdown," IEEE Trans. Ind. Appl., vol. 35, no. 6, pp. 1347–1357, Nov./Dec. 1999.

[82] P. Guglielmi, E. Armando, G. Pellegrino, and A. Vagati, "Optimal design of IPM-PMASR motors for wide constant power speed range," in Proc. PCIM, Nurnberg, Germany, 2007, pp. 1–6.

[83] G. Pellegrino, P. Guglielmi, A. Vagati, and F. Villata, "Core loss and torque ripple in IPM machines: Dedicated modeling and design trade off," in Proc. IEEE ECCE, Sep. 20–24, 2009, pp. 1911–1918.

[84] Bilewski, M.; Fratta, A.; Giordano, L.; Vagati, A.; Villata, F.; , "Control of high-performance interior permanent magnet synchronous drives," Industry Applications, IEEE Transactions on , vol.29, no.2, pp.328-337, Mar/Apr 1993

[85] L. Harnefors, M. Jansson, R. Ottersen and K. Pietiläinen, "Unified Sensorless Vector Control of Synchronous and Induction Motors", IEEE Trans. Ind. Electron.,vol.50, No.1, February 2003, pp.153-160.

[86] I. Boldea, M.C. Paicu and Gh.-D. Andreescu, "Active Flux Concept for Motion-Sensorless Unified AC Drives", IEEE Trans. Power Electron., Vol.23, No.5, September 2008, pp. 2612-2618.

[87] Guglielmi, P.; Pastorelli, M.; Vagati, A.; , "Cross-Saturation Effects in IPM Motors and Related Impact on Sensorless Control," Industry Applications, IEEE Transactions on , vol.42, no.6, pp.1516-1522, Nov.-dec. 2006

[88] B. Stumberger, G. Stumberger, D. Dolinar, A. Hamler, and M. Trlep, "Evaluation of saturation and cross-magnetization effects in interior permanent-magnet synchronous motor," Industry Applications, IEEE Transactions on, vol. 39, no. 5, pp.

1264 – 1271, sept.-oct. 2003.

[89] K. Rahman and S. Hiti, "Identification of machine parameters of a synchronous motor," Industry Applications, IEEE Transactions on, vol. 41, no. 2, pp. 557 – 565, march-april 2005.

[90] R. Dutta and M. Rahman, "A comparative analysis of two test methods of measuring - and -axes inductances of interior permanent-magnet machine," Magnetics, IEEE Transactions on, vol. 42, no. 11, pp. 3712–3718, nov. 2006.

[91] P. Guglielmi, M. Pastorelli, and A. Vagati, "Impact of cross-saturation in sensorless control of transverse-laminated synchronous reluctance motors," Industrial Electronics, IEEE Transactions on, vol. 53, no. 2, pp. 429 – 439, april 2006.

[92] E. Armando, P. Guglielmi, G. Pellegrino, M. Pastorelli, and A. Vagati, "Accurate modeling and performance analysis of ipm-pmasr motors," IEEE Trans. on Industry Applicat., vol. 45, no. 1, pp. 123 –130, 2009.

[93] N. Bianchi and S. Bolognani, "Magnetic models of saturated interior permanent magnet motors based on finite element analysis," in IEEE Industry Applications Conference IAS 1998, vol. 1, Oct. 1998, pp. 27–34 vol.1.

[94] K. Meessen, P. Thelin, J. Soulard, and E. Lomonova, "Inductance calculations of permanent-magnet synchronous machines including flux change and self- and cross-saturations," Magnetics, IEEE Transactions on, vol. 44, no. 10, pp. 2324 – 2331, oct. 2008.

[95] A. Wijenayake and P. Schmidt, "Modeling and analysis of permanent magnet synchronous motor by taking saturation and core loss into account," in IEEE Conference on Power Electronics and Drive Systems PEDS 1997, vol. 2, May 1997, pp. 530 –534 vol.2.

[96] T. Frenzke, "Impacts of cross-saturation on sensorless control of surface permanent magnet synchronous motors," in European Conference on Power Electronics and Application EPE 2005, 0 2005.

[97] G. Pellegrino, E. Armando, and P. Guglielmi, "Direct-flux vector control of ipm motor drives in the maximum torque per voltage speed range," Industrial Electronics, IEEE Transactions on, vol. 59, no. 10, pp. 3780–3788, oct. 2012.

[98] A. Yoo and S.-K. Sul, "Design of flux observer robust to interior permanent-magnet

synchronous motor flux variation," Industry Applications, IEEE Transactions on, vol. 45, no. 5, pp. 1670 –1677, sept.-oct. 2009.

[99] L. Le and W. Wilson, "Synchronous machine parameter identification: a time domain approach," Energy Conversion, IEEE Transactions on, vol. 3, no. 2, pp. 241 –248, jun 1988.

[100] E. Boje, J. Balda, R. Harley, and R. Beck, "Time-domain identification of synchronous machine parameters from simple standstill tests," Energy Conversion, IEEE Transactions on, vol. 5, no. 1, pp. 164 –175, mar 1990.

[101] Armando, E.; Bojoi, R.I.; Guglielmi, P.; Pellegrino, G.; Pastorelli, M., "Experimental Identification of the Magnetic Model of Synchronous Machines," Industry Applications, IEEE Transactions on , vol.49, no.5, pp.2116,2125, Sept.-Oct. 2013

[102] Buja, G.S.; Kazmierkowski, M.P.; , "Direct torque control of PWM inverter-fed AC motors - a survey," Industrial Electronics, IEEE Transactions on , vol.51, no.4, pp. 744- 757, Aug. 2004

[103] Inoue, Y.; Morimoto, S.; Sanada, M.; , "Control Method Suitable for Direct-Torque-Control-Based Motor Drive System Satisfying Voltage and Current Limitations," Industry Applications, IEEE Transactions on , vol.48, no.3, pp.970-976, May-June 2012

[104] Pellegrino, G.; Bojoi, R.I.; Guglielmi, P.; , "Unified Direct-Flux Vector Control for AC Motor Drives," Industry Applications, IEEE Transactions on , vol.47, no.5, pp.2093-2102, Sept.-Oct. 2011

[105] Morimoto, S.; Sanada, M.; Takeda, Y., "Wide-speed operation of interior permanent magnet synchronous motors with high-performance current regulator," Industry Applications, IEEE Transactions on , vol.30, no.4, pp.920,926, Jul/Aug 1994

[106] Jae Suk Lee; Chan-Hee Choi; Jul-Ki Seok; Lorenz, R.D.; , "Deadbeat-Direct Torque and Flux Control of Interior Permanent Magnet Synchronous Machines With Discrete Time Stator Current and Stator Flux Linkage Observer," Industry Applications, IEEE Transactions on, vol.47, no.4, pp.1749-1758, July-Aug. 2011

[107] Kukrer, O.; , "Discrete-time current control of voltage-fed three-phase PWM inverters," Power Electronics, IEEE Transactions on , vol.11, no.2, pp.260-269, Mar 1996

[108] Maes, J.; Melkebeek, J.; , "Discrete time direct torque control of induction motors using back-EMF measurement," Industry Applications Conference, 1998. Thirty-Third IAS Annual Meeting. The 1998 IEEE , vol.1, no., pp.407-414 vol.1, 12-15 Oct. 1998

[109] Kenny, B.H.; Lorenz, R.D.; , "Stator- and rotor-flux-based deadbeat direct torque control of induction machines," Industry Applications, IEEE Transactions on , vol.39, no.4, pp. 1093- 1101, July-Aug. 2003

[110] Preindl, M.; Bolognani, S., "Model Predictive Direct Speed Control with Finite Control Set of PMSM Drive Systems," Power Electronics, IEEE Transactions on , vol.28, no.2, pp.1007,1015, Feb. 2013

[111] N. Bianchi and S. Bolognani, “Magnetic models of saturated interior permanent magnet motors based on finite element analysis,” in IEEE Industry Applications Conference IAS 1998, vol. 1, Oct. 1998, pp. 27–34 vol.1.